Laser Metal Deposition of Aluminium-Copper alloys for Repair applications

Stéphane Touzé

THÈSE DE DOCTORAT DE

L'ÉCOLE CENTRALE DE NANTES
COMUE UNIVERSITE BRETAGNE LOIRE

ECOLE DOCTORALE N° 602
Sciences pour l'Ingénieur
Spécialité : Génie Mécanique

Par **Stéphane TOUZÉ**

Laser Metal Deposition of Aluminium-Copper alloys for Repair applications

Thèse présentée et soutenue le 16 septembre 2019 à l'Ecole Centrale de Nantes (France)

Unité de recherche : UMR 6183, Institut de Recherche en Génie Civil et Mécanique (GeM)

Rapporteurs :

Anne-Marie Habraken	Directrice de Recherches FNRS, Université de Liège
Yann Quinsat	Professeur Agrégé (HDR), Ecole Normale Supérieure Paris-Saclay

Composition du Jury :

Président :	Patrice Peyre	Directeur de Recherche CNRS, Arts et Métiers ParisTech-CNRS-CNAM
Rapporteurs :	Anne-Marie Habraken	Directrice de Recherches FNRS, Université de Liège
	Yann Quinsat	Professeur Agrégé (HDR), Ecole Normale Supérieure Paris-Saclay
Examinateur :	Lucas Dembinski	Enseignant-Chercheur, Université de Technologie Belfort-Montbéliard
Dir. de thèse :	Jean-Yves Hascoët	Professeur des Universités, Ecole Centrale de Nantes
Co-dir. de thèse :	Matthieu Rauch	Maître de Conférences (HDR), Ecole Centrale de Nantes

Invité :

Philippe Spilers	Directeur d'activité, APS Coating Solutions

Remerciements

Je souhaiterais tout d'abord remercier chaleureusement Jean-Yves Hascoët et Matthieu Rauch d'avoir accepté de m'accueillir dans leur équipe de recherche et de m'encadrer pendant ce travail de thèse qui aura été particulièrement enrichissant, tant d'un point de vue professionnel que personnel.

Je salue également les contributions des autres membres de l'équipe, en particulier Thierry Broquin et Gilles Carabin, qui ont su me faire profiter de leur expérience et de leur maîtrise des machines. J'adresse également tous mes vœux de réussite à mes camarades doctorants (Tugdual, Gatien, Alexia, Uzoma, Olivier, Vincent, Jérôme...) ainsi qu'à Benoit, Perrine et Manjaiah, avec qui j'ai pu avoir de nombreux échanges profitables au cours de mes travaux.

Je voudrais également remercier Philippe Spilers de m'avoir permis d'effectuer cette thèse CIFRE en partenariat avec l'entreprise APS Coating Solutions, ainsi que tous les partenaires du projet Nenufar pour nos fructueux échanges lors des comités de pilotage.

Je souhaite adresser également mes sincères remerciements à l'ensemble des membres du jury (Anne-Marie Habraken, Yann Quinsat, Patrice Peyre, Lucas Dembinski, Philippe Spilers) pour avoir accepté de lire ce travail de thèse et de m'offrir leurs commentaires et questionnements.

Enfin, je souhaite exprimer mon infinie gratitude à mes parents pour leur soutien indéfectible tout au long de ces années, et notamment pendant ma vie de thésard.

Abbreviations

AM: Additive Manufacturing
BED: Backscatter Electron Detector
CAD: Computer-Aided Design
CAM: Computer-Aided Manufacturing
CFD-DEM: Computational Fluid Dynamics – Discrete Element Method
CNC: Computer Numerical Control
COV: Coefficient of Variation
DED: Direct Energy Deposition
EBM: Electron Beam Melting
ECN: Ecole Centrale de Nantes
HAZ: Heat Affected Zone
LMD: Laser Metal Deposition
LoG: Laplacian of Gaussian
PDE: Partial Differential Equation
PMZ: Partially Melted Zone
PSD: Particle Size Distribution
ROI: Region of Interest
SED: Secondary Electron Detector
SEM: Scanning Electron Microscope
SLM: Selective Laser Melting
UTBM: Université de Technologie Belfort-Montbéliard
vdW: van der Waals
WAAM: Wire-Arc Additive Manufacturing

Table of Contents

Table of Figures

List of Tables

Introduction

Additive manufacturing has recently emerged as a new paradigm for fabricating functional industrial parts made of metallic alloys. In contrast to more traditional metalworking processes such as machining, forming and casting, it proceeds by locally depositing thin layers of material to gradually build towards a near net-shape component using computer-based numerical controllers.

Otherwise known as 3D printing, this manufacturing approach was born in 1981 and has long been restricted to other classes of materials such as polymers using processes based on material extrusion or photo-polymerization. Due to the low mechanical properties of these materials, early industrial applications were mostly confined to rapid prototyping applications to improve the design cycle of new parts by providing on-demand physical models without the need for investing in new tooling with each design iteration.

Recent developments in additive manufacturing processes have allowed to move from polymers towards a much larger range of materials, including metallic alloys for which there is a tremendous amount of possible industrial applications. Indeed, this class of materials is widely used in many industries to manufacture functional load-bearing parts, notably in the aeronautic, aerospace, marine and automotive sectors.

One major advantage of additive manufacturing technology is its capacity to deal with geometrical complexity, thus enabling the efficient fabrication of arbitrarily-shaped objects through the integration of this class of processes with CNC-CAM software suites. Lowering the constraints on part geometry offers the possibility of completely redesigning existing parts so that they can accomplish their function more optimally. Another advantage lies the quality of the deposited material, which in the case of metallic alloys offers a very refined microstructure due to the rapid solidification conditions, especially with laser-based additive manufacturing processes, thereby providing improved mechanical properties.

Among the current categories of metal additive manufacturing processes, Direct Energy Deposition processes such as Laser Metal Deposition locally feed and melt the alloy material as needed in the deposition region. This allows to generate functionally graded material deposits, where the composition of the material can be arbitrarily varied throughout the volume of the part. Another promising application of this category of processes is the ability of repairing and remanufacturing existing parts. In that respect, these processes represent an

alternative to traditional welding processes such as gas-tungsten arc welding that are commonly used in industry for repair purposes in addition to joining applications. Some families of alloys such as high strength Aluminium-Copper alloys are however notorious for their low weldability, and are thus so far very challenging to either join or repair with traditional welding processes. Indeed, Al-Cu alloys are prone to a number of solidification defects such as hot cracking, copper segregation and gas porosities, which leads to a high rejection rate of repairs performed with arc-based welding processes.

This work evaluates the feasibility of using the Laser Metal Deposition process as a replacement of the gas-tungsten arc welding process for repairing high performance aeronautical castings made of a high strength Al-Cu alloy for operation in the compressor stage of a jet engine. The rapid solidification conditions encountered by the powder-based material during Laser Metal Deposition are expected to yield surface repairs of higher quality with greater reliability and efficiency thanks to the computer-based numerical controls. A number of challenges must however be addressed before Laser Metal Deposition technology can be used in this context. The processability of cohesive, low-flowability Al-Cu powders has to be evaluated, and the quality of the rapidly solidified material must also be assessed. Additionally, a method has to be developed to automate the repair process and easily provide the machine code required to carry out the repair. Overcoming these challenges should enable a more widespread use of Laser Metal Deposition with low-weldability alloys, notably for repair and remanufacturing applications, and accelerate the penetration of metal additive manufacturing technology into the industrial landscape.

Chapter I: Additive Manufacturing of Aluminium Alloys for Repair Applications

Abstract

This chapter provides a review on additive manufacturing of aluminium alloys, with a focus on aluminium-copper alloys and industrial repair applications with the Laser Metal Deposition process. Section I is a review of the general properties and characteristics of aluminium and aluminium-copper alloys, followed by a description of various welding and additive manufacturing processes that are relevant to the fabrication and repair of aluminium parts. Section II exposes the challenges of repairing aluminium castings with traditional methods, and subsequently explores the potential use of the Laser Metal Deposition additive manufacturing technology as a repair and remanufacturing process for high-value aluminium castings. Section III formulates the research axes of the present thesis and gives an outline of the research plan and avenues of resolution pursued in this work.

I. Additive Manufacturing of Aluminium Alloys

a. Aluminium and Aluminium-Copper Alloys

i. Pure Aluminium

Aluminium is the most abundant metal and third most abundant element within Earth's crust after oxygen and silicon. It was discovered quite recently, in the 19th century, as it is usually naturally found combined with oxygen and other elements, making it difficult to isolate. First identified in 1807 by Davy, the element Aluminium was first isolated by Oersted in 1825, and was first characterized in 1845 by Wöhler. It is generally obtained from bauxite, an ore rich in aluminium oxides and hydroxides that was named after Les Baux-de-Provence in France where it was first found in 1821 by Berthier. Deville initiated the industrialization of aluminium production in 1856 in France, inducing a ten-fold decrease in price by 1859, albeit yielding fairly impure aluminium with varying properties. Mass production of pure aluminium was really enabled by two discoveries that made its extraction much more economical and reliable: the Hall-Héroult process in 1886, where aluminium is smelted into a pure melted form from dissolved aluminium oxide (alumina Al_2O_3) through an electrolytic reduction, and the Bayer process in 1887, where bauxite is dissolved into alumina using sodium hydroxide (Sverdlin 2003). These processes are still in use today for producing most of the primary aluminium worldwide. Secondary aluminium, recycled from scrap aluminium, need not go through this electrolytic process again as it can be remelted for direct reuse, which only consumes about 3 to 20% of the energy required for producing primary aluminium (Lumley 2018).

Up until being produced at industrial scale, aluminium was considered a precious metal for its silvery color and rarity as it could only be extracted through complicated chemical processes involving costly compounds. Once more expensive than gold or silver, aluminium soon became much more widespread and affordable with the advent of electricity and the discovery of the aforementioned Bayer and Hall-Héroult processes. It started to be used for manufacturing common tools and items as well as for industrial purposes. Praised for its lightness, it was selected by the Wright brothers as a base material for casting the engine crankcase of the first steerable aircraft in human history in 1903, paving the way for a long-standing use of aluminium and its alloys in the aircraft manufacturing industry (D. G. Eskin 2008; Lumley 2018). Part of everyday life since the middle of the 20th century, its yearly production has reached over 50 000 metric tons worldwide since 2013 and keeps on growing every year (Brown et al. 2018).

The chemical element Aluminium has an atomic number of 13 and belongs to the group 13 of the periodic table, also called the boron group, whose elements possess three electrons in their valence layer. These elements present a relatively low melting point and high electronegativity (660.37°C and 1.61 on the Pauling scale for aluminium, respectively) compared to other types of metals. ^{27}Al is the only stable isotope of aluminium, and its most stable radioactive isotope ^{26}Al, with a half-life of about 700 000 years, only exists in trace quantities on Earth as a product of cosmic radiations interacting with argon in the atmosphere. The standard atomic weight of aluminium is thus very close to 27 (i.e. about 26.98). In solid state, it typically adopts face-centered cubic crystalline structure (Hatch 1984).

Aluminium has the electron configuration $1s^2 2s^2 2p^6 3s^2 3p^1$ and can be categorized as a post-transition metal (or sometimes as a metalloid) along with tin, lead and mercury as well as coinage metals such as copper, gold and silver. With only 3 electrons in the valence shell, aluminium is most stable in its third oxidation state (Al^{3+}) and is thus naturally found combined with oxygen, mostly in the form of the amphoteric aluminium(III) oxide α-Al_2O_3, i.e. alumina. Its high affinity for oxygen triggers the formation of a thin, passivation layer of alumina on the surface of aluminium in contact with the atmosphere. Alumina α-Al_2O_3 is a refractory, inert material, with a relatively high melting point (above 2050°C), high hardness and abrasion resistance, as well as low thermal and electrical conductivity. Unlike rust formation in steels, this oxidation reaction is self-limiting in the sense that the oxide layer forms a barrier that prevents further oxidation of the bulk metal. The thickness of this passivation layer is typically on the order of around 5 nanometers for pure aluminium in standard atmospheric conditions (Hatch 1984). Aluminium thus generally offers good corrosion resistance in atmospheric environments. The porous protective layer can only be made thicker by anodizing, by increasing the humidity to form a layer of hydroxides on top of the oxides, by increasing the ambient temperature, or by increasing the partial pressure of oxygen but only when at very low ambient pressures (i.e. under 133 Pa).

Aluminium is light (about 2700 kg/m^3 at room temperature), ductile, soft, easily machinable or extrudable, nonmagnetic, highly reflective of visible and infrared radiations, and is a good electrical and thermal conductor. However, with a yield strength usually between 10 and 30 MPa depending on the impurity level, pure aluminium (> 99.5wt%Al) does not give satisfactory mechanical properties for most industrial applications (Hatch 1984). The impurities generally provide a slight increase in strength, but practical uses of aluminium for manufacturing load-bearing parts is really enabled by alloying, heat treatment and cold working.

ii. Aluminium-Copper alloys

In 1903, Wilm discovered by chance that Al-4wt%Cu-1.5%Mg would slowly harden at room temperature after quenching, leading to the industrial production in 1909 of Duralumin (Al-Cu-Mg-Mn), one of the first precipitation hardening aluminium alloys and currently designated as 2017 by the Aluminum Association nomenclature. Aluminium-Copper alloys, or aluminium series 2000 (2xxx for wrought alloys, 2xx.x for casting alloys), were thus historically the first aluminium alloys of industrial relevance as they have been used ever since the beginning of aircraft manufacturing. While more recent alloy systems such as Aluminium-Lithium-Copper have been developed as a replacement, legacy alloys such as 2014, 2024 and 2219 are still widely adopted as alloys based on this newer system still present issues regarding corrosion resistance and fracture toughness (Muster et al. 2009).

The addition of copper, generally between 1 and 10wt%Cu and more commonly between 4 and 6.3wt%Cu, leads to a heat treatable alloy with high strength and toughness at both room and elevated temperatures (Kaufman and Rooy 2004). Copper being much more soluble in aluminium at high temperature (maximum of 33.15wt% in liquid state) than at low temperatures (maximum of 5.65wt% in solid state), various phases are formed during solidification (Hatch 1984). The appreciable variation in solubility with temperature enables the use of heat treatments, generally a solution heat treatment followed by precipitation aging that causes an improvement in both strength and hardness. During aging, the first precipitates to form from the solid solution are typically plate-like clusters called Guinier-Preston (GP) zones that are coherent with the aluminium matrix. With increased aging time and temperature, those precipitates successively transform into various phases with a decreasing degree of coherency with the primary matrix. Typically, the aging steps for Al-Cu binary alloys are:

$$\text{Supersaturated solid solution} \rightarrow \text{GP} \rightarrow \theta'' \rightarrow \theta' \rightarrow \theta$$

where GP (GP1) are Guinier-Preston zones, θ'' (GP2) and θ' (Al_2Cu) are metastable phases and stable non-coherent θ-phase is the hardening phase copper aluminide Al_2Cu (Hatch 1984). Precipitation hardened Al-Cu casting alloys are among the strongest aluminium alloys available, especially at high temperatures, and are therefore commonly employed in the manufacture of aircrafts, among other types of vehicles, due to their high strength-to-weight ratio as well as fatigue resistance and damage tolerance (Muster et al. 2009).

An increase in copper content generally leads to an increase in hardness, but the impact on other properties such as strength and ductility depends on whether the copper is mostly found in solid solution or at the grain boundaries (Mondolfo 1976). The strength increase is

the highest for dissolved copper, where most of the ductility is retained. When found at the grain boundaries, typically as intermetallic compound Al_2Cu, copper content leads to a lack of ductility and the strength is lower due to the high brittleness of this phase.

Generally, the addition of copper leads to solid solution strengthening and significant dispersion hardening after solid solution heat treatment, quenching and aging because of the increased solubility of copper as temperature increases, as indicated by the shape of the solvus in the Al-Cu thermodynamic phase diagram (figure 1.1). Compared to Al-Mg alloys, Al-Cu alloys typically have a higher yield strength and ultimate tensile strength over a larger temperature range (Zolotorevsky et al. 2007).

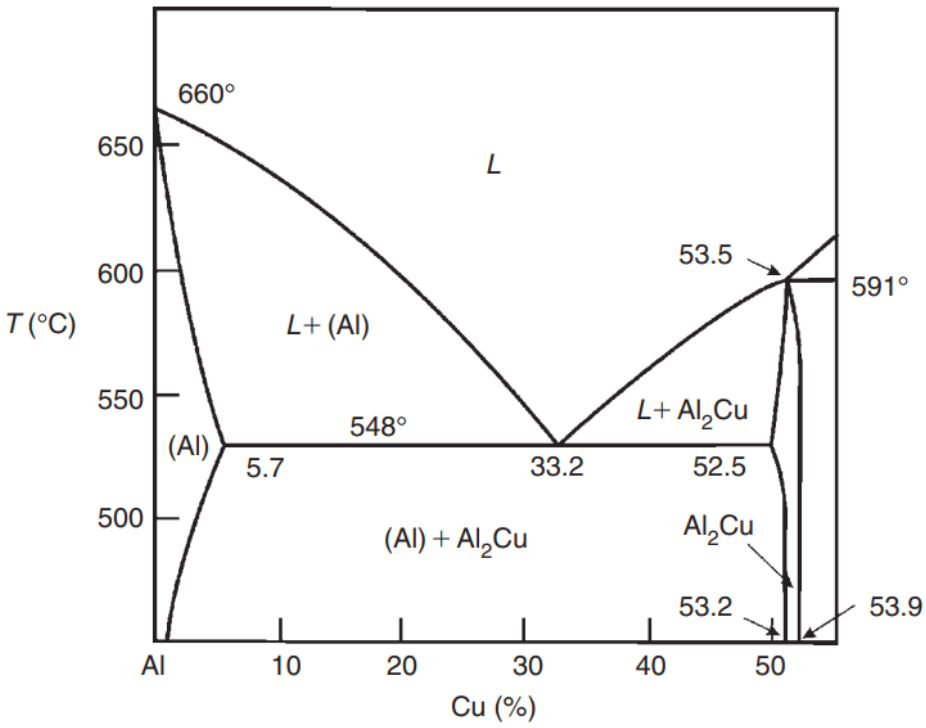

Figure 1.1: Phase Diagram of Al-Cu binary alloy (Zolotorevsky et al. 2007)

The copper content cannot be excessively increased however, as it also increases the alloy's susceptibility to corrosion (Muster et al. 2009), especially in Al-Cu cast alloys with dendrite coring and intermetallic particles Al_2Cu at grain boundaries (Mondolfo 1976). Thus, in practice, most aluminium-copper alloys do not go much beyond 6.3 wt%Cu (wrought aluminium alloy 2219).

Table 1.1 offers a qualitative comparison of major properties of cast aluminium alloys, including Al-Cu (series 2000, heat treatable), Al-Si and Al-Si-Cu (series 4000, heat treatable) and Al-Mg (series 5000, not heat treatable). The strength and thermal stability of Al-Si-Cu is improved compared to Al-Si at the price of a reduction in castability and corrosion resistance.

Al-Cu cast alloys are generally the strongest, especially at higher temperatures, but are also the least castable and weldable.

Alloy	Strength	Forma-bility	Thermal Stability	Corrosion Resistance	Castability	Weldability
Al-Cu	3	3	3	1	1	1-2
Al-Si	1	2	1	2	3	3
Al-Si-Cu	2	1-2	2	1	2-3	3
Al-Mg	1-2	3	1	3	1-2	3

Table 1.1: Properties of cast aluminium alloys (1 = worst, 3 = best) (Zolotorevsky et al. 2007)

In the present work, a specific Al-Cu casting alloy denominated as AU5MVZr or 224.0 is studied for processing by the Laser Metal Deposition additive manufacturing process. The 224.0 ingots were fabricated by the company ARCONIC (formerly ALCOA). The chemical composition of the ingots is shown in table 1.2. In addition to main alloying elements Cu, Mn, Ti, Zr, and V, some traces of Fe, Si, Zn, Mg and Ni are also present (< 0.05wt%).

Alloy	Si	Cu	Mg	Mn	V	Zr	Ti	Fe
AU5MVZr	0.03	4.7	7e-4	0.23	0.08	0.13	0.16	0.03
Standard 224.0	< 0.06	4.5–5.5	-	0.2–0.5	< 0.1	< 0.2	< 0.35	< 0.1
2219	< 0.2	6.3 (5.8 – 6.8)	< 0.02	0.3 (0.2 – 0.4)	0.1 (0.05 – 0.15)	0.18 (0.1 – 0.25)	0.06 (0.02 – 0.1)	< 0.3
2024	< 0.5	4.4 (3.8 - 4.9)	1.5 (1.2 – 1.8)	0.6 (0.3 – 0.9)	-	-	< 0.15	< 0.5

Table 1.2: Composition in wt% of alloys AU5MVZr (based on chemical analysis), 224.0 from (Kaufman and Rooy 2004), 2219 and 2024 from (Kaufman 2000)

Manganese is the most widespread ancillary addition to aluminium alloys, and is added to most commercial Al-Cu cast alloys. It can form precipitates such as $Al_{20}Cu_2Mn_3$ in the form of submicron dispersoid particles that serve to control grain structure and growth (Muster et al. 2009) and offer some dispersion strengthening (Sverdlin 2003). Because of the limited solubility of manganese in aluminium, the manganese can induce the formation of ternary compounds that deplete the Cu content in the solid solution, for example through the invariant reaction: Liquid → Al + Al_2Cu + $Al_{20}Cu_2Mn_3$. This precipitate is incoherent with the aluminium matrix and is usually found at the grain boundaries. In non-equilibrium conditions where cooling rate is above 10^3 K/s, the solubility of manganese increases up to 5wt% which can prevent the formation of the ternary compounds, leaving only binary or unary compounds such as Al_2Cu and Al_6Mn (Mondolfo 1976). Since the ratio of copper to manganese content exceeds 5 in the case of AU5MVZr, the mechanical properties are mostly governed by copper.

Manganese however provides a slight increase in corrosion resistance, reportedly decreases the diffusion of copper and, depending on the composition, can enhance the GP zone formation and stabilize the θ' phase (Mondolfo 1976). In the specific case of Al-Cu-Mn system, even additions of Mn below 1wt% have a significant impact as it significantly increases the thermal stability of the alloy (Zolotorevsky et al. 2007).

Additions of Zr induces the precipitation of Al_3Zr dispersoids, usually in low volume fraction so that dispersion strengthening is limited. However, similarly to other finely dispersed intermetallic precipitates with low solubility and low diffusivity in aluminium, they limit the movement of grains and prevent static recrystallization, which significantly strengthens grain and subgrain boundaries (Sverdlin 2003). The content in dispersoids should nonetheless be carefully controlled as they can induce the nucleation of microvoids by decohesion at the matrix interface.

Generally, addition of Mn as well as other transition metals such as Ti, Zr and V, allows for additional strength as well as grain refinement that leads to better formability (particularly Ti and Zr) and improved resistance to corrosion (especially with Zr, Mn and V). However, traces of Fe and Si can be detrimental as they form "sharp" constituents that can negatively impact mechanical properties such as elongation, fracture toughness and fatigue resistance (Zolotorevsky et al. 2007).

Cast alloy 224.0 belongs to premium strength casting aluminium alloys alongside 201.0, 204.0, 206.0 and 249.0, which are all based on legacy cast alloy 295.0 (Kaufman and Rooy 2004). 224.0 can maintain high mechanical performance at relatively high service temperature (around 230°C) compared to other aluminium alloys, and can thus be employed for manufacturing impellers or compressor volutes in jet engines, typically through an investment casting process. Although currently classified as inactive by the Aluminum Association (Kaufman and Rooy 2004), there are still a few specific industrial applications for alloy 224.0, notably for manufacturing components of jet engines that require a high strength at a relatively high service temperature. However there is a relative lack of available experimental data for this particular alloy. Some physical and mechanical properties of cast alloy 224.0 in tempers T62 (solution heat treatment followed by artificial aging) and T7/T72 (solution heat treatment followed by artificial overaging) are shown in table 1.3 and table 1.4, respectively. Figure 1.2 gives the yield strength and elongation typically found for other heat-treatable aluminium alloys for comparison (Lumley 2018).

Alloy	Process	Density (g/cm^3)	Melting Range (°C)	Thermal Conductivity (W/m.K at 25°C)	Specific heat (J/kg.K at 20°C)	Poisson ratio
224.0-T62	Sand Casting	2.81	550-645	117	963	0.33
224.0-T72	Sand Casting	2.81	550-645	n/a	963	0.33

Table 1.3: Physical properties of cast alloy 224.0 (Kaufman and Rooy 2004)

With premium quality casting practices, cast alloy 224.0-T7 is publicly reported to reach 420 MPa in ultimate tensile strength and 330 MPa in tensile strength (Kaufman and Rooy 2004). The Secondary Dendrite Arm Spacing (SDAS) of alloy 224.0 can be estimated with the classical relation $SDAS = K(G.V)^n$ using $K = 236$ and $n = -0.4$, where G and V represent the thermal gradient and solidification velocity in standard units, respectively (CIRAL et al. 1996). Conversely, the cooling rate $G.V$ can be deduced from SDAS measurements, which are typically between 10 and 100µm for Al-Si and Al-Si-Cu castings (Okayasu et al. 2012). Taking $SDAS = 40$ µm, the cooling rate $R = GV$ is estimated at 84.6 K/s.

Alloy	Process (specimen type)	Ultimate Tensile Strength (MPa)	Tensile Strength $R_{p0.2}$ (MPa)	Shear Ultimate Strength (MPa)	% Elongation
224.0-T72	Sand Casting (test bars)	380	275	240	10 (5D gauge)
224.0-T7	Sand Casting (premium castings)	420	330	n/a	4 (4D gauge)

Table 1.4: Mechanical properties of 224.0 at room temperature (Kaufman and Rooy 2004)

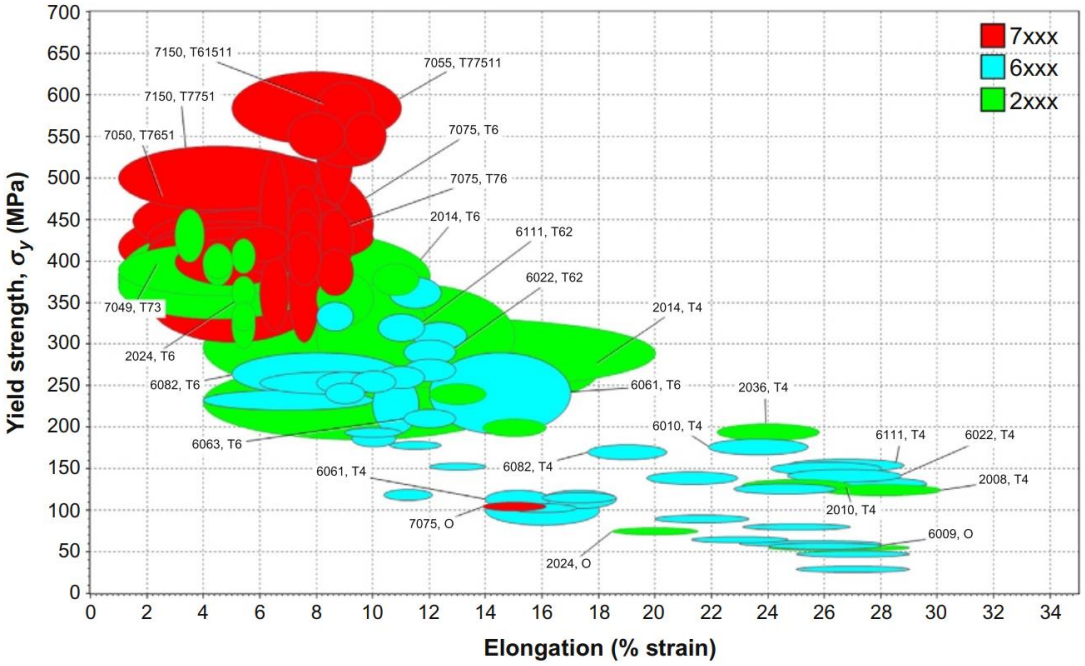

Figure 1.2: Comparison of mechanical properties for various industrial heat-treatable aluminium alloys (Lumley 2018)

iii. Solidification of Aluminium-Copper Alloys

In the perspective of enabling the use of high strength cast alloy 224.0 with the Laser Metal Deposition additive manufacturing process, which involves the laser melting of the material, it is worth considering the general solidification behavior of aluminium-copper alloys with other fusion-based processes.

Cast and wrought aluminium alloys series 2000 are known to be particularly prone to solidification and liquation cracking, and thus necessitate specific casting or welding methods to avoid these types of defects (Kaufman and Rooy 2004; Mathers 2002; Sasabe 2012).

Curves of crack sensitivity as a function of composition for various alloying elements are reproduced in figure 1.3, which shows that the peak crack sensitivity is generally between 2 and 4wt%Cu.

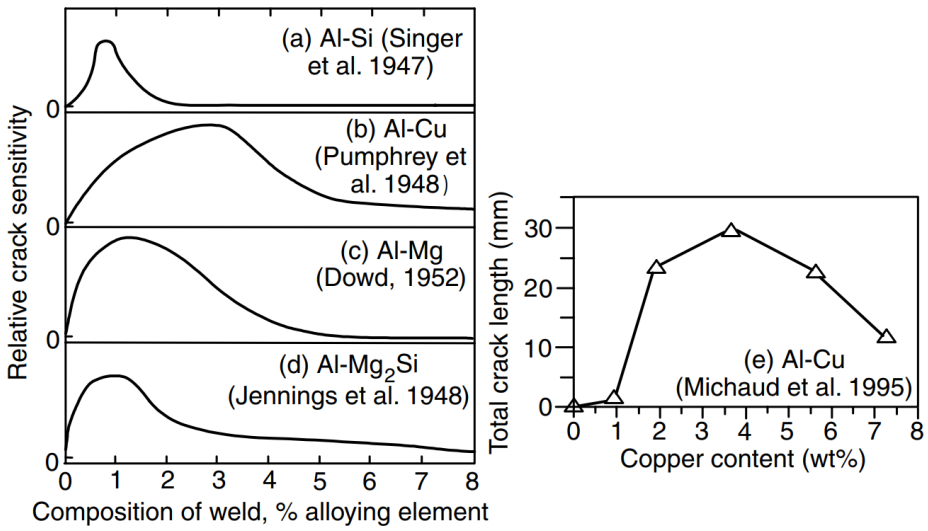

Figure 1.3: Crack sensitivity curves of aluminium alloys (Kou 2003)

Figure 1.4 displays micrographs of the microstructure of Al-Cu welds with increasing copper content obtained with the gas-metal arc welding process. With 4wt%Cu (2219 + filler 1100), a solidification crack is formed whereas with 8wt%Cu (2219 + filler 2319 with extra Cu), the cracks are healed by excess eutectic liquid.

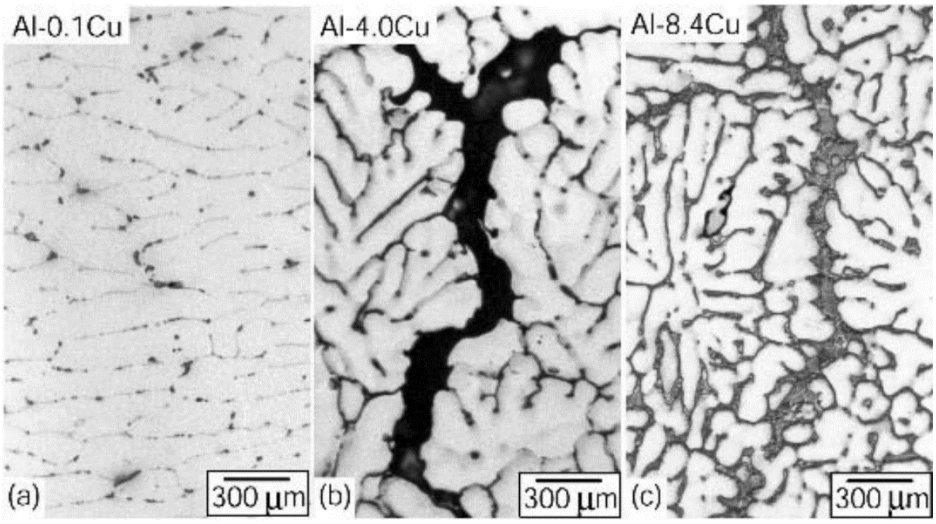

Figure 1.4: Microstructure of GMAW weldments with increasing copper content - (a) 1100 + filler 1100 (b) 2219 + filler 1100 (c) 2219 + filler 2319 with extra Cu (Kou 2003)

At very low copper concentrations, the extent of microsegregation is small and the alloy solidifies almost as a pure metal. At very high concentrations, the copper-rich eutectic liquid can fully backfill the intergranular voids created by the presence of thin eutectic liquid at the grain boundaries, which favors void formation and thus hot crack initiation (Kou 2003). In between lies a particularly detrimental concentration range where there is enough copper to generate a thin liquid film at intergranular boundaries, but insufficient excess liquid to heal the nascent cracks. The ideal range of copper content for cast alloy 224.0 for manufacturing

high performance aeronautical castings is between 4.5 and 4.8wt%Cu as lower copper concentrations favor hot cracking while higher concentrations lead to linear (i.e. banded or plate-like) segregations (Planchamp et al. 1993).

Aluminium-copper alloys were originally deemed unweldable due to their sensitivity to hot cracking. Increasing the copper content up to 6.3wt%Cu, as in aluminium 2219 (Al-Cu6.3-Mn-V-Zr-Ti), led to much more weldable alloys as more liquid eutectic is available near the end of solidification to back-fill hot cracks that may be forming in the interdendritic area during the cooling phase (see figure 1.6). Alloy 2219 and 2195 are essentially the only aluminium alloys series 2000 considered to be weldable.

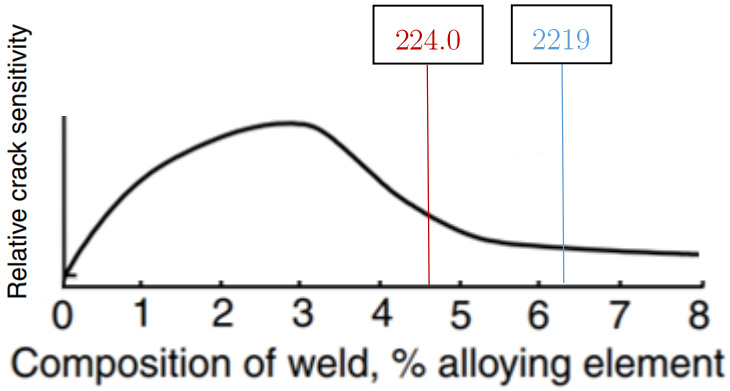

Figure 1.5: Crack sensitivity of aluminium alloys 224.0 and 2219 as a function of copper content (wt%)

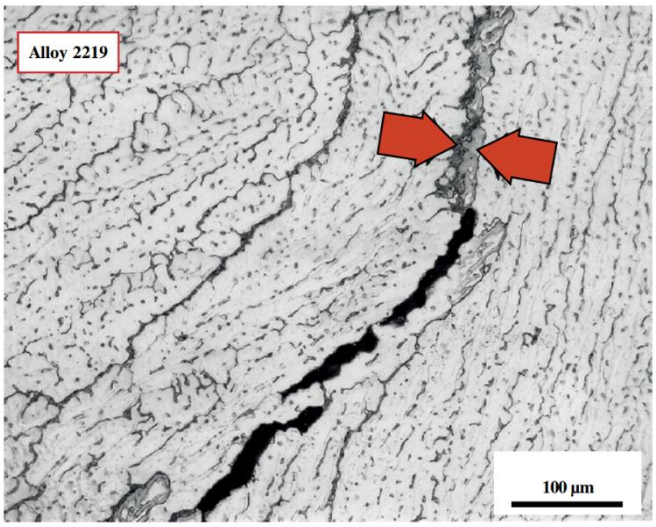

Figure 1.6: Solidification crack in alloy 2219, partially healed by liquid eutectic (red arrows) (Lippold 2015)

It is therefore apparent that there is a close relationship between the segregation of copper and the presence of solidification and liquation cracks in Al-Cu alloys. The copper enrichment of the remaining liquid during solidification creates a thin copper-rich liquid layer at the grain boundaries, which tends to induce the creation of voids bearing the form of the

neighbouring grain boundaries (figure 1.6) (Kou 2003). The presence of low-melting-point compounds within the material can also generate liquation cracks in the partially melted zone (PMZ) of the heat affected zone (HAZ).

Fundamentally, the segregation phenomenon in aluminium-copper alloys is due to the lower solubility of copper in solid versus liquid aluminium. Upon solidification, the solid phase becomes saturated in solute copper atoms that are rejected towards the liquid phase beyond the solid/liquid interface (i.e. solidification front). Although solidification is a non-equilibrium process that requires a thermal or chemical gradient to progress, the interface may be approximately considered to be in a local thermodynamic equilibrium when the solidification rate is sufficiently slow for the atoms to easily self-organize upon the passage of the solidification front (Pfeiler 2007). This is usually the case with casting processes, for which equilibrium phase diagrams can be safely employed (Zolotorevsky et al. 2007). In the solid-liquid zone, an equilibrium partition ratio or equilibrium segregation coefficient k_e can be defined as follows:

$$k_e = \frac{C_S}{C_L} \tag{1.1}$$

where C_S and C_L are the composition of the solid and liquid at temperature T.

On a linearized binary phase diagram (see figure 1.7), where the solidus and liquidus are approximated as lines with constant slopes m_S and m_L, the equilibrium segregation coefficient is constant ($k_e = 0.14$ for Al-4.5wt%Cu). Liquidus temperature T_L is then calculated as:

$$T_L = T_m + m_L C_L \tag{1.2}$$

For $k_e < 1$ ($m_L < 0$), the initial solid cannot contain as much solute as the melt and thus rejects it towards the liquid phase which gets enriched in solute elements. The solute content of the forming solid, which grows from the solute-rich liquid, also increases.

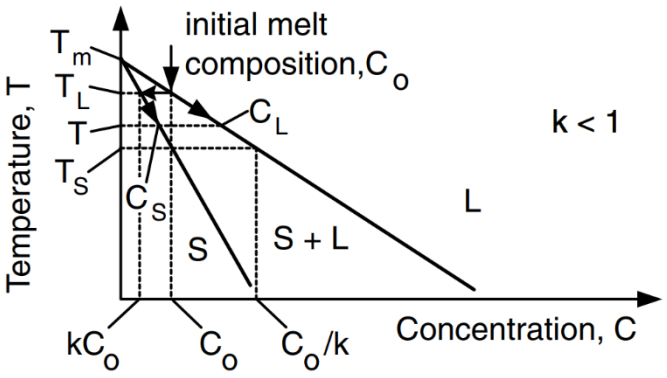

Figure 1.7: Solidification in a linearized binary phase diagram (Kou 2003)

Assuming complete diffusion in the solid and liquid phases, the classic lever rule can be applied to find the solute concentration of the liquid and solid phases as a function of liquid fraction f_L or solid fraction f_S. Using solute conservation and the relation $f_S + f_L = 1$, the equilibrium lever rule reads:

$$C_L f_L + C_S f_S = C_0 \tag{1.3}$$

Using the relation (1.1), the liquid composition $C_L(f_L)$ can be expressed as a function of f_L (Kou 2003):

$$C_L = \frac{C_0}{f_L + k_e(1 - f_L)} \tag{1.4}$$

$$C_S = k_e C_L = \frac{k_e C_0}{f_L + k_e(1 - f_L)} \tag{1.5}$$

At the onset of solidification, i.e. at liquidus temperature T_L with $f_L = 1$, the initial solid and liquid are at composition $k_e C_0$ and C_0, respectively. The compositions of the liquid and solid phases are assumed to be uniform throughout the solidification process, with solid composition increasing from $k_e C_0$ to C_0 and liquid composition from C_0 to C_0/k_e. At the end of solidification, i.e. at solidus temperature T_S with $f_L = 0$, the solid has a uniform composition of C_0 and there is therefore no segregation in the solidified material.

The lever rule is a very simplified solidification model that makes the strong assumption of equilibrium solidification, where equilibrium is maintained not only at the interface but throughout the whole solid and liquid phases. The liquid is assumed to be uniform in composition at any stage, which supposes complete mixing, either due to strong convection current in the melt pool or complete solute diffusion in the liquid. Similarly, the solid is assumed to be uniform in composition, which assumes complete diffusion of solute atoms

within the solid. This ideal case can only be representative of near equilibrium solidification with a very high diffusivity of solute in both solid and liquid phases. Unlike what is observed experimentally however (CIRAL et al. 1996; Dumant 1996; Kou 2003; Planchamp et al. 1993), the lever rule does not predict the occurrence of solute segregation in the fully solidified metal.

Another common solidification model is the Scheil (or Scheil-Gulliver) solidification model, or non-equilibrium lever law, which assumes complete diffusion in the liquid but no solute diffusion in the solid. Equilibrium is only assumed to occur locally at a planar interface. Because the solute does not backdiffuse into the solid, all the solute rejected by the solidifying material goes to the liquid phase. Both liquid and solid solute concentrations rise more rapidly than in the lever rule case, going beyond C_0/k and C_0 respectively. Based on solute conservation, the following Scheil equations for solute segregation can be derived (Kou 2003):

$$C_L = C_0 f_L^{k_e - 1} \tag{1.6}$$

$$C_S = k_e C_0 f_L^{k_e - 1} = k_e C_0 \ 1 - f_S \ ^{k_e - 1} \tag{1.7}$$

For a linear phase diagram with solidus and liquidus as straight lines, the average solid composition $\overline{C_S}$ as a function of solid fraction f_S can be obtained by integration, yielding the following relation:

$$\overline{C_S} = C_0 \big(1 - \ 1 - f_S \ \big)^{k_e} / f_S \tag{1.8}$$

The solid or liquid fraction can be expressed as a function of temperature, thus allowing the calculation of the solidification path f_S versus T.

$$f_L = 1 - f_S = \left(\frac{T_m - T_L}{T_m - T} \right)^{\frac{1}{1 - k_e}} = \left(\frac{-m_L \ C_0}{T_m - T} \right)^{\frac{1}{1 - k_e}} \tag{1.9}$$

This non-equilibrium solidification model, which assumes zero solute diffusion in the solid, predicts the highest solute segregation possible since all of the solute rejected from the solid phase goes into the liquid phase. For Al-Cu alloys, copper diffusivity in liquid and solid aluminium is on the order of 10^{-9} and 10^{-13} m^2/s respectively, hence several orders of magnitude smaller in the solid phase than in the liquid phase. Solid diffusivity of copper may thus be considered to be approximately zero, making the Scheil model rather suitable for Al-Cu alloys solidification in near equilibrium solidification conditions. The lever rule and the Scheil equations represent the two extremes of segregation level for near equilibrium solidification of binary alloys. The actual segregation behavior lies somewhere in between, requiring the effect

of solid backdiffusion or limited liquid diffusion to be accounted for through other models (Kou 2003).

While the above models can serve as a first assessment of the solidification behavior for slow solidification rates, as in casting processes, they cannot be applied to the faster solidification conditions found in welding and laser-based AM as the assumption of local equilibrium at the solid/liquid interface does not hold (Kou 2003). Moreover, the interface is assumed to be planar, although in real solidification conditions, the interface may become unstable and yield various sizes and types of microstructure depending on the local thermal gradients and cooling (or solidification) rates, as shown in figure 1.8, which can influence the solute segregation behavior. Temporal variations in cooling rate can also induce the formation of a banded segregation pattern (Kou 2003).

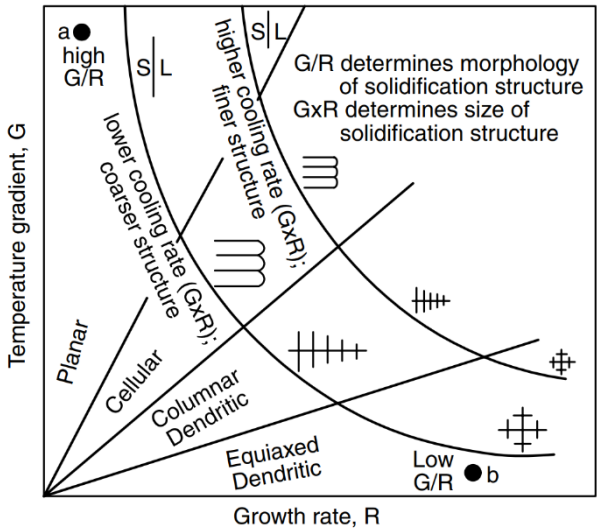

Figure 1.8: Morphology and Size of microstructure depending on solidification conditions (Kou 2003)

When the velocity of the solid/liquid interface is sufficiently high, kinetic effects can induce a variation in liquidus and solidus curves and thus lead to a velocity-dependent partition coefficient (Abbaschian and Lima 2003; Boettinger and Coriell 1984). In such cases, deviations from the equilibrium phase diagram are observed, and kinetic corrections have to be considered (Gill and Kurz 1995; Trivedi 1994). At very high solidification rates (> 1 m/s), the solidus merges with the liquidus so that $k_e \rightarrow 1$ and diffusionless, partionless, segregation-free solidification occurs due to the solute trapping effect (Galenko 2007). Several authors also published solidification microstructure maps of Al-Cu alloys in rapid solidification conditions, showing that various microstructures can develop, such as banded, planar, cellular and dendritic, depending on the solute concentration and solidification rate (Gill and Kurz 1993, 1995; Kurz and Trivedi 1994; Zimmermann et al. 1991). These microstructural maps are typically given for a specific thermal gradient, so that they cannot be universally reapplied to predict the microstructural features obtained with arbitrary rapid solidification conditions.

Several criteria of varying complexity have been proposed to predict the hot cracking susceptibility of alloys based on analytical models and a given solidification path (Coniglio and Cross 2013; Kou 2015a; b; Rappaz et al. 1999; Sheikhi et al. 2015). For a given a solidification path f_S versus T, a particularly simple criterion for hot cracking susceptibility, here called Kou criterion (Kou 2015b), can be defined as follows:

$$max \;\; dT/d(\sqrt{f_S}) \tag{1.10}$$

This criterion rates the cracking susceptibility based on the maximum steepness of the curve T versus $\sqrt{f_S}$. It was shown to successfully predict the relative weldability of various aluminium alloys during welding (Kou 2015b).

Hence, an accurate prediction of the solidification path must be used to correctly characterize the hot cracking sensitivity of an alloy. In rapid solidification conditions, as found in laser-based process such as LMD, the Scheil model and its variants cannot accurately predict the actual solidification path and segregation level as they assume the interface to be in thermodynamic equilibrium. Advanced models relying on phase field methods, where the solid and liquid phases are represented by one or several continuous field variables, have been developed for the numerical simulation of non-equilibrium solidification with a velocity dependent partition coefficient $k(V)$ (Galenko et al. 2011).

b. Wire-Arc Processing of Aluminium-Copper Alloys

i. Gas Tungsten Arc Welding

The Gas Tungsten Arc Welding (GTAW) or TIG (Tungsten Inert Gas) welding process is often used for producing high quality weldments, notably when joining thin components. It generally requires highly skilled operators to reliably produce good quality welds. This process employs a non-consumable, tungsten electrode and optionally a filler wire (figure 1.9). For aluminium welding, the power source is usually set in alternating current (AC) mode so that the oxide film can be removed on the positive half-cycle of the electrode, and the weld bead is formed during the negative electrode half-cycle (Mathers 2002).

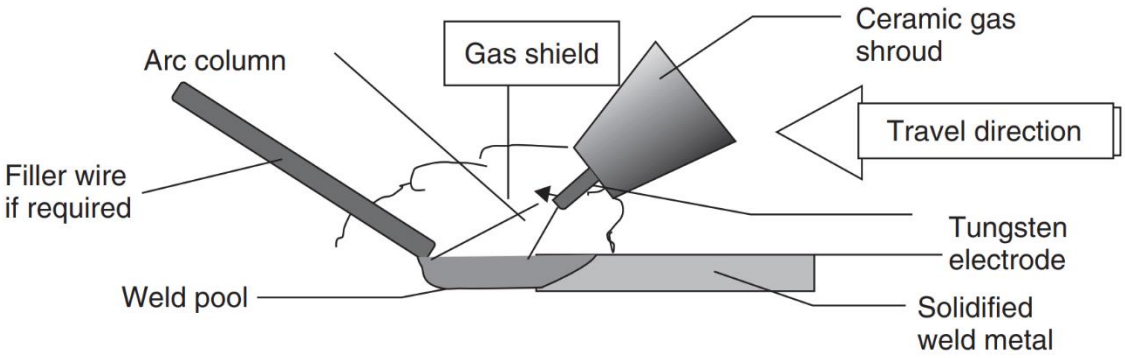

Figure 1.9: Gas Tungsten Arc Welding process (Mathers 2002)

Investigations on the GTAW of alloy 2219-T87 with filler wire 2325 concluded that mechanical properties are higher at a cryogenic temperature of -196°C than at room temperature. The authors observed a dendritic structure in the fusion zone (FZ), and recrystallized grains and enlarged θ precipitates in the HAZ (Lei et al. 2014). Using a pulsed arc mode can be beneficial as it can reduce the liquation in the PMZ. The temper also has an impact as temper T6 induces more liquation than temper T87 (Rao et al. 2005).

Multipass GTAW was used to additively manufacture components with filler wire 2319, generating an equiaxed microstructure with light bands between layers. The mechanical properties are significantly reduced compared to literature values for 2219-T62 due to a lack of precipitation strengthening in the manufacturing process (Bai et al. 2016).

Autogenous GTAW of a 2024 alloy lead to an equiaxed dendritic microstructure in the centre of the weld provided high welding speeds and low power densities were selected. The finer microstructure is due to higher cooling rates, which shorten grain growth and reduce the scale of the secondary dendrite arm spacing. The microsegregation behavior can be described by the Scheil model as copper backdiffusion in the solid is negligible, however the concentration in the dendrite core increases with the welding speed (Norman et al. 1999).

ii. Gas Metal Arc Welding

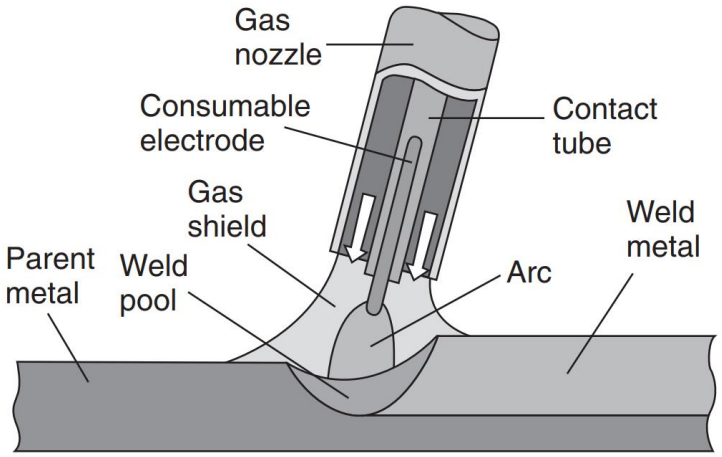

Figure 1.10: Gas Metal Arc Welding process (Mathers 2002)

The Gas Metal Arc Welding (GMAW) or Metal Inert/Active Gas (MIG/MAG) welding process is among the most widely used arc welding processes for welding aluminium alloys as it typically offers deeper penetrations than GTAW, high welding speeds, and good oxide film removal capability. In this process, a metal wire is continuously fed through a welding torch to serve as both a consumable electrode and filler metal (figure 1.10). The wire is melted by an electric arc with inert gas shielding to prevent oxidation during welding. This welding process can be operated either manually or automatically by mounting the welding torch on a robotic arm. The power source is typically configured in direct current (DC) positive mode, although more recent developments in power sources permit the use of AC mode (Mathers 2002).

Most of the literature on GMAW with Al-Cu alloys concerns wrought alloys 2219, which was designed specifically for weldability, as well as 2024, which has a low weldability but is of great industrial relevance, in the aeronautics and aerospace sector especially, due to its high strength properties.

Some authors studied the segregation and cracking mechanisms of alloy 2219-T851 during GMAW with filler alloy 2319 (Huang and Kou 2000, 2004; Kou 2001). Significant liquation is observed in the PMZ at grain boundaries and in locations where large Al_2Cu particles are present. An unfavorable microstructure arises in the form of banded segregations, where phases alternate between ductile α-Al and brittle θ-Al_2Cu. Strong copper segregation causes the dendrite cores to have a low copper content whereas the interdendritic zones contain both coupled eutectic $\alpha+\theta$ and copper-rich eutectic θ. The mechanical strength of the PMZ is lowered by the presence of segregates. No manganese segregation is observed however. In

partial penetration GMAW welds of alloy 2219, liquation cracking was suppressed by the use of a high copper content filler wire (2319 + extra Cu) (Huang and Kou 2003).

A comparative study of GTAW and GMAW of alloy 2219-T87 with filler 2319 showed that the GTAW is more favorable that GMAW for aluminium-copper welding as the thermal cycle is less severe in the fusion zone (FZ) and heat affected zone (HAZ), so that transverse contraction is reduced and tensile mechanical properties are higher (Arunkumar et al. 2015).

Alloy 2024 has a greater liquation tendency than 2219, although this tendency is more pronounced with filler 1100 than with 4043 (Al-Si) (Huang et al. 2004). Hot cracking can be mitigated by the use of filler 5356 (Al-Mg) with extra Cu. This finding was supported by a liquation cracking criteria based on the calculation of solidification path f_S versus T using the Scheil solidification model based on phase diagrams and a variable partition coefficient k_e (Cao and Kou 2006).

iii. Wire-Arc Additive Manufacturing

The Wire-Arc Additive Manufacturing (WAAM) process, which belongs to the family of Direct Energy Deposition (DED) processes, enables the layered manufacturing of fully dense parts using GMAW equipment and typically a multi-axis robotic arm on which the welding torch is mounted. Multipass GMA weld beads are fused onto each other to generate the geometry of the component. This process is still in research & development, although industrial use cases are emerging (Hascoët et al. 2017; Péchet et al. 2019; Quérard et al. 2018). The WAAM process provides several advantages including the ability to manufacture large scale components in reasonable time thanks to the high feedrate of material. It also usually employs established welding processes and can be implemented with commercial welding equipment and standard robotic arms (Hascoët et al. 2018b).

Some limitations such as warpage and residual stresses created by high heat input, dimensional inaccuracies, process stability and the presence of typical welding defects, must still be addressed (Kerninon et al. 2008). To improve the quality of aluminium alloy deposits, research has been conducted on the use of Cold Metal Transfer (CMT) technology (Fronius International GmbH 2013; Selvi et al. 2018) and its various modes in order to reduce the heat input and thus limit the effect of heat on part geometry and properties (Hascoët et al. 2018b). This allowed the manufacture of large scale structures such as stiffeners on both flat and curved metal sheets with wire 5356A in CMT Pulsed Advanced (CMT-PADV) mode (Hascoët et al. 2018b). Deformations were observed away from the clamps used to secure the substrate, which could be reduced by an improved clamping system and a preheating phase.

Experiments with 2319 filler alloy on single and multilayer deposits also concluded that the arc mode has a significant influence on the size and number of gas pores. The CMT-PADV arc mode is shown to be the most suitable for WAAM processing of aluminium alloys as it nearly eliminates the gas porosities, provides a low heat input, permits proper oxide cleaning of the wire, and generates fine equiaxed grains (Cong et al. 2015).

An analysis of WAAM deposits of Al-Cu-Mg with a pulsed arc and tandem wires of Al-Cu and Al-Mg alloys showed that an increase in wire feed speed increased solidification cracking (Gu et al. 2018). Liquation microcracks initiate and propagate within the interlayer equiaxed zone, which is identified as the partially melted zone during deposition. An inverse correlation between hardness and cracking susceptibility is observed. The latter can be influenced by the presence of trace elements such as Ti and Zr in the wire, by the ratio of Cu to Mg, as well as by the type of microstructure. The density of the deposits, which is affected by the presence of cracks and gas pores, reached 99.75%. Microporosities are observed in all samples, with a pore size comprised between 5 and 130µm depending on the wire feed speeds. Gas pores not only reduce the final part density but can also act as crack initiation sites and thus increase the cracking susceptibility. The presence of cracks further reduces the density and mechanical properties of the part.

c. Laser-Based Processing of Aluminium-Copper Alloys

i. Laser Welding

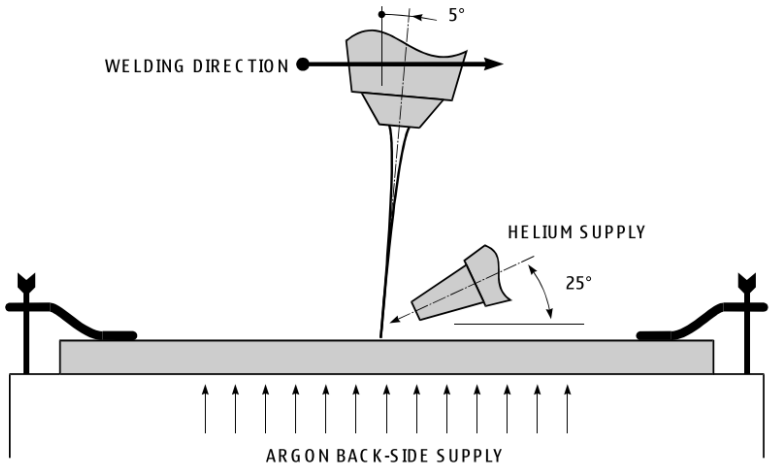

Figure 1.11: Laser welding process for aluminium processing with copper nozzle and back-side shielding (Alfieri et al. 2015)

Laser Welding is increasingly employed in major industries such as automotive and aerospace as a laser heat source can provide large energy densities in highly localized regions, which can help reducing the global heat input during welding and thus limit defects such as deformations and residual stresses (Mathers 2002).

Difficulties are however encountered with laser welding of aluminium alloys as the coupling of the beam with the solid material is limited compared to other alloys such as steels. Indeed, aluminium is amongst the most reflective materials due to its high density of free electrons. The laser radiation absorptivity can be as low as about 1% at wavelengths beyond 10µm, and generally increases with decreasing wavelength, although an intermediate peak is present around 800nm where absorptivity is on the order of 10%. These values however strongly depend on the roughness of the surface to be welded. In the liquid state, the absorptivity slightly increases although it remains quite low. The use of lasers with appropriate wavelengths such as Nd:YAG lasers emitting at a wavelength of 1060nm, which is in a favorable region of absorptivity for most metals, can facilitate the welding process by reducing the necessary energy input (Quintino et al. 2010).

Laser welding can be performed in either heat conduction mode or keyhole mode, the keyhole regime being generally used for welding aluminium alloys. Suitable welding procedures must be followed to avoid defects such as porosity and hot cracking, especially for aluminium-copper alloys which generally present a high cracking susceptibility. The use of back-side shielding gas and an angular deviation of 5° is also advised, as shown on figure 1.11 (Alfieri et al. 2015). Gas porosities are frequently observed, either due to the vaporization of alloy elements such as magnesium, which is particularly volatile, or the 20-to-1 difference in hydrogen solubility in liquid versus solid aluminium, respectively, so that hydrogen gas may become trapped in the rapidly solidifying material (Quintino et al. 2010).

Laser welding of aluminium alloys is also challenging due to the fact that a thin oxide layer of alumina, a refractory material with a high melting point (above 2050°C), is spontaneously generated upon contact with oxygen. Higher heat input may be used initially to trigger the onset of melting, but the overall heat input of the laser must remain carefully controlled to avoid major defects. Aluminium presents a high thermal conductivity and heat capacity, so that it necessitates a relatively high energy input per unit mass in order to see an increase its temperature, but it also has high thermal expansion coefficient and is thus highly susceptible to thermal deformations, which further complicates the optimization of the laser welding process parameters. Variations in laser absorptivity can also occur, notably because of variations in alloy composition throughout the material. In addition, the viscosity of liquid aluminium is relatively low, which can lead to instabilities in the melt pool, especially in keyhole mode (Quintino et al. 2010). Although the above considerations are also to some extent applicable to other welding processes such GTAW and GMAW, they are particularly

salient with laser-based welding due to the high energy densities, high thermal gradients and rapid cooling which require particularly fine control of the processing conditions.

Aluminium-Copper alloys present the added difficulty of being highly susceptible to hot cracking. Pulsed laser welding of aluminium alloys with several compositions between 0.96 to 7.28wt%Cu revealed that the cracking sensitivity curve peaks for composition Al-3.73wt%Cu, and that the extent of cracks could be reduced by pulse shaping (Michaud et al. 1995). Fusion lines with laser welding in continuous mode showed no cracking at 5wt%Cu, while lower compositions displayed a cracking sensitivity versus laser scan speed that also presents a peak of maximum cracking susceptibility (Abbaschian and Lima 2003). The shape is similar to the cracking sensitivity curves versus composition (Kou 2003). The presence of a maximum at an intermediate composition is reportedly caused by the size of interdendritic pores and the microsegregation phenomenon.

For alloy 2024, it was shown that porosity is diminished by the use of dry helium as shielding gas, the removal of the oxide layer, the chemical or mechanical cleaning of the wire as well as the use of a twin laser spot (Verhaeghe and Hilton 2004). Autogenous welding studies noted that beyond a critical speed (50 mm/s), transverse hot cracking in the FZ increased with speed, with the cracks propagating along interdendritic regions. This critical speed could be increased to 120 mm/s using a trailing electric arc (Hu and Richardson 2006). In pulsed laser spot welding, the cracking sensitivity of alloy 2024-T4 is reported to increase with energy density. An overlap between spots along with a decrease in welding speed allowed to limit the number of cracks but caused an increase in their average length (Sheikhi et al. 2009). The high cracking susceptibility is also observed with 2024-O in laser spot welding, in addition to the presence of porosities and a weakening of the HAZ (Ghaini et al. 2009).

Alloy 2024 is deemed to be particularly sensitive to small deviations in laser focus. It is reported that a negative defocusing of 0.5mm tends to reduce the extent of macroporosity, although further defocusing significantly increased the porosity level (Alfieri et al. 2015). In contrast, another study showed that a positive defocusing of 0.5mm of the laser spot in continuous laser welding allowed to recover 77% of the yield strength of base metal alloy 2024-T3 with a limited porosity content (Caiazzo et al. 2013). Increasing the preheating temperature may also help reduce the number and length of hot cracks in pulsed laser spot welding (Sheikhi et al. 2015).

ii. Selective Laser Melting

In Selective Laser Melting (SLM), also called Powder-Bed Fusion (PBF) or Laser Beam Melting (LBM), powders are preplaced in a chamber and are subsequently melted by a laser, as shown in figure 1.12. Successive layers are formed by lowering the entire bed after the top

layer of powder has been processed by the laser, at which point a wiper blade sweeps over the bed to deposit a new layer of powder that will be selectively melted to form the next layer of the part to be fabricated.

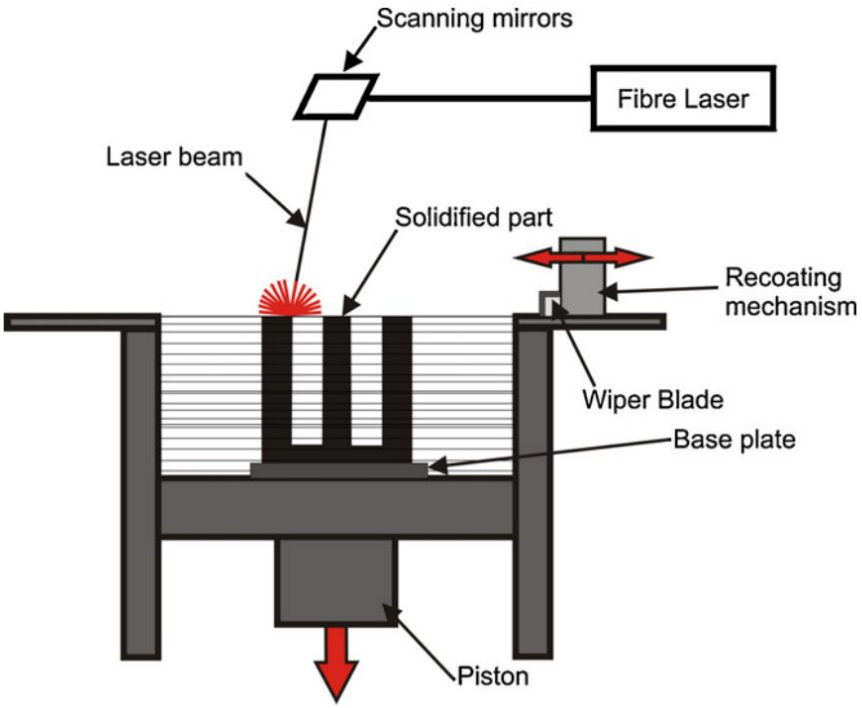

Figure 1.12: Selective Laser Melting process (Louvis et al. 2011)

Selective Laser Melting of aluminium powders remains challenging, not only because of the difficulties in laser processing of aluminium alloys (low laser absorptivity, high thermal conductivity etc.), but also because of the relatively low flowability of aluminium powders, especially if residual moisture is present (Louvis et al. 2011; Olakanmi et al. 2015). Another major hurdle is the presence of oxide films on the powder particles as these oxides are eventually trapped within the melt pool, which can affect wetting properties and create weaknesses in the fabricated part (Louvis et al. 2011).

SLM experimental results on aluminium alloys found in the literature mostly concern pure Al, Al-Si, Al-Si-Mg and Al-Mg alloys (Olakanmi 2013; Olakanmi et al. 2015). There are comparatively much fewer published studies dedicated to Al-Cu alloys.

Fusion lines, thin walls and cubes were fabricated with alloys 2219 and 2618, leading to 99.9% dense cubes, although no correlation was found between volumetric energy density and part density (Ahuja et al. 2014). In contrast, it was reported elsewhere that in the case of an Al-Cu-Mg-Mn alloy, an increase in energy density beyond some threshold improved the density of the build, leading to 99.5% dense parts without cracks or major defects. The energy density required for this 2024-like wrought aluminium alloy is 5 times greater than what is required for cast Al-Si10-Mg, i.e. 340 J/mm^3 and 60-75 J/mm^3 respectively (Zhang et al. 2016).

iii. Laser Metal Deposition

Laser Metal Deposition (LMD), is relatively recent metal AM process that bears many other names such as Laser Direct Metal Deposition (LDMD), Direct Metal Deposition (DMD), Laser Engineered Net Shaping (LENS), Construction Laser Additive Direct (CLAD), Laser Freeform Fabrication (LFF), Laser-Based Metal Deposition (LBMD), or Direct Light Fabrication (DLF). It is a powder-based DED process where the feedstock material is provided in powder form, typically obtained by gas or plasma atomization of an ingot of the base material. The powder is brought directly as needed at the location of laser energy input using an inert carrier gas. Two main embodiments are essentially possible depending on how the powder is delivered (figure 1.13).

In coaxial projection LMD, the powder is transported inside a projection nozzle and essentially travels alongside the laser beam within the nozzle, albeit in a separate flow channel. Two classes of coaxial nozzles are available: continuous nozzles, where the powder forms a continuous particle stream at the nozzle outlet, and discrete nozzles where the powder travels through separate channels within the nozzle to yield multiple streams of powder at the outlet. Various embodiments of continuous nozzles exist, depending on the relative position of the carrier gas/powder channel and the shielding/shaping gas channel. In figure 1.13 hereafter, the shielding gas is on the outer channel to keep the powder flux from excessively spreading upon exiting the nozzle outlet. In a different design published in patent n°EP057458B1, a shape gas channel is located between the central gas and carrier gas channels in order to carve the outlet powder flux into a hollow cone to avoid premature reflections of the laser by particles located above the focus plane (Freneaux et al. 1993).

In side projection LMD, the powder does not travel through the nozzle and is instead directed towards a single (or possibly multiple) side injection nozzle that laterally blows the powder towards the melt pool.

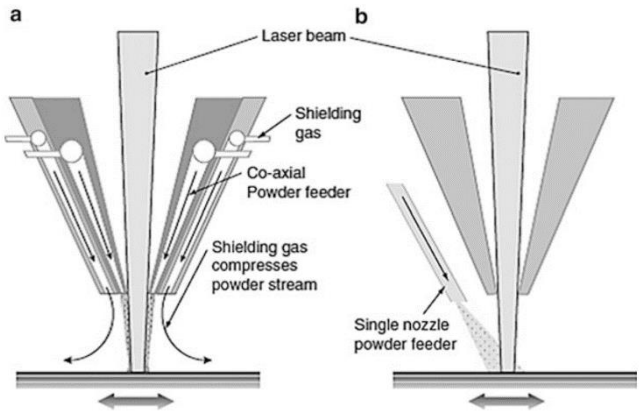

Figure 1.13: Laser Metal Deposition process. a) coaxial nozzle b) side powder nozzle (Gibson et al. 2015)

The projection nozzle can be mounted either on a robotic arm or inside a numerically-controlled machine tool equipment such as the one displayed in figure 1.14. The path taken by the nozzle along with the process parameters are entered as machine code (typically G-code) into the LMD system based on the part geometry defined by a Computer-Aided-Design (CAD) file.

Figure 1.14: MultiCLAD LF4000 LMD system at the Rapid Manufacturing Platform of Ecole Centrale de Nantes

The main advantages of the LMD process and DED processes in general compared to Selective Melting processes such as SLM and EBM (Electron Beam Melting) are:

- Versatility: LMD can be used for fabricating new parts, including directionally solidified, single crystal structures and functionally graded parts, as well as repairing, refurbishing or surface cladding existing parts (Gibson et al. 2015)

- Controllability: The chemical composition and type of microstructure can be tightly controlled by locally varying the mixture of powders and process parameters to change the effective composition of the melt as well as local thermal gradients and solidification rates (El Cheikh et al. 2012c; Muller et al. 2013)

LMD is not bound to depositing on a featureless substrate, and is thus often used on existing parts to add features and functionality, depositing surface coatings (e.g. wear or corrosion resistant coatings), experimenting with new material compositions and producing functionally graded materials (FGM) with non-uniform composition (Muller 2013; Muller et al. 2013). It can also be used for hybrid manufacturing where subtractive manufacturing (i.e. machining) and additive manufacturing capabilities are combined inside a single manufacturing center (Kerbrat et al. 2011).

Some of the limitations of the LMD process are the quality of the surface finish of the raw deposits, which generally lies in between the SLM and WAAM processes. A finishing operation is thus generally required. Also, more support structures are needed for complex geometries compared to SLM, where the powder-bed provides some level of support. This can however be avoided in some cases by using multi-axis deposition, at the cost of an increase in complexity for generating the toolpaths.

The fine level of control of the deposition process offered by LMD also implies that great care must be taken in setting parameters and scan paths if optimal properties are targeted, both in terms of deposit geometry and material integrity. For instance many studies focused on the prediction and optimization of single bead deposits geometry (El Cheikh et al. 2012a; b; c), scan paths optimization (Kerninon et al. 2008) or on powder feedrates control in FGM (Muller 2013). The flexibility of the LMD process, and AM processes in general, also generated much interest in novel design approaches for AM (Ponche 2013; Ponche et al. 2012, 2014).

For all its advantages, challenges remain with LMD for processing some classes of alloys, in particular aluminium alloys. In addition to difficulties with laser-based processing of such alloys, the flow of powder must also be stable to obtain good results. Aluminium powder particles are rather light compared to other materials such as 316L steel, and are typically covered by an oxide layer that forms spontaneously upon contact with oxygen. Surface adhesion forces (e.g. van der Waals, capillary, electrostatic forces) can become prevalent over other forces such as the force of gravity, so that particle agglomerates may form inside the reservoir, the pneumatic system and the powder projection nozzle, thereby impeding the flow of powder particles. LMD is therefore extremely sensitive to powder flowability issues as a constant, uniform powder feedrate is necessary to ensure optimal deposit quality with constant processing parameters and avoid lack of fusion defects, i.e. insufficient material feeding in localized regions forming pores or voids. However, this challenge is scarcely reported in the literature on LMD. To the author's knowledge, no published results are available regarding the flowability of cast Al-Cu powders in the context of LMD processing, which will be the focus of the next chapter. This lack of literature on the flowability of aluminium powders for LMD processing, and LMD processing of aluminium alloys in general, can be explained by the fact that, unlike other type of alloys such as titanium alloys, interest in AM of aluminium alloys is much more recent as these alloys are generally well suited for manufacturing by conventional processes such as machining. Coupled to the aforementioned challenges with laser processing of aluminium and the typically low flowability of aluminium powders, AM processing of these alloys did not seem to offer significant technological and economic advantages until recently, after research and development efforts allowed to overcome some of the technical challenges associated with AM processing of aluminium (Gibson et al. 2015).

LMD experimental results with aluminium alloys available so far in the literature are mostly dedicated to Al-12Si (4047) alloys or similar (Dinda et al. 2012; Isanaka et al. 2016; Rumman et al. 2019; Zhao et al. 2014). Very few publications on Al-Cu alloys processing by LMD are available. A recent review reinforces this assessment, as it only reports early experiments by NASA with the EBFFF (Electron Beam Free Form Fabrication) wire-based DED process on weldable aluminium alloy 2219, other DED applications with Al-Cu alloys being essentially restricted to alloy 2219 with the WAAM process (Lumley 2018). Very recently however, some authors studied the hardness and microstructure of single-bead deposits with wrought alloy 2024 powders, and developed a predictive model of single-bead geometry based on process parameters (Caiazzo et al. 2017; Caiazzo and Caggiano 2018). Another publication focused on LMD processing of Al-Cu-Ag-Mg-Ti-Zr powders made with a powder blending technique, using multiple side projection nozzles to build multi-track walls in an effort to study the effect of post-deposit heat treatments on microstructure and microhardness (Sweny et al. 2018).

The flowability issues encountered experimentally with Al-Cu powders in coaxial LMD processing have not yet been directly addressed in the literature, so that the feasibility of multi-layer deposits of low-weldability, low-flowability cast Al-Cu powders by coaxial LMD has not been clearly demonstrated thus far. Moreover, the copper microsegregation phenomenon, hot cracking tendencies and overall material integrity of Al-Cu alloys after LMD processing have not yet really been explored.

d. Summary of AM processes

Capability & Characteristics/ Process	LMD	WAAM	SLM
Build Envelope	++	+++	+
Layer Thickness	++	+++	+
Surface Finish	++	+	+++
Resolution	++	+	+++
Build rate	++	+++	+
Heat Input	+	+++	+
Repairs & Remanufacturing	Yes	Yes	Very limited
Multimaterials & Material Gradients	+++	++	No
Surface Cladding	Yes	Yes	No

Table 1.5: Summary of AM process characteristics and capabilities.
Adapted from (Gibson et al. 2015; Lumley 2018)

In many aspects, LMD offers a compromise between WAAM and SLM, for instance in terms of build envelope, layer thickness, surface finish, deposit resolution and build rate. However, LMD particularly shines by the number of possible applications (repair, remanufacture, surface cladding/coating, FGM, single crystal structures etc.) while offering reasonably fine resolutions and limited heat input and thus limited residual stresses and deformations. Hence, while both LMD and WAAM processes enable part repair and remanufacture (i.e. feature addition on an existing part), the solidification conditions mechanical properties obtainable by LMD are generally superior to WAAM as it is a laser-based process, which can better focus energy in localized regions compared to arc-based processes. It thus provides rapid cooling and high thermal gradients and thereby a more refined microstructure, which is highly desirable for low-weldability Al-Cu alloys as it should induce high mechanical properties while limiting the susceptibility to hot cracking and solute microsegregation.

II. Repairing with Laser Metal Deposition

a. Castings Defects

Al-Cu cast alloys present a limited castability as the solidification range (T_{liq}-T_{sol}) is relatively large, unlike Al-Si alloys which provide the highest castability thanks to a relatively small solidification range and a relatively large amount of eutectic component within the microstructure. Obtaining a large proportion of eutectic components with Al-Cu alloys is also possible, but only at the cost of increasing copper content to an extent where brittleness increases and strength diminishes (Zolotorevsky et al. 2007). The high tendency of these high-strength alloys towards hot shortness usually limits their use to relatively simple casting designs (ASM International 2009).

Despite issues with their castability, cast alloys 2xx.x such as 224.0 are still used to manufacture some premium high-performance castings. Some casting defects do arise from the foundry process, sometimes to the extent where the part must be repaired or be scraped to later be recast.

The company Howmet CIRAL (ARCONIC, ex-ALCOA) currently makes use of cast alloy 224.0 for the manufacture of a compressor volute for turbojet engines using an advanced lost wax process with rapid cooling. This alloy offers high strength at relatively high service temperatures (about 230°C), making it highly suitable to this type of applications provided the casting can actually be satisfactorily manufactured.

In confidential Research & Development studies (CIRAL et al. 1996; Dumant 1996; Planchamp et al. 1993), the presence of linear, dot and diffuse segregation is reported in premium 224.0 castings, which induces a 1 to 2% reduction in elongation and up to 2.5% decrease in yield strength due to the formation of brittle intermetallic Al_2Cu. A linear banded structure can result from the segregations, where phases successively alternate between Al_2Cu phases and ductile aluminium. It is created in part by the thermal contraction of the solidifying alloy, which leaves voids or hot cracks that are eventually backfilled with copper-rich liquid eutectic. The presence of hot cracks, not filled by eutectic at the end of solidification, is also noted. Optic and microscopic observations further revealed that the Al_2Cu phases play a dominant in role in crack initiation and propagation. The segregation phenomenon during lost wax casting with rapid cooling is particularly favored by a high thermal gradient and a high copper content. Changing the casting process parameters did not allow to suppress this phenomenon. Lowering the thermal gradient and using beryllium as a grain refiner limited the extent of the linear segregations but did not reduce the diffuse segregation, which is present throughout all of the analyzed samples. Because of the low diffusivity of copper in the solid

aluminium matrix, solution heat treatment cannot resorb the segregated zones (CIRAL et al. 1996; Planchamp et al. 1993). In addition to the segregation and hot cracking tendencies of cast alloy 224.0, issues with its castability can lead to other common casting defects such as pinholes, blowholes, inclusions, gas porosity, shrinkage, cold cracks etc.

b. Conventional Repair Processes

When local casting defects are located near the surface, foundries usually perform some amount of repairs in order to recover the design specified geometry. A distinction can be made between the "rework" of a casting, which is always performed before heat treatment and usually at the foundry, and the "repair" of a casting where no post-weld heat treatment is applied as it is for example carried out by aircraft maintenance crews to reuse damaged castings (ASM International 2009). In this work, "repair" will imply that the local geometry and mechanical properties of the part must be recovered. Many techniques are currently employed to repair surface defects such as cracks, including hammer peening, vee-and-weld, stop-hole, crack stitching, bonded crack patches, grinding, and pulsed electron beam irradiation (Marazani et al. 2017).

The reparability of 224.0 premium high-value castings by manual GTAW (CIRAL et al. 1996; Planchamp et al. 1993) is however rather limited as GTAW surface repairs generally present a 20 to 30 % failure rate for repaired zones spanning 10mm or more (Dumant 1996). This welding repair process is usually performed manually by a skilled human operator so as to be able accommodate the various repair geometries and configurations. Indeed, the location of the casting defects is generally not very predictable, nor are the size and shape of these defects. As some significant variability is inevitable with a manually operated process, the repeatability of GTAW repairs with a low-weldability material is not very satisfactory in an industrial context. When a GTAW repair is successful however, the mechanical properties of the part are satisfactorily recovered (CIRAL et al. 1996).

While cast aluminium parts can generally be fairly easily recycled by directly remelting the material and recasting the part, it still consumes time, energy, and human labor. Moreover, with low-castability alloys such as 224.0, the recasting process may again generate the same type of defects. It is therefore highly desirable to be able to reliably repair such high performance, high value castings to avoid performing multiple recycling/recasting cycles.

To ensure a more satisfactory success rate and repeatability of local surface repairs, thus minimizing the need for part recycling/recasting and making the overall manufacturing process more robust and less unpredictable, it is proposed to replace the conventional GTAW repair process by an LMD-based repair process.

c. Laser Metal Deposition as a Repair Process

The Laser Metal Deposition process belongs to the category of DED processes where the material to be deposited is directly brought as needed into the zone of energy input. It can therefore be used for repairing parts where a surface defect has been machined out and must be cladded to recover the initial geometry and mechanical properties of the part. It can also be employed to augment the initial geometry and functionality of the part by adding extra features that were not planned in the design phase or were not deemed to be manufacturable with conventional manufacturing processes.

Repairing with LMD instead of more standard processes such as GTAW can potentially provide several advantages. As a numerically-controlled process, it could in principle be automated to perform basic repair tasks, provided a suitable laser scan path and process parameters (laser power, scan speed, powder mass flowrate etc.) can be identified and translated into machine code. This is unlike standard welding processes used for surface repairs, which are typically performed manually by a highly skilled human operator. Automating this task would allow for greater repeatability, especially with low-weldability alloys for which the failure rate can be quite high, e.g. up to 30% for alloy 224.0 (Dumant 1996). Another potential advantage of performing repairs by LMD lies in the fact that it is a laser-based process that generally gives rise to rapid solidification with high thermal gradients and cooling rates in highly localized regions (Marazani et al. 2017; Pinkerton et al. 2008). Such solidification conditions not only minimize deformations and residual stresses but also create a refined microstructure that is beneficial in terms of hot cracking resistance. Indeed, the area of grain boundaries is greater in fine-grained microstructures so that detrimental phases such as low-melting-point Al_2Cu at the grain boundaries are less concentrated. The healing of nascent cracks is promoted as liquid feeding is generally enhanced. A fine equiaxed grain structure is also less rigid and can better deform to accommodate contractions strains. The potential for hot cracking is therefore more limited (Kou 2003). Moreover, during rapid solidification with laser-based processes, the solidification reaction is far away from equilibrium, so that it can become diffusion limited in the sense that solute atoms cannot easily diffuse towards the liquid phase due to the travel speed of the solidification front. This solute trapping effect can go as far as yielding a partitionless ($k_e \rightarrow 1$), i.e. segregation-free, microstructure for very fast solidification rates (Boettinger and Coriell 1984).

Published experimental studies on LMD repair and remanufacturing applications so far concern standardized grooves (Graf et al. 2012; Pinkerton 2010; Pinkerton et al. 2008), turbine blades and blisks (Bi and Gasser 2011; Kathuria 2000; Nowotny et al. 2007; Wilson et al. 2014), marine crankshafts (Koehler et al. 2010), cast cylinder heads of direct injection engines (Liu et al. 2016c), gas turbine burners (Petrat et al. 2016) as well as damaged tools and moulds

(Pinkerton 2010). These applications use various materials such as steel 316L, Ti-6Al-4V, or nickel-based superalloys, and essentially conclude that the mechanical properties of the component are recovered after repair, yielding a refined microstructure and good substrate bonding in the repaired zone. Experiments on single track deposits with high-strength aluminium alloy 7075 for potential repair applications were also disclosed (Cottam et al. 2011). It has been shown that larger grooves with inclined surfaces are generally preferable for defect repairs (Graf et al. 2012). The use of LMD for repair applications is however still fairly recent and relatively few published works are available (Marazani et al. 2017). There are currently no known published results regarding the repair of high-strength aluminium castings by LMD.

The characteristics of the LMD process make it highly suitable for automating the repair operations. Some research work has been conducted in that direction, however it is mostly dedicated to the specific geometry of turbine blades, for which specific techniques such as Prominent Cross Section allow to reconstruct the defective blade region to be repaired based on data from a non-contact measurement system such as laser scanners (Gao et al. 2008; Piya et al. 2011; Wilson et al. 2014; Zhao et al. 2018). Some recent studies developed methods focused on surface cavities with more arbitrary geometries (Zhang et al. 2018a, c; b). Another study focused on the digital chain, process planning and STEP-NC representation of a repair or remanufacturing operation (Um et al. 2017).

Although there are quite a few published works on the experimental aspects of LMD repairs, there is a relatively smaller body of work on the automation of the repair process chain. There are also no known publications on LMD repairs of high performance castings with low-weldability, low-flowability aluminium alloy powders.

III. Thesis Summary

a. Research Context

This doctoral thesis was funded by a CIFRE ("Convention Industrielle de Formation par la Recherche") and FUI project ("Fonds Unique Interministériel") called NENUFAR ("Nouveaux Emplois et Nouveaux Usages de la Fabrication Additive pour la Réparation"), which is a collaborative endeavor involving private companies and institutes (APS Coating Solutions, Arconic / ex-ALCOA, BeAM, IREPA Laser, CRMA Aero Repair, Institut de Soudure, Turbine Casting), French public research laboratories (Laboratoire GeM at Ecole Centrale de Nantes, PIMM at ENSAM ParisTech, ICB at Université de Technologie de Belfort-Montbéliard, ONERA, LEM3 at Université de Lorraine) with funding from French public investment bank BPI France and labelling by competitive clusters (EMC2, Materiala, Pôle des microtechniques, Pôle Nucléaire de Bourgogne, ASTech, Pôle Véhicule du Futur).

This consortium was built to accelerate the adoption of metal AM technologies in France by focusing on repair applications of high value castings made of low-weldability alloys, including alloy 224.0/AU5MVZr, that are difficult to repair with conventional welding-based methods. The general goal of the NENUFAR project was to assess the potential for LMD and FSW (Friction Stir Welding) to perform repairs on high performance, high value aeronautical castings by establishing adequate protocols and process parameters.

It was recognized early on that alloy 224.0 is not only hard to weld, as are most Al-Cu alloys, but also hard to process in powder form due to flowability issues. To perform the repair of the 224.0 test part, a volute of a centrifugal compressor for turbojet engines manufactured by Howmet CIRAL (Arconic), the issues related to flowability, melting and solidification of Al-Cu powders during LMD processing had to be overcome and suitable process parameters had to be uncovered. Moreover, the LMD repair operation had to be made adaptable to various surface defect geometries and locations, and means to obtain the corresponding toolpath to generate the appropriate G-Code for the CNC (Computer Numerical Control) machine.

As detailed in the next section, the research work undertaken as part of the doctoral program followed 3 major axes in order to reach those objectives. The first research axis concerned the experimental aspects of processing aluminium and aluminium-copper powders by LMD, both in terms of powder flowability (chapters 2 and 3) and laser melting/solidification (chapter 5). The second axis focused on numerical simulations of LMD, including powder transport (chapter 3) and laser melting/solidification (chapter 5). The third axis sought to increase the efficiency and robustness of the repair operation by developing a

method to partially automate LMD repairs and thereby take full advantage of this numerically-controlled process (chapter 4).

b. Research Focus

i. Aluminium Alloys Processing by LMD

1. Flowability of Aluminium Powders in LMD

While there are many potential advantages in using Laser Metal Deposition for repair applications, especially in the case of high value aluminium castings, there are currently several limitations regarding aluminium alloys powders that prevent the use of this additive manufacturing process for fabricating and repairing aluminium parts.

Among the major issues encountered during preliminary experiments of LMD processing of aluminium-copper powders is the lack of flowability of these powders, which can prevent their proper transport between the powder reservoir and the powder projection nozzle. Thus, before any considerations regarding process parameterization, solidification condition and resulting material and mechanical properties of the deposit, the limitations regarding powder flowability must be overcome.

The first hurdle starts at the reservoir, where the powder is stored in a closed chamber and gravity-fed towards a distribution system. In this free flowing regime, where gravity is the sole driving force of the granular flow, the flowability depends mostly on powder quality (sphericity, rugosity, presence of satellites…), granulometry, bulk and surface composition as well as powder storage conditions and preconditioning.

A second flowability issue potentially arises in the forced regime phase, or pneumatic transport, where a carrier gas drives the powder particles from the reservoir outlet towards the powder projection nozzle. Depending on the gas-flow characteristics as well as on the geometry of the piping system, powder accumulation may occur within the pipes, possibly to the point of clogging the system and thus inducing heavy maintenance. A similar problem can take place within the projection nozzle, where agglomerates of powder can obstruct the pathway for the particle flow. In addition, heat accumulation within the nozzle during deposition may lead to a sintering of the particles onto the nozzle surface and create a hot spot that can potentially damage the nozzle.

One of the objectives of this work is thus to better understand the causes behind the lack of flowability of metal powders, experimentally test the flowability of such powders in

various conditions, and finally develop the means to improve the flowability of cohesive aluminium-copper powders and thereby enable their use for LMD processing.

2. Processing of Aluminium Alloys by LMD

Aluminium alloys have a number of desirable properties that make them particularly attractive for manufacturing, especially in the aeronautics and aerospace industries. The perspective of using additive manufacturing for processing these alloys is rather enticing as it would unlock new possibilities in terms of part design and life cycle. However, laser processing of aluminium can be challenging due to numerous factors including high reflectivity, effusivity and fluidity as well as the presence of an oxide layer. Additionally, aluminium-copper alloys are particularly prone to solidification cracking during welding, and demonstrate high levels of microsegregation after casting. The heat input must therefore be carefully controlled to provide favorable solidification conditions that avoid potential solidification or liquation cracking defects. Other typical defects encountered with other aluminium alloys during welding or casting, such as gas porosities, should also be limited.

Another objective of this study is thus to experimentally uncover a suitable range of process parameters that allows LMD processing of this alloy with a favorable outcome in terms of material integrity and mechanical performance.

ii. Simulation-based Optimization of LMD

Experimental trials, whether they are aimed at optimizing the processing parameters or at improving the process itself, are often time consuming and costly. The perspective of optimizing the Laser Metal Deposition process numerically is thus also investigated in this work.

The first major axis of study regards the numerical optimization of the geometry of the powder projection nozzle for lighter metal powder particles, firstly to enhance the flowability of the particles within the nozzle by preventing powder accumulation on its surfaces and, secondly, to reduce accessibility issues, for example by increase the working distance of the nozzle.

A second axis was directed towards the simulation of the melt pool during LMD so as to provide an estimate of the temperature and velocity fields of the melt pool as well as of the geometry of the deposit for a given material and processing conditions.

The third axis consisted in investigating models for the prediction of the microstructure obtained during LMD, and more particularly for predicting the level of copper microsegregation that can be expected depending on processing conditions.

iii. Repair Method for DED processes

To fully enable the repair of casting parts with the aluminium-copper alloy of the present study, the path of the optimized LMD system must also be generated in addition to the processing parameters. One of the main potential advantages of the LMD process over manual processes such as GTAW is the ability to automatically perform most of the repair operation, thus providing more efficiency and repeatability. Automation however requires information on the location and geometry of the part defect within the machine coordinate system in order to generate the appropriate machine program for the LMD system. The means for gathering and processing such information must be investigated and implemented in order to ultimately perform a quasi-automated repair of local surface defects on high value aluminium castings. It is ultimately hoped that LMD repairs on 224.0 cast alloys can outperform traditional manual GTAW repairs in terms of success rate, efficiency and performance.

c. Thesis Outline

The upcoming chapters explore each of the research topics exposed previously in order to conjointly address the following overarching research questions:

- How can Laser Metal Deposition be optimized for low weldability, low flowability (cohesive) alloy powders?

- How can Laser Metal Deposition, and DED processes in general, be automated for basic repair operations?

Chapter 2 focuses on evaluating and improving the flowability of cohesive aluminium powders in the granular flow regime.

Chapter 3 investigates the flowability of aluminium powders during pneumatic transport and nozzle flow. It also describes the optimization of the nozzle for enhancing the flowability in the forced regime as well as improving nozzle accessibility.

Chapter 4 describes a method for the automated repair of a high value aluminium-copper casting by LMD along with its implementation.

Chapter 5 exposes numerical and experimental investigations of the melt pool behavior, deposit geometry as well as microsegregation level and hot cracking susceptibility of an aluminium-copper alloy processed by LMD.

Chapter 6 gives concluding remarks on the preceding chapters and offers some perspectives and potential future research avenues for the development of additive manufacturing technologies for repair and remanufacturing applications.

Chapter II: Flowability of Cohesive Aluminium Powders

Abstract

In this chapter, the flowability of cohesive AM powders is evaluated using analytical and experimental methods. A funnel flowability test method with a vibrational assistance is presented to enable quantitative flowability measurements with low-flowability powders that do not flow through typical flowmeters. The flowability of several metal AM powders with low to high cohesiveness is then measured using the proposed method, and the effect of relative humidity content is discussed. A flowability criterion is also presented and evaluated for various metal AM powder samples based on analytical models of adhesion forces. The experimental and theoretical results are compared through a statistical analysis. A heat treatment was also demonstrated to provide significant enhancement in powder flowability, enabling the use of cohesive aluminium powders for LMD processing.

I. Flowability criterion

a. Cohesive Aluminium-Copper Powders

In the present work, Aluminium-Copper 224.0 powders (essentially Al-Cu4.7-Mn-Ti-V-Zr) are the base material to be fed into the LMD system for performing homogeneous repairs of high-value, high-performance 224.0 castings. The supplied 224.0 powders were made at Université de Technologie Belfort-Montbéliard (UTBM) by an inert gas atomization process, where ingots of a base 224.0 alloy were melted inside a crucible to form a thin layer of liquid metal falling inside a large reservoir. The liquid metal layer is then atomized into small droplets at the top of the reservoir using a flow of Argon gas accelerated through a de Laval nozzle (Allimant et al. 2009). The liquid droplets cool down and solidify as they fall to eventually form solid metal particles that are collected at the bottom outlet of the reservoir. The gas atomization process typically yield metal particles with good sphericity since the liquid metal droplets seek to minimize their surface energy and thus naturally adopt a spherical shape. Inert gas atomization process are therefore frequently employed to manufacture metal AM powders as particle morphology or sphericity is often deemed to be an important factor for powder-based AM processing. Many factors are at play during atomization, including the surface tension of the liquid metal, the level of oxidation, gas flow pattern inside the reservoir etc. These factors can significantly affect the particle size distribution (PSD) as well as the quality of individual particles (surface oxidation, particle agglomeration, satellite formation etc.).

To select a particular range of particle sizes, a sieving operation is usually performed to filter out particles with characteristic sizes above and below some limits. For instance, SLM processes typically use aluminium powders near the 20-63µm range, as SLM requires good particle packing inside the powder-bed to obtain fully dense parts while retaining a good flowability to properly coat the powder-bed with a rake or roller (Tan et al. 2017). Commercial metal AM powders dedicated to LMD processes are often made of larger powder particles, typically in the 45-90µm range. LMD puts little constraints on the packing efficiency, which is favored by a wider PSD as smaller particles can fit in the interstices between larger particles (Tan et al. 2017), but it is more stringent on powder flowability than SLM as it is dependent upon the flowability in different regimes, i.e. free surface/packed bed (reservoir) and aerated/fluidized (distribution system and LMD nozzle).

The 224.0 aluminium casting powders used in the present work came from two main batches, here called lots A and B (or 224.0-A and 224.0-B), which originated from different 224.0 ingots that were gas atomized with different atomization parameters. The powder from

lot A was provided in sieve granulometries 20-80µm, 45-90µm, 63-80µm, 80-100µm and 100-125µm, and the powder from lot B was supplied in larger granulometries (90-125µm, 125-150µm and 150-250µm). The designation of the granulometries is used for simplicity as it refers to the sieve nominal mesh aperture sizes, but are only a rough indicator of the PSD. The actual parameters of importance are the type of PSD, which typically follows a log-normal law for gas atomized metal powders, and the D-values d_{10}, d_{50} and d_{90} (volume-based in this work), which correspond to the 10%, 50% and 90% intercepts of the cumulative volume distribution curve. An example of a volume-based log-normal PSD for powder sample 224.0-B 90-125µm obtained by laser diffraction according to standard ISO 13320 is reproduced in figure 2.15. Other basis for distribution calculation could be the number of particles or the surface area.

Beyond the commonly used median diameter d_{50}, other common measures of particle size $d_{p,q}$ can be obtained by the expression $d_{p,q} = \frac{\sum_{i=1}^{n} n_i d_i^p}{\sum_{i=1}^{n} n_i d_i^q}$ where n_i and d_i and the number and diameter of particle i among a total of n particles. The most common of those mean diameters are the arithmetic or number mean $d_{1,0}$, the volume to surface ratio mean $d_{3,2}$ (Sauter mean diameter) and mean diameter over volume $d_{4,3}$ (de Brouckere mean diameter). For a single non-spherical particle, the Sauter diameter represents the diameter of the sphere with the same volume/surface ratio. It is frequently employed when dealing with surface-based phenomena such as adhesion forces, and could therefore be more applicable than median diameter d_{50} in relating interparticle cohesion forces to flowability measures (Capece et al. 2015, 2016). The actual meaning of the Sauter mean diameter for a polydisperse distribution of spherical particles was established only recently as being the equivalent diameter of a collection of identical spherical particles which present the same total surface area and the same total volume as the original distribution but with a different number of objects (Kowalczuk and Drzymala 2016). It is very sensitive to the presence of fine particles in the PSD. The de Brouckere mean diameter $d_{4,3}$ of a single non-spherical particle is the diameter of the spherical particle with the same volume as the original particle, and is most sensitive to the presence of large particles in the PSD (Özbilen 2014). In practice, equivalent diameters $d_{50}, d_{4,3}$ and $d_{3,2}$ of gas atomized metal AM powders have similar magnitudes, with $d_{4,3} > d_{50} > d_{3,2}$. For instance, for powder sample 224.0-B 90-125µm, $d_{50} = 108.9$µm, $d_{4,3} = 112.6$µm and $d_{4,3} = 105.9$µm. A summary of D-values of the 224.0 powder samples from lots A and B are given in table 2.6.

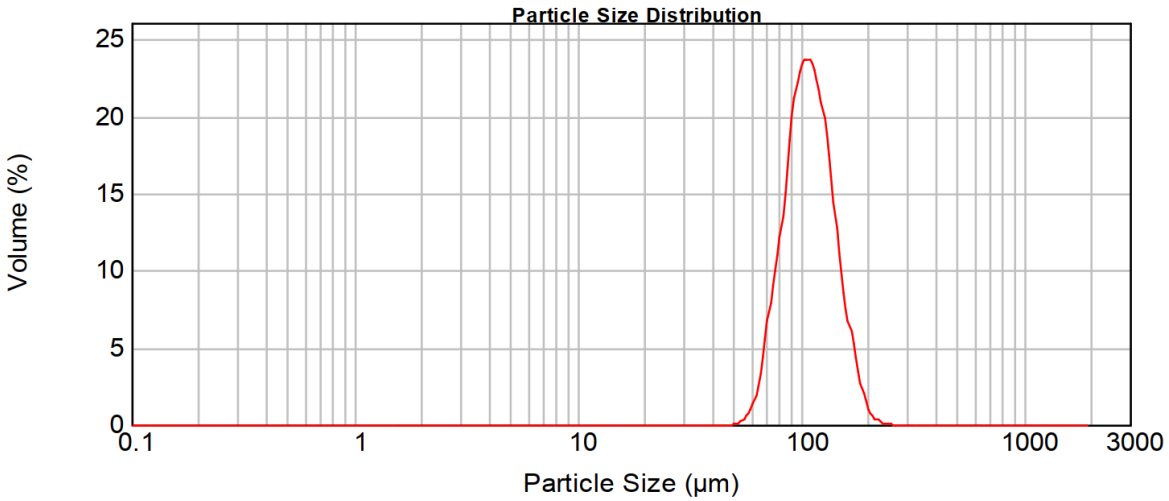

Figure 2.15: Log-normal PSD for powder sample 224.0-B 90-125µm ($d_{50} = 108.9$µm)

Material	Sieve Granulometry	d_{10}	d_{50}	d_{90}	$d_{3,2}$	$d_{4,3}$
224.0-A	20-80	21.1	39.2	74.7	35.3	44.2
224.0-A	45-90	42.1	60.6	87	58.2	62.9
224.0-A	63-80	n/a	n/a	n/a	n/a	n/a
224.0-A	80-100	69.9	101	147.6	n/a	n/a
224.0-A	100-125	82.2	120	175.6	n/a	n/a
224.0-B	90-125	79.2	108.9	149.9	105.9	112.6
224.0-B	125-150	104.8	143.4	195.9	139.1	147.6
224.0-B	150-250	146.6	203.3	281.2	197.1	209.9

Table 2.6: D-values of powder samples from lots 224.0-A and 224.0-B

A macroscopic visual inspection of the powder samples readily suggested potential issues regarding the use of some of the 224.0 powder samples with the LMD system. Indeed, as dry sand looks and behaves differently than flour, some cohesive powder samples (particularly 224.0-A 20-80µm) form agglomerates that are visible on the free surface and already hint at a low in-process flowability. Some authors actually found that such an optical flowability evaluation could be correlated to the avalanche angle and surface fractal of iron- and nickel-based powders (Spierings et al. 2015). The sieving process further demonstrated the cohesive character of this aluminium-copper powder since ultrasonic sieving was required instead of a more common sieving with mechanical vibrations in order to prevent interparticle cohesion and particle adhesion to the sieve mesh.

Preliminary tests with the LMD system clearly established that the in-process flowability of the 224.0-A powders was not satisfactory as the powders either did not flow at all from the reservoir or flowed irregularly, which is not acceptable for LMD as a constant, or at least controlled, powder flowrate is required to avoid a lack of material feeding in the deposits. Based on visual observations at the reservoir and LMD nozzle outlets, the overall in-process flowability of 224.0-B powders was more satisfactory. In an attempt to uncover

differences between lot A and B, the 224.0 powders were analyzed by a Scanning Electron Microscope (SEM) JEOL NeoScope JCM-6000Plus coupled to an Energy-Dispersive Spectroscopy (EDS) system. Powder particles from samples 224.0-A 80-100µm and 224.0-B 90-125µm, with similar D-values, were imaged by SEM under various magnification levels in Secondary Electron Diffusion (SED) mode, as shown on figure 2.16.

In both cases, the sphericity of individual particles is fairly satisfactory, although sample 224.0-B 90-125µm contains some elongated particles. Both samples contain satellites, i.e. small particles solidly attached to larger ones. However, the presence of satellites and particle agglomerates of random shape seems more widespread in sample 224.0-A 80-100µm. These particle agglomerates, as illustrated in figure 2.17, and particle satellites are formed during the atomization process where liquid particles collide and remain in contact due to surface tension, and eventually form a solid bond as they cool down and solidify inside the atomization tower reservoir (Özbilen 2014). Such particle agglomerates are less frequently encountered in sample 224.0-B 90-125µm, where a number of smaller particles that were not sieved out remain separated from the larger particles instead of forming satellites or particle agglomerates. This evaluation of particle shape however remains qualitative. A thorough quantitative analysis of particle shape distribution on a larger sample should ideally be conducted, which is beyond the scope of the present work. SEM imaging of the sections of powder particles (not shown) reveal no major porosities inside the particles and therefore should not induce excessive porosities in the LMD deposits.

224.0-A 80-100µm

224.0-B 90-125µm

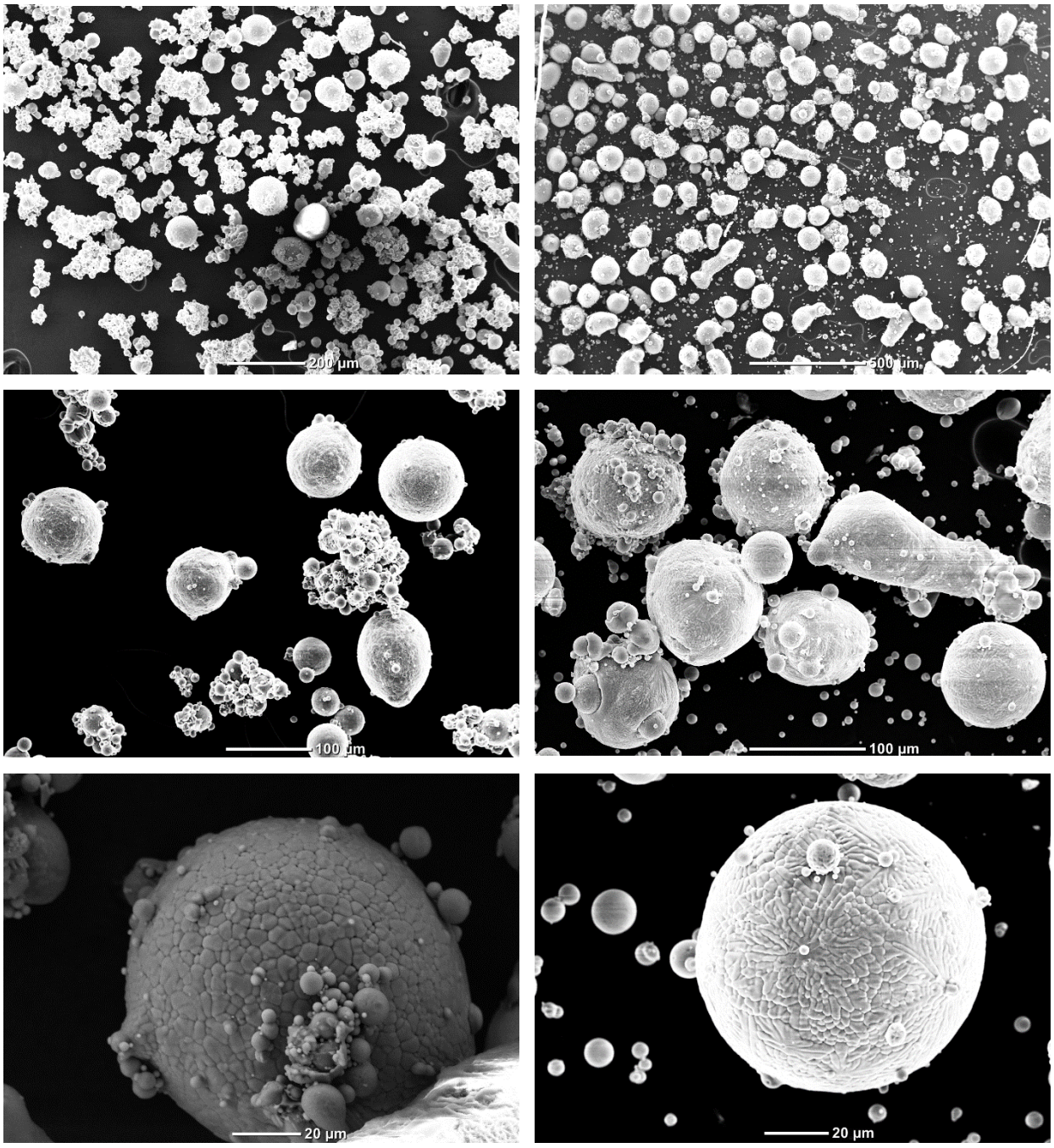

Figure 2.16: Powder 224.0-A 80-100µm (left column) – Powder 224.0-B 90-125µm (right column)

224.0-A 80-100µm

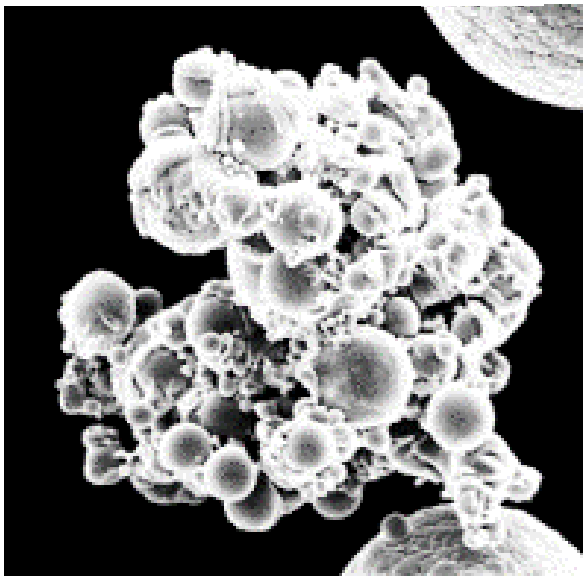

Figure 2.17: Particle agglomerate from sample 224.0-A 80-100µm

The chemical compositions for ingots and powder samples 224.0-A and 224.0-B are presented in table 2.7 based on results provided by UTBM/Bureau Veritas. The composition of heavier elements (Cu, Mn, Ti, Zr, V) were measured by Plasma Emission Spectroscopy while oxygen content was measured by Reducing Melting Infrared Absorption. Trace elements (content < 0.05 wt%), which are grouped together in table 2.7, include Fe, C, Co, Si, Zn, Ni and Mg.

Material	**Form**	**Al**	**Cu**	**Mn**	**Ti**	**Zr**	**V**	**O**	**Other**
224.0-A	Ingot	>93.47	5.5	0.22	0.16	0.12	0.097	0.003	<0.43
224.0-A	Powder	>93.71	5.2	0.23	0.16	0.12	0.098	0.045	<0.44
224.0-B	Ingot	>94.46	4.86	0.22	0.15	0.10	0.08	0.003	<0.12
224.0-B	Powder	>94.89	4.42	0.21	0.15	0.10	0.08	0.027	<0.12

Table 2.7: Elemental composition (wt%) of ingots and powder samples 224.0-A 80-100µm and 224.0-B 90-125µm

The results do not demonstrate any major differences between the ingot and powder of each lot A and B, except for copper and oxygen content that appear to be significantly reduced and increased, respectively, after atomization.

Powder sample 224.0-B falls short of alloy 224.0 specification for copper content (4.6wt%Cu), while sample 224.0-A in both ingot and powder form is beyond of the copper content specification (5.0wt%Cu). Copper content is generally higher in sample A, but it is noted that the uncertainty in copper concentration measurements is between 0.13 and 0.16wt%Cu, which is much higher than for other elements. Moreover, another chemical

analysis provided by ingot supplier Arconic yielded 4.73wt%Cu for the base ingot 224.0-A, which further questions the validity of copper compositions obtained for sample 224.0-A. Complementary measurements were thus carried out by Energy Dispersive Spectroscopy on powder particles from samples 224.0-A 80-100µm and 224.0-B 90-125µm. While significant uncertainty is associated with this approach so that it may not be directly used for quantitative assessments, it nevertheless also suggests that copper concentration is lower in powder sample B.

Oxygen levels of ingots A and B are much lower than the atomized powder, indicating an increase in oxidation level in both cases due to the atomization process. However, powder sample B has a lower oxygen content than powder sample A, possibly hinting at lower surface oxidation levels in sample 224.0-B.

The variation in chemical composition between powders 224.0-A and 224.0-B, notably in terms of copper concentration, should not significantly affect interparticle forces and material density, so that the difference in powder flowability between the powder samples A and B should essentially arise from differences in granulometry, particle morphology and possibly surface oxidation levels.

b. Interparticle Forces

In the same way that microstructural features of a solid, non-granular material allow to predict its macroscopic properties (strength, hardness etc.), the bulk behavior of powders such as their flowability should in principle be deducible from the knowledge of interaction forces between individual particles and between particles and walls, in addition to surface or body forces such as gravity. Investigating the nature of those interactions at the microscopic scale and how they vary with particle characteristics (composition, size, roughness etc.) and environmental conditions (relative humidity, temperature etc.) should thus yield a better comprehension of bulk powder behaviors at the mesoscopic scale.

When a powder is placed inside a funnel-like reservoir, it is mostly in a mix of free surface and packed bed conditions under low consolidation stresses and the effect of interstitial gas on powder bulk behavior is mostly negligible. The main forces acting upon each individual particle are then the force of gravity and particle-particle or particle-wall interaction forces. When attractive, these forces are said to be cohesive (similar materials) or adhesive (dissimilar materials) as they promote the formation of particle agglomerates that hinder the flowability of the powder.

The interaction forces generally consist of the van der Waals forces, the capillary (liquid bridge) force, and the electrostatic force if charged particles are present (Castellanos 2005; Shah et al. 2017).

Solid bridge forces can also be generated from solid-state chemical reactions, from material adsorption and recrystallization in an evaporated liquid bridge, or from contact fusion and solidification (Shah et al. 2017). Particle satellites and agglomerates as seen in the 224.0 powder samples could be classified under such interactions. Once formed, these interactions create rigid assemblies of irregular shapes that can seldom be broken unless the particles are subjected to a mechanical action (milling, grinding etc.). Mechanical interlocking forces are promoted by the entanglement these irregular particles and hinder the flowability, but they are difficult to measure experimentally or estimate analytically.

If the powder material contains ferromagnetic (or ferrimagnetic) elements, such as iron, cobalt and nickel, a magnetic force can arise from the persistent magnetization induced by a prior or ongoing exposure to an externally applied magnetic field. Paramagnetic elements such as aluminium and titanium are however much weaker magnets when under the influence of an externally applied magnetic field, and they do not retain their magnetization once the applied magnetic field vanishes. Magnetic forces can thus generally be ignored during standard LMD processing, especially when dealing with aluminium powders where Fe, Ni and Co elements are typically only present in trace amounts.

The van der Waals, capillary and electrostatic interaction force models between rough spherical particles are detailed hereafter. These models contain a number of parameters that can be difficult to measure or evaluate precisely, but they nonetheless give a clearer picture of the impact of powder properties (PSD, chemical composition, surface roughness etc.) and environmental conditions (temperature, relative humidity) on cohesion forces and will eventually be used to compute a PSD-dependent flowability criterion, the population-dependent granular Bond number Bo_g^* (Capece et al. 2015, 2016).

i. Van der Waals Forces

The van der Waals (vdW) forces are intermolecular forces of quantum mechanical nature that are typically dominated by the London dispersion force arising from electron cloud fluctuations, which create instantaneous induced dipoles between both polar and non-polar molecules and atoms. The vdW forces also include the Debye force, i.e. polarization or induction force, which is the interaction between a permanent and an induced dipole, as well as Keesom forces, which are of purely electrostatic nature and arise from the interaction between two permanent dipoles. These two forces require the presence of permanent dipoles

and are thus generally less universal and dominant than the London dispersion forces, which are applicable to all materials since all materials are polarizable (Leite et al. 2012). At the atomic or molecular scale, those three forces are generally very short-range as they vary as $1/D^7$, where D is the separation distance between two molecules or atoms. They are also non-additive as the presence of neighbouring molecules affect the interaction (Israelachvili 2011).

Pioneering work by Hamaker nonetheless assumed pair-wise additivity between molecules to show that a longer range force is obtained when integrating molecular contributions over macroscopic bodies, so that the vdW force actually varies as $1/D^3$ between two macroscopic smooth spherical particles i and j (Hamaker 1937).

$$F_{vdW} = \frac{A}{6D^3}\left(\frac{R_i R_j}{R_i + R_j}\right) \tag{2.1}$$

with sphere radii $R_i, R_j \gg D$ and Hamaker coefficient A is a measure of surface energy that is often given as a material constant and is typically on the order of 10^{-20}~10^{-19} J.

It can be shown that Hamaker coefficient A is positive for bodies made of identical materials interacting through air or vacuum, so that the dispersion force is then always attractive and can only be repulsive when different materials are interacting. This macroscopic dispersion force can remain significant up to separation distances of 10µm, and is the main interaction force between particles of uncharged fine dry powders (Castellanos 2005; Shah et al. 2017). A more accurate description of the dispersion force for macroscopic bodies was later formulated by Lifschitz by considering the material constituents as a continuum, yielding an integral expression for A that depends on material properties such as the frequency-dependent dielectric permittivity and the refraction indices of the interacting media (Israelachvili 2011). It also naturally includes the Debye and Keesom forces. Metals behave differently than other common materials due to the presence of free electrons, and must be treated accordingly by employing the appropriate frequency-dependent law of the dielectric permittivity to obtain finite results. The Hamaker coefficient of metals therefore has a different analytical expression than dielectric materials and is generally relatively large, usually in the range 25-50.10^{-20} J (Israelachvili 2011).

Nonretarded values of the Hamaker coefficient A_{131} (two identical media 1 interacting through a media 3), or simply A_{11} when media 3 is vacuum/inert air, are listed in table 2.8 for various materials of interest, with air and water as media 3. For most condensed media, the values of the Hamaker coefficient fall in the range 4-40 x 10^{-20} J. Theoretical values obtained from Lifschitz theory and its approximations (e.g. Tabor-Winterton model) as well as spectral data tend to agree well with experimental results (Israelachvili 2011).

Material (media 1)	$A_{131}(=A_{11})$ (media 3 : inert air or vacuum) x10^{-20} J	A_{131} (media 3 : water) x10^{-20} J
α-Al_2O_3	15.2[a] ; 16[b]	3.67[a] ; 5.3[b]
TiO_2	15.3[a]	5.35[a]
Al	33[d] ; 25.6[e]	18.4[e]
Fe	26[d]	10.08[h]
Cu	28.4[d'] ; 40[c,d'] ; 46[d] ; 27.8[e] ; 24.82[e] ; 27.20[e']	14.4[e] ; 11[f]
Metals (Au, Ag, Pt...)	~40[c]	19.4[h]
PTFE	3.63[e]	0.33
H_2O	3.7[c]	-

Table 2.8: Nonretarded Hamaker coefficients
a: based on the full Lifschitz theory (Bergström 1997)
b: (Götzinger and Peukert 2003)
c: reported in (Israelachvili 2011)
d: calculation from (Osborne-Lee 1988)
d': reported in (Osborne-Lee 1988)
e: calculation from (Jiang and Pinchuk 2016)
f: calculation from (Lefèvre and Jolivet 2009)
g: calculation from (Leite et al. 2012)
g' : experimental value from (Leite et al. 2012)
h: estimated using a combining rule

So-called mixing rules or combining laws can be used to estimate Hamaker coefficients between various combinations of media based on Hamaker coefficients of individual media. These simple rules can slightly overpredict the actual values but the error is only of a few percent at most (Götzinger and Peukert 2003; Israelachvili 2011; Osborne-Lee 1988). Given the value A_{11} of two identical media interacting through vacuum or inert air (or equivalently A_{131} where media 3 is air/vacuum), the value A_{131} for interactions through water as media 3 can be approximated as $A_{131} = A_{313} \approx (\sqrt{A_{11}} - \sqrt{A_{33}})^2$, where Hamaker coefficient for water $A_{33} = 3.7 \times 10^{-20}$ J. Such combinations are reserved to cases where dispersion forces dominate, and are reportedly less applicable to media with a high dielectric constant, which is the case of water and metal oxides (Israelachvili 2011). However, comparing results between a mixing rule and a more accurate equation showed little differences for a hydrous metal oxide system where dispersion forces still dominate (Lefèvre and Jolivet 2009), which suggests that mixing rules could nonetheless be applied to such materials to obtain a reasonable estimate of the Hamaker coefficient.

The nonretarded values given in table 2.8 are suitable for separation distances that are smaller than the bodies' characteristic dimension (e.g. particle radius). For large separation distances, i.e. beyond 5nm, the travel time of electromagnetic waves can become significant

with respect to the fluctuation time of instantaneous induced dipoles and thereby induce a retardation effect (Casimir effect) which must be accounted for in the calculation of the vdW force (Israelachvili 2011). The separation distance D used in calculating the vdW force between bodies in contact is usually taken as the intermolecular equilibrium separation distance. Common values found in the literature for non-metallic materials are 0.15, 0.165, 0.3 and 0.4nm, which are well below the retardation limit (Huang et al. 2015; Israelachvili 2011; LaMarche et al. 2016, 2017).

The vdW force as expressed in equation 2.1 considers perfectly smooth spherical particles. However, surface roughness impacts the local surface curvature and the true contact area, and thus the force distribution in the contact region between particles. Asperities reduce the local surface curvature and thereby diminish the magnitude of the vdW interaction forces. It has been shown that non-metallic particles of different sizes but similar topography exhibited similar interaction forces, and that small (< 75µm) cohesive irregular particles flow better than small cohesive smooth particles (Castellanos 2005). A decrease in adhesive forces also leads to a smaller rolling resistance (Wilson et al. 2017). However, for larger particles (> 2mm), the reverse can be true as smoother spherical particle better roll onto one another and thus exhibit a better flowability, as could be intuitively expected (Castellanos 2005). Comparatively larger particles are in fact also heavier and are therefore less impacted by the interparticle forces as the force of gravity dominates. The absence of asperities increases the local surface curvature and thus increases the strength of vdW forces, but it also diminishes the potential for mechanical interlocking and interparticle friction, and can therefore ultimately yield a better flowability. Metal AM powders dedicated to LMD generally present median particle diameters d_{50} around 75µm or higher, so that it is unclear whether an increase in nanoscale surface roughness would increase or decrease the flowability of cohesive metal AM powders such as 224.0 casting powders.

Several forms of the vdW force between two spherical particles with different diameters have been published depending on how the nanoscale roughness is modelled, e.g. as hemispheres, immersed spheres, or double immersed spheres (Capece et al. 2015; Castellanos 2005; Chen et al. 2008; LaMarche et al. 2017; Liu et al. 2016a; Rabinovich et al. 2000a; b). The various roughness geometries of these vdW force models are represented in figure 2.18. The Rumpf vdW force model (Rumpf 1990) considered a hemispherical asperity of known size on a surface interacting with a smooth sphere, and consists of two terms. A first term describes the "contact" force between the asperity and the smooth sphere, and a second term corresponds to the "noncontact" force between the bulk materials of the macroscopic bodies, which is independent of asperity size.

The size of the asperities is however usually unknown and difficult to measure, so vdW force models were eventually formulated in terms of more common measures of surface

roughness, i.e. root-mean-square roughness rms and peak-to-peak distance λ over 1 or 2 scales (LaMarche et al. 2017; Rabinovich et al. 2000a; b). The Rumpf model (Rumpf 1990) has been reformulated in terms of rms roughness and peak-to-peak distance λ, but was shown to largely underpredict the magnitude of adhesion forces, notably because the center of the hemispherical asperities is constrained to be on the surface, which cannot accurately describe the geometry of nanoscale roughness. It was thus modified to represent asperities as simple and double immersed spheres and was formulated in terms of rms roughness and λ over both small and large scales (Rabinovich et al. 2000a; b). The Rabinovich model only considered one-sided roughness however, the other surface being smooth. A more recent formulation of this model extended it to the case of two rough spherical particles with different diameters and roughness parameters (Liu et al. 2016a), which corresponds to equation 2.2 given hereafter.

Roughness measurements at the nanoscale are typically carried out by Atomic Force Microscopy (AFM), which requires expensive equipment, precise calibration and skilled operators. The two-scale roughness parameters λ_{kl} and rms_{kl} (see figure 2.18.d) can be extracted from raw AFM roughness amplitude measurements by applying high and low pass FFT filters. Care must be taken however to discard Gibson artefacts (due to abrupt changes in roughness amplitude) and "atomic-scale-noise" artifacts (due to measurement noise on the order of the atomic radius) that can arise from the filtering process. When precise roughness measurements are not available, a widely quoted value of 200nm for the mean asperity size has been used as a "natural" roughness for many non-metallic materials (Capece et al. 2014, 2016; Huang et al. 2015). When asperities are below 10nm, it has been reported that they can generally be ignored so that the vdW force model for smooth bodies can be used (Chen et al. 2008; Rabinovich et al. 2000a), however it has been shown through AFM adhesion force measurements that roughness values as small as 1.6nm were enough to induce a nearly five-fold decrease in adhesion force magnitude (Rabinovich et al. 2000b).

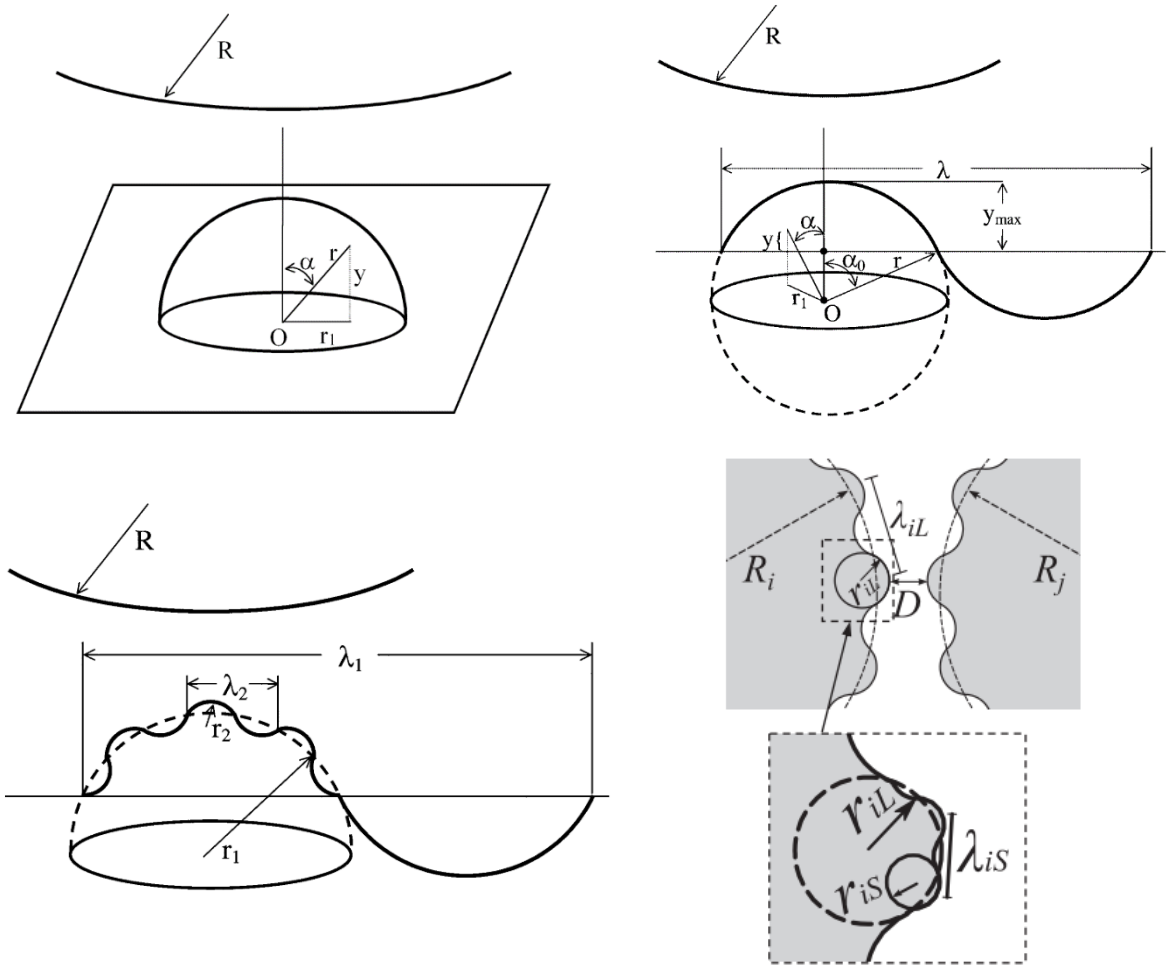

Figure 2.18: Particle roughness models.
a) one-sided hemisphere (Rumpf 1990)
b) 1-scale one-sided immersed sphere (Rabinovich et al. 2000a)
c) 2-scale one-sided double immersed spheres (Rabinovich et al. 2000b)
d) 2-scale two-sided double immersed spheres (Liu et al. 2016b)

$$F_{vdW_{ij}} = \frac{A_{ij}}{6}\left[\frac{R_iR_j}{(R_i+R_j)(D+y_{iL}+y_{iS}+y_{jL}+y_{jS})^2} + \frac{R_ir_{jL}}{(R_i+r_{jL})(D+y_{iL}+y_{iS}+y_{jS})^2} + \frac{R_ir_{jS}}{(R_i+r_{jS})\ D+y_{iL}+y_{iS}\ ^2} + \frac{r_{iL}R_j}{(r_{iL}+R_j)(D+y_{jL}+y_{jS}+y_{iS})^2} + \frac{r_{iS}R_j}{(r_{iS}+R_j)(D+y_{jS}+y_{jL})^2} + \frac{r_{iL}r_{jL}}{(r_{iL}+r_{jL})(D+y_{iS}+y_{jS})^2} + \frac{r_{iL}r_{jS}}{(r_{iL}+r_{jS})\ D+y_{iS}\ ^2} + \frac{r_{iS}r_{jL}}{(r_{iS}+r_{jL})(D+y_{jS})^2} + \frac{r_{iS}r_{jS}}{(r_{iS}+r_{jS})D^2}\right] \tag{2.2}$$

$$r_{kl} = \frac{\lambda_{kl}^2}{32k_1 rms_{kl}},\ y_{kl} = k_1 rms_{kl} \quad with\ k = i,j\ and\ l = S,L$$
$$k_1 = 1.817$$

Although further work is required to confirm the validity of equation 2.2, a satisfactory agreement with AFM measurements has been obtained (LaMarche et al. 2017; Liu et al. 2016a). Additional care in treating surface roughness in the vdW force models generally provides significant enhancement in predictive accuracy, further indicating that surface roughness plays a major role in the vdW interactions between rough particles and must be accurately evaluated (Castellanos 2005; Laitinen et al. 2013; LaMarche et al. 2017; Liu et al. 2016a).

The sensitivity of adhesion forces to surface roughness is especially important for rigid bodies such as alumina particles as the contact region is non-deforming (Götzinger and Peukert 2003). Aluminium has a very high affinity for oxygen, so that aluminium powder particles are often oxidized due to the rapid and spontaneous formation of a porous alumina layer upon contact with oxygen from the atmosphere. The width of this alumina layer is typically limited to about 5nm as aluminium oxidation in dry air is a self-limiting reaction, unless the alumina layer is thickened by anodization (Hatch 1984). In dry ambient air, this alumina layer offers a natural protection of the bulk metal against oxidation, and is expected to also be present on gas atomized aluminium powder particles. Plastic deformation between contacting aluminium particles should thus be negligible due to the high Young modulus (~370 GPa) of the alumina layer (Götzinger and Peukert 2003) and the relative rigidity of the bulk aluminium compared to many other organic, non-metal particle materials.

As there are no AFM roughness measurements available for the gas atomized aluminium powders under study, roughness values of smooth alumina particles from the literature are used to evaluate adhesion forces between aluminium particles. The 2-scale *rms* roughness rms_S, rms_L and peak-to-peak distances λ_S, λ_L of alumina particles Al_2O_3 with diameters between 5 and 15µm measured by AFM are reproduced in table 2.9 (Laitinen et al. 2013). These 2-scale values of nanoscale roughness are used hereafter for calculating the vdW force between aluminium particles according to equation 2.2, and are considered to be constant for all particle sizes. It is noted that these values are in fact much smaller than the "natural" asperity size of 200nm cited earlier, but they concern smooth, surface melted alumina particle (Götzinger and Peukert 2003).

Material	$\boldsymbol{rms_S}$	$\boldsymbol{rms_L}$	$\boldsymbol{\lambda_S}$	$\boldsymbol{\lambda_L}$
Alumina	1.5-12nm	12nm	0.7µm	10.2µm

Table 2.9: Roughness parameters for alumina particles (Laitinen et al. 2013)

There is some ambiguity as to what the value of the Hamaker constant should be, i.e. aluminium and alumina values, for naturally oxidized aluminium particles with a 5nm

thickness of the alumina layer. This thickness is much smaller than the particles' diameter (~100µm) but is also an order of magnitude higher than the equilibrium separation distance (< 1nm) between neighbour particles. For simpler geometries, combining rules could be used to determine the equivalent Hamaker coefficient, by treating the alumina layer as an adsorbed layer (Götzinger and Peukert 2003; Israelachvili 2011). Metal and metal oxides however typically present a Hamaker coefficient with similar orders of magnitude, although there is a relative lack of published values for these systems, so the Hamaker values for metals found in the literature (table 2.8) are used in the subsequent calculations for simplicity.

For two 224.0 aluminium particles of diameter 100µm with roughness parameters taken from table 2.9, Hamaker coefficient $A = 293$ zJ and equilibrium separation distance $D = 1$nm, the vdW force is $F_{vdW} = 36.4$ nN, which is about 24 times higher than particle weight. There is however a lot of uncertainty with this calculated value due to a lack of experimental data regarding roughness and equilibrium separation distance. The force model should however capture the relative change in vdW force magnitude with varying parameters.

ii. Capillary Force

The capillary force arises from the formation of liquid bridges (or capillary bridges) due to the condensation of water vapor contained in the ambient atmosphere, even at relatively low relative humidity levels. The geometry and force generated by the liquid bridge can be calculated based on the geometry of the interacting particles and relative humidity RH, defined as the the ratio of partial water vapour pressure to saturation vapour pressure of the air at the dry bulb temperature T. The capillary force contains three major contributions from surface tension, capillary pressure and buoyancy, the latter effect being ignored as gravitational effect are typically negligible for small capillary bridges. As illustrated in figure 2.19, the geometry of the capillary between two surface asperities modeled as double immersed spheres (as in the vdW force model of equation 2.2) is defined by the bridge half-width a_1, the bridge curvature a_2 and the half-filling angle β (LaMarche et al. 2016).

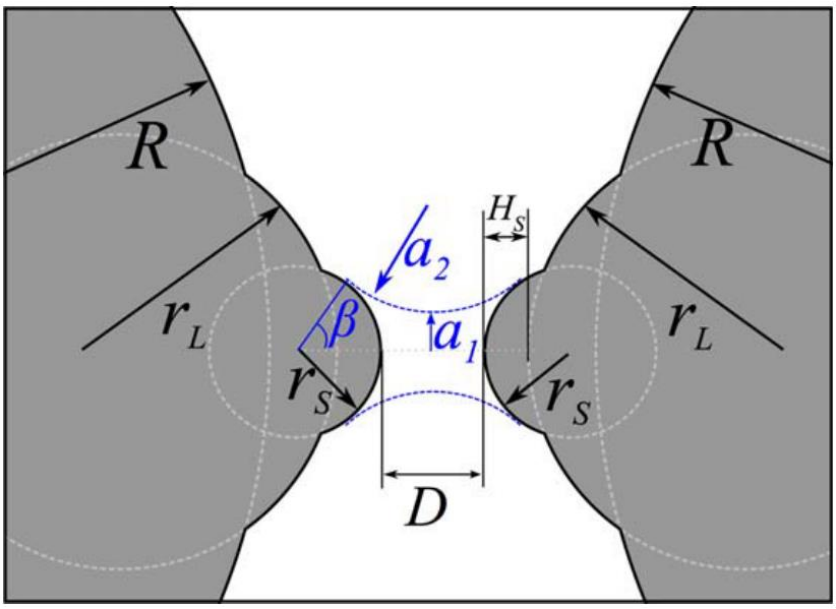

Figure 2.19: Liquid bridge between surface asperities modeled as double immersed spheres (LaMarche et al. 2016)

The surface tension component of the capillary force is proportional to circumference of the gas-liquid-solid contact line, approximated by the circumference $2\pi a_1$ of the bridge, and water surface tension $\sigma = 72 \times 10^{-3}$ N/m. The capillary pressure contribution arises from the pressure drop Δp_l across the bridge's curved surface acting on the cross-sectional area πa_1^2 of the contact line. According to this so-called gorge approximation, the capillary force is then expressed as the sum of these two components, neglecting buoyancy effects:

$$F_{cap} = 2\pi a_1 \sigma + \pi {a_1}^2 \Delta p_l \tag{2.3}$$

Assuming that the bridge is in equilibrium with the vapor in the surrounding atmosphere, the Kelvin equation can be used to calculate the pressure drop Δp_l in terms of relative humidity RH:

$$\Delta p_l = -\overline{\rho_l} R_g T \ln\, RH \tag{2.4}$$

where T is temperature (K), $\overline{\rho_l} = 5.56 \times 10^4$ mol/m^3 is the molar density of water and $R_g = 8.314$ J/mol.K is the universal gas constant.

To compute the bridge half-width a_1, the shape of the bridge can be related to the pressure drop Δp_l through the Laplace-Young equation by neglecting gravitational effects for small bridges:

$$\Delta p_l = -\sigma \left(\frac{1}{a_2} + \frac{1}{a_1} \right) \tag{2.5}$$

Assuming that the contact angle of the bridge with the asperity is zero, half-width a_1 and curvature a_2 are related to the half-filling angle β, the separation distance D and large or small asperity size r_l $(l = S, L)$ through the following equations (LaMarche et al. 2016):

$$a_1 = R\left[\left(1 + \frac{D}{2r_i}\right)\tan\ \beta\ - \left(1 + \frac{D}{2r_i}\right)\sec\ \beta\ + 1\right] \tag{2.6}$$

$$a_2 = \left[\left(1 + \frac{D}{2r_i}\right)\sec\ \beta\ - 1\right] \tag{2.7}$$

To solve for a_2, equations 2.6 and 2.7 are substituted in equation 2.5 to express Δp_l as a function of β, r_l and D. Combining Kelvin equation 2.4 and Laplace-Young equation 2.5, β can be numerically resolved given r_l, D and RH. The above equations were derived for a monodisperse granular system with particles of equal sizes. To account for polydispersity, the radius R is here evaluated as the geometric mean of the radius of the interacting particles. Roughness parameters are assumed to be uniform throughout the PSD, and a single contact region between particles and thus a single capillary bridge is considered. Similarly to (LaMarche et al. 2016), the asperity size r_l is selected depending on RH, such that when $RH < 85\%$, asperity size is set to r_S as the bridge size is assumed to be small, whereas for $RH \geq 85\%$, the liquid bridge gets larger and asperity size r_L is chosen with separation distance D being adjusted for the extra bridge length by adding the small asperity height on both sides, i.e. $2H_S$. The reported $85\%RH$ threshold has been established by wet fluidization experiments with glass beads of similar size and density as aluminium AM powders. It is unclear whether it is applicable to metal AM powders, but such relative humidity levels are not reached in the present experiments.

For two 224.0 aluminium particles of diameter 100µm in air at 25°C and $41\%RH$ with roughness parameters taken from table 2.9 and equilibrium separation distance $D = 1$nm, the capillary force is $F_{cap} = 29.3$ nN, which is about 20 times higher than the particle weight and is on the same order of magnitude as the vdW force calculated previously. Again, there is a lot of uncertainty with this calculated value due to lack of experimental data regarding roughness and equilibrium separation distance. The force model should nonetheless capture the relative change in capillary force magnitude with varying parameters.

iii. Electrostatic Force

Electrostatic charges can accumulate on the surface of an initially uncharged particle upon contact with other materials due to the triboelectrification phenomenon, which combines contact charging and frictional charging effects (Matsusaka et al. 2010; Matsusaka and Masuda 2003; Oguchi and Tamatani 1993). It can for instance occur from (repeated) rolling or sliding contacts between dissimilar materials, from which can result an exchange of electrons to equalize their surface work functions (Ireland 2010; Peart 2001).

Charged particles generate a coulombic image force when in the vicinity of a surface such as an uncharged grounded conducting media, in which case an imaginary charge of opposite sign arises inside the grounded conductor to create an attractive electrostatic force (see figure 2.20). The particle surface charge can uniformly redistribute over the surface, or form islands as local patches of high charge density (Peart 2001). With the attractive image force arising from the interaction with a surface, the particle's surface charges typically concentrate in the particle region closest to the image charge due to the attractive coulombic force, so that the particle charge distribution becomes non-uniform over its surface (Feng and Hays 2003). Charge dissipation time is relatively large for insulator materials such as pharmaceutical powders, so that electrostatic forces can become an issue during powder handling of (Peart 2001; Shah et al. 2017). For neutral metal AM powders such as aluminium powders, it is less clear how charges tend to accumulate and dissipate on the particle surface as aluminium is a good conductor but is usually covered on its surface by a thin layer of oxides (alumina), and possibly hydroxides, which are insulating and therefore impede the flow of charges, thus potentially leading to large charge dissipation times if the particle does become charged.

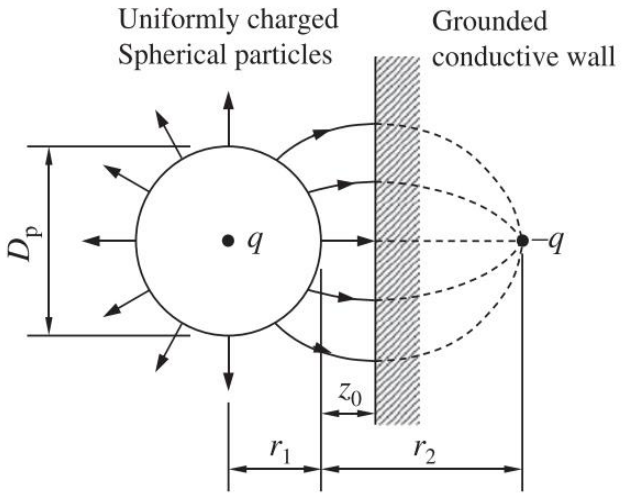

Figure 2.20: Image force induced on a grounded conductive wall by a uniformly charged spherical particle (Matsusaka et al. 2010)

So-called triboelectric series are traditionally used to qualitatively assess the relative tendency of contacting materials to charge positively or negatively (Pan and Zhang 2019; Peart 2001), which are presented in table 2.10 for a few materials. It has however been shown that these series can be cyclic and thus cannot be solely relied upon to evaluate the charging behavior of materials (Pan and Zhang 2019). Moreover, there can be a size effect where smaller particles have an increased charge transfer and may charge more negatively than larger particles of the same materials (Castellanos 2005; Ireland 2010; Pan and Zhang 2019; Shah et al. 2017). Thus polydisperse blends of dissimilar particles with a wide PSD can have particles with varying charge levels and sign, which can lead to attractive electrostatic forces that increase the cohesiveness of the powder. The tribocharging level is also dependent on temperature and humidity (Matsusaka et al. 2010; Pan and Zhang 2019). It has also been generally assumed that tribocharging could only occur between different materials, i.e. materials with different work functions. However, experimental results have shown that similar materials can in fact get tribocharged, which can be explained by non-equilibrium surface states (Pan and Zhang 2019). AM powder particles also frequently encounter different materials by contact with surfaces from the walls of the reservoir, the piping system and the projection nozzle of the LMD system, including materials such as teflon (distribution system) and copper (nozzle). The pneumatic piping system is however typically designed to avoid the generation of electrostatic charges.

Positively charged (+)	**Glass**
	Wool
	Nylon
	Aluminium
	Paper
Reference	Cotton
	Wood
	Stainless Steel
	Hard Rubber
	Copper/Nickel/Brass
	PVC
Negatively charged (-)	Teflon

Table 2.10: Triboelectric series – adapted from (Peart 2001)

It has generally been reported that dry fine neutral powders from a unique base material and without an externally applied electric field are typically dominated by van der Waals forces, so that electrostatic forces are usually negligible (Castellanos 2005; Feng and Hays 2003). It is however unclear whether this is also true for cohesive metal AM powders such as 224.0 powder samples during in-process LMD testing.

Charge measurements of powders flowing on steel pipes were provided by UTBM for powder samples 224.0-A 20-80µm and 224.0-A 100-125µm, as well as Al-Mg 10-40µm and Al10SiMg 20-63µm powders for comparison. The results indicate that powder samples 224.0-A 20-80µm and 100-125µm charged negatively at around -0.3 µC/kg. Powder Al10SiMg also charged negatively but to a lesser extent, at around -0.2 µC/kg. In contrast, powder Al-Mg charged positively around +0.3µC/kg. This suggests that both the charging sign and density can vary with aluminium alloy composition, but are not as affected by granulometry. The triboelectric series (table 2.10) however indicates that aluminium should charge positively against stainless steel, which is only the case for the Al-Mg powder. The alumina content and more generally particle surface properties are also significant factors that could explain this difference in charging behavior between aluminium powders (Oguchi and Tamatani 1993).

To evaluate the actual electrostatic force that may stem from the measured charge levels, the image force based on uncharged surfaces such as grounded conductors can be simply estimated using the Coulomb force model (Peart 2001). These grounded conducting surfaces can for example be found in the reservoir or in the projection nozzle of the LMD process. More accurate expressions of the particle image force exist for charged spheres, with or without an external electric field being applied, but they include dimensionless coefficients that depend on many parameters such as the dielectric constant (Feng and Hays 2003). For a qualitative assessment, the basic coulombic force model is used (Matsusaka et al. 2010; Peart 2001). The image charge of a charged particle in a flat grounded conductor is symmetrical to the particle charge but with opposite sign. The image force F_{im} induced by on a grounded flat conductive surface (e.g. copper LMD nozzle) at a separation distance D is thus here expressed as:

$$F_{im} = \frac{Q_p^2}{4\pi\epsilon_0 D^2} \tag{2.8}$$

where Q_p is the particle charge assuming that the charges are uniformly distributed on the surface, so that particle and image charges can be approximated as equivalent point charges $\pm Q_p$ separated by distance $D = D_p + 2z_0$ (see figure 2.20).

To estimate the value of image force F_{im} from the tribocharging mesurements, the Sauter mean diameter $d_{3,2}$ can be used to convert a polydisperse granular system to a monosized granular system with equal surface/volume ratio, which is relevant for surface phenomena such as adhesion forces (Kowalczuk and Drzymala 2016). For sample 224.0-A 20-80µm, the Sauter mean diameter is given as $d_{3,2} = D_p = 35.34$ µm and material density is $\rho = 2841$ kg/m^3 based on atomic composition and a mixture rule. The corresponding particle mass is $m_p \approx 6.6e \times 10^{-11}$ kg. Assuming the measured specific charge $\overline{Q} = -0.3$ µC/kg is evenly distributed on the surface of the Sauter-equivalent particles, and that particle-surface

separation distance $z_0 = 1$nm with vacuum permittivity $\epsilon_0 = 8.85 \times 10^{-12}$ F/m, the resulting coulombic image force is $F_{im} \approx 3.45 \times 10^{-14}$ N. If charges are instead concentrated near the point nearest to the grounded conductor due to electrostatic attraction, then $D = 2z_0$ and $F_{im} \approx 8.72 \times 10^{-7}$ N. The image force calculation is thus highly dependent upon separation distance D and surface charge distribution, which have unknown values. In comparison, the particle weight is $W_p = m_p g \approx 6.4 \times 10^{-10}$ N or 0.64 nN, which is 4 orders of magnitude lower. For conducting materials like metals, the surface charges causing the attractive image force should dissipate rapidly (Peart 2001). It is unclear whether the thin, insulating alumina layer on naturally oxidized aluminium particles is sufficient to retain charges in local surface regions over significant periods of time.

In the present work, electrostatic forces are ignored as triboelectric charging is a complex phenomenon that is not easily amenable to a simple and accurate analytical model, while the vdW force from equation 2.2 and the capillary force model from equation 2.3 are accounted for in the calculation of the flowability criterion Bo_g^* presented hereafter as they are the most prevalent forces in fine dry neutral granular materials such as AM aluminium powder. This can be further justified by results from Rumpf in 1962 reported in (Zhu et al. 2007) where the vdW, capillary, electrostatic (from contact potential and excess charge) forces and weight of particles are compared, as illustrated in figure 2.21. The density was taken as 3000 kg/m^3 (i.e close to aluminium), Hamaker constant is 65 zJ (i.e. much lower than most metals), and equilibrium separation distance is set to 0.165nm. These calculations indicate that electrostatic forces from contact charging have a much lower magnitude than vdW and capillary forces.

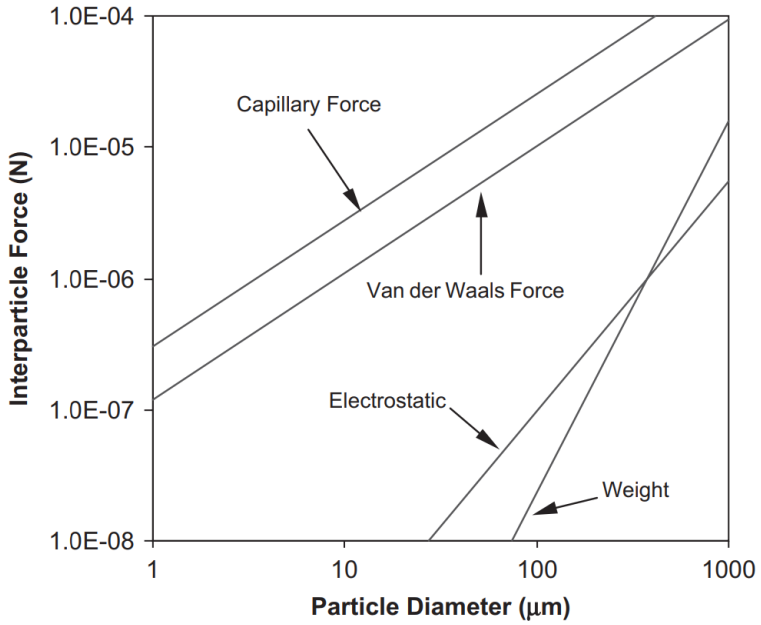

Figure 2.21: Comparison of main interparticle forces calculated by Rumpf, as reported in (Zhu et al. 2007)

c. Flowability Criterion

A typical characteristic number for a granular material is the granular Bond number Bo_g, which is generally defined as the ratio of interparticle attractive forces or adhesion forces F_a to other surface or body forces such as the gravitational weight W of a single particle (Capece et al. 2014, 2015, 2016; Castellanos 2005).

$$Bo_g = F_a/\mathrm{W} \tag{2.9}$$

with $F_a = F_{vdW} + F_{cap}$ (ignoring electrostatic and other forces) and $W = mg$, where m is the particle mass and g is the gravitational constant.

While generally pertinent to evaluate bulk powder properties such as flowability from particle level interactions, the granular Bond number Bo_g cannot fully explain these bulk behaviors as it fails to account for the entire distribution of particle sizes since it focuses on a single particle. An aggregate granular Bond number was proposed to include the presence of agglomerates in fine cohesive toner powders (Castellanos 2005), which was shown to better explain the flowability enhancement obtained by dry coating pharmaceutical powders (Huang et al. 2015), but it remains limited as it does not explicitly include the characteristics of the PSD. A population-dependent granular Bond number Bo_g^* was suggested as a remedy (Capece et al. 2014, 2015), which is a weighted mean of the granular Bond number Bo_g between discrete groups of particle sizes:

$$Bo_g^* = \left(\sum_{k=1}^{L} \sum_{l=1}^{L} \frac{w_{kl}}{Bo_{g,kl}} \right)^{-1} \tag{2.10}$$

$$Bo_{g,kl} = \frac{F_{a,kl}}{W_{kl}} \tag{2.11}$$

To compute this flowability criteria, the PSD curve is discretized into L groups with equal particle sizes. For instance, gas atomized metal AM powders such as 224.0 powders follow the log-normal distribution, which is analytically expressed as follows:

$$f\ x|\mu,\sigma\ = \frac{1}{x\sigma\sqrt{2\pi}} \exp\left(-\frac{(\ln\ x\ - \mu)^2}{2\sigma^2} \right) \tag{2.12}$$

where x is the particle diameter, μ and σ are the mean and standard deviation of the normally distributed variable $\ln(x)$. They can be expressed in terms of D-values d_{50} and d_{16}, or

equivalently d_{50} and d_{84} (Lavernia and Chang 1997), but for simplicity it is assumed here that $d_{16} \approx d_{10}$ and $d_{84} \approx d_{90}$ so that μ and σ are expressed in terms of more commonly reported D-values:

$$\mu = \ln(d_{50}) \tag{2.13}$$

$$\sigma = \ln\left(\frac{d_{50}}{d_{16}}\right) = \ln\left(\frac{d_{84}}{d_{50}}\right) \approx \ln\left(\frac{d_{90}}{d_{50}}\right) \approx \ln\left(\frac{d_{50}}{d_{10}}\right) \tag{2.14}$$

The interaction force $F_{a,kl} = F_{vdW,kl} + F_{cap,kl}$ and mean weight W_{kl} are computed between every group pairs k and l. The weighing factor w_{kl} is calculated based on the fractional surface area occupied by each group with respect to the total surface area of particles, thereby providing a measure of the probability that particles from two different groups will interact with each other. Using a coordination number instead could prove to be more accurate but it is fairly difficult to evaluate in polydisperse granular systems (Capece et al. 2015, 2016).

This population-dependent granular Bond number Bo_g^* has been successful in predicting the flowability of pharmaceutical powders (Capece et al. 2015, 2016) and wheat flour (Siliveru et al. 2017) as it could be correlated to the often reported flow function coefficient ffc obtained from shear cell testing methods. This Bo_g^* criterion is general in nature but has not yet been applied to metal AM powders. The applicability of this population-dependent granular Bond number Bo_g^* in predicting bulk powder properties such as flowability should be restricted to cohesive, low-flowability powders that are dominated by vdW forces, i.e. $Bo_g^* \geq 1$, as the flowability and bulk behavior of non-cohesive powders $Bo_g^* < 1$ depend on many other factors such as particle shape (Capece et al. 2015, 2016).

The flowability criterion Bo_g^* (Capece et al. 2014, 2015, 2016) has previously been evaluated using the so-called "multi-asperity" Rumpf model (Chen et al. 2008) based on the Sauter mean diameter $d_{3,2}$ instead of median diameter d_{50} since it is particularly relevant to surface phenomenon such as adhesion forces. It has been applied to nanoparticle coating of cohesive pharmaceutical powders, with 3 nanoparticle contact points between monosized spherical powder particles. Harmonic and geometric means were used to extend the model to polydisperse granular systems, yielding equivalent combined diameters, asperity sizes, Hamaker constants, and particle weights.

In the present work, a more recent and accurate model (equation 2.2) is used to calculate the van der Waals force $F_{vdW,kl}$, where particle polydispersity and *rms* roughness are naturally accounted for (LaMarche et al. 2017; Liu et al. 2016b). The contribution of the capillary force $F_{cap,kl}$ is also included in the computation of adhesion force $F_{a,kl}$, as it conveniently adopts the same 2-scale *rms* roughness approach to the vdW force formulation.

It is here adapted to a polydisperse system by using the geometric mean of the particle radii, as done by (Capece et al. 2015, 2016) for calculating vdW forces on a polydisperse system with a monodisperse vdW force model (Chen et al. 2008). The median diameter d_{50} is used for particle diameters as the Sauter mean diameter $d_{3,2}$ is not known for many powder samples, and is typically close to median diameter d_{50} for gas atomized metal powders.

Tangential forces such as rolling/sliding particle-particle and particle-wall friction or viscous forces from the capillary bridges are ignored for simplicity as they are dependent upon relative particle motion. The analysis is focused on an initially static configuration, i.e. right before flow initiation, so that dynamic effects can be deemed negligible until particle flow is triggered, at which point friction forces and fluid interactions must be accounted for, usually by way of computer simulations. It has been shown that unlike most coarse granular materials, fine cohesive powders in free surface flow do not go through the inertial regime where particle collisions dominate the flow. Instead they tend to transition directly from a plastic regime, dominated by gravitational stresses, to fluidization and suspension regimes where particle-fluid interactions are prevalent (Castellanos 2005). This is for instance observed in funnel flowability experiments of the present work, where cohesive 224.0 powders would flow in a rat hole/core flow pattern, forming a center pipe hole where finer particles get fluidized by the local fluid motion while the surrounding bulk powder remains static due to stable bridges formed by interparticle force chains. Very cohesive powders can remain fully static due to arching bridges, while less cohesive powders form a funnel flow, where particles near the funnel centerline flow faster than those on the sides. High flowability powders (e.g. 316L) tend discharge in a mass flow regime, where all particles essentially have the same velocity. Wall friction effects are reported to have a significant influence on the transition from mass to funnel flow regimes, and a high Hausner Ratio HR is said to increase the probability of bridging (Polizzi et al. 2016).

The Bo_g^* calculations of the present work consider the presence of vdW and capillary interparticle forces only, and assume the particles to be rigid, non-porous, spherical without satellites, and with a single contact region between particle pairs. Base material densities are estimated based on available literature data, and missing values are calculated through a mixture rule based on alloy composition and base element atomic densities at room temperature (Valencia 2008). A code has been written in MATLAB to perform the calculations.

For an hypothetical reference aluminium powder 224.0 45-90µm with $d_{10} = 45$µm, $d_{50} = 65$µm, $d_{90} = 90$µm (span = 0.69), Hamaker constant $A = 293$ zJ, density $\rho = 2841$ kg/m^3 in air at 25°C and 41%RH with roughness parameters taken from table 2.9 and equilibrium separation distance $D = 1$nm, the calculated population-dependent granular Bond number is $Bo_g^* = 172.18$, which is much higher than unity, the usual flowability threshold.

Due to the uncertainty in the parameters used for calculating the vdW and capillary forces, the flowability criterion will be used here in relative terms to compare the influence of various parameters (material density, PSD etc.) on flowability according to the adhesion force models. To explore the influence of some key parameters, this calculated value can be taken as a reference value $Bo^*_{g,ref}$ and a relative population-dependent granular Bond number is defined as $Bo^*_{g,rel} = Bo^*_g / Bo^*_{g,ref}$, so that $Bo^*_{g,rel} = 1$ for this reference aluminium powder.

Before assessing the correlation between the $Bo^*_{g,rel}$ criterion and flowability measurements in the next section, a basic evaluation of its sensitivity to material parameters and environmental conditions can be obtained with the following calculations and comparing the results to unity. Material density is directly proportional to particle weight, so changing the powder material to 316L ($\rho \approx 8000$ kg/m^3) gives $Bo^*_{g,rel} = 0.34$. Halving the Hamaker constant leads to $Bo^*_{g,rel} = 0.70$, and doubling it implies $Bo^*_{g,rel} = 1.50$. Halving the relative humidity gives $Bo^*_{g,rel} = 0.78$, while doubling it induces $Bo^*_{g,rel} = 2.48$. Doubling the median diameter d_{50} of the aluminium powder while keeping the span constant yields $Bo^*_{g,rel} = 0.12$. Conversely, halving the median diameter at constant span indicates $Bo^*_{g,rel} = 7.79$. Halving the span while keeping $d_{50} = 65$µm gives $Bo^*_{g,rel} = 0.90$, while doubling it induces $Bo^*_{g,rel} = 1.57$. These numerical applications, summarized in table 2.11, show that the values are not symmetrical, which means there are significant non-linear effects associated with common PSD parameters such as d_{50} and span on flowability according to this model. There is also a strong effect of the separation distance and *rms* roughness parameters, which are however kept constant in the present work throughout all samples due to a lack of relevant experimental data.

Material	**Density (g/cm^3)**	**Hamaker constant (zJ)**	$\boldsymbol{d_{50}}$ **(µm)**	**span**	**%RH**	$\boldsymbol{Bo^*_{g,rel}}$
224.0	2.841	293	65	0.69	41	1
316L	8.0	293	65	0.69	41	0.34
224.0	2.841	146.5	65	0.69	41	0.70
224.0	2.841	586	65	0.69	41	1.50
224.0	2.841	293	65	0.69	20.5	0.78
224.0	2.841	293	65	0.69	82	2.48
224.0	2.841	293	130	0.69	41	0.12
224.0	2.841	293	32.5	0.69	41	7.79
224.0	2.841	293	65	0.345	41	0.90
224.0	2.841	293	65	1.38	41	1.57

Table 2.11: Variation of flowability criterion $Bo^*_{g,rel}$ with powder properties based on a hypothetical 224.0 powder

II. Flowmeter Testing of Cohesive Aluminium Powders

a. Flowability Testing Methods

The flowability of metal AM powders is a critical bulk powder property for AM processes such as SLM and LMD where the material feedstock is provided in powder form. Indeed, the processability of an AM powder notably depends on its propensity to being displaced in bulk in a smooth, homogeneous manner without consolidating in the process, whether it be under the effect of the gravitational force, a mechanical action or a fluidizing carrier gas flow. The flowability property is however not clearly defined as it is an umbrella term used for characterizing the overall behavior of powder particles when subjected to various loads or stresses (Vock et al. 2019). The flowability measures and indices that characterize the ability to flow of a given powder are thus ultimately tied to the chosen apparatus and characterization technique, which are not necessarily representative of the in-process conditions encountered in AM processes, and more particularly LMD.

A number of flowability characterization technique and devices exist, ranging from aerated or fluidized conditions where stress levels are low (e.g. fluidized bed, powder rheometer FT4) to free surface conditions (e.g. rotating drum, Hall or Carney flowmeters, Angle of Repose AoR, Hausner Ratio HR, Carr index or Compressibility index C, optical evaluation) to packed bed or consolidated conditions (e.g. Jenike or Schultze shear cells) (Carson and Pittenger 1998; Leturia et al. 2014; Spierings et al. 2015; Vock et al. 2019). Most of the publications on metal AM powder flowability found in the literature so far mostly focused on SLM, where satisfactory powder flowability in packed bed and free surface conditions is necessary in order to properly rake or roll new coating layers of powder onto the powder bed. In LMD, powder particles are also found under aerated conditions as they are fluidized by an inert carrier gas (e.g. argon) at the reservoir outlet for pneumatic transport towards the nozzle, while the powder inside the reservoir is essentially in free surface/packed bed conditions. The powders are thus exposed to a wider range of flow conditions in LMD than in SLM or EBM.

It can be argued that among the many characterization techniques and devices available, hopper flowmeters are among the more representative flowability tests for AM processes as the powder is in low consolidation conditions with small compressive stresses, which somewhat mirrors the conditions of a powder in typical funnel-like powder reservoirs, although no standard AM powder flowability testing method has been clearly established (Spierings et al. 2015).

b. Standard Funnel Flowmeter Testing

Flowability testing with through hoppers makes use of either a Hall flowmeter (ASTM B213-11) or a Carney flowmeters (ASTM B964-09), which only differ by the diameter of the hopper aperture (2.5 and 5 mm respectively) (Carson and Pittenger 1998). The Carney flowmeter, whose aperture is larger, is generally employed when powders are too cohesive to flow through the Hall flowmeter. Several alternative flowability measures are available with such flowmeters: static discharge time (per unit volume), dynamic discharge time, and Angle of Repose AoR. The latter, sometimes also called avalanche angle (especially when performing dynamic measurements, for examples with a rotating cylinder), can be measured as the angle with respect to the horizontal plane of the pile of powder after it has been discharged through the hopper flowmeter and brought to rest on a plate underneath. AoR measurements are however not very repeatable for even slightly cohesive powders (Carson and Pittenger 1998). Moreover, highly cohesive powders cannot flow through either the Hall or Carney flowmeter to begin with, so that a static AoR measurement with the hopper flowmeter cannot relied upon. Rotating drums can provide a dynamic alternative to the AoR measurement but the results are difficult to interpret for cohesive powders as the powder flow does not reach a steady state avalanche angle and behaves erratically (Castellanos 2005).

The standard procedure for flowability testing using Hall and Carney funnel flowmeters is described by ASTM B213-13 and ASTM B964-09, respectively (see figure 2.22). It involves pouring a fixed mass of powder (usually 50 to 200g depending on the material) inside the funnel while blocking the discharge orifice with a dry finger. Upon removal of the finger, a stopwatch is started and the total powder discharge time is measured. If the powder does not flow through the Hall funnel, the Carney funnel can be used as it presents a lager discharge orifice that facilitates the passage of powder particles. According to the ASTM standards, only a single light tap on the funnel is permitted at the start of the test to initiate the flow, or, with the Carney funnel, a wire can also be moved up and down the funnel without penetrating the density cup. The procedure is to be repeated at least 3 times to yield an average flowability measurement, as each run is influenced by the initial packing configuration of particles when poured inside the funnel, especially with cohesive, low-flowability powders.

Preliminary testing with the Hall and Carney flowmeters demonstrated that the flowability of aluminium-copper powders 224.0/AU5MVZr is generally quite poor. Indeed, 224.0 powder samples remained static and did not flow through the Hall flowmeter. The powders occasionally flowed in the Carney funnel but it was not a common occurrence. More often, a stable bridge or a stable rat hole pattern (see figure 2.24) would form until another manual tap came to destabilize the structure. Flowability testing of cohesive, low-flowability powders using Hall or Carney funnels therefore does not allow to discriminate between cohesive

powders as they typically do not readily flow through the discharge orifice. Initiating the flow of cohesive powders using manual taps or by manually moving a wire up and down the funnel further diminishes the repeatability of the flowability testing procedure, which is already highly dependent on the initial packing configuration of the particles inside the funnel, and thus on the operator performing the tests.

Figure 2.22: Standard Hall Flowmeter testing

To retain the pertinence of a funnel-based approach for flowability testing of powders for AM applications while enabling flowability measurements of cohesive, low-flowability powders, it is necessary to devise a more systematic and repeatable method for triggering and sustaining the flow of cohesive powder particles inside a funnel.

c. Vibration-Assisted Funnel Flowmeter Testing

The funnel flowmeter approach for powder flowability testing can be extended to low-flowability, cohesive powders by applying an external excitation that is controllable and capable of triggering and sustaining the flow of cohesive powder particles through the discharge orifice.

Vibrations have previously been used to initiate a flow of powder through capillaries using 1kHz pulses (Yang and Evans 2005, 2007) and ultrasounds (Matsusaka et al. 1995), glass pipettes and containers at up to 100Hz (Dunst et al. 2018), vibration-controlled capillary steel nozzles for polymer powder dispensing in SLM with up to 970Hz piezo-induced vibrations (Stichel et al. 2014, 2016),. It is noted that vibrations can induce compaction or dilation within the powder depending on vibration mode and particle properties (material, morphology etc.), the latter effect leading to better flowability while the former impedes powder flow (Stichel et al. 2016). Vibrations have also been used to improve the packing efficiency of powders before a compaction process (Yang and Evans 2007).

Some studies focused on improving hopper discharge rate through transversal and axial low-frequency vibrations, i.e. up to 300Hz, where it was shown that specific vibrational

conditions must generally be met to effectively obtain some improvement (Fayed and Otten 1997; Staffa et al. 1977). It has also been shown that horizontal vibrations on small-scale funnels generated by a pneumatic vibrator (at an unreported frequency) and applied before discharge could actually hinder flow initiation and promote bridge formation in pharmaceutical powders, and should therefore be avoided during powder handling and storage (Polizzi et al. 2016). Flow initiation was found to be most significantly dependent on the Hausner ratio (tapped/bulk density ratio), the half-opening angle ϕ and orifice diameter D of the funnel (see figure 2.23), and most importantly on the presence or absence of vibrations before discharge. The hopper scaling parameter $\tan \phi \ /D$ was proposed as a size-independent geometric parameter for predicting bridge formation in hoppers of various materials and geometries. Larger orifice diameters D were reported to decrease the bridging tendency, while wall friction promoted the transition from mass flow to funnel flow (see figure 2.24). Funnel fill level or measurements from shear cell testers and powder rheometers appeared to be much less significant in predicting bridging conditions (Polizzi et al. 2016).

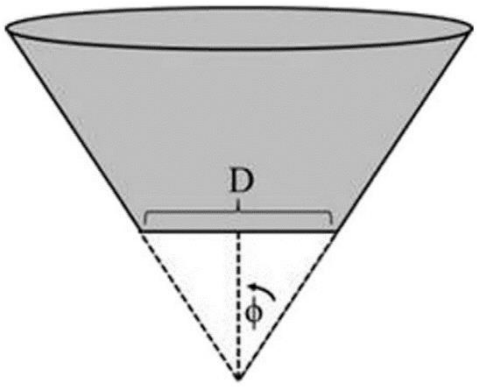

Figure 2.23: Hopper half-opening angle and diameter used to define a scaling parameter (Polizzi et al. 2016)

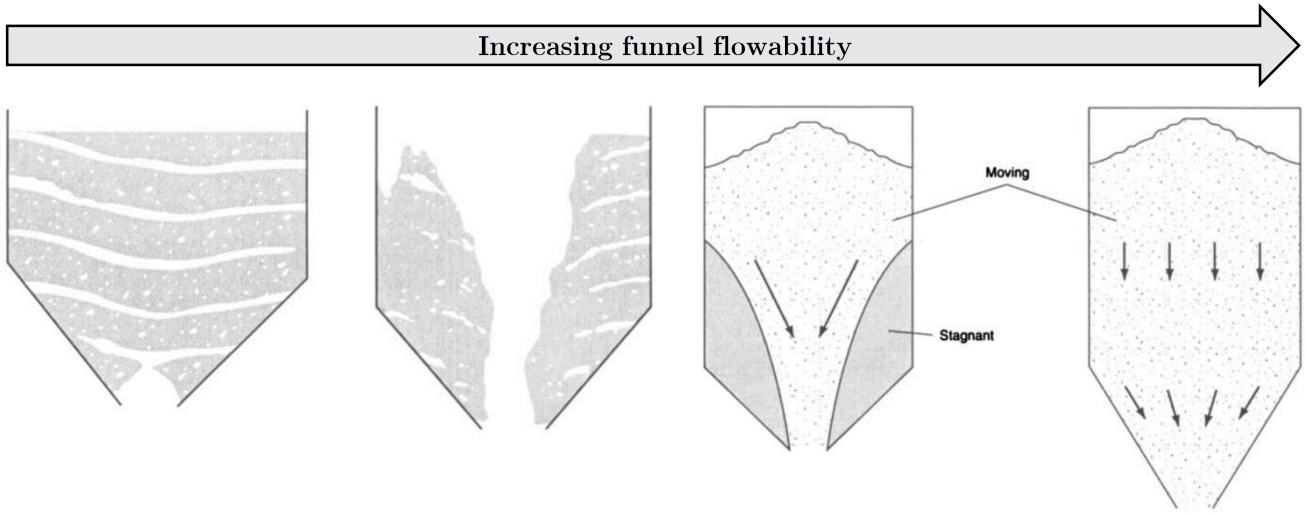

Figure 2.24: Funnel flow patterns – Bridging, Stable rat hole, Funnel flow, Mass flow (from left to right). Adapted from (Carson and Pittenger 1998)

Thus, previous studies show that the effect of vibrations on hoppers can be beneficial or detrimental to the discharge time of fine cohesive powders. It has not been established whether vibrations can be advantageous for the specific case of cohesive metal AM powders and, if so, under what vibrational conditions. Moreover, the previously tested frequency range is usually fairly low (<1kHz), except for instances using ultrasonic assistance (>20kHz), mostly with small capillaries. There is a relative lack of published results regarding the 1-10kHz range, which incidentally turned out to be most favorable for improving the flowability of metal AM powders in the experiments described hereafter.

A funnel flowability testing method for cohesive metal AM powders is here presented, in which lateral vibrational excitations are applied to powder samples through the funnel wall during discharge. This allows to evaluate the flowability of otherwise non-flowing powders in standard Hall and Carney funnel flowmeters. Because of the relatively large mass of standard Hall and Carney funnels (319g), a lighter funnel (5.5g) with a geometry approaching that of the Carney funnel was used instead to facilitate the transmission of vibrations through the walls and to the powder bulk. To provide the vibrational excitation, a disk-shaped piezoelectric transducer is mounted against the lateral outer wall of the funnel and is connected to a function generator that can generate signals in the 1Hz-100kHz frequency range at a maximum amplitude of $10V_{pp}$. The piezoelectric actuator weighs 3g for a 50mm diameter and is rated for 30Vca, draws 1.5mA of current for an acoustic pressure of up to 75dB over a frequency range of 0.5 to 20 kHz. The use of a piezoelectric transducer enables relatively high frequency vibrations to be transmitted to the funnel walls and the powder particles. Vibrations can induce a local particle displacement that breaks the particle force chains, thus triggering and sustaining the flow of particles inside the funnel by preventing the formation of stable arching bridges.

The substitute funnel has a discharge orifice diameter $D = 6$mm, which is slight larger than the Carney orifice diameter (5mm), and the same half-opening angle as the Hall and Carney funnels ($\phi = 30°$). The hopper scale-up parameter $\tan \phi \ /D$ (Polizzi et al. 2016) of this funnel is relatively close to the value obtained for the Carney funnel (about 0.227, 0.113 and 0.096 for Hall, Carney and substitute funnels, respectively). It is a thin-wall funnel made of a plastic material instead of aluminium and thus does not strictly follow the ASTM standards in terms of orifice diameter, material and surface finish. Plastic materials are non-conductive, which could induce some extra electrostatic charges due to the triboelectrification phenomenon (Matsusaka et al. 2010). However it permits the effective transmission of piezo-induced vibrations towards the powder bulk, which is otherwise not possible with a more massive standard flowmeter. The dimensionless vibrational acceleration can be defined as $\Gamma =$

$2\pi af/g$ (Fayed and Otten 1997; Yang 2006) to relate experimental results with various frequencies f under gravitational acceleration g, however the displacement amplitude a of the funnel-piezoelectric actuator assembly is unknown so the frequency and amplitude are given based on values selected at the function generator.

To relate the performance of the funnel used in the experiments to standard funnels, the flowability of a 25cm^3 volume of a reference 316L 15-45µm powder was measured with standard Hall and Carney funnels and the substitute funnel (without vibrations) over 3 repetitions. The average (standard deviation) of flowability measurement (discharge time/volume) for the Hall, Carney and substitute funnel respectively are 0.15 (0.003), 0.27 (0.001) 1.41 (0.013) s/cm^3. The flowability of this free flowing 316L powder is thus about twice as high when measured with the substitute funnel compared to the Carney funnel. It is noted that the variability of repeated flowability measurements generally decreases with improved flowability, which is also observed in the flowability experiments presented hereafter.

The vibration-assisted hopper flowability measurements of various powders essentially followed the standard ASTM method, with the added vibrational assistance from a piezotransducer. The quantity of powder is however measured in terms of volume rather than mass by filling the 25cm^3 volume of the standard density cup, which almost entirely fills the funnel reservoir and thus maximizes the sample volume that can be tested with the funnel. Volume-based rather than mass-based flowability measurements are arguably more pertinent as powder reservoirs and distribution systems typically control the volume flowrate of powder rather than the mass flowrate. Light manual taps are applied to the density cup to pack the powder and thereby reduce powder volume variability due to random initial packing configurations. Indeed, it has been shown that fine cohesive powders present a memory effect which can make their behaviour highly dependent upon their history (Castellanos 2005). The initial memory of the powder inside the funnel induced by pouring must therefore be erased, which is done by manually shaking the funnel laterally to homogenize the packing distribution of particles throughout the funnel in an attempt to reduce the measurement variability due to initial packing conditions. The function generator is activated at the desired frequency, the discharge orifice is opened and the total discharge time is recorded.

The measurements are here given in units of cm^3/s as the ratio of total discharged volume (25 ± 0.5 cm^3) to total discharge time (± 0.5 s). Higher flowability values therefore mean a better funnel flowability, unlike flowability measurements with the more usual unit of s/50g for standard funnel flowability testing. The flowability measure thus here corresponds to an average volumetric flowrate through the funnel orifice. This inverted flowability measure is adopted here to cope with no-flow results (i.e. infinite discharge time) and thereby obtain a finite result to enable calculations.

Preliminary funnel flowability tests with 224.0-A cohesive aluminium powder samples showed that the piezoelectric transducer could provide a flowability enhancement by initiating and sustaining the flow of an otherwise non-flowing powder sample. This is unlike previous results for pharmaceutical powders where pre-discharge vibrations led to consolidation that prevented flow initiation (Polizzi et al. 2016).

For a given funnel-piezotransducer assembly, the impact of vibrations on funnel flowability generally depends on the frequency, the amplitude and waveform of the signal. At a fixed generator frequency, an increase in voltage amplitude generally provided a relative improvement in flowability, i.e. a decrease in discharge time. A triangular waveform provided less improvement than a sine or square waveform, as shown in figure 2.25. This could be intuitively expected as an increase in the root-mean-square (*rms*) amplitude of the electric signal is translated as an increase in the vibrational displacement of the piezoelectric disk attached to the funnel wall. The *rms* amplitude is itself determined by the maximum or peak amplitude A_p and the type of waveform ($V_{rms} = A_p$ for a square wave, $V_{rms} = A_p/\sqrt{2}$ for a sine wave, and $V_{rms} = A_p/\sqrt{3}$ for a triangle wave). Thus, increasing the amplitude A_p or changing the waveform from triangular to sinusoidal to square increases the average vibrational power transmitted to the funnel wall and ultimately to the bulk powder, which could be expected to improve the flowability of metal AM powders. The experimental results were however more ambiguous for the sine and square waveforms. A lower discharge time would be expected for the square, but this was not strictly observed for powders 20-80µm and 45-90µm, for which the sine waveform seemed to produce slightly better results on average. Due to the variability between repeated measurements, the significance of this observation is unclear and further work would have to be conducted to elucidate the impact of waveform on powder flowability. To limit the parameter space in the subsequent experiments, the amplitude was set to a maximum of $A_p = 5\ V$ (or 10 V_{pp}) and the waveform was chosen to be sinusoidal.

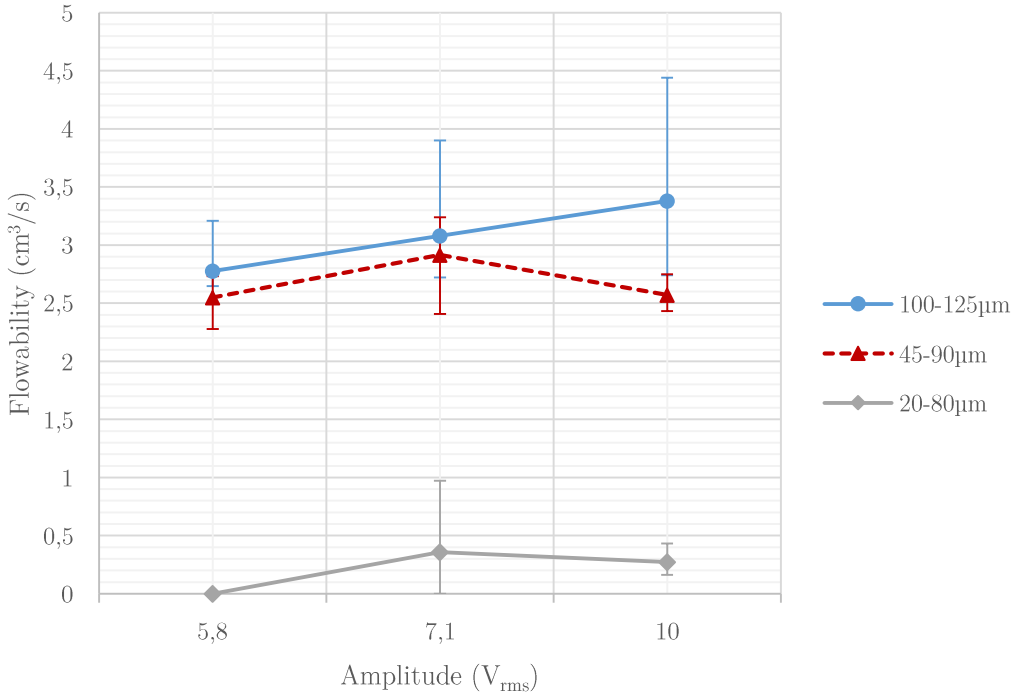

Figure 2.25: Influence of waveform on flowability in vibration-assisted funnel flowability testing at 3kHz of cohesive aluminium powders 224.0-A (20-80µm, 45-90µm, 100-125µm)

i. Influence of frequency on aluminium powder flowability

The first set of vibration-assisted funnel flowability experiments aimed at establishing the frequency-dependence of the flowability enhancement provided by the piezoelectric transducer mounted on the funnel. For each of the two cohesive powders described in table 2.12, the discharge time was measured for approximately 25cm^3 of powder with function generator frequencies ranging between 1kHz and 10kHz using a sine waveform with an amplitude of $10V_{pp}$. The measurements were refined around 3kHz by adding measurements at 2.5 and 3.5kHz. Funnel flowability measures of cohesive powders are highly dependent upon the initial particle packing configuration inside the funnel, so each condition was tested 6 times and "no flow" results were recorded as a null flowability (cm^3/s).

Powder	Composition	Sieve Granulometry (approx.)
224.0-A	Al-Cu4.7-Mn-Ti-V-Zr	63-80µm
AM205	Al-Cu5-Ti-B-Ag-Mg-Si	20-63µm

Table 2.12: Powder samples characteristics for frequency-dependence testing

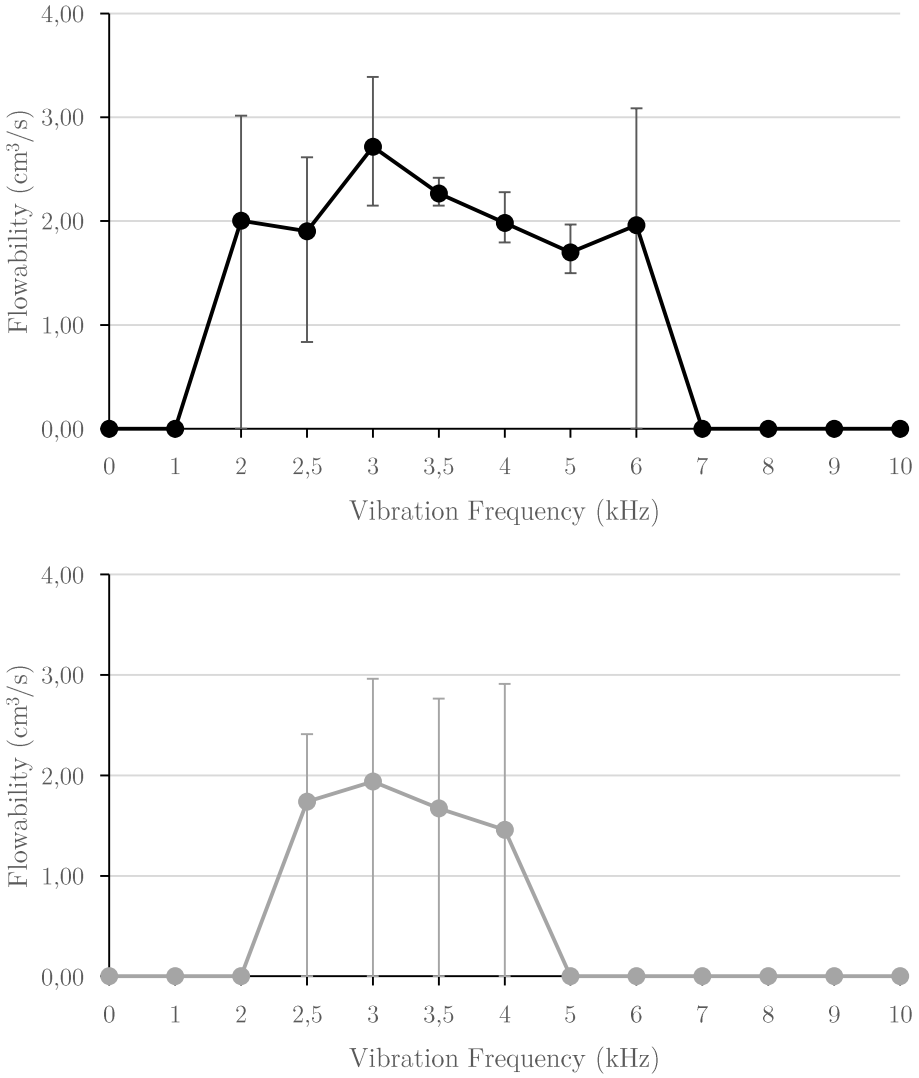

Figure 2.26: Powder flowability over frequency range 1-10kHz
top : 224.0-A 63-80µm – bottom : AM205 20-63µm
Error bars set to minimum and maximum flowability values obtained for each condition

Based on the results showed in figure 2.26, it is apparent that both aluminium powders 224.0 63-80µm and AM205 20-63µm present a minimum discharge time in the 2.5-3.5kHz frequency range. However AM205 displayed significantly more variability. The signal frequency was set at 3kHz for all of the subsequent funnel flowability testing of cohesive powder samples. Additional tests beyond the 1-10kHz range, i.e. in the 0.1-1kHz and 10-100kHz ranges, did not reveal other flow enhancing conditions. In addition, it is noted that continuously diminishing the frequency from 10kHz to 6kHz for powder 224.0 63-80µm, and from 10kHz to 4kHz for powder AM205 23-60µm, did trigger the flow of powder, which was otherwise stuck in a no-flow condition at 10kHz.

ii. Influence of particle size distribution on aluminium powder flowability

A recent review on metal powders for SLM reported that an increase of median diameter d_{50} or a decrease of PSD width (i.e. span or uniformity ratio) induced an increase in flowability (Vock et al. 2019). This however has not yet been thoroughly established in the literature, especially for cohesive aluminium AM powders such as the 224.0 powder samples of the present study as no established method for cohesive AM powder flowability testing has been settled upon.

Funnel flowability tests with and without vibrational assistance at 3kHz with a sine waveform were performed with the substitute funnel to measure the flowability of cohesive aluminium powders 224.0-A, 224.0-B, AM205, Al7Si6Mg, and non-cohesive powders Al12Si, Ti6Al4V, 316L, 38MnSiV. The average flowability measurements are presented in table 2.13, along with available PSD parameters (median diameter d_{50}, span $\frac{d_{90}-d_{10}}{d_{50}}$), and are also illustrated in Figure 2.27. The standard deviation over the 3 to 6 repeated measures for each condition are given in parentheses. For samples with unknown D-values (224.0-A 63-80µm, 316L 45-90µm, Al12Si-B 45-90µm), crude estimates are made from sieve granulometries to compute Bo_g^* as it is generally observed that the sieve granulometries roughly correspond to d_{10} and d_{90} in practice. It is however noted that for some samples with known PSD, the D-values can be fairly remote from sieve granulometries, which is a sign of powder cohesiveness and poor sieving performance (e.g. when using mechanical rather than ultrasonic vibrations).

The population-dependent granular Bond number Bo_g^* was estimated for each experimental condition based on available PSD and material data, assuming average roughness values from table 2.9 for all power particles. As the metal AM powders tested were all gas atomized, they could be expected to have a similar range of *rms* roughness. It is however noted that these powders are from different materials, so they do not present the same type of surface oxides, and *rms* roughness values could significantly differ in practice. The effect of vibrations is not accounted for in the calculation of Bo_g^* as they are used for flowability enhancement to enable the quantification of the funnel flowability of otherwise non-flowing cohesive metal AM powders.

The values of Bo_g^* are very sensitive to the values of the Hamaker coefficient, particle density, *rms* roughness parameters and separation distance D. Hamaker coefficients of metallic materials are not widely reported, so average values from literature data (table 2.8) are used when available, considering only the base element of the alloy (Al, Fe), and a generic value of $30\text{x}10^{-20}$ J is used for Ti6Al4V powders to remain close to values for Al ($29.3\text{x}10^{-20}$ J) and Fe ($26\text{x}10^{-20}$ J). Considering the lack of experimental data for metal AM powders, the separation

distance is here set to $D = 1$nm so that vdW forces remain at reasonable levels compared to capillary forces and particle weights, but this value should be further investigated.

Because there are many model parameters with limited available experimental data for metal AM powders, Bo_g^* is here given in relative terms as $Bo_{g,rel}^*$ by normalizing all Bo_g^* results with the value $Bo_{g,ref}^* = 184.1$ estimated for marginally flowing powder (without vibrations) Al12Si-B 45-90µm, so that $Bo_{g,rel}^* = Bo_g^*/Bo_{g,ref}^*$. This allows to recover the usual threshold $Bo_{g,rel}^* < 1$ for satisfactory flowability.

The calculations are also quite dependent on the discretization and truncation of the continuous infinite log-normal PSD model, i.e. the particle size interval for each discretized group and the lower and upper limits of diameter values. The particles are here grouped in 1µm-wide diameter intervals over which the particle diameter is assumed constant. The diameter for the lower and upper limits of the discretized log-normal PSD are set to d_{10} and d_{90} (volume-based), which does leave out a 20% volume on the extreme sides of the PSD, but using standard D-values makes the criterion more readily applicable to common experimental data and should nonetheless still capture the effect of PSD parameters for a log-normal law. If a PSD model other than log-normal is used, other truncation limits may be more appropriate, depending on the tail behavior of the PSD. This consideration is however beyond the scope of the present work as gas atomized metal AM powders seem to universally follow a log-normal distribution, even after sieving.

The temperature and relative humidity of the powder samples before flowability testing were measured with a thermo-hygrometer. The values were in the range 24.4°C to 25.9°C and 40.3%RH to 42.3%RH for the tested powders, so that temperature and relative humidity are assumed to be uniformly equal to 25°C (298K) and 41%RH for Bo_g^* calculations. In comparison, the relative humidity of the ambient air was slightly lower at around 37%RH.

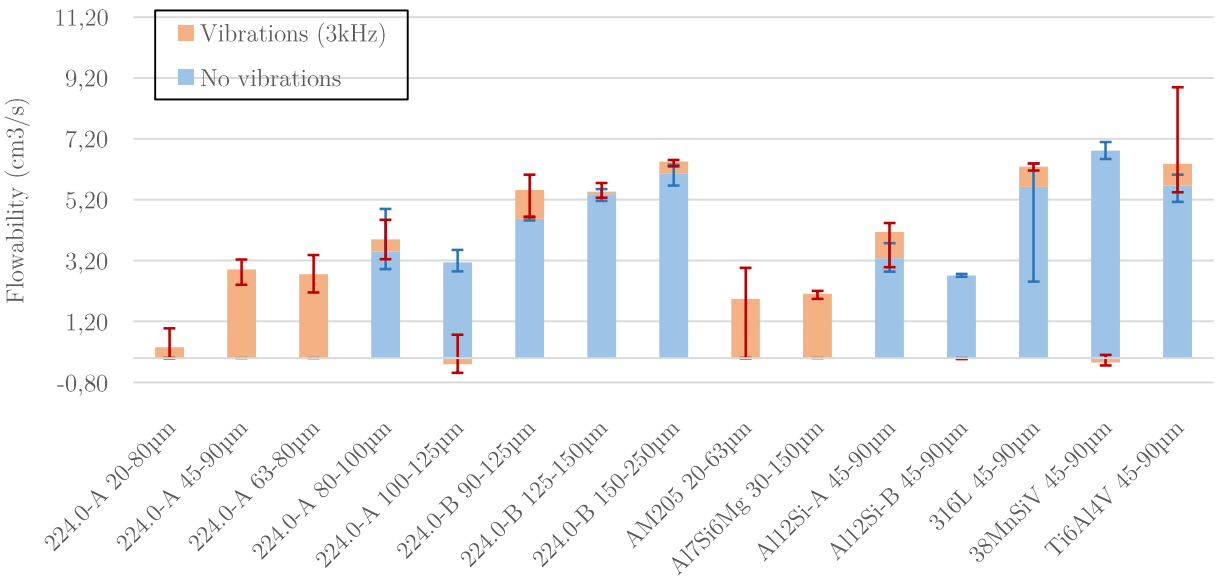

Figure 2.27: Flowability measurements of powder samples, with and without vibrations

Powder	d_{50}	Span	Flowability (no vibrations) [cm³/s]	Flowability (with vibrations) [cm³/s]	$Bo^*_{g,rel}$
224.0-A 20-80µm	39.2	1.37	0,00 (0)	0,36 (0.26)	4.27
224.0-A 45-90µm	60.6	0.74	0,00 (0)	2,91 (0.25)	1.12
224.0-A 63-80µm	70*	0.43*	0,00 (0)	2,75 (0.39)	0.74
224.0-A 80-100µm	101.0	0.77	3,49 (0.73)	3,90 (0.69)	0.24
224.0-A 100-125µm	120.0	0.78	3,14 (0.22)	2,93 (0.37)	0.14
224.0-B 90-125µm	108.9	0.65	4,58 (0.05)	5,51 (0.69)	0.19
224.0-B 125-150µm	143.3	0.64	5,38 (0.13)	5,47 (0.20)	0.08
224.0-B 150-250µm	203.3	0.66	6,06 (0.33)	6,45 (0.08)	0.03
AM205 20-63µm	39.16	0.86	0,00 (0)	1,94 (1.07)	5.4
Al7Si6Mg 30-150µm	78.6	1.40	0,00 (0)	2,11 (0.09)	0.90
Al12Si-A 45-90µm	62.4	0.67	3,27 (0.42)	4,14 (0.51)	1.08
Al12Si-B 45-90µm	65*	0.69*	2,71 (0.03)	2,70 (0.01)	1.0
316L 45-90µm	65*	0.69*	5,63 (1.53)	6,28 (0.09)	0.31
Fe38MnSiV 45-90µm	67.2	0.71	6,81 (0.22)	6,65 (0.14)	0.28
Ti6Al4V 45-90µm	64.0	0.53	5,66 (0.31)	6,39 (1.68)	0.31

Table 2.13: Flowability measurements (with and without 3kHz vibrations) and $Bo^*_{g,rel}$ estimates for various metal AM powder samples (* : estimates from sieve granulometries). Flowability values are given as the mean over repeated measures, with standard deviation shown in parenthesis. Values in green are considered satisfactory, while values in red are unsatisfactory and values in black are intermediate.

Figure 2.28 and figure 2.29 show semi-log scatter plots of average flowability test results versus $Bo^*_{g,rel}$ estimates, respectively without and with vibrational assistance. The vibrational excitations at 3kHz provide a sharp enhancement in flowability for the more cohesive metal AM powders (e.g. AM205, 224.0-A, Al7Si6Mg), while the gain is less substantial for the powder samples with higher flowability (e.g. Ti6Al4V, 316L). In particular, the flowability of 224.0-A 20-80, 45-90 and 63-80µm samples is drastically improved as the no-flow conditions are effectively suppressed, leading to a disappearance of the sharp jump in flowability observed

throughout 224.0-A samples when vibrations are applied to the funnel. It is noted that some samples are not performing as well as could be expected, such as 224.0-A 100-125µm, which has higher D-values and a span comparable to 224.0-A 80-100µm, but yet does not flow quite as well. It also has a slightly worse flowability with vibrations than without on average, but the values are within one standard-deviation of each other so the difference is not very significant. In the case of powder 224.0-B samples, which present an increasing granulometry but a roughly constant span, the flowability improves with diminishing $Bo^*_{g,rel}$ and increasing median particle diameter d_{50}.

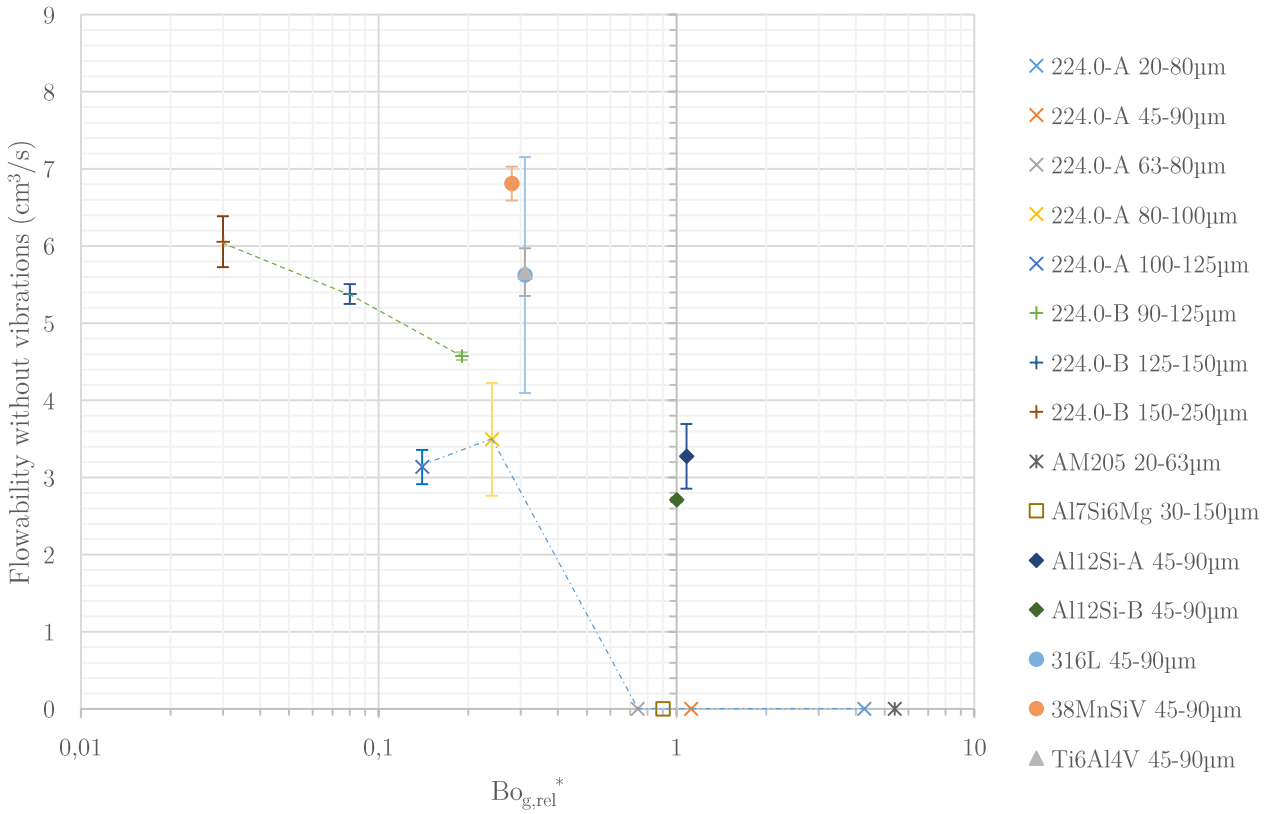

Figure 2.28: Average flowability without vibrations vs. calculated $Bo^*_{g,rel}$

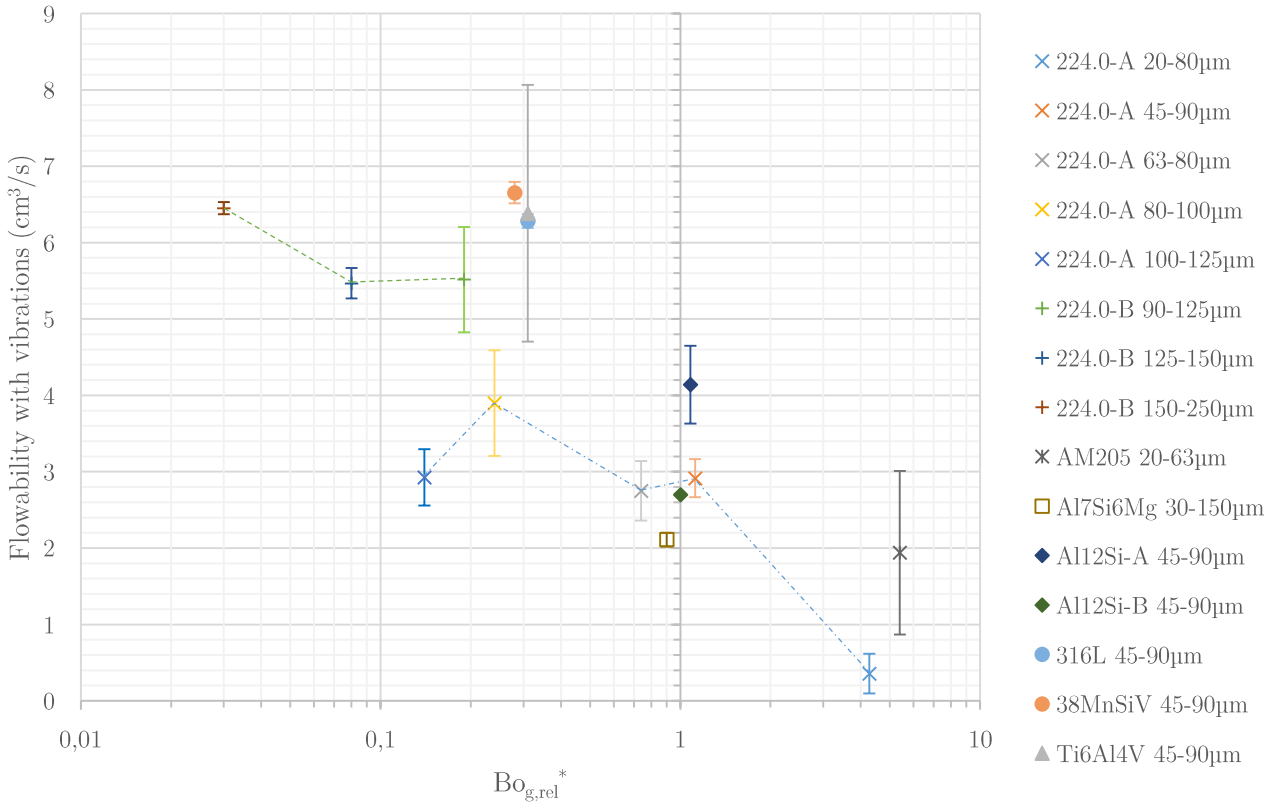

Figure 2.29: Average flowability with vibrations at 3kHz vs. calculated $Bo^*_{g,rel}$

The flowability measurement dataset contains 82 data points without vibrations and 110 data points with vibrations at 3kHz for a total of 192 data points, from which 5 points were discarded from the following statistical analysis as they represented unusually high or low flowability measurements, possibly due to particularly favorable and unfavorable initial packing configurations inside the funnel.

An ANOVA (ANAlysis Of VAriance) based on a F-test was first conducted on the flowability measurement dataset without vibrations using $\ln(Bo^*_{g,rel})$ as the unique independent factor. It shows that this factor and its higher order terms $\ln(Bo^*_{g,rel})^2$ and $\ln(Bo^*_{g,rel})^4$ account for about 60% of the variability of the response ($R^2_{adj} = 0.60, R^2_{pred} = 0.59$).

A second ANOVA was performed over the entire dataset, i.e. with and without vibrational assistance. A number of factors were considered, including $\ln(Bo^*_{g,rel})$, d_{50}, span, specific volume and presence of vibrations (Boolean value), leading to the ANOVA results shown in table 2.14. All the factors of the model have a p-value $<< 0.05$, and around 80% of the response variability can be explained by these factors and their interactions, without overfitting the data as adjusted and predicted R^2 values are close to one another ($R^2_{adj} = 0.81, R^2_{pred} = 0.80$). While lack of fit is significant as the pure error is much smaller than the

lack of fit error within the residual and represent 16% of the total sum of squares, R^2_{pred} is ultimately the criterion of interest for assessing the model.

	Sum of Squares	dof	F-value	p-value	Coef.
Model	594,79	6	129,59	< 0.0001	
A-Vibrations	11,12	1	14,53	0,0002	0.835
C- ln($Bo^*_{g,rel}$)	44,96	1	58,77	< 0.0001	-26.933
E-span	31,00	1	40,53	< 0.0001	-1.897
H-specific volume	5,61	1	7,33	0,0074	23296.76
AC	9,99	1	13,06	0,0004	0.845
CH	28,05	1	36,67	< 0.0001	69384.02
Intercept					-4.869
Residual	137,69	180			
Lack of Fit	121,58	23	51,51	< 0.0001	
Pure Error	16,11	157			
Total	732,48	186			

Table 2.14: Results of ANOVA over the entire flowability dataset

The vibrations factor and its interaction with $\ln(Bo^*_{g,rel})$ however only explain a limited amount of the variability based on sum of squares and F-values for the entire flowability dataset. This can be explained by the fact that vibrations mostly improve the flowability of highly cohesive, non-flowing powders such as 224.0-A 20-80µm and AM205 20-63µm that flow in a rat-hole regime. Less cohesive powders such as 316L and Ti6Al4V that discharge under a funnel or mass flow regime are hardly affected by the presence of vibrations. Restricting the flowability dataset to low flowability powders (224.0-A, 224.0-B, Al7Si6Mg, AM205) for a total of 127 data points, the ANOVA with the same set of factors shows that factor vibrations does become the predominant factor with an F-value of 35.03 (p-value < 0.0001) yielding a model with $R^2_{pred} = 0.78$. Vibrations thus do provide a significant flowability enhancement for the most cohesive powder samples (i.e. samples with lowest flowability measurements without vibrations).

The rest of the variability, as measured by the lack of fit test, must originate from other significant factors that were not accounted for in calculating $Bo^*_{g,rel}$ (differences in roughness, particle morphology/agglomerates/satellites, electrostatic forces from tribocharging etc.). A morphology factor could be added to the set of factors based on qualitative SEM observations of the powder samples, with a value of 0 given to samples with the least favorable morphologies due to satellites and agglomerates (224.0-A, Al7Si6Mg), a value of 0.5 for intermediate samples (224.0-B, AM205, Al12Si-B) and a value of 1 for the best samples with good sphericity and few satellites (316L, Ti6Al4V, Fe38MnSiV, Al12Si-A). This leads to a significant model where the most significant terms by far are $\ln(Bo^*_{g,rel})$ (F-value = 952.7) and morphology (F-value = 411.9). This ad-hoc morphology factor suggests that mechanical interlocking forces induced

by particle satellites and agglomerates are almost as significant as other interaction forces (vdW, capillary) represented by $\ln(Bo^*_{g,rel})$. The morphology values however remain qualitative and a more objective measure of particle morphology should be developed to better quantify this aspect.

Finally, to identify the significant factors in explaining the flowability in vibrated samples, an ANOVA was performed on the flowability measurements with vibrations only, and the corresponding results are displayed in table 2.15. This high order model accounts for about 95% of the observed variability in the flowability measurements without overfitting the data ($R^2_{adj} = 0.953$ and $R^2_{pred} = 0.949$). Lack of fit, although significant according to the F-test ($p < 0.0011$), is in practice minimal as its sum of squares is small compared to the sum of squares of the residual, and even smaller compared to that of the model and its individual terms.

	Sum of Squares	**dof**	**F-value**	**p-value**	**Coef.**
Model	328,85	11	196,46	< 0.0001	
C- $\ln(Bo^*_{g,rel})$	41,33	1	271,62	< 0.0001	14191,0347
E-span	39,70	1	260,86	< 0.0001	-348,94548
H-specific volume	40,40	1	265,50	< 0.0001	-1,77E+07
CE	39,69	1	260,85	< 0.0001	-7646,55
CH	40,75	1	267,79	< 0.0001	-6,76E+07
EH	40,06	1	263,25	< 0.0001	9,97E+05
C²	43,70	1	287,17	< 0.0001	2826,71932
H²	38,01	1	249,78	< 0.0001	2,34E+10
CEH	39,80	1	261,57	< 0.0001	2,17E+07
C²H	43,61	1	286,56	< 0.0001	-8,04E+06
CH²	41,40	1	272,05	< 0.0001	7,75E+10
Intercept					3346,49268
Residual	14,46	95			
Lack of Fit	2,31	3	5,82	0,0011	
Pure Error	12,15	92			
Total	343,31	106			

Table 2.15: Results of ANOVA over the flowability with vibrations dataset

These results show that the span, specific volume and $Bo^*_{g,rel}$ allow to account for 95% of the variability according to the cubic model. Adding both the span and specific volume as separate factors significantly improves the predictability of the statistical model, despite the density and PSD-dependence of $Bo^*_{g,rel}$. It can also be noted that median diameter d_{50} is not directly significant, but its effects are accounted for in $Bo^*_{g,rel}$. This is reflected in 224.0-B samples, where increasing d_{50} at a constant span improved both the flowability and $Bo^*_{g,rel}$. It

is also noted that the morphology factor is no longer helpful in explaining the observed variability.

Considering these ANOVA analyses, it can be inferred that vibrations allow to overcome adversarial effects that were unaccounted for in $Bo^*_{g,rel}$ and in the other factors of the ANOVA, such as mechanical interlocking forces due to particle agglomerates/satellites. These forces promote the formation of stable force chains between particles, and thus lead to static arch bridges and rat holes that prevent particle flow.

Indeed, it was experimentally observed that these static patterns transited to a funnel flow regime when subjected to vibrational excitations at 3kHz, and never reoccurred during discharge when the vibrational excitations were maintained. The effect of vibrations on samples naturally discharging in a funnel flow regime was significant but the general flowing pattern remained essentially unchanged as the transition to a mass flow regime due to vibrations was never noted. Vibrations had a much less significant impact on samples already flowing in a mass flow regime without vibrations. Vibrations therefore mostly serve to avoid the formation of static patterns (bridge, rat hole) and promote flow initiation of cohesive powders. Their impact on flowability is thus hardly significant for metal AM powders that already flow well. Once a sustained flowing regime is reached through vibrational assistance, criterion $Bo^*_{g,rel}$, span and specific volume are revealed to be very good predictors of powder flowability, demonstrating that the flowability of vibrated powder samples during discharge are mostly dependent upon the PSD, adhesion forces and particle weights as represented by $Bo^*_{g,rel}$, span and specific volume. Prior to flow initiation by vibrations, the ignored factors (mechanical interlocking, static friction etc.) most likely dominate over included factors such as PSD and vdW/capillary adhesion forces.

The mechanical interlocking forces caused by particle agglomerates and satellites are thus primary candidates in explaining the better flowability of samples 224.0-B compared to 224.0-A. Besides the larger particle sizes of 224.0-B, the varying content of particle agglomerates and satellites is the most striking difference between these samples. The difference in PSD cannot fully explain the difference in flowability. To confirm this statement, a quantitative evaluation of the content of agglomerates and satellites in both 224.0 samples A and B should be conducted and the influence of interlocking forces included in the model, but this is beyond the scope of the present work. Moreover, variations in surface roughness, which could not be measured experimentally, could also to some extent contribute to this difference in behavior as they directly impact the vdW and capillary forces.

iii. Influence of temperature and humidity on aluminium powder flowability

To test the effect of lower humidity and higher temperature on cohesive powder flowability, powders 224.0-A 63-80µm and 224.0-B 90-125µm were dried at 180°C for 10 hours before performing funnel flowability tests (table 2.16). These temperature and time levels were determined based on preliminary in-process LMD flowability experiments (not shown), starting at a more common value of 80°C and 2 hours where no noticeable improvement of in-process flowability was observed. Larger drying time and temperature however provided a clear improvement in cohesive 224.0 powder flowability during LMD processing.

To relate the observed in-process improvement to funnel flowability, the temperature and relative humidity RH (%) of the dried and non-dried powder samples was measured by a thermo-hygrometer before funnel flowability testing. The dried metal powder samples cool down rapidly when exposed to ambient air, from 180°C down to about 80°C right after drying. The temperature and relative humidity measurements are thus given as a range of measurement values obtained before and after the flowability tests performed at room temperature. As the response time of the thermo-hygrometer is fairly large compared to the powder cooling time, the given values are only indicative. The $Bo^*_{g,rel}$ values were estimated based on averages of experimental measurements of T and RH and available experimental and literature data, using the same $Bo^*_{g,ref}$ as before. Again, the relative humidity of the ambient air was measured at about $37\%RH$.

It is clear that drying at a relatively high temperature (180°C) during a relatively large time (>10h) provided a clear enhancement in flowability for the more cohesive powder (224.0-A 63-80µm), while the improvement is much less significant for a less cohesive powder (224.0-B 90-125µm). This can already be observed by visual inspection of dried samples of cohesive powder 224.0-A 63-80µm, which are visibly less agglomerated than the non-dried samples.

Powder	T (K)	RH (%)	Flowability (no vibrations) [cm³/s]	Flowability (with vibrations) [cm³/s]	$Bo^*_{g,rel}$
224.0-A 63-80µm	25.7	40.5	0 (0)	2,75 (0.39)	0.74
Dried 224.0-A 63-80µm	80-30	8-18	3.16 (1.18)	4.10 (1.75)	0.54
224.0-B 90-125µm	25.8	41.7	4,58 (0.05)	5,51 (0.69)	0.19
Dried 224.0-B 90-125µm	80-40	8-17	5.06 (0.03)	6.11 (0.09)	0.14

Table 2.16: Average flowability measurements (standard deviation) of dried and undried powder samples 224.0-A 63-80µm and 224.0-B 90-125µm

To explain the cause for the improved flowability with this heat treatment, the effect of drying on interparticles forces can be discussed. It has previously been argued that mechanical interlocking forces have a major influence on powder flowability, in addition to vdW and capillary adhesion forces, but their magnitude should not be impacted by the drying process. The Hamaker coefficient depends on both temperature and humidity, however the temperature-dependent, zero-frequency contribution $A_{\nu=0}$ is typically limited to about 1% for metals (Israelachvili 2011). Moreover, the presence of water, either as an interaction media (table 2.8) or as an absorbed layer (Götzinger and Peukert 2003; Israelachvili 2011), tends to reduce the Hamaker coefficients and thus the magnitude of vdW forces. Electrostatic forces, if any, would also be increased by a lower humidity content. In contrast, capillary forces do decrease in magnitude with relative humidity according to the capillary force model, as can be intuitively expected. The decrease in relative humidity caused by the drying process must be sufficient to turn cohesive powders such as 224.0-A 63-80µm into flowable powders, despite the presence of mechanical interlocking forces and slightly increased vdW forces.

In the literature, it has been shown experimentally that a thin water layer and a hydroxide layer are almost always present on the surface of dried smooth alumina particles at 30°C, even at very low relative humidity levels. Their surface properties thus depend on preparation and thermal history, e.g. drying at 100°C removes the water molecules from the surface (Götzinger and Peukert 2003). Because untreated aluminium in ambient air is spontaneously covered by a thin alumina layer due to oxidation (Hatch 1984), aluminium particles such as 224.0 powder samples can also be expected to adsorb water molecules of the ambient air onto the alumina layer. This can induce an increase in capillary forces compared to fully dry particles without adsorbed water molecules. Because the alumina layer is generally porous, water molecules should also be found within the thin alumina layer. The standard

value for water boiling point (100°C at 1atm) does not account for interface or kinetic effects present in real systems, as is often the case with purely thermodynamic properties, so that a larger drying temperature is required for an effective drying process in the case of naturally oxidized aluminium AM powders. Although commonly reported drying temperature and time are usually in the range of a few hours at about 100°C, drying for a relatively long time (e.g. 10h) at a temperature of 180°C can provide the necessary activation energy for adsorbed liquid water to exit the alumina layer in a vapor phase and yield fairly dry aluminium powders.

Another cause for the flowability improvement of powder 224.0 after heat treatment lies in the fact that the proposed heat treatment closely resembles a tempering heat treatment used to strengthen this particular alloy (Planchamp et al. 1993) so that an increase in particle hardness can be expected, which should have positive effect on powder flowability although this effect remains to be explored further.

III. Improving the Flowability of Cohesive Aluminium Powders for LMD processing

a. Environmental Conditions

The proposed heat treatment significantly improved the flowability of cohesive, low-flowability powder 224.0-A 63-80µm. This can be attributed to the diminution of water molecules onto the surface alumina layer of aluminium particles, which in turn leads to reduced capillary forces. An increase in surface oxidation level and hardness of the particles induced by the heat treatment could also impact the interactions between particles, either in terms of friction forces or triboelectric charging and thus electrostatic forces, although the exact flowability improvement mechanism is unclear at this point and would require further investigation on the evolution of particle surface properties with the heat treatment.

This flowability improvement enabled the use of the marginally flowing powder 224.0-A 63-80µm for LMD processing. However, the distribution system had to be modified to ensure that the powder path in a purely granular state (i.e. negligible particle-gas interactions) was sufficiently large to enable the safe passage of the powder, as in funnel flowmeters where a larger discharge orifice diameter facilitates the flow of powder.

b. Particle Size Distribution

Generally, the particle size distribution has a significant impact on flowability, as shown by both flowability measurements and estimates of the flowability criterion $Bo^*_{g,rel}$. Reducing the span and increasing the median diameter, everything else remaining equal, increases the flowability of the powder, which is one of the main factors for powder processability by LMD. This is unlike SLM where a compromise has to be found for the PSD as good packing is also necessary to avoid defects. Other factors such as the presence of agglomerates and satellites are also key factors in explaining the low flowability of the 224.0 AM powder samples.

There are physical bounds on the PSD that can be obtained in practice. The type of PSD is mostly governed by the fabrication process, and all of the tested gas atomized metal AM powders follow a log-normal distribution. There are many parameters involved in an inert gas atomization process that can notably influence the range of particle sizes and the tendency to form agglomerates and satellites. Generally, the median diameter is hard to change significantly, so that extensive sieving must be done after atomization to obtain the desired range. Moreover, the PSD span of the atomized powder can only be lowered to a certain extent by optimizing parameters so, again, a sieving process must be carried out, preferably with ultrasonic assistance for the more cohesive, lower flowability powders. However sieves come in standard mesh aperture sizes so that there is no practical way of lowering the span below what can be obtained with standard sieve mesh sizes (e.g. 63-80µm), which are also only a loose indicator of granulometry for cohesive powders.

While there is no theoretical lower limit to the span for LMD processing, the median diameter d_{50} should remain well below characteristic aperture sizes encountered in the distribution system and projection nozzle as well as laser beam spot size (i.e. melt pool size). With laser beam spots as small as 600µm and nozzle channels as thin as 0.5mm, as in the LMD system used in the present work, median diameter d_{50} should ideally be in the range 100µm to 200µm.

IV. Summary

To better assess the flowability of AM powders, a flowability criterion was calculated using more accurate vdW and capillary force models compared to previous work (Capece et al. 2015). It allows to estimate the relative impact of powder properties (e.g. density, granulometry, roughness) and environmental conditions (e.g. relative humidity), which are conveniently combined into a single criterion.

A new funnel-based flowability testing method using high frequency vibrations was also presented. It demonstrates that there exists a resonant frequency for which the flowability of cohesive Al-Cu powders is drastically improved. It is hypothesized that the vibrations induce a local displacement of particles that negates mechanical interlocking forces and possibly other cohesion forces, thereby initiating and sustaining the flow of cohesive AM powders through the funnel. Advantageously, this method enables flowability measurements of otherwise non-flowing powders while retaining a funnel-based flowability measurement approach, which is fairly representative of conditions encountered inside the powder reservoir of the LMD system of the present study.

A heat treatment was devised for cohesive aluminium powders using a higher drying temperature and longer drying time than what is usually recommended for AM powder processing. While the cause for the flowability improvement remains to be fully elucidated, it is thought that the drying process removes part of the adsorbed water layer, and may also modify the surface oxidation level of the particles, which can impact interparticle cohesion forces and triboelectric charging effects. This heat treatment, together with adjustments in the LMD distribution system, enabled the use of cohesive aluminium powders for LMD processing.

Chapter III: Gas-Particle Flow of Cohesive Aluminium Powders during Laser Metal Deposition

Abstract

This chapter is dedicated to the experimental and numerical study of gas-particle flow through the LMD nozzle. The first section presents two sets of experiments on the powder jet dynamics at the nozzle outlet. The first one aims at analyzing the variability in the powder jet geometry in various conditions for 2 granulometries (80-100µm and 100-125µm) of the cohesive aluminium AM powder 224.0-A using a standard, low-speed camera. The second set of experiments employed a high-speed camera to enable particle tracking and thereby assess the velocity of AM powder particles at the nozzle outlet in various conditions. The second section focuses on the CFD-DEM numerical simulation of the gas-particle flow, both inside the nozzle and at the nozzle outlet. After a brief review of LMD particle flow modeling, the outlet particle velocity as well as the impact of adhesion forces on particle flow inside the nozzle are simulated with a CFD-DEM model. The third section presents a new design aimed at diminishing agglomeration effect encountered with cohesive aluminium powders and increasing the standoff distance to improve the nozzle accessibility for repair applications, which is evaluated with a CFD-DEM simulation.

I. Experimental investigation

Once cohesive aluminium powders 224.0 in a granular flow regime could be made to flow properly from the reservoir (see chapter 2), their in-process flowability could be further assessed by investigating their aerated or fluidized flow behavior. Upon leaving the reservoir, the particles are fluidized by an inert gas (e.g. argon) upon entering the pneumatic piping system to transport the particles to the LMD deposition head where they are accelerated by the projection nozzle towards the melt pool region. Although the internal flow of particles inside the LMD system cannot be directly observed, investigating the powder jet at the nozzle outlet through optical imaging helps evaluating its geometry and stability, which are key aspects for parameterizing the LMD process and ensuring good deposit quality. An estimate of particle velocities would also be of interest as it gives the particle travel time between the nozzle outlet and deposit region for a given working distance, thus giving an upper bound on the scan speed of the LMD head as particle travel time should remain small compared to the characteristic travel time of the laser spot. Particle velocity can also serve to directly compare simulation results with the experiments.

a. Powder jet angle

i. Experimental procedure

To observe the flow of particles exiting from the LMD nozzle outlet, the latter was placed inside a light box in order to illuminate the aluminium particles exiting the nozzle at various flowrate and pressure settings. In a first approach, a standard camera was used to capture the particle flow at 30 frames per second (fps).

To assess the difference between powder granulometries, slightly cohesive samples 224.0-A 80-100µm and 224.0-A 100-125µm were selected for the experiments. Because 224.0 powder samples have to be dried and shielded from humidity to properly flow from the reservoir, the granulometry is considered as a “hard-to-change” factor in designing the experimental plan. To limit the number of conditions to be tested as well as the number of changes in granulometry during the experiments, a split-plot I-optimal response surface design is adopted with 3 numerical factors (carrier gas pressure, carrier gas flowrate, powder flowrate) on 3 levels, and 1 “hard-to-change” categorical factor (granulometry) on 2 levels over 2 groups, for a total of 17 experimental runs (see table 3.). The measured responses are the mean cone

angle and the coefficient of variation (COV) defined as the ratio of the standard deviation of the cone angle to the mean of the cone angle.

ii. Image analysis of powder jet

The relatively high velocity of particles compared to the camera's exposure time and shutter speed implies that particles cannot be singled out from the images. However, the path of the particles is visible so that the conical geometry of the powder jet and its variation through time can be evaluated from the image sequence. This assumes that these 2D images captured at 30 fps provide a reasonable sampling of the true time variation of the actual 3D powder jet.

For each of the 17 runs, 500 consecutive frames are extracted from the captured image sequence when the powder jet is most stable (i.e. well after the onset and before the interruption of powder flow). At an average of 30 fps, this represents about 17 seconds of observation.

Due to the number of images to be evaluated, the image analysis task is handled automatically through a MATLAB code coupled to open-source image analysis software ImageJ, the latter doing the image pre-processing tasks while the former is used to perform edge detection on the pre-processed images, segment the powder jet as a 2D cone and calculate the half-opening angle of the powder jet cone on each image. An ImageJ script is called by the MATLAB code to successively perform several intensity processing, thresholding and binary operations to yield an outline of the powder jet, as shown in figure 3..

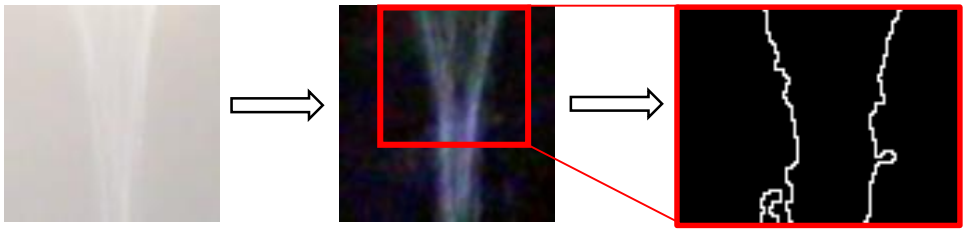

Figure 3.30: Original cropped image (left) – Cropped image after intensity pre-processing (middle) – Pre-processed image after binary operations (right)

The MATLAB code then applies a Canny edge detection filter following by a Hough transform to identify straight lines within the image, as illustrated in figure 3.31. There are a few parameters to set for the Hough transform that can influence the segmentation outcome (number and threshold of Hough peaks, the minimum length of each line, the gap-closing length etc.), which are kept constant throughout all cases.

The line segmentation process generates multiple small finite straight lines that espouse the irregular outline on either side of the powder jet image. The left and right sides of the powder jet are automatically segmented by computing an approximate bisector of the segmented lines and their corresponding end points. Several possibilities are available for finding a single straight line from the smaller finite lines, such as averaging over the many finite lines on either side. However there are some outlying line orientations due to the irregularity of the detected edges, so that it can skew the average results and give an unrepresentative cone angle. Instead the largest finite line on either side is taken to be the most representative one. The two corresponding end points are then used to compute the equation of the infinite straight lines that extends between and beyond those two points.

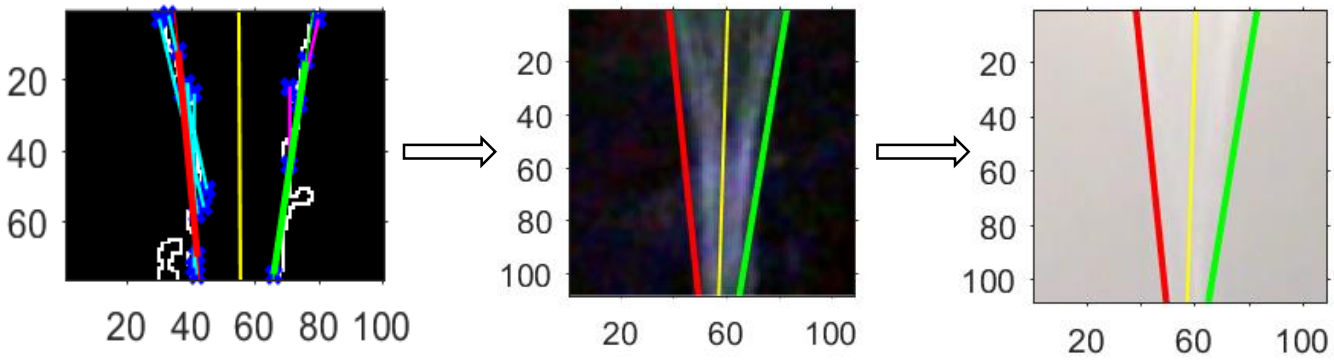

Figure 3.31: Segmentation process of powder jet angle on each frame. Cone straight lines and bisector are shown in red, green and yellow (resp.). Small finite lines from Hough segmentation are in cyan (left side) and magenta (right side).

Performing these operations on both sides yields intersecting lines forming a cone, from which the opening angle of the cone can be evaluated as the acute angle formed by the red and green segmentation lines (figure 3.31).This analysis is then run automatically on the 500 frames sample images of each of the 17 trial experiments, for a total of 8500 frames analyzed with the proposed method.

Because particle flow is a highly dynamical phenomenon where particle behavior can be somewhat erratic due to gas interaction effects and interparticle collisions, the captured images sometimes display particle ejections that fall outside of the normal powder jet range. The automated segmentation code may then count these outlier particle paths when segmenting the cone lines, thereby yielding incorrect values for the estimated cone angle. Hence, a cone angle with the wrong sign or excessively low or high magnitudes (below 5° or above 45°) are discarded as they reflect segmentation errors, often due to poor image quality or the presence of particle ejections that disturb the segmentation process. Indeed, sensible values of the cone angle are typically in a range of 15 to 20°. It is also noted the powder jet in reality presents an approximate conical shape that is truncated as the particles do not converge

towards a singular point but rather over a more or less diffuse region, so that the current cone representation of the jet is only an approximation.

iii. Statistical analysis of powder jet angle

Granulometry	Gas Pressure (bar)	Gas flowrate (L/min)	Powder flowrate (%)	Mean Cone angle (°)	Std. dev. Cone angle (°)	COV
80-100µm	3,5	2	50	15,49	5,98	0,386
80-100µm	3,5	8	20	20,70	8,77	0,424
80-100µm	1,5	8	50	19,49	7,05	0,362
80-100µm	1,5	5	20	18,90	7,58	0,401
80-100µm	1,5	2	80	19,16	5,81	0,303
80-100µm	3,5	5	80	17,09	6,20	0,363
80-100µm	2,5	2	20	19,75	6,23	0,315
80-100µm	2,5	8	80	17,24	6,11	0,354
100-125µm	3,5	5	20	20,65	8,81	0,427
100-125µm	3,5	8	50	16,88	7,00	0,415
100-125µm	3,5	8	80	15,07	5,51	0,366
100-125µm	2,5	2	80	17,02	5,22	0,307
100-125µm	3,5	2	20	15,95	5,70	0,357
100-125µm	1,5	5	80	14,16	5,04	0,356
100-125µm	1,5	8	20	15,49	7,47	0,482
100-125µm	2,5	8	20	16,31	7,73	0,474
100-125µm	1,5	2	50	16,64	5,61	0,337

Table 3.17: Geometry of conical jet of powders 224.0-A 80-100µm and 100-125µm based on the proposed segmentation method

The average and standard deviation of the powder jet cone angle estimates obtained by performing the proposed image segmentation process over 500 consecutive frames for each tested condition are shown in table 3..

An ANOVA study reveals that the powder flowrate and the shape gas flow rate are significant factors (p-value < 0.05) in explaining the measured variance in powder cone angle. The adjusted and predicted R^2 values are relatively close, but they can only explain at most about 2/3 of the variability, the rest being imputable to other factors not explicitly accounted for in the experiments as well as the natural variability of the LMD process.

p-value (shape gas)	**p-value (powder flowrate)**	**p-value (model)**	**R^2-adj.**	**R^2-pred.**
0.0008	0.0017	0.0001	0.679	0.583

Table 3.18: ANOVA results for powder jet angle variation

$$COV = 36.88 + 1.19 \times Shape\ gas\ flowrate - 0.11 \times Powder\ flowrate \tag{3.1}$$

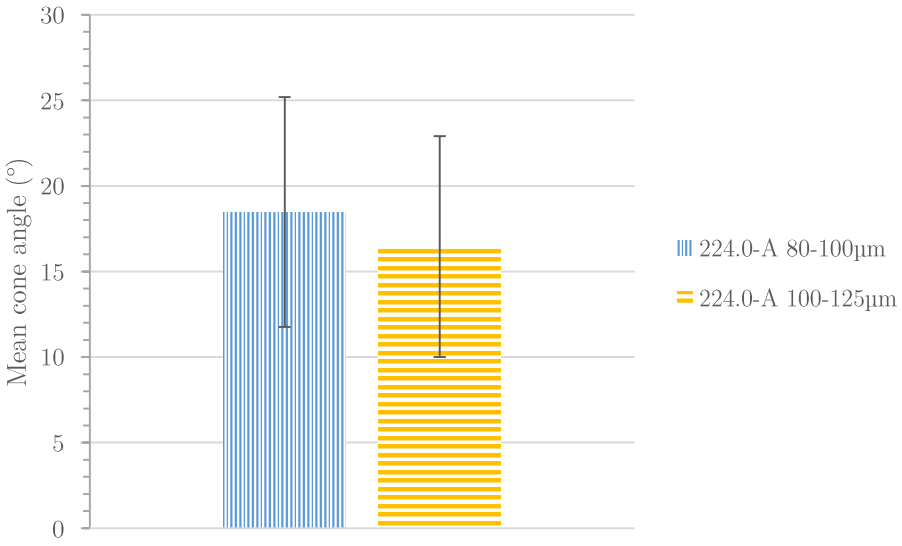

Figure 3.32: Mean of the mean cone angles vs granulometry (error bars set as the mean standard deviation of mean cone angle over all conditions tested for each granulometry)

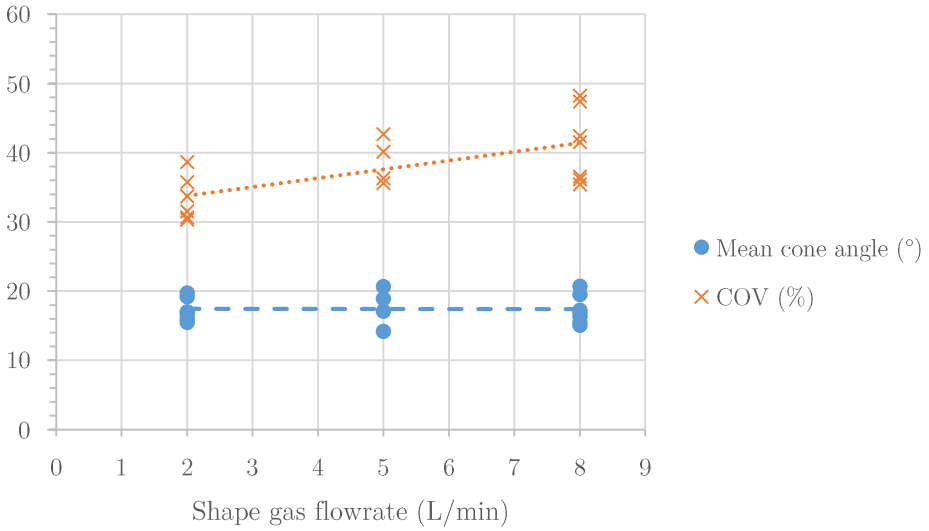

Figure 3.33: Mean cone angle (°) and COV (%) vs. Shape gas flowrate (L/min) with trend lines

The granulometry (80-100µm vs. 100-125µm) does not appear to play a significant role, as suggested by figure 3.32 where a large overlap in mean velocity values is observed. The values displayed for each granulometry are the mean of the mean cone angles, and the error bars correspond to the mean of the standard deviation for all tested condition (powder flowrate, pressure). The two granulometries are fairly close to one another so that the variation caused by this factor may be too small to be significant in the present experiments. The shape gas flowrate has a significant impact of powder jet angle variation considering its low p-value, as can be observed on figure 3.33. The powder flow rate also appears to be a significant factor although it has a more limited impact. This can be explained by the higher particle concentration that can lead to a wider spread of the powder jet, although this effect could also arise from the segmentation process, which can be sensitive to particle concentration as it impacts the intensity of the powder jet on the images and thus alters the segmentation results. To clarify this effect, which is small in any case given the small value of the coefficient in the linear model, the segmentation process should be made more robust to pixel intensity variation between conditions. For instance this could be done during the pre-processing phase where the 8-bit images should be normalized in terms of pixel intensity (i.e. grey-level) to give more comparable thresholding outcomes.

Supplementary investigations could be conducted to extend the experiments to the case of other powder materials (e.g. 316L) with varying shape gas flowrates to evaluate the material-dependence of the observed cone angle variability.

b. Powder particle velocity

i. Experimental procedure

While a standard camera capturing at 30 fps allows to observe the general geometry of the powder jet, it does not allow to single out individual particles and thus cannot be used for particle velocity estimates. Such particle velocity measurements are seldom available although they are an important aspect of the LMD process. Indeed, the particle velocity limits the scan speed, as noted previously, but also determines the preheating time of particles by the laser before reaching the melt pool. This preheating effect could at least partially melt the particles before entering the melt pool. This is however not very documented in the literature on LMD, and the actual phase of the particles entering the melt pool for a given material and operating parameters is essentially unknown in most cases. It is also noted that particle impact velocity and melting state (solid/partially melted/liquid) could also play a role in melt pool stability during deposition of aluminium alloys, which are relatively fluid (i.e. low viscosity) in the melted state and are thus prone to instabilities, but this has not yet been investigated in details in the literature.

To experimentally evaluate the particle velocity exiting the LMD deposition head, a high speed camera capturing at 12,000 fps was targeted at the nozzle outlet. Image sequences of 3 powder samples (224.0-A 100-125µm, Al12Si-A 45-90µm, 316L 45-90µm) with varying carrier gas flowrate and shape gas flowrate were obtained. A full experimental plan could not be unrolled due to experimental constraints, so the experimental conditions were focused around the usual operating point of the LMD system. Other factors such as central gas flowrate and gas pressure were kept constant at nominal values of 1.5 L/min and 1.5 bar. The powder volume flowrate was kept approximately constant although the mass flowrate varied with the type of powder. In the limit of dilute flows where particle density in the gas phase is small, powder flowrate is not expected to have a major influence on particle velocity. The high-speed camera being actively cooled by ambient air, it could not be safely placed inside the LMD system due to the presence of fine particles that could damage the system. The images were therefore captured from quite afar and had to be significantly cropped to focus on the region of interest at the nozzle outlet. The resolution of the original images was already fairly low at 640x640 pixels, as is customary with high-speed cameras, so the resulting cropped images available for analysis had a very low resolution, which complicated the particle tracking process and required adequate pre-processing. For better particle visibility in these low-resolution images, the powder flowrate was thus set at reasonably low values.

ii. Particle tracking

Because of the low resolution of the images, the particles were difficult to track as the pixel size is larger (~300µm) than particle size (~50-100µm). The particles were still visible as the extensive spot lighting targeted at the nozzle outlet induced some light diffraction around the particles, albeit creating a blurry effect which, combined with the low resolution, posed a serious challenge to the detection of the particles during the tracking process. Moreover, the powder jet is a 3D structure that is here projected on a 2D image, so that significant particle overlap could occur.

A pre-processing phase was thus required to facilitate the particle detection process, as shown on figure 3.34. A particle tracking plugin (TrackMate) of the image analysis software ImageJ was then used to segment and track the particles within the pre-processed images. The particle tracking algorithm must be finely tuned to minimize tracking errors, such as when a track jumps to another location due to particle segmentation errors between frames. These errors could however be limited through the appropriate parameterization of the tracking algorithm. A Laplacian of Gaussian (LoG) particle detector was used with a Gaussian blob diameter estimated at 1.1mm and a threshold at 0.5, followed by a Linear Assignment Problem (LAP) tracking algorithm with a 2mm maximum linking distance and without gap-closing, track splitting or track merging. As seen on figure 3.35, the resulting particle paths are generally reasonably smooth (i.e. few unphysical sharp turns and particle backtracking) and properly oriented downwards despite the low initial resolution of the region of interest in the captured images. Upon visual inspection, the segmented tracks seem to adequately follow the particle paths, albeit with a few errors that should be averaged out over the fairly high number of tracks obtained per experimental condition.

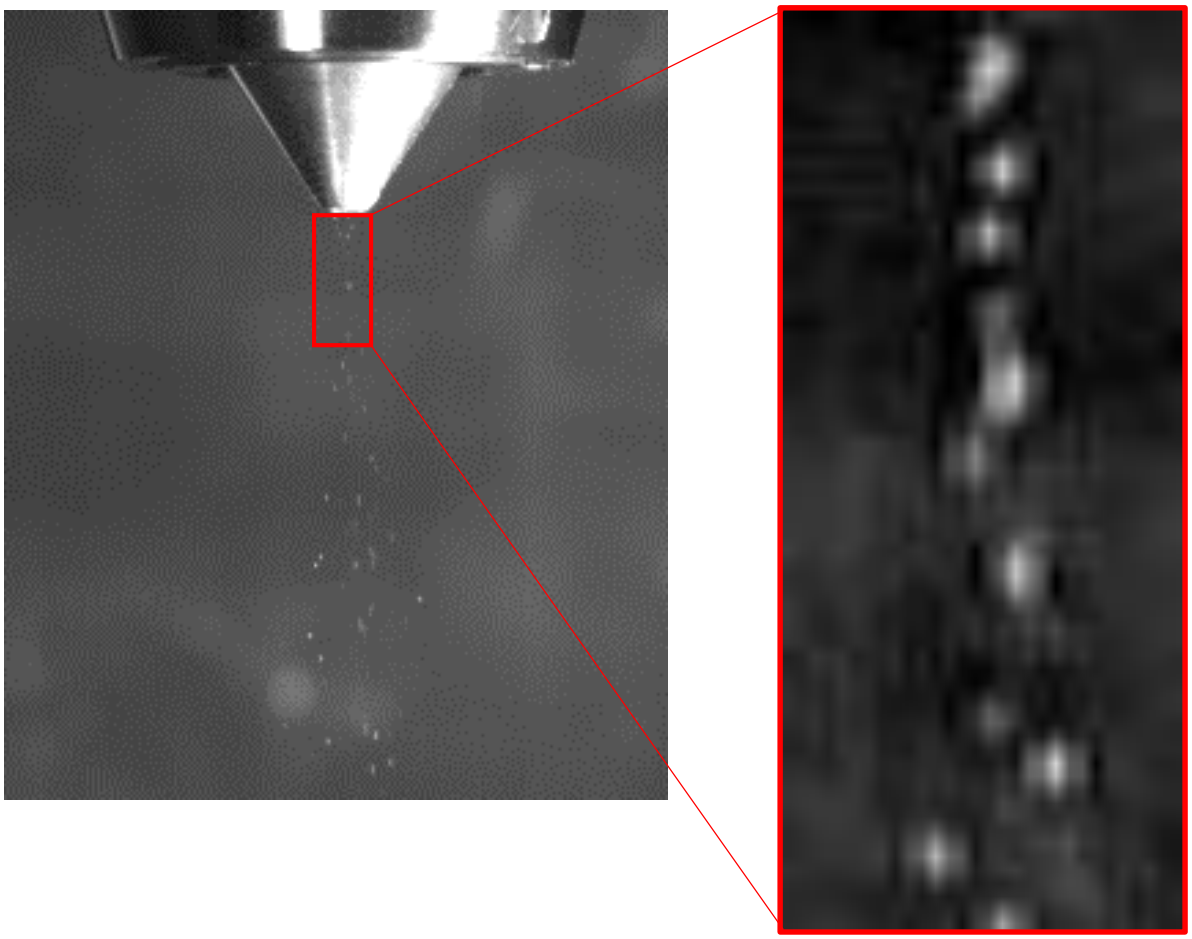

Figure 3.34: Cropping of captured images before pre-processing

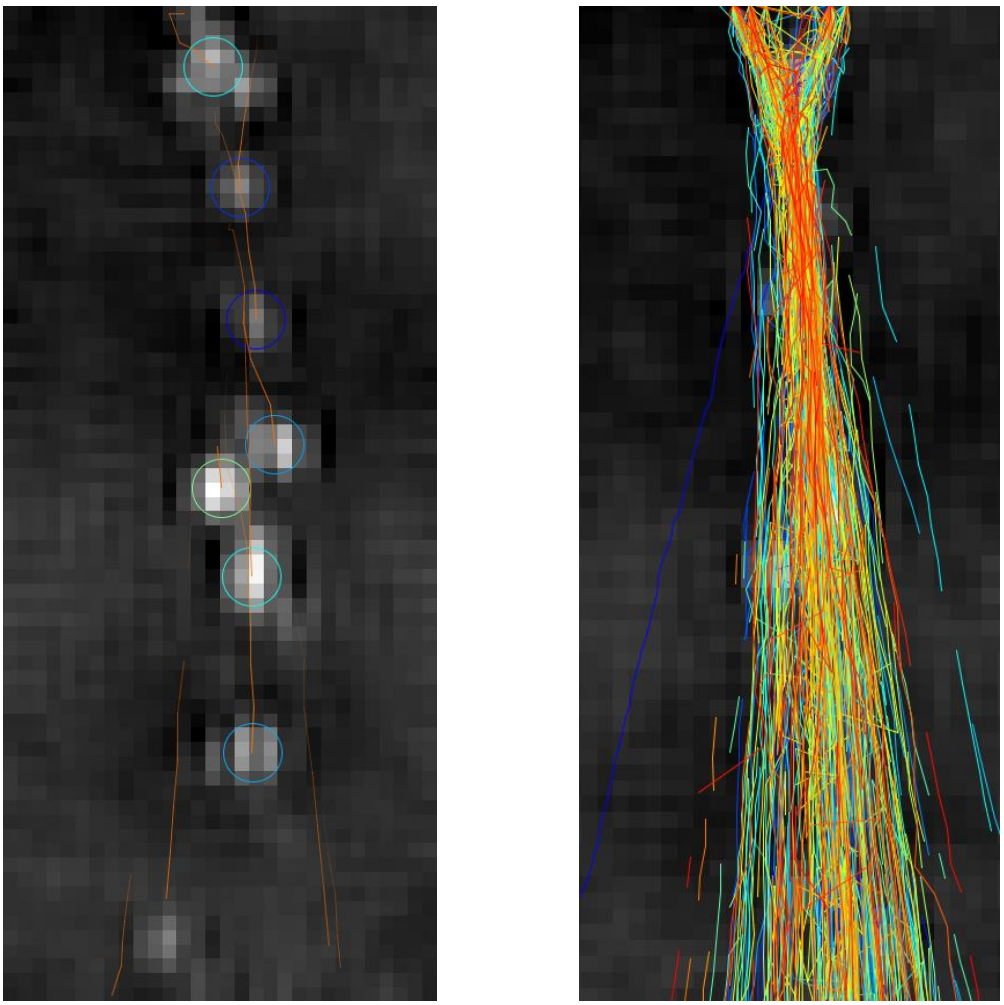

Figure 3.35: Tracks of individual spots (left) – Complete set of tracks (right) over 1000 consecutive frames captured at 12,000 fps corresponding to a single experimental condition

iii. Statistical analysis

The results from the particle tracking experiments are shown in table 3.19, where 1000 consecutive frames captured at 12,000 fps have been analyzed for each of the 17 experimental conditions to yield average measurements of particle velocity. The mean velocity and coefficient of variation (COV) of the particle velocity over all tracks are presented together with the number of particle tracks and their average duration. The mean COV of the velocity within each track is also shown to evaluate the mean velocity variation along particle paths. While the track duration obtained is usually limited to less than 50-70 frames (with an average < 10 frames in all cases), there are a few hundred tracks per experimental condition, which should allow for a relatively reliable estimate of particle velocities.

Material	Carrier Gas Flowrate (L/min)	Shape Gas flowrate (L/min)	Powder flowrate (%)	# tracks	Mean Track duration (#frames)	Mean Velocity over all tracks (m/s)	COV of Mean Velocity over all tracks (%)	Mean COV of Velocity within tracks (%)
316L	2.8	5	25	454	3.64	4.69	65.52	42.01
316L	2.8	5	50	313	4.39	4.59	63.38	58.23
316L	1.8	5	25	482	3.13	5.02	72.31	36.35
316L	3.8	5	25	480	3.74	5.09	63.05	44.51
316L	2.8	2.5	25	553	4.32	3.86	76.01	50.48
316L	2.8	7.5	25	365	3.15	5.22	66.66	42.78
Al12Si-A	2.8	5	25	200	3.280	6.48	46.81	31.24
Al12Si-A	2.8	5	50	451	5.062	6.22	55.44	48.74
Al12Si-A	1.8	5	25	189	3.407	5.93	65.82	39.67
Al12Si-A	3.8	5	25	230	3.939	6.31	53.34	36.01
Al12Si-A	2.8	2.5	25	322	4.634	5.51	55.75	40.60
Al12Si-A	2.8	7.5	25	138	2.239	7.56	55.58	26.84
224.0-A	2.8	7.5	25	673	5.29	8.24	48.58	27.19
224.0-A	2.8	5	25	498	6.42	7.59	46.41	21.43
224.0-A	2.8	5	50	760	7.77	7.61	38.64	22.08
224.0-A	3.8	5	50	639	5.83	7.60	43.61	27.21
224.0-A	3.8	7.5	50	601	5.61	8.53	48.36	26.92

Table 3.19: Particle tracking results in terms of mean particle velocity and particle velocity variations within and between tracks

There is a significant variation of velocity within and between tracks, so that the mean velocities are only indicative of the order of magnitude of the particle velocity. An ANOVA analysis of the results shows that the significant factors are the powder material and the shape gas flowrate (see table 3.20). The carrier gas flowrate seems insignificant although it was only varied over a relatively small range compared to the shape gas flowrate. Unsurprisingly, the powder flowrate is insignificant as the flow remains reasonably dilute so that increasing particle concentration in the flow of carrier gas does not significantly affect the flow field. It is also noted that the relatively high variability of mean velocities as measured through particle

tracking is not accounted for in the ANOVA analysis, although the mean velocities were taken over a fairly large number of tracks and the COV remains on the same order of magnitude throughout all tested conditions, so that the changes in mean velocities should remain significant.

p-value (shape gas)	p-value (material)	p-value (model)	R^2-adj.	R^2-pred.
< 0.0001	< 0.0001	< 0.0001	0.971	0.956

Table 3.20: ANOVA results from particle tracking analysis

$$Mean\ velocity\ \ 316L\ = 3.072 + 0.0033 \times Shape\ gas\ flowrate \tag{3.2}$$

$$Mean\ velocity\ \ Al12Si\ = 4.663 + 0.0033 \times Shape\ gas\ flowrate \tag{3.3}$$

$$Mean\ velocity\ \ 224.0\ = 5.903 + 0.0033 \times Shape\ gas\ flowrate \tag{3.4}$$

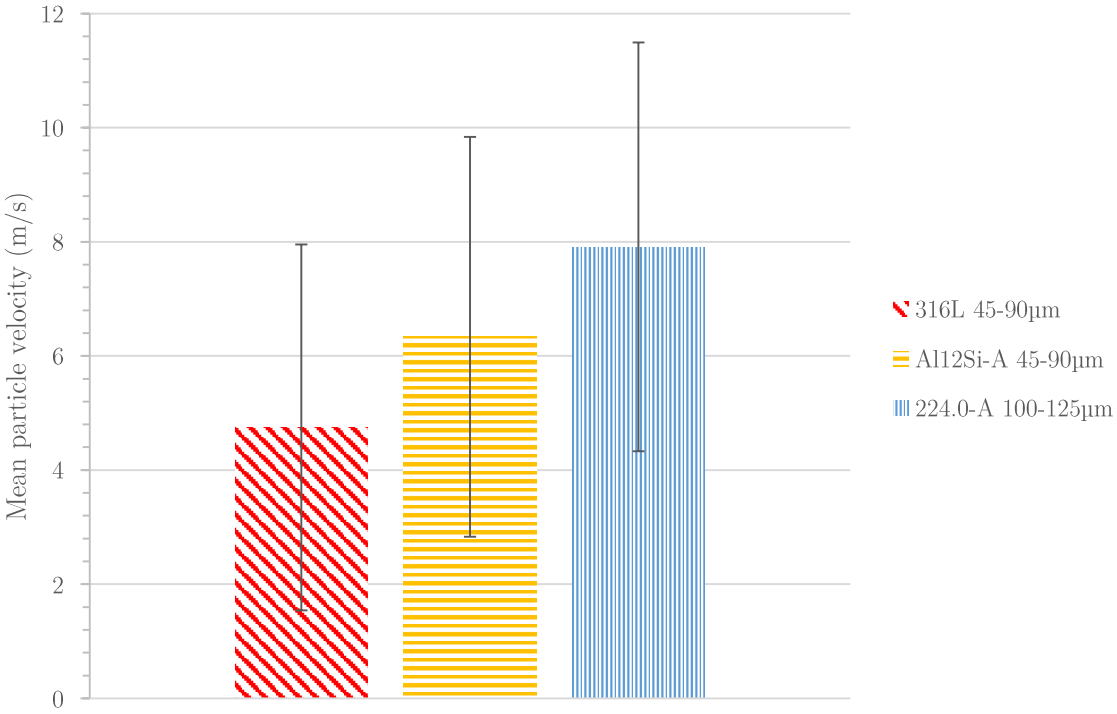

Figure 3.36: Mean of the mean particle velocities vs. powder sample over all tested conditions (error bars set as the mean of the standard deviation of the mean velocity between particle tracks)

The adjusted and predicted R^2 values are in close agreement so that the model is not overfitting the data, which can be expected for a simple linear model. Moreover, these values are fairly close to unity, so that the identified significant factors explain much of the observed variability in mean particle velocity. The influence of the shape gas is the same for all 3 materials tested, as the coefficient of the shape gas flowrate (expressed in L/min) is the same in the 3 model equations. The intercept is however different for each powder material. The

highest mean velocity is obtained with powder 224.0-A 100-125µm, whereas 316L 45-90µm has the lowest mean velocity and powder Al12Si-A falls somewhere in between. The higher velocity of aluminium based powders compared to the stainless steel powder could be partially explained by the smaller density of aluminium particles, which have a small inertia and thus get accelerated more easily by the gas flow. While this is sensible for comparing 316L and Al12Si powders as they present a similar granulometry, this is not sufficient to explain the difference in mean velocity of the 224.0-A powder. Indeed, the median diameter of powder 224.0-A is almost twice as high as that of the 316L powder, while its density is only about 3 times as low. Thus, a median-sized particle of 224.0-A is slightly heavier than a median-sized particle of 316L, yet the 224.0-A powder flows faster. Performing the ANOVA analysis by including the granulometry and the material density as two distinct factors does not lead to a satisfactory representation of the variability as the R^2 values are then below 50%.

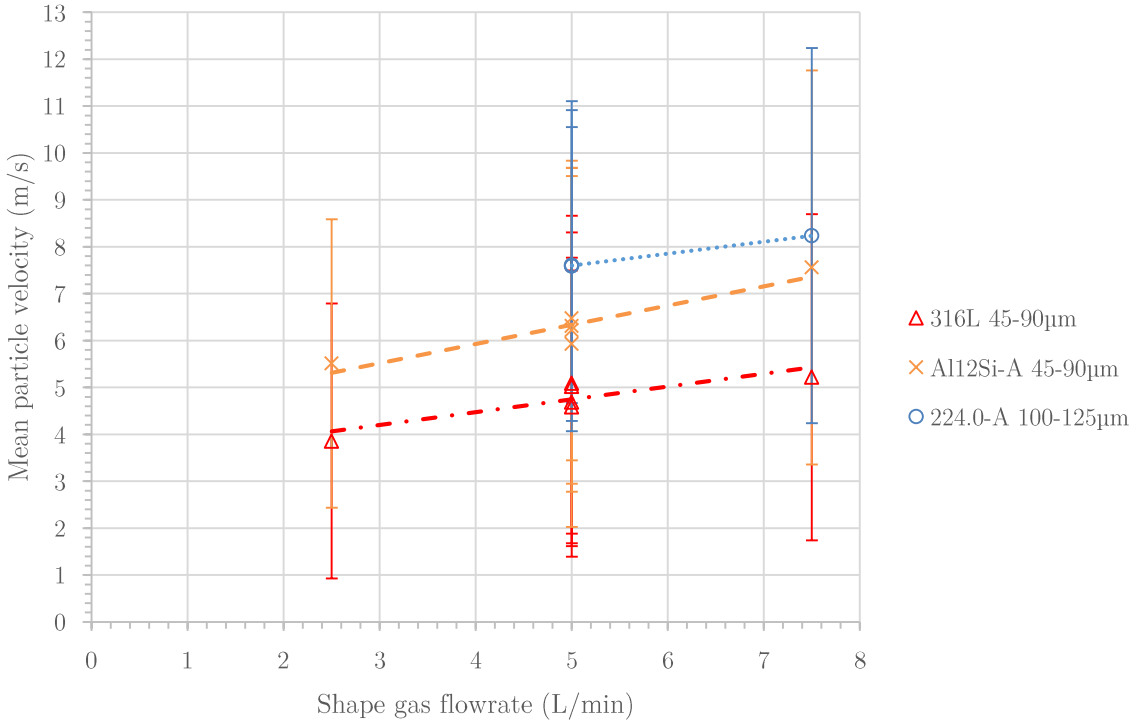

Figure 3.37: Mean of the mean particle velocities vs. shape gas flowrate for each powder sample (error bars are set as the mean of the standard deviation of the mean velocity between particle tracks)

A supplementary explanation for the higher velocity of 224.0-A compared to Al12Si and 316L could lie in the comparatively greater drag force from the gas due to the higher surface area of the larger particles, thereby compensating the difference in particle inertia and leading to a greater acceleration over a given distance (e.g. the nozzle channel length) for particles of similar density (224.0-A and Al12Si-A). However this discrepancy in mean velocity between Al12Si-A and 224.0-A would require further scrutiny, especially considering the relatively high variability of the mean velocity in each tested condition, whether it is within a

track or in between tracks. This variability is illustrated in figure 3.37, where significant overlap is observed between mean particle velocities, as evidenced by the error bars calculated as the mean of the standard deviation of the mean velocities between tracks over all tested conditions for each powder sample. Moreover, there is a significantly smaller number of tracks detected in the tests with Al12Si-A powder, which could indicate that the tracking process is not as accurate and that the mean velocity value is not as representative as in the other 2 samples. What is rather certain from these results however is that the 316L particles travel more slowly on average than aluminium particles 224.0-A and Al12Si-A, and that powder flowrate has little impact on mean velocity, unlike the shape gas flowrate which has a major influence together with the type of powder (density and granulometry). Further work should revisit the results obtained for Al12Si-A and carry out supplemental experiments with powders of various density and granulometry to elucidate their influence on mean velocity. The effect of carrier gas flowrate should also be explored in more depth as the range of values assessed are probably too limited compared to the range of values used for shape gas flow rate. The particle size could also be a major factor in the observed variability in particle velocity, however the high-speed images obtained from the experiments present a very low resolution and are ultimately a 2D representation of a 3D phenomenon so that the depth information is suppressed. In that respect, the particles cannot be reliably segmented in terms of particle diameter based on the available experimental data.

c. Aluminium powder cohesiveness inside the LMD nozzle

The marginally flowable aluminium powders 224.0-A 80-100µm and 100-125µm could be used in-process to make LMD deposits after appropriate pre-processing and adjustments in the distribution system. However, even in their fluidized state, some flowability issues were observed inside the copper nozzle where powder particle accumulated on walls with low inclination with respect to the horizontal plane, where particle-particle and particle-wall interaction forces can counterbalance the force of gravity and fluid-induced shear stresses. In addition to vdW and capillary forces, the occurrence of triboelectrification and resulting electrostatic (image) forces between the grounded conducting copper nozzle and aluminium 224.0 particles cannot be excluded, especially if the oxidation level of the particles means that sufficient local charge accumulation can be maintained. While electrostatic interactions may contribute to the initiation of powder agglomeration on the walls, other cohesion forces (i.e. vdW or capillary forces) are however most likely at play between identical aluminium particles forming the agglomerate. The accumulated powder particles are easily removed by a weak mechanical action, demonstrating that they are not adhering by a surface melting or sintering

effect. However they can eventually obtrude the flow of powder and thus force the interruption of the LMD deposition process. In some occurrences, powder agglomerates also form on the steeply inclined nozzle surface at the nozzle outlet as the particles seemingly become partially sintered or melted upon contact with the hot surface. This can not only disturb and even impede the flow of particles, but can also damage the nozzle by inducing deformations from excessive heat concentration precisely where the wall geometry is most critical for powder jet quality. These two forms of powder adhesion in the nozzle cones are displayed in figure 3.38.

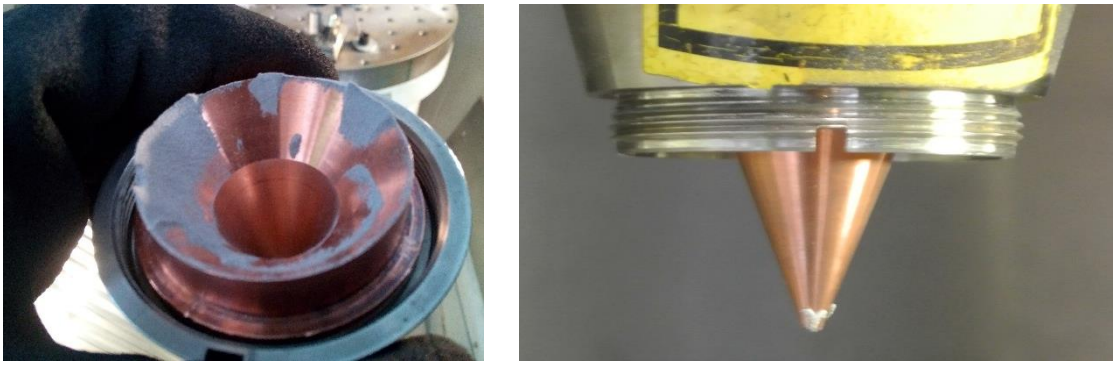

Figure 3.38: Particle adhesion on inner wall of outer nozzle cone (left) - Particle sintering/melting on outer wall of intermediate nozzle cone (right)

It is hypothesized that the wall adhesion behavior of the cohesive 224.0 powders on the inner wall of the outer nozzle cone is promoted by the design of the nested copper nozzles, where a “buffer region” with high fluid and particle recirculation can be expected with the current geometry. This would promote particle-wall collisions at relatively lower velocities, in which case adhesion/cohesion forces could become dominant over gravity and fluid forces. It is noted that this wall adhesion effect is not observed with less cohesive aluminium powders such as Al12Si-A. Based on the conclusions of the previous chapter, capillary and mechanical interlocking forces must play a large role in 224.0-A powder cohesiveness in addition to the ubiquitous vdW forces, and most likely are a major factor in sustaining the agglomerate structure formed on the inner wall of the outer nozzle cone. The inside of the nozzle cannot be directly observed however. Hence, a numerical investigation of gas-particle flow is conducted to elucidate the behavior of particles during nozzle flow.

II. Numerical investigation on Aluminium Particle Flow during LMD

a. CFD-DEM modeling

Several modeling paradigms are available for multiphase gas/particle flows, including the Eulerian-Eulerian approach and the Lagrangian-Eulerian approach (Garg et al. 2012a; Li et al. 2012). The CFD-DEM (Computational Fluid Dynamics-Discrete Element Method) paradigm uses the Lagrangian-Eulerian approach by modeling every single particle as a discrete object interacting with a fluid continuum. Unlike an Eulerian-Eulerian approach (e.g. Two-Fluid model) where a lot of unknown terms arise from the representation of particles as a continuous phase, CFD-DEM allows to explicitly account for interparticle forces and collisions through analytical models, so that most terms can be straightforwardly interpreted in physical terms. However it is computationally very expensive, so that it is not always applicable to large-scale systems with many particles, even with current supercomputers.

Most of the published works so far on gas-particle flow simulations in LMD nozzles have used analytical models (Pinkerton and Li 2004; Tan et al. 2018), or dispersed phase models where interparticle interactions, such as collisions and van der Waals forces, are ignored (Arrizubieta et al. 2014; Kovalev et al. 2018; Srdja Zekovic, Rajeev Dwivedi 2006; Tabernero et al. 2010; Wen et al. 2009). Lagrangian-Eulerian simulations that include particle collisions have been conducted to study the pre-heating effect of the laser (Ibarra-Medina and Pinkerton 2010). A review on numerical modeling of LMD gas-particle flow as well as melt pool and deposit geometry has been published (Pinkerton 2015), showing that there is a continuing body of work being published on modeling various aspects of the LMD process, including a CFD-DEM model of the pneumatic transport of Al and Cu powder mixtures (Li et al. 2018). There are however no known publications that brought the focus on the cohesive flow of aluminium powders inside LMD nozzles and the wall adhesion phenomena. Indeed, cohesive aluminium powders are seldom used in the first place due to the challenge posed by these powders during their transport in the pneumatic system and LMD nozzle. Moreover, adhesion phenomena require the modeling of interparticle cohesion and contact forces, which are particularly resource intensive, especially when the particle flow is fully coupled with the gas flow.

In this work, the open-source CFD-DEM simulation software MFiX v18.1.5 (Multiphase Flow interface eXchange) was setup on the LIGER supercomputer of the High Performance Computing Institute at Ecole Centrale de Nantes (France) to simulate the gas/particle flow (Garg et al. 2012b; a; Syamlal et al. 1993) through various nozzle geometries under various

boundary and initial conditions while accounting for interparticle collision and cohesion forces, as shown in the following sections. The calculations could only be carried out in Shared-Memory Parallel (SMP) mode so, to keep the simulation time reasonable, the nozzle geometry was modeled in 2.5D so that the gas/particle flow was effectively resolved on a 2D plane corresponding to a vertical slice of the full nozzle geometry, and a 1mm-thickness was included to make room for the 3D particles. This thickness is about an order of magnitude higher than the particle diameter to limit the influence of the front and back walls.

The MFiX software uses a cartesian cut-cell meshing scheme, where the cells composing the mesh are either blocked, cut or fully preserved depending on where they are located with respect to the simulation domain, the geometry of which being defined by a STL file. The blocked cells that are outside of the simulated region can be discarded to speed up the calculations through a re-indexing method. The cells falling on the simulated region boundary are cut to follow the boundaries of the simulation domain, and specific provisions are made in the MFiX code to account for various cut-cell geometries when solving the gas and solids equations. This approach not only facilitates the meshing process but also allows for a smaller cell count compared to more common meshing schemes, which keeps the simulation time reasonable. It is however best suited to problems focused on particle dynamics with a reasonably simple domain geometry.

The CFD-DEM model equations are not detailed here but can be found in (Garg et al. 2012b; a). Essentially, the particles are modeled in a Lagrangian reference frame using Newton's second law, and "soft-sphere" particle collisions are accounted for by a linear spring dashpot model (LSD), as in the present work, or by a non-linear Hertzian-spring-dashpot (HSD) model. Van der Waals forces are modeled with the Rumpf model (Rumpf 1990), although it is limited in accuracy (Rabinovich et al. 2000a; b). The gas phase is described in a Eulerian reference frame where fluid equations are formulated with momentum transfer terms between the gas and solid phases that are evaluated based on various drag force models (Garg et al. 2012b; Syamlal et al. 1993). The MFiX software is extremely complex and is still being actively developed although the first implementation dates back to the early 1990's (Syamlal et al. 1993). It can also include chemical reactions and energy equations and has been extensively applied to the fluidization behavior of particles in chemical reactors. However, it is equally well suited to simulating the gas/particle flow during LMD processing as it involves similar physical phenomena, although no known publications have used this code for such a purpose.

There are many parameters that must be set in a CFD-DEM model regarding the properties of the gas, solids and walls as well as the assumptions to be made for the gas-particle and particle-particle interactions. Mixture rules, phenomenological laws (e.g. Sutherland's law for gas viscosity) and a material property database help determine most of

the gas properties. Less obvious parameters settings are the particle-particle/particle-wall collision parameters for the LSD contact model (normal and tangential restitution coefficients, friction coefficient etc.). The HSD model parameters are more conveniently directly derived from common material properties (e.g. Young's modulus, Poisson ratio) but this model is prohibitively expensive to use computationally compared to the LSD model. Indeed, the calculated normal spring constant for the HSD model is typically much higher than for the LSD model, so that much smaller time steps are needed to evaluate the particle-particle contact interaction. In practice, small values on the order of 1000 N/m, as used for bronze spheres, can be used for the LSD model without excessively affecting particle dynamics (Malone and Xu 2008). The LSD model parameters have been correlated with known material properties such as yield strength and Young's modulus (Jackson et al. 2010; Marinack et al. 2013; Navarro and de Souza Braun 2013), although the values are not constant as they notably depend on the impact velocity, which is generally unknown. These parameters have also been measured empirically for various metallic materials (Brake et al. 2017; Uzi and Levy 2018). Approximate values based on literature data are given in table 3.21 along with other important parameters, although these values should be assessed more precisely in future work for the particular case of gas atomized metal AM powder particles. Moreover, it is noted that the MFiX code considers these parameters as constants, so that the velocity dependence cannot be accounted for. Regarding the Hamaker constant used to model the vdW force according to the Rumpf model, a common value of 300 zJ is used for all the metallic materials for a lack of more precise data. An average of the values given in chapter 2 (table 2.8) could also be used, although the uncertainty on the vdW force model is already quite high due to the model being used and the lack of roughness data, so that including more refined values is not considered pertinent as it could bias the simulation results.

Particles are also affected by drag and lift forces induced by interactions with the gas phase. This momentum exchange is represented by a drag force model and is a major aspect of CFD-DEM modeling. Fluid drag is essentially composed of skin drag, due to friction between the gas and the particle surface, and form drag that comes from energy dissipation due to boundary layer separation and eddy formation in the wake of a particle, thereby forming an adverse pressure gradient between the leading side and wake side of a moving particle. Multiple models have been proposed in the literature, and the Syamlal-O'brien drag force model is adopted here (Syamlal et al. 1993), as it has been shown to provide adequate accuracy compared to other models such as the Gidaspow model (Agrawal et al. 2018).

Parameter	Aluminium particles	Stainless steel particles	Copper walls
Restitution coefficient (normal)	0.75	0.8	0.65
Sliding Friction coefficient	0.2	0.3	0.4
Normal spring constant (N/m)	1000	1000	1000
Hamaker constant (zJ)	300	300	300
Outer cutoff distance (µm)	100	100	100
Inner cutoff distance (nm)	0.165	0.165	0.165
Asperity size (nm)	12	12	n/a

Table 3.21: CFD-DEM parameters

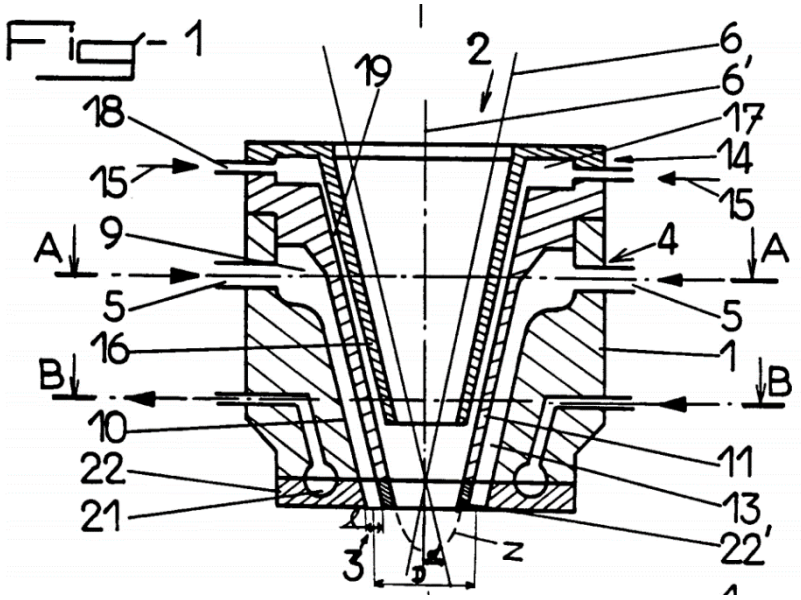

Figure 3.39: LMD nozzle schematic from patent EP0574580B1 by IREPA Laser

The LMD nozzle is formed by 3 concentric copper cones as shown in patent EP0574580B1 (see figure 3.39). The geometry of the carrier gas/particle flow channel, defined as channel 13 in figure 3.39, is shaped by the interstitial space between the outer and intermediate cones of the LMD deposition head and contains a homogenization chamber 9. The shape gas channel 18 is designed to ensure a hollow powder jet geometry at the nozzle outlet to limit interactions between the laser beam and the particles prior to entering the melt pool. Its geometry is defined by the spacing between the intermediate and inner nozzle cone, and thus becomes very narrow near the channel outlet to impart the necessary acceleration to

the flowing gas. The central gas channel is shaped by the inner channel geometry of the inner nozzle cone, which is also the optical path of the laser beam. This central gas flow serves to avoid the backflow of particles up the laser path, which can pollute and eventually damage the optical lenses. In the nozzle geometry used for the 2.5D CFD-DEM simulations, the shape and central gas channels are merged and simplified as a unique straight channel to reduce the computational load as the region of interest is inside the carrier gas channel and at the nozzle outlet.

The boundary conditions are not explicitly known as direct experimental measurements of gas and particle velocities at the inlet of these channels cannot be performed. This is in fact the reason why computer simulations are necessary in the first place as the gas/particle flow cannot be directly observed with the current LMD system. Approximate values for the gas velocities can be computed from the known experimental values of the gas flowrates. Using mass conservation and assuming that the velocity field is uniform across the inlet pipe section, the velocity of the carrier gas when it enters the carrier gas flow channel on the left and right side of the nozzle can be estimated at about 4.2 m/s for a flowrate of 2.8 L/min. The gas velocity in the combined shape+central gas channel in the simulated nozzle geometry is similarly evaluated based on the sum of the flowrates from the shape gas channel (i.e. 5 L/min) and central gas channel (i.e. 1.5 L/min). The inlet particle velocity is another unknown that is difficult to estimate experimentally beyond the simple constraint that particle inlet velocity is typically lower than the inlet gas velocity. An arbitrary value of 1 m/s is used in the present work for a lack of a better estimate although, as noted previously, there is a "buffer" or "recirculation" zone in the carrier gas channel (see region 9 in figure 3.39) that will promote the recirculation of both gas and powder particles, as demonstrated by the following simulations. The resulting outlet velocities are thereby partly decoupled from the inlet boundary conditions so that their precise value is not paramount in obtaining sensible values at the channel outlet, provided the values are on the correct order of magnitude. With an inlet carrier gas velocity of 4.2 m/s, a value of 1 m/s for particle inlet velocity seems suitable as it remains below the gas velocity.

This buffer region is referred to as a "homogenization chamber" in patent EP0574580B1. This design can be interpreted as providing a buffering effect to smooth out variations in powder flowrate as the chamber forms a reservoir of fluidized powder particles. It also acts to reduce particle velocity to ultimately leave more time for the particles to get preheated in-flight by the laser. While this buffer region may generally be advantageous, it is thought to be detrimental in the case of cohesive aluminium powders as particles with lower velocities tend to adhere more readily to walls and other particles under the effect of van der Waals, capillary and possibly electrostatic forces. Thus, instead of a smoothing effect, it can

lead to particle accumulation inside the carrier gas channel that drastically limits the duration of the LMD deposition.

As multiphase flows typically present a complex, dynamic behavior, it is useful to first evaluate a few characteristic numbers to assess the type of flow conditions that can be expected and thus the adequate modeling assumptions that can be made (Marshall and Li 2014). In table 3.22 are presented the physical parameters used to estimate the range of characteristic numbers of the gas-particle flow shown in table 3.23. The characteristic lengths used are the inlet pipe diameter (4mm) and the thickness of the exit channel of the nozzle (0.5mm). The particle diameters are taken as the d_{10} and d_{90} values of each powder samples so that an approximate range of values for the characteristic numbers is obtained for the experimental flow conditions. In the simulation, the particle distribution is constrained to be monosized with a unique particle diameter set as the median diameter d_{50} of the sample. The particle volume flowrate is estimated based on the mass flowrate, set here as 2 g/min, and assuming monosized spheres of median diameter d_{50} (although $d_{4,3}$ could be more appropriate but is not available for all samples and typically remains close to d_{50} for gas atomized metal powders) with the material density being calculated from the atomic composition of the alloy and a mixture rule.

Characteristic Properties	**Argon**	**224.0-A 100-125µm**	**Al12Si-A 45-90µm**	**316L 45-90µm**
Flowrate [m^3/s]	5e-5	1.17e-8	1.25e-8	4.17e-9
Particle diameter (µm)	n/a	82-176	45-90	45-90
Density (kg/m^3)	1.784	2841	2657	8000

Table 3.22: Typical parameters for carrier gas and metal particles to assess characteristic numbers of the multiphase flow during LMD

The characteristic numbers in table 3.23 are evaluated based on (Marshall and Li 2014) using values from table 3.22. Some numbers are given on a range based on 4 calculated values using particle diameters d_{10} and d_{90} in the inlet pipe (4mm diameter) and nozzle exit channel (0.5mm-thick), where the fluid velocity is evaluated at 4.2 m/s and 35 m/s respectively based on carrier gas flowrate (2.8 L/min in nominal conditions) and mass continuity. A constant powder mass flowrate of 2 g/min is assumed for the 3 materials.

Characteristic number	224.0-A 100-125µm	Al12Si-A 45-90µm	316L 45-90µm
Stokes	210 - 5.37e5	59 - 1.31e5,	178 - 3.95e5
Reynolds (fluid)	1340 - 1400	1340 - 1400	1340 - 1400
Reynolds (particle)	5780 - 2.65e8	894 - 3.31e7	2.69e3 - 9.97e7
Particle volume concentration	2.35e-4	2.69e-4	8.93e-5
Length Scale ratio	0.02-0.35	0.01-0.18	0.01-0.18
Mass loading	0.40	0.40	0.40
Momentum coupling	6.96e-7 - 1.8e-3	3.05e-6 - 1.69e-3	1.01e-6 - 2.24e-3
Bagnold	1020 - 2.62e6	295 - 6.55e5	730 - 1.62e6

Table 3.23: Range of characteristic number of the gas-particle flow in the 2.5D carrier gas channel

In all cases, the Stokes number (ratio of particle to fluid response time) is well above unity so that particles respond slowly to fluid forces and thus do not closely follow the fluid streamlines. The fluid Reynolds number (ratio of inertial to viscous fluid forces) for the simulated internal flow is in the laminar regime, so that turbulence effects can be ignored in the CFD-DEM model. The particle Reynolds number is here crudely estimated using the assumption that the Stokes number is small, so as to get rid of the particle slip velocity in the equation as it is generally unknown. However it is still found that the particle Reynolds number is large with respect to unity, as is typical of pneumatic flows (as opposed to colloidal and aerosol suspensions). In that case, the simple Stokes drag force model cannot be applied. The particle volume concentration (ratio of particle volume to total volume), here estimated using gas and particle volumetric flowrates, shows that the gas-particle flow is very dilute as it is well below unity. The momentum coupling parameter is roughly estimated using the inadequate assumption that Stokes drag is applicable to enable the analytical calculation of this parameter. It is linked to the mass loading (ratio of particle to fluid mass flowrates) and is well below 10% so that one-way coupling between the particles and flow field could be assumed (i.e. particles do not affect the flow field and their dynamic behavior can be solved for separately from the fluid). In this work however, full coupling is assumed as the assumptions used for calculating this parameter is not verified. The relative values for various materials however give interesting information on the flow despite the fact that they are only crude estimates. Finally, the Bagnold number, which assesses the importance of particle collisions, is particularly instructive for gas-particle flows. It is proportional to the Stokes number and also depends on the particle volume concentration with respect to maximum packing conditions. When it is below 40, the particle flow is dominated by viscous fluid forces, whereas when it is above 400, particle collisions dominate and the flow is in a grain inertia

regime. Except for Al12Si-A particles of 45µm in diameter that are in between those thresholds and thus are in an intermediate regime, the particle flow is essentially in an inertial regime dominated by collisions according to these estimates, so that the effect of the interstitial fluid forces should remain small.

Overall, these characteristic numbers evaluated for 3 different powder samples with various density and particle sizes tend to show that the particles should only be weakly affected by the fluid forces as their behavior is mostly governed by collisions. However, the length scale ratio (ratio of particle diameter to characteristic fluid length) are not very small compared to unity when inside the thin nozzle channel, so that numerical modeling rather than simple analytical drag and lift flow models must be used to correctly assess the entire flow field (Marshall and Li 2014).

b. Powder recirculation and adhesion in LMD nozzle

To study the particle behavior inside the carrier gas channel, a simplified geometry can be used in a first approach where only a single 2.5D carrier gas channel is considered, as shown in figure 3.40. The fact that the flow field at the nozzle outlet is not accounted for can slightly affect the velocities of the gas and particles inside the nozzle, however the simulation still provides valuable insight into particle behavior with the great benefit of a very significantly reduced computational time compared to the simulating the entire 2.5D geometry, which is shown in the next section.

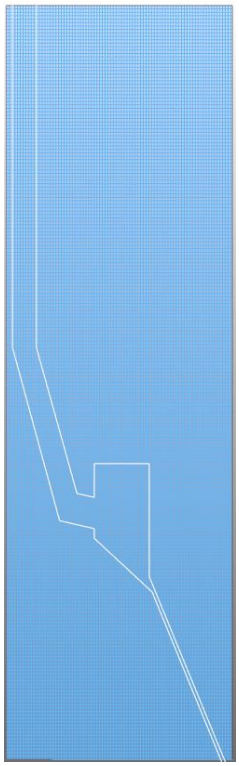

Figure 3.40: Single 2.5D carrier gas flow channel geometry on a 160x220 Cartesian grid

The solid phase is modeled as monosized spherical aluminium particles with diameter 120µm and density of 2841 kg/m^3, i.e. powder 224.0-A 100-125µm with particles of median diameter d_{50}. The inlet gas velocity is estimated at 4.2 m/s, where the gas is argon, and inlet particle velocity is somewhat arbitrarily set at 1 m/s. This simulated condition is setup to correspond to the nominal operating point of the current LMD system, with the limitation that the geometry is in 2.5D to keep the computation time reasonable. No-slip boundary conditions are set on the side walls, while free slip conditions are applied to the front and back walls to close the 2.5D domain. The outlet boundary condition is set directly at the channel outlet as a pressure outflow at a standard atmospheric condition of 1 atm. Full coupling between the fluid and particles is assumed, and a Euler time integration scheme is used. The initial mesh size is made of 160 by 220 cells, which is just high enough to solve for the flow inside the thin nozzle exit channel. The flow field computed inside this channel is thus not resolved very finely and the boundary layer may thus not be adequately captured in this region. However this is also the region where particle velocity is the highest due to gas acceleration, so that the boundary layer effect on particle velocity should be relatively small in practice. This relatively small mesh size is typical of CFD-DEM models with MFiX since this modeling approach does not scale particularly well with mesh size. It however allows for more reasonable computation times while still yielding qualitatively correct particle behaviors. This CFD-DEM code has actually been shown to provide quantitatively accurate results for various granular flow and fluidization problems (Li et al. 2012).

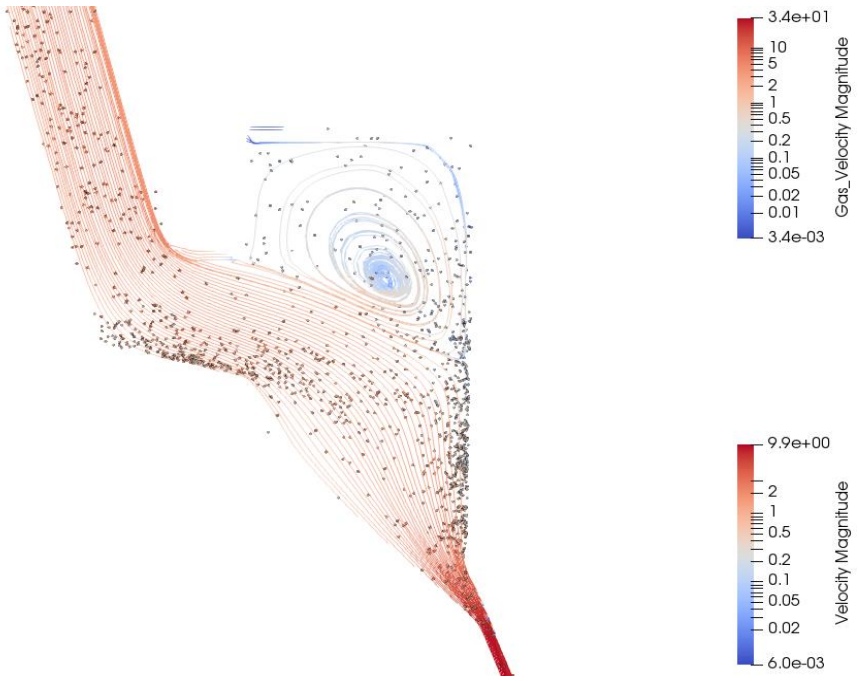

Figure 3.41: Aluminium particles and fluid streamlines with a stable vortex at the top

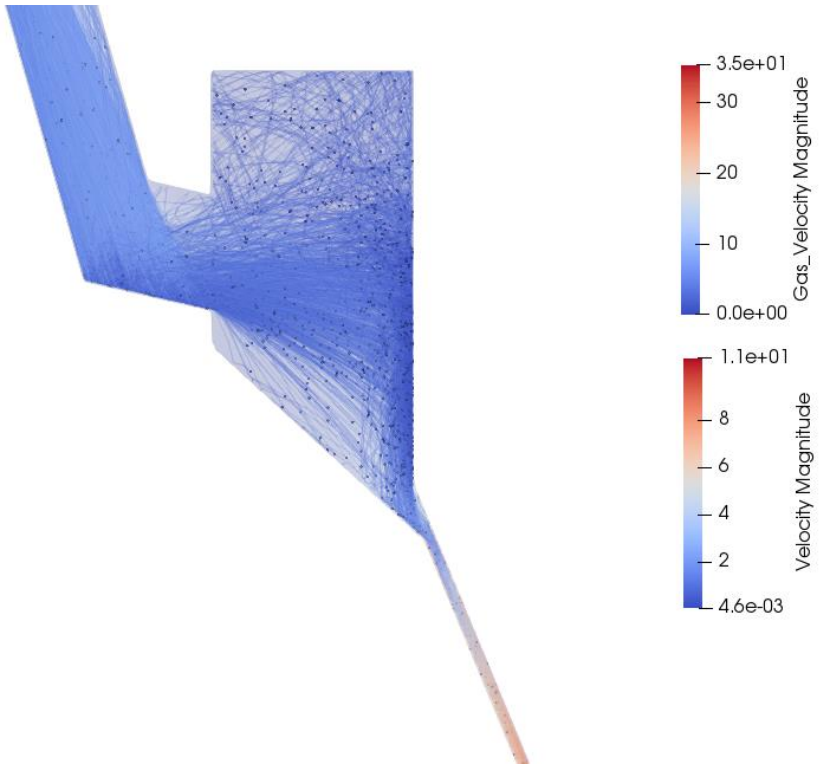

Figure 3.42: Particle trajectories in the buffer region

Based on the simulation, and despite the uncertainty in the simulation parameters and boundary conditions, it is clear that a fluid vortex tends to form inside the buffer region, as illustrated in figure 3.41. Moreover, the rebound pattern of the particles before entering the

buffer region, shown in figure 3.42, promotes their recirculation as they can get caught up in the fluid vortex following an upward rebound. While it may offer a smoothing effect for less cohesive, denser powders such as stainless steel, this buffer region is considered to be mostly detrimental in the case of light cohesive powders such as 224.0-A as it promotes particle adhesion due to reduced particle momentum. Figure 3.43 shows the mean, maximum and minimum particle velocity inside the nozzle at each time step, starting when the particles enter the domain and stopping at 0.1s when particles have started exiting the nozzle. The mean and maximum particle velocity initially increase until 0.04s where the minimum velocity drops due to impact with the bottom of the inlet pipe in the sharp turn it makes toward the buffer region. The minimum velocity further drops with time as the particles enter the buffer region where there is a recirculation effect due to a detrimental rebound and the presence of a fluid vortex. Once particles exit the buffer region, they are accelerated in the lower part of the carrier gas channel due to increased fluid velocity and reach about 10 m/s before exiting the domain. This value for the particle velocity is on a similar order of magnitude as the experimental results from the high-speed camera captures and the particle tracing process shown in the previous section, where particle velocity at the nozzle outlet for powder 224.0-A 100-125µm is estimated at an average of about 7.6 m/s in nominal conditions.

For comparison, the same simulation conditions are used for Al12Si-A 45-90µm (particle diameter 65µm and density estimated at 2657 kg/m^3) and 316L 45-90µm (particle diameter 65µm and density estimated at 8000 kg/m^3), and the results are displayed in Figure 3.43 and Figure 3.44. The maximum particle velocity reaches about 10m/s for 224.0-A, 14 m/s for Al12Si-A and 9.5 m/s for 316L particles, which is more in line with what can be intuitively expected, unlike the particle tracking results where 224.0-A flowed the fastest at the nozzle outlet. In both the tracking experiments and the CFD-DEM simulations, the 316L particles flowed the slowest. Indeed, they are heavier and relatively small so that they are not as influenced by fluid forces and thus are not as accelerated as the aluminium particles in the nozzle exit channel. However, the difference in maximum velocity is small between 224.0-A and 316L as the particle size difference partially compensates for the variation in density, so that the particles experience a similar acceleration. The Al12Si-A are the lightest and thus undergo a larger momentum increase from fluid forces.

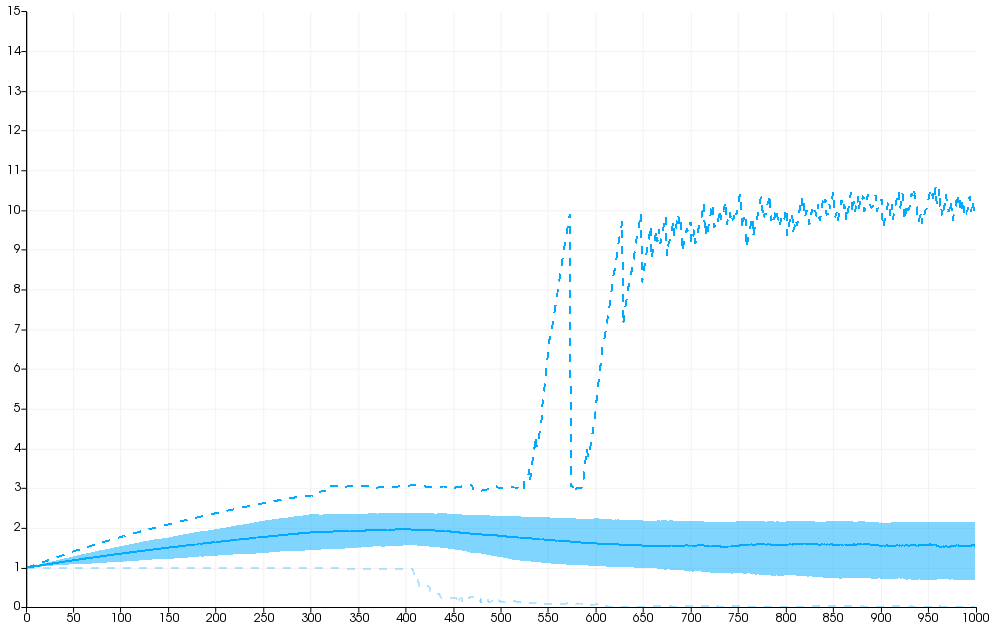

Figure 3.43: Time-variation of the velocity of aluminium particles 224.0 (diameter 120µm) inside the carrier gas channel – mean: solid line – minimum: light dashed line – maximum: dark dashed line – quartiles: colored region

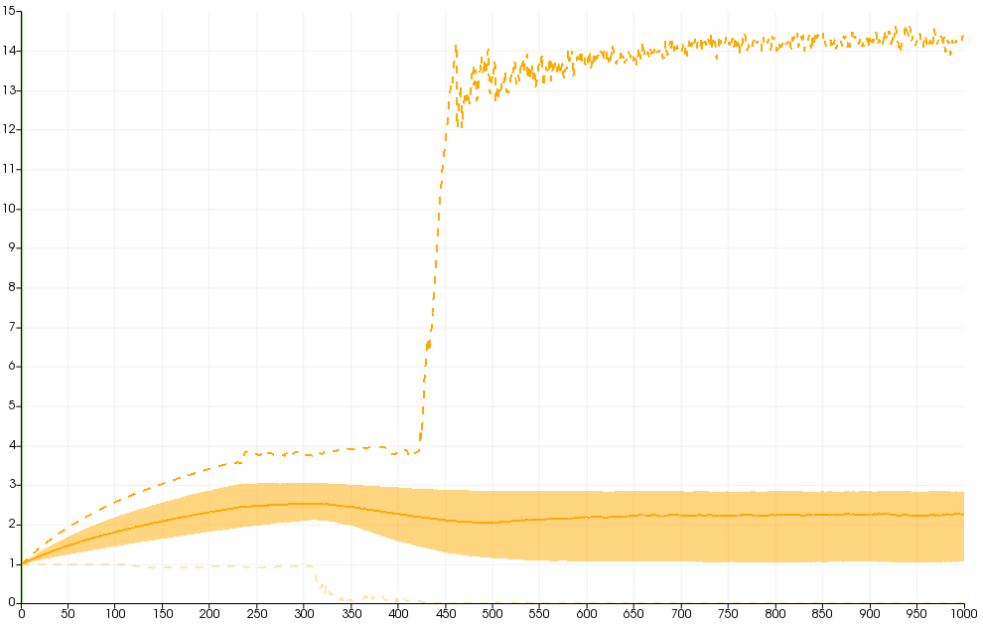

Figure 3.44: Time-variation of the velocity of aluminium particles Al12Si-A (diameter 65µm) inside the carrier gas channel – mean: solid line – minimum: light dashed line – maximum: dark dashed line – quartiles: colored

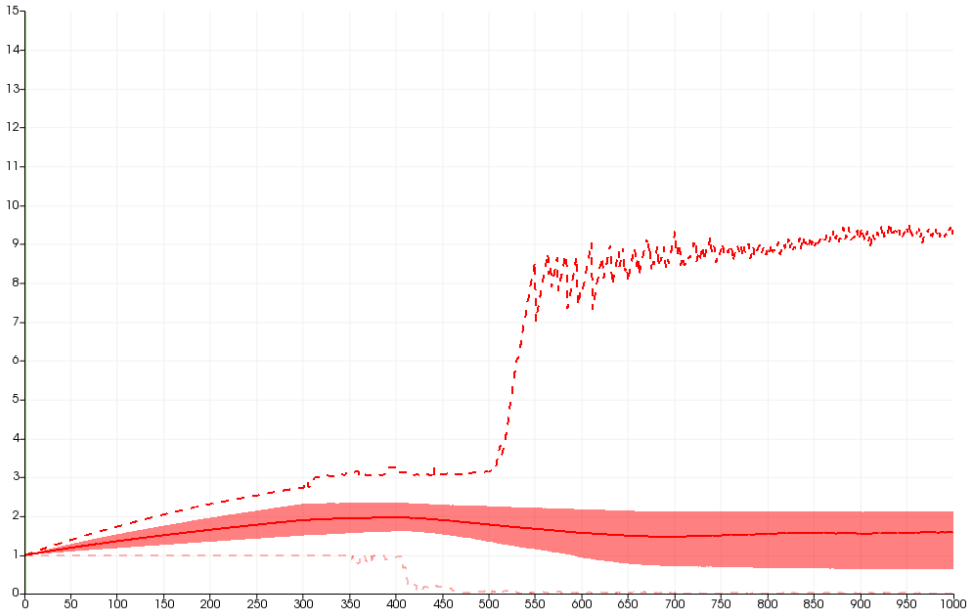

Figure 3.45: Time-variation of the velocity of stainless steel particles 316L (diameter 65µm) inside the carrier gas channel – mean: solid line – minimum: light dashed line – maximum: dark dashed line –

The actual particle adhesion against the nozzle wall is not actually well captured by the current simulation despite the inclusion of vdW forces. This can stem from several causes, starting with the vdW force model that is based on the Rumpf model (Rumpf 1990), which has been shown to underpredict vdW forces and moreover is based on the value of asperity size, which is not usually known or easily measurable experimentally (Rabinovich et al. 2000a; b). In addition, the contribution of capillary forces is not accounted for, and neither are the triboelectric charging effect and the potential attractive electrostatic forces that it may generate. These forces are longer range than both vdW and capillary forces, and could promote the attraction of particles towards the walls, while in the shorter range, the vdW, capillary and mechanical interlocking forces are most likely responsible for the adhesion. Moreover, the accumulation effect inside the nozzle may require longer simulation time, which was here limited to 0.1s to keep computational time reasonable.

To evaluate the sensitivity of the particle flow to adhesion forces, a similar CFD-DEM simulation can be run with the Hamaker constant being artificially increased ten-fold to a value of 3000 zJ, as shown in figure 3.46. This can be justified by the inaccuracy of the Rumpf model and the uncertainty in *rms* roughness parameters. It can also compensate for other adhesion forces (capillary, mechanical interlocking) that are potentially at play but are not currently modeled in the MFiX 18.1.5 software. After a simulation time of only 0.1s, there is a large accumulation of aluminium particles at the entrance of the buffer region and against the walls of the buffer region due to the strong vdW interactions. This can be compared with the results for a more usual value of 30 zJ shown in figure 3.47, in which there is hardly any adhesion of particles to the nozzle walls. The particle behavior is thus rather sensitive to

adhesion forces as an order of magnitude increase in the Hamaker constant gives rise to strong wall adhesion and particle accumulation. The particle exit velocity is then around 7 m/s, which is very close to the mean experimental value, whereas it is about 10 m/s with the normal value for the Hamaker constant. This suggests that there is also significant particles interactions inside the nozzle exit channel due to the adhesion phenomenon that diminishes the acceleration of individual particles.

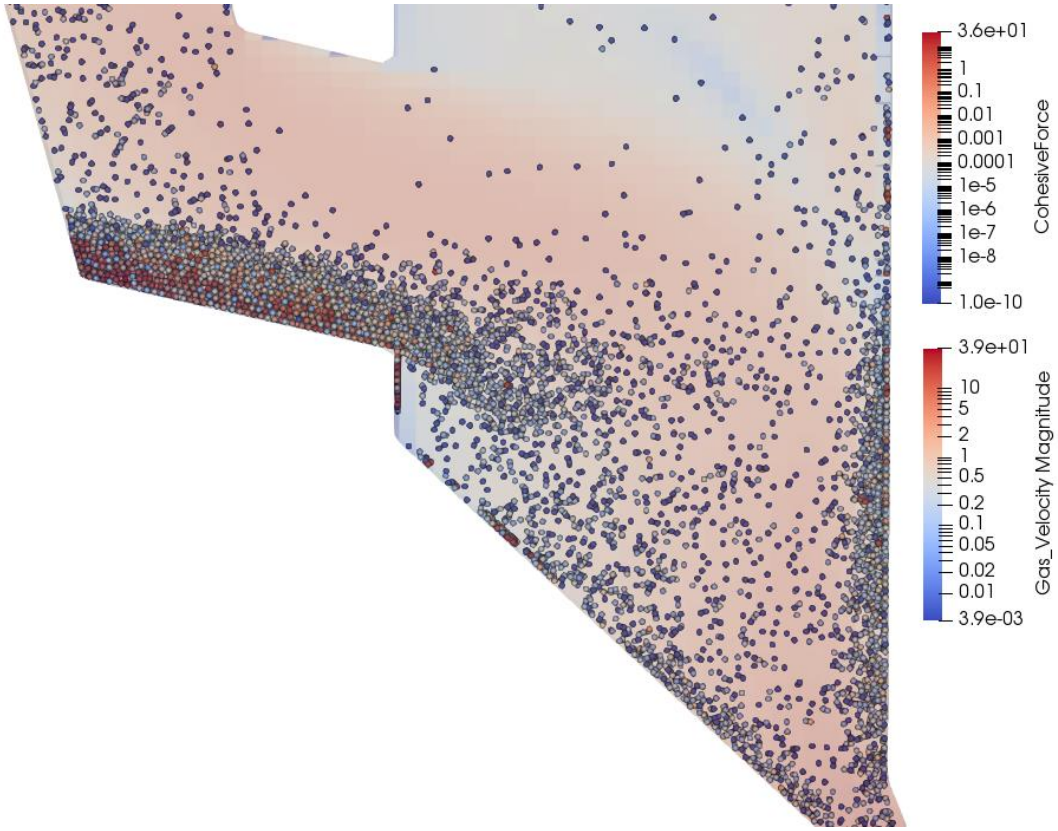

Figure 3.46: Aluminium particle flow in the buffer region with Hamaker constant artificially increased to 3000 zJ (simulation time = 0.1s)

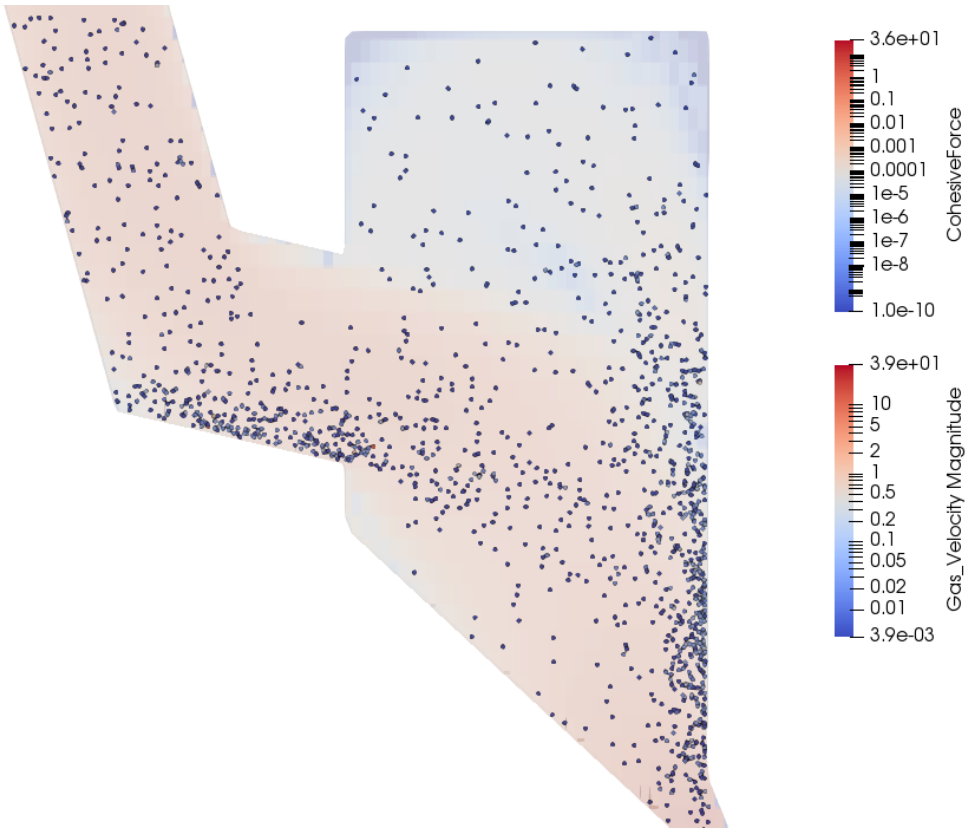

Figure 3.47: Aluminium particle flow in the buffer region with Hamaker constant set at 300 zJ (simulation time = 0.1s)

c. Powder Jet at the Nozzle Outlet

The geometry of the powder jet and the particle velocity at the nozzle outlet are also quantities of interest that require the particle/gas flow both inside and outside the nozzle to be simulated for a more accurate estimate, including the simplified shape/center gas channel. The computational time is significantly increased due to the larger domain size (400x400 cells, including full, cut and blocked cells). The same particle and fluid inlet velocities as in the previous simulations are applied for the two carrier gas channels. The shape+center gas channel, merged into a single straight pipe for simplicity and reduced computational load, is set to have an inlet gas velocity of 61 m/s, which was crudely estimated based on mass conservation and a combined inlet volume flowrate of 6.5 L/min. The bottom surface is set as a no-slip wall at a 6mm standoff distance from the nozzle outlet to simulate the presence of a substrate. Atmospheric pressure outflow boundary conditions are applied on the far left and right sides of the domain.

It would be typical to take advantage of the symmetry of the geometry to reduce the size of the simulated domain. However, there is some randomness in the particle input as the

particles are generated automatically by the MFiX code, so that the particle trajectories are slightly different between the two carrier gas channels. It is thus pertinent to simulate both carrier gas channels to provide an instantaneous comparison of the variability in particle behavior that can be expected inside the nozzle and to more realistically emulate the powder jet outside the nozzle.

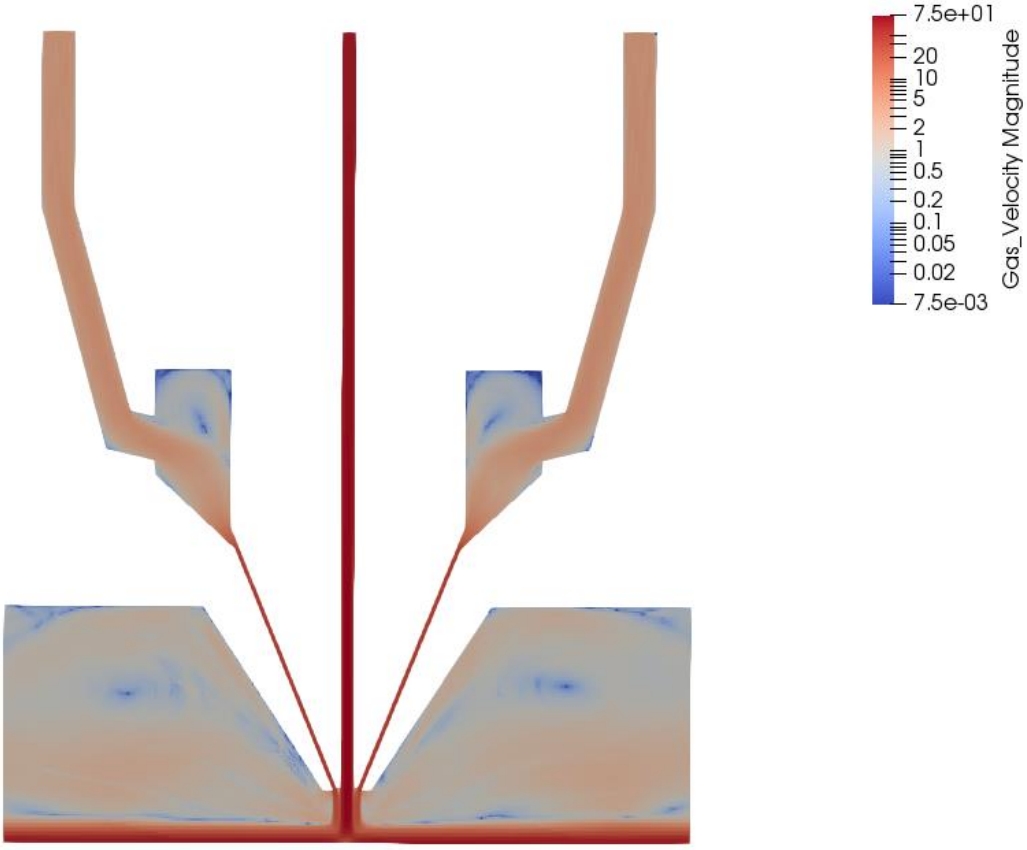

Figure 3.48: Gas velocity in 2.5D LMD nozzle geometry

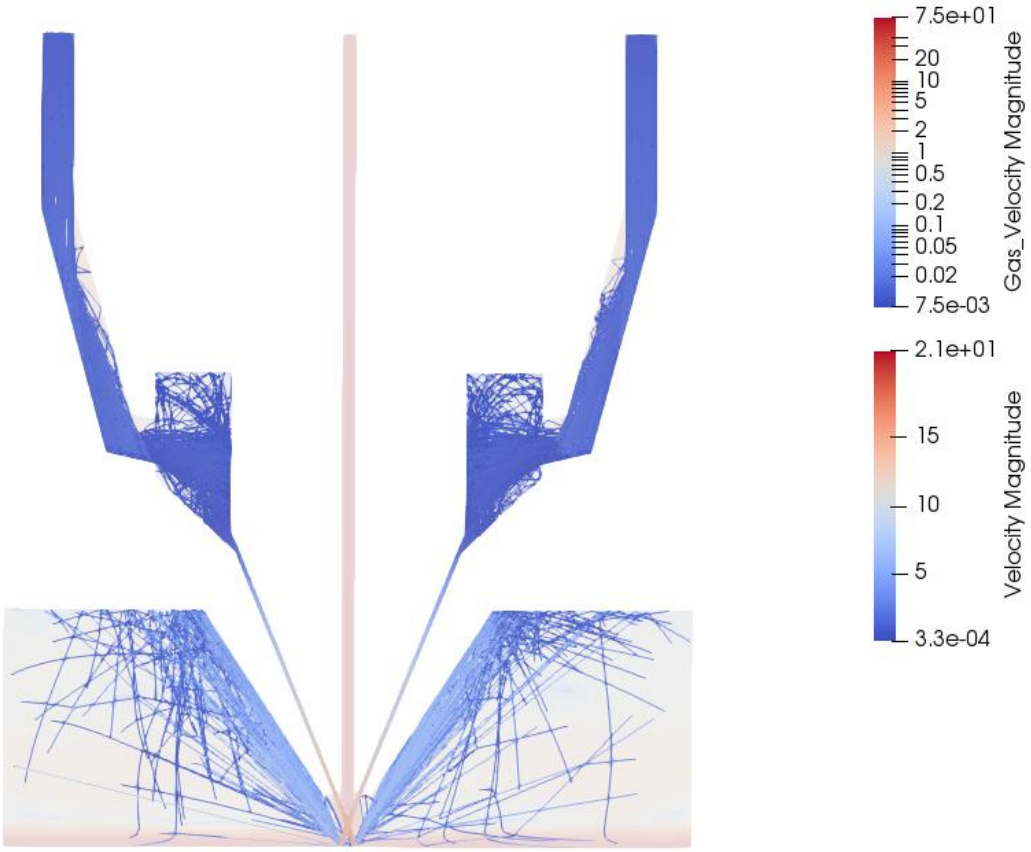

Figure 3.49: Flow of 120µm aluminium particles in 2.5D LMD nozzle geometry (gas phase is rendered semi-transparent for clarity)

The gas velocity field is shown in figure 3.48 and the particle trajectories are displayed in figure 3.49. A focus on the nozzle outlet is available in figure 3.50, showing the spread of the powder jet and the particle acceleration at the nozzle outlet due to the shape+central gas flow. The powder jet focal plane is measured to be located 3.48mm from the nozzle outlet, which corresponds to the design specification of the nozzle. The maximum particle velocity at the nozzle outlet is significantly higher (about 20 m/s) than in the previous simulations where the domain was limited to the carrier gas channel. This is due in part to the difference in the location of the pressure outflow boundaries, set further away from the nozzle outlet in the full 2.5D nozzle geometry. It also shows that the simulation can capture the acceleration of the particles at the nozzle outlet due to the shape+central gas channel, although this effect is not very significant in this case.

To evaluate the influence of the shape+central gas channel velocity, the inlet velocity is doubled to a value of 122 m/s. The Hamaker constant is also increased ten-fold as done previously. Other boundary conditions are not modified. The focal plane of the powder particles is then slightly displaced downwards by a value of 3.64mm. The maximum particle velocity is slightly lower however, possibly due to the increase in adhesion that diminishes the acceleration of particles in the nozzle exit channel.

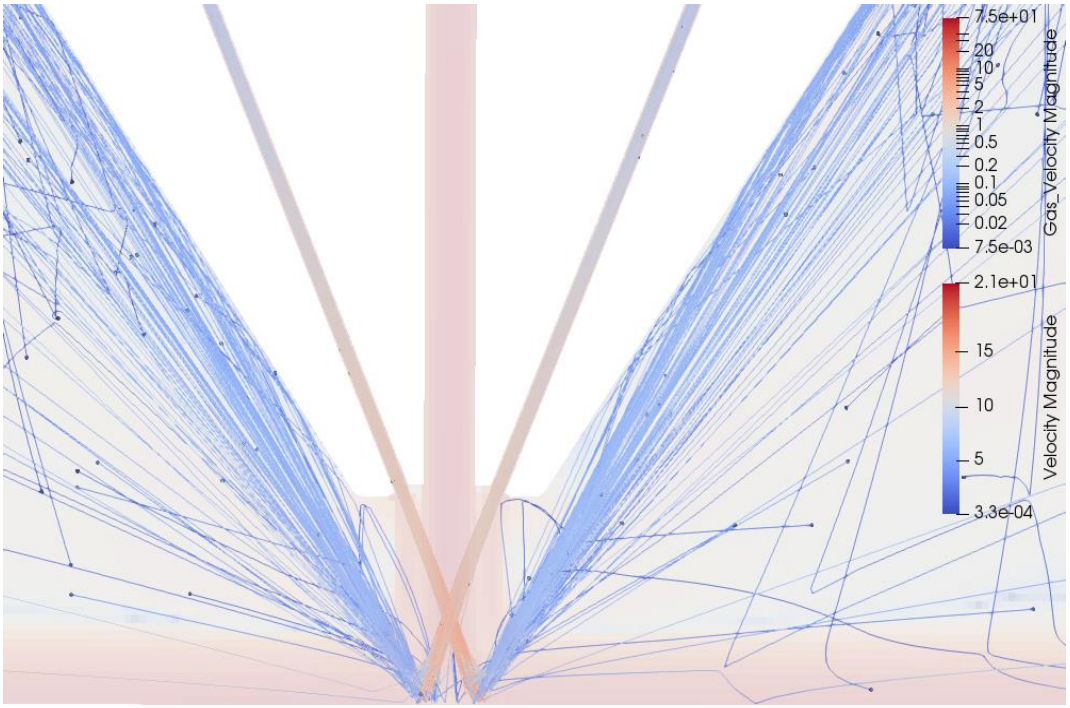

Figure 3.50: Flow of 120µm aluminium particles at the nozzle outlet

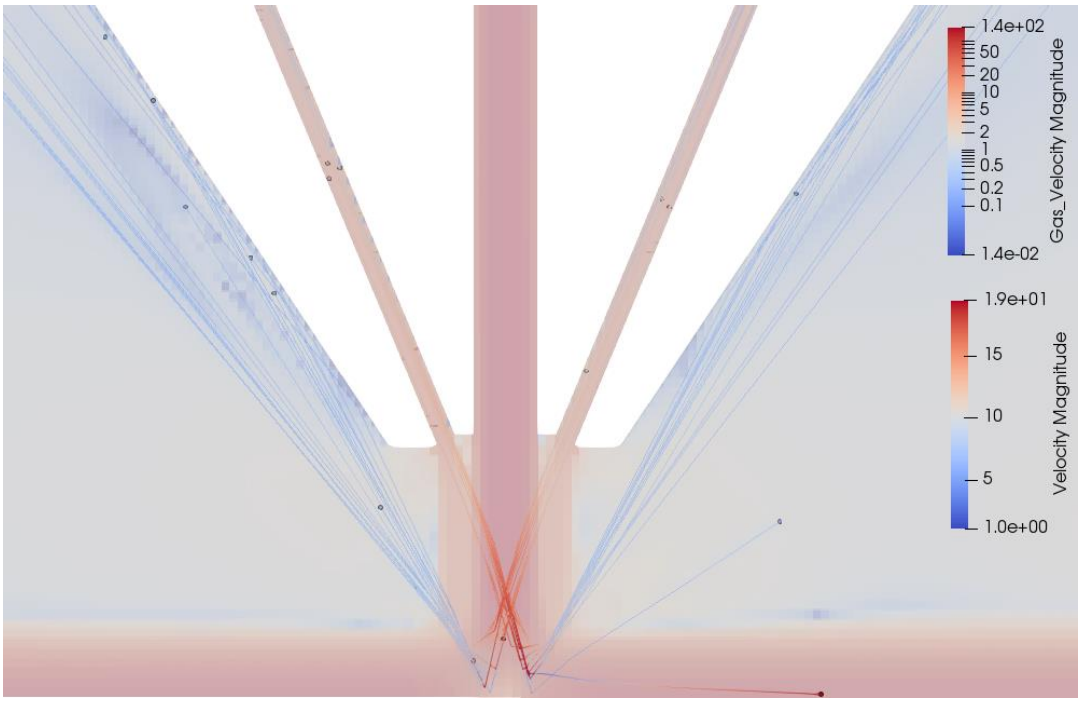

Figure 3.51: Flow of 120µm aluminium particles at the nozzle outlet with increased shape+central gas velocity

In future work, the CFD-DEM code could be modified to include a more accurate vdW force model based on *rms* roughness values (LaMarche et al. 2017; Liu et al. 2016a) as well as a capillary bridge force model (LaMarche et al. 2016) in an attempt to better capture the adhesion of aluminium particles to the copper walls. Indeed, the particle behavior is very sensitive to the magnitude of the vdW forces, which shows that accounting for other adhesion effects (e.g. capillary bridges, mechanical interlocking) could help explain the particle accumulation in the buffer region. There is also generally a significant uncertainty in the CFD-DEM parameters due to lack of experimental data for metal AM powders, so that a full sensitivity analysis would be required to validate the results, at least in qualitative terms.

A grid convergence study should be also conducted to determine the dependency of the results on the mesh size. The Cartesian mesh could also be refined near the symmetry axis of the 2.5D geometry at the nozzle outlet to better capture the particle acceleration induced by the momentum from the shape+central gas flow, and the sensitivity to boundary conditions (e.g. inlet gas and particle velocity) should be explored further to better capture the experimentally observed variation in particle velocity with the material and particle size. The effect of turbulence was also not considered, which can be justified inside the nozzle as noted previously but does not hold outside of the nozzle. Moreover, carrying out the simulation on a 3D domain based on the full geometrical model of the nozzle would unveil a more complete view of the particle flow behavior inside the nozzle, such as the lateral motion of the particles around the annular buffer region. However, these possible improvements are currently prohibitively expensive computationally.

Another limitation of the current model is that it only considers monosized spherical particles, whereas in practice the particle diameters are log-normally distributed, which should induce variations in particle velocity and promote interparticle cohesion. The sphericity assumption could be appropriate for gas atomized metal AM powders of good quality (e.g. without satellites or agglomerates), however this is not quite the case of the cohesive aluminium powder under study. A modification of the code could be made to include non-sphericity effects in gas-particle interactions but the mechanical interlocking forces resulting from particle-particle interactions would still not be captured.

Even with these limitation, the CFD-DEM results still provide valuable insight into the particle flow behavior inside the nozzle, which cannot be observed directly, as well as outside the nozzle. These results notably suggest that the so-called buffer region or homogenization chamber is indeed a zone of particle recirculation with reduced average particle and gas velocity. Moreover, the rebound pattern of the particles entering the buffer region promotes this recirculation effect, which is seen as detrimental in the case of cohesive aluminium powder particles as it increases the likelihood of wall adhesion and thus particle

accumulation inside this region. Excessive particle accumulation may also occur at the entrance of the buffer region if adhesion forces are sufficiently large.

These considerations suggest that a modification of the buffer region could partially avoid these accumulation effects for cohesive aluminium powders, which calls for a design modification of the outer and intermediate nozzle cones that define the buffer region geometry.

III. LMD Nozzle optimization

As previously seen from experiments and numerical simulations, the cohesiveness of aluminium powders can lead to their accumulation inside the carrier gas channel. Moreover, the LMD deposition under study is design to have a working distance on the order of 5mm, which is fairly low for repair applications as it requires the LMD head to be close to the defective surface, and thus interfere with the rest of the part and prevent safe access to the region of interest.

While the inlet direction of the particles before entering the buffer region cannot be modified without redesigning the entire head, the nozzle cones however can be easily replaced. So the adversarial rebound pattern cannot be suppressed but the recirculation effect can be prevented with an adequate redesign of the outer and intermediate nozzle to provide a more favorable rebound pattern against the walls of the buffer region. Additionally, the width and angle of the annular nozzle outlet can be modified as well to increase the standoff distance of the LMD head and thereby generally provide easier access for part repairs.

The new design is made to provide a downward rebound of the particles hitting the outer wall of the intermediate nozzle cone after entering the buffer region. The inner wall of the outer cone are more inclined to minimize particle adhesion. In addition, the top edge of the outer cone is made thicker to make the copper cone less fragile. The outlet channel is also made slightly wider to allow safe passage of the cohesive particles, and annular outlet diameter is also increased to make the standoff distance larger. A major advantage of this new design is that it only affects the cone geometry. Thus it does not require a full redesign of the LMD head but rather only of the nozzle cones, which are by design interchangeable on the LMD head.

A CFD-DEM simulation of this new design is run in the same nominal conditions used previously, i.e. with a shape+central gas channel velocity of 61 m/s. The gas velocity field at the nozzle outlet is displayed figure 3.52. The focal plane of the powder jet is approximately doubled to a value of 7.01mm compared to the original design. The travel path of the particles is longer so that the deviation of the particle trajectories due to the shape+central gas channel

flow is more clearly visible. The standoff distance is successfully increased while retaining a converging powder jet geometry. The vortex formation and the recirculation of particle is also avoided, and most of the particles rebound directly downward upon hitting the intermediate nozzle wall so that they are guided towards the nozzle outlet, although some particles are occasionally propelled backwards towards the inlet pipe due to an adversarial rebound against the intermediate cone. In future work, this new nozzle design should be tested experimentally to assess whether the accumulation effect is indeed partially or completely suppressed.

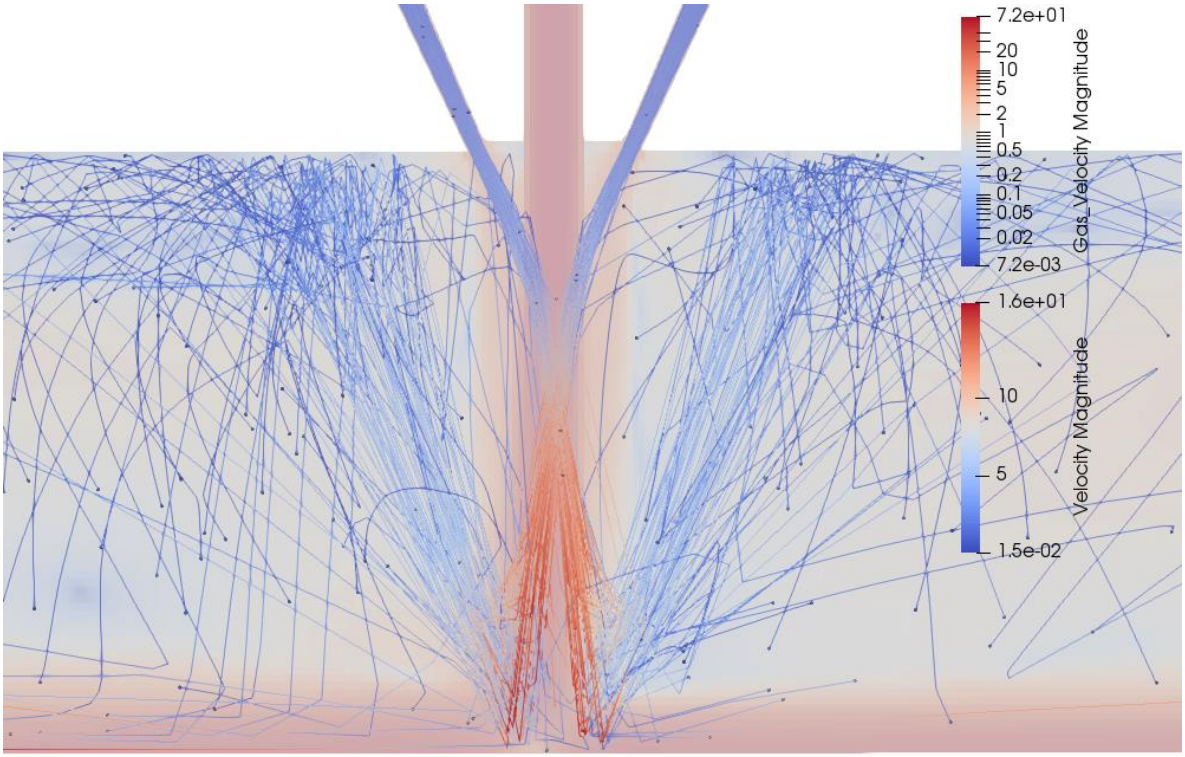

Figure 3.52: Particle trajectories at the outlet of the new nozzle cone design

IV. Summary

This chapter first presented two methods for assessing the powder jet at the nozzle outlet. The first method was based on images captured at a low shutter speed and a low resolution, for which an image segmentation code was developed to evaluate the powder jet angle and its time variations. It resulted that the shape gas flowrate was the most significant factor, while no granulometry effect was noted. The variability of the cone geometry with aluminium powders is however naturally fairly large according to the segmentation results. The second method relied on images taken at a much higher framerate to capture individual particles. The resolution was however quite poor due to experimental constraints, yet adequate image pre-processing enabled the particle tracking algorithm to identify single particles so that particle velocities could be evaluated. Despite significant variation in particle velocities along and between tracks, it was concluded that lighter and larger particles such as 224.0-A 100-125µm flowed faster than smaller, heavier particles such as 316L.

A 2.5D CFD-DEM simulation on a supercomputer of LMD gas-particle flow was pursued to assess the behavior of particles inside the nozzle, where direct observations cannot be performed. It was noted that the buffer region induced a recirculation of particles that can be detrimental with cohesive powders as it can lead to their accumulation inside the nozzle. A new design of the outer and intermediate cones was proposed, and CFD-DEM simulations suggested that a more favorable particle rebound and a suppression of the recirculation phenomenon can be obtained by removing the buffer region. The standoff distance could also be increased to provide better clearance for the LMD head during deposition and thus potentially diminish accessibility constraints often encountered during LMD repairs.

Chapter IV: Repair methodology for the Laser Metal Deposition process

Abstract

This chapter first presents the experimental setup for performing repairs of premium Al-Cu castings with the LMD process. A repair methodology is then presented in an effort to increase the automation level of the repair operation. As part of this repair methodology, a repair volume segmentation algorithm, here called InterSAC, is introduced and its implementation shown in details along with a few case studies.

I. Repair Methodology

a. Introduction

Defects frequently arise from the lost wax casting process of premium high-strength 224.0 alloys. In addition to defects commonly found in castings, such as porosities, blowholes, pinholes and inclusions, defects such as segregations and hot cracks are particularly prevalent with this type of alloy.

The Maintenance, Repair and Overhaul (MRO) industry has traditionally used welding processes such as Gas-Tungsten Arc Welding (GTAW) to perform surface repairs on aluminium castings. However, welding processes are usually operated manually, so that the results highly depend upon human skill and performance. In addition, welding processes like GTAW typically induce high residual stresses, large thermal deformations and a large Heat Affected Zone (HAZ) due to the high amount of heat transferred to the repair area, and substrate bonding can be relatively weak due to shallow penetration (Pinkerton et al. 2008; Piya et al. 2011; Sexton et al. 2002; Wilson et al. 2014). Using such welding processes for repair operations therefore limits the range of materials that can be used for consist repairs, excluding for instance low-weldability alloys such as cast alloy 224.0 and most Al-Cu alloys besides 2219. Indeed, as previously exposed, traditional repairs of 224.0 premium high-strength castings performed with the GTAW process lead to a relatively high failure rate, on the order of 20 to 30% for defects larger than 10mm, due to hot cracking, porosities and segregations in the welded zone (Dumant 1996). When welding repairs are not successful, the part must be melted and entirely recast despite the limited castability of alloy 224.0 so as to hopefully better meet the stringent specifications of aeronautical parts.

In order to improve the repair process success rate and thus limit the need for recasting entire parts when a successful repairs could salvage them for industrial use, it is proposed to use LMD instead of a welding process to perform surface repairs on metallic parts such as aluminium castings. This process presents several advantages over conventional welding processes: higher precision, limited and controllable heat input, and propensity to automation as the toolpaths are programmed in machine code (Pinkerton et al. 2008). The rapid solidification conditions provided by LMD should yield a refined microstructure, less solute segregation and a diminished sensitivity to hot cracking.

A basic scenario for the repair and remanufacture of a premium high-strength casting could be summarized as follows. A foundry manufactures a premium aluminium casting with limited castability and a high propensity to near-surface defects such as segregations, hot cracks, or porosities. The casting is controlled by either destructive or non-destructive

inspection techniques (radiography, tomography, die penetrant inspection etc.). When a potentially harmful defect is identified by an operator, a repair operation can be considered depending on the accessibility, size and criticality of the defect. If a repair is not deemed possible, the part is entirely scraped and recycled, i.e. the part is remelted and recast to hopefully yield a better outcome and meet design specifications. Because aluminium can easily be recycled through direct remelting, the repair operation currently only makes sense in economic terms for premium, high-value, high performance castings that are difficult to cast.

When a surface (or near-surface) defect appears to be repairable, the faulty region is manually machined out with a ball nose end mill to remove the material while limiting the occurrence of sharp corners, which are usually detrimental to the welding process.

With low-castability, low-weldability alloys such as 224.0, an improvement in the repair process could reduce the need for recasting entire parts, thereby saving up on the cost associated with the casting process (energy consumption, cost of human labor etc.). Thus, instead of performing the repair operation with a GTAW process, the repair can be carried out by a LMD additive manufacturing process, possibly in-house or at a subcontractor's facilities. Indeed, as LMD machines are still rather costly at the present time, it may not quite make sense yet for a foundry to invest in such AM equipment if only to perform modest amounts of repairs. However, a subcontractor could take charge of the repair activity of multiple foundries and part manufacturers in general, possibly also adding remanufacturing capabilities to add features that are unfeasible to manufacture with current manufacturing techniques. At scale, and with the appropriate expertise, such an investment in AM repair and remanufacturing technology could possibly be profitable. In that scenario, the foundry would send the defective part for repair once the defect(s) has been located and machined out. The LMD process is then used to deposit material inside the carved out cavities to recover the geometry and the mechanical properties of the design-specified part, possibly after some surface finish and heat treatment operations. Typically, the deposited material is of the same chemical composition as the base material of the defective part.

In a variant, the part to be repaired was manufactured satisfactorily but has experienced some damage or wear during operation. If the part is to be reused quickly, an onsite repair may be performed, for example by aircraft maintenance crews in the case of aeronautical parts, to make the part usable again. In this scenario, standard repair process could also possibly be replaced by the LMD process, and the repair could be performed directly onsite if a portable LMD system is used, or for example at a specialized subcontractor's facilities.

In both AM repair scenarii, the local surface (or near-surface) defects are machined out, usually with a portable hand tool, prior to being sent or setup for LMD repair.

To trigger the advent of LMD as a repair process, it is desirable to make the LMD repair operation as reliable and efficient as possible. In addition to using suitable parameters for a given material and powder feedstock, the LMD repair operation should also involve as little human intervention as possible by providing some level of automation, particularly for defining the toolpaths of the LMD nozzle. As the LMD process is numerically-controlled, the toolpaths must in the end be translated into machine code through the use of appropriate Computer-Aided Manufacturing (CAM) software.

When the defective part is mounted inside the LMD workspace, no precise information is available to the LMD system for locating the cavities and defining the geometry of the deposit that will fill those cavities to recover the geometry and properties of the part. If CAD data is available, it is usually a nominal, design-specified geometry generated prior to manufacturing that may not precisely fit the actual part dimensions. This is especially true with aluminium alloy castings as significant amounts of deformations can be expected upon cooling, notably because of the relatively high thermal expansion coefficient of aluminium alloys. Moreover, the part is typically manually mounted inside the working space of the LMD system, so that the exact location and orientation of the part, and thus of the defect, with respect to the machine reference frame is not known a priori.

The literature on repairs with AM processes such as LMD has so far been mostly focused on the materials and process parameters. For instance, (Pinkerton et al. 2008) focuses on repairing slots with H13 steel and statistically analyzing the material and mechanical performance of the deposit, whereas (Graf et al. 2012) studied the refill of grooves by LMD with stainless steel and a titanium alloy, and (Petrat et al. 2016) researched process parameters and rebuild strategies for repairing a gas turbine burner with Inconel 718. Also, (Pinkerton 2010) reviewed the theory and some applications of LMD, including case studies of industrial repairs.

The literature is scarcer regarding the automation of the repair process, whether it be with the LMD process (Gao et al. 2006, 2008; Piya et al. 2011; Wilson et al. 2014), welding processes or CNC machining (Bremer 2005; Yilmaz et al. 2010).

Many methods rely on a CAD model for reconstructing the repair volume. Typically, the repair volume of a defective part can be recovered by comparing its nominal CAD model to range data (Bremer 2005; Jones et al. 2012; Quinsat et al. 2017; Um et al. 2017; Zhang et al. 2015). However, such nominal CAD models may be unavailable due to confidentiality issues, or might be too inaccurate to be relied upon, as is usually the case for aluminium alloy castings (Gao et al. 2006, 2008; Yilmaz et al. 2010). Moreover, for localized surface repairs, the knowledge of the entire geometry of the part is usually unnecessary as only local geometrical data is really necessary to perform the repair.

Some studies have therefore been focused on non-CAD-based automated repairs, usually for specific types of part such as turbine blades, whose overall geometry and function is known a priori. In such cases, a 3D range scanning step is involved in order to detect the defective area, reconstruct the repair volume and then generate appropriate scan paths trajectories. Methods used in those studies, reviewed in (Wu et al. 2013), include polygonal modelling and surface fitting (Gao et al. 2005, 2006), piecewise Hermite interpolation with linear compensation (Chen et al. 2009), surface extension with cross-section curves (CSC) (Gao et al. 2008), sweeping CSC (Yilmaz et al. 2010), and Prominent Cross-Section with CSC lofting and Boolean operations (Piya et al. 2011; Tao et al. 2015; Wilson et al. 2014). Those methods are however limited to blade-like parts whose shape and function are known a priori. They necessitate a significant amount of user intervention, not only for pre-processing the range data from the 3D laser scanner that typically contains measurement errors and artefacts, but also for reconstructing the digital model of the repair volume, which often requires the use of commercial CAD/CAM software packages (Gao et al. 2006, 2008; Piya et al. 2011; Wilson et al. 2014; Wu et al. 2013; Yilmaz et al. 2010). Another approach relying on a random walk algorithm allows to segment cavities of arbitrary shape based on raw range data without relying on a CAD model (Hitchcox and Zhao 2018). However this method is not robust to measurement artefacts such as spurious peaks and deformed edges as it does not rely on a priori information regarding the actual shape of the cavity.

With the above considerations, it appears necessary to devise a robust method to automatically identify the geometry of the defective region within the LMD workspace, without relying on CAD data and despite measurement errors in the geometrical data provided by the range scanner, so as to subsequently generate the corresponding toolpaths and perform the repair with LMD.

b. Overview of DED Repair Method with the InterSAC algorithm

A surface repair process generally involves the following steps:

1. Detection of a defect
2. Rough machining of the defect area
3. Repair of the machined cavity
4. Finishing operations

Step 1 may for example consist in visual inspection or imaging techniques (X-rays). Step 2 serves to prepare to area to be repaired by machining out the surface defect into a surface cavity. Step 3 corresponds to the actual deposit of material in the cavity using a DED process such as LMD. Step 4 includes any post-deposition treatments (chemical, heat…) and final surface machining operations.

The primary goal of the proposed repair method, represented in figure 4.53, and its InterSAC (Intersection SAmple Consensus) segmentation algorithm (Hascoët et al. 2018a; Touzé et al. 2018), is to link step 2 to step 3 by enabling the construction of a CAD model of the repair volume based on the raw geometrical data of the surface cavity and its neighborhood as provided by a range scanner (i.e. without pre-processing besides cropping the dataset to the region of interest), and thus without relying on the CAD model of the entire part. This digital model is then used to generate scan paths for the refill of the cavity by LMD or other DED processes. A secondary goal of InterSAC is to assist step 4 by providing a surface along which the final machining may be performed.

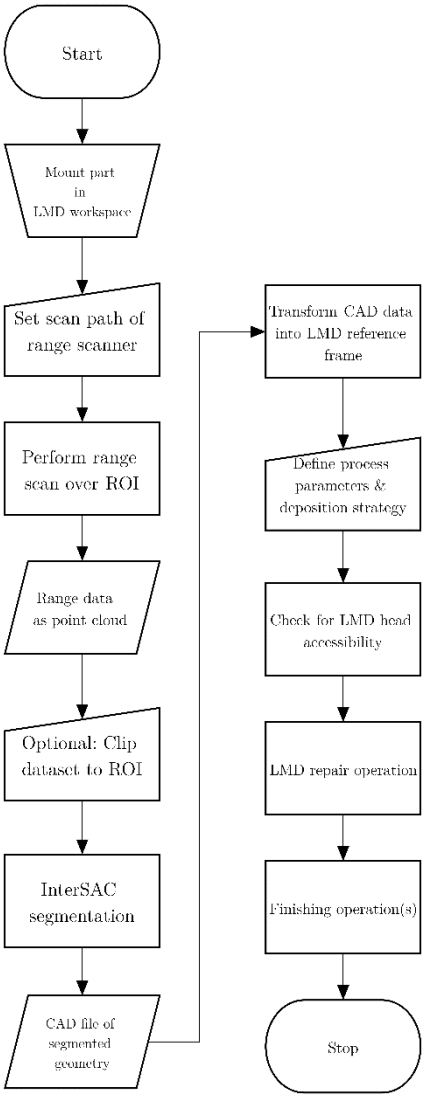

Figure 4.53: Flowchart of repair process

In the case of a purely additive manufacturing repair process, as shown in figure 4.53, the part is first placed inside a conventional machining center and the defect is manually milled into a cavity of appropriate shape (i.e. primitive shape such as a sphere, cylinder, cone…) using a manually generated toolpath and an appropriate milling tool (e.g. ball nose mill). The part is then moved into an LMD machine by a human operator for the repair operation. The location of the cavity on the part's surface in the LMD machine reference frame is typically not known with precision at this stage.

A laser range profilometer is directly mounted on the LMD projection head in order to provide the necessary local geometrical data to digitally reconstruct the repair volume and subsequently perform the LMD repair operation. The fixed transformation between the laser scanner and LMD nozzle reference frames can then be determined and used in all repair operations performed with that experimental setup. The human operator mounting the part in the LMD workspace orients the part in such a way that the cavity can be accessed by the LMD projection head and the range scanner. The range scan is then performed on the cavity region based on a scan trajectory and speed determined by the operator.

The envelope of the repair volume corresponding to the surface cavity within the range dataset is formed by the bottom surface of the cavity and a top surface (figure 4.54) whose shape corresponds to that of the surface surrounding the cavity (a.k.a. the "neighbouring surface"), i.e. the local shape of the part in the vicinity of the defect area. When this repair volume is correctly refilled, the local geometry of the part can be recovered.

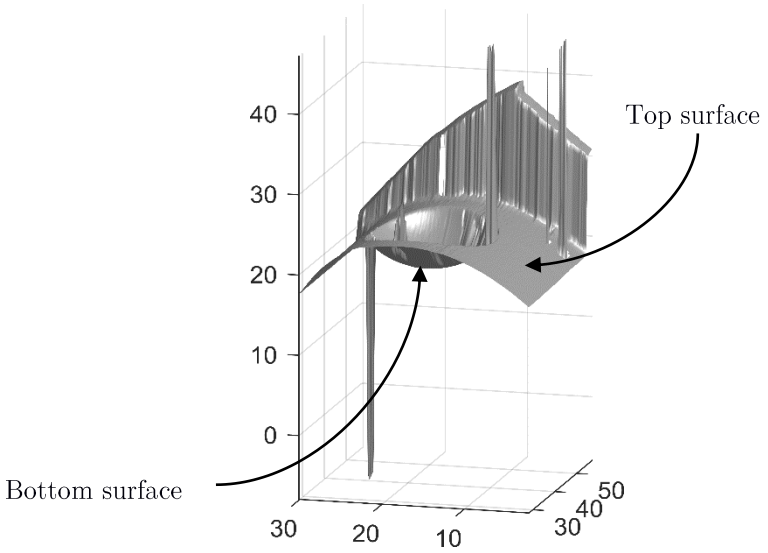

Figure 4.54: Range data of a cavity on a reflective surface showing the bottom and top surfaces and spurious peaks due to the reflectivity of the surface and the concavity of the geometry

II. Experimental Setup

a. Hybrid Laser Metal Deposition system

The Laser Metal Deposition manufacturing center used in the present work (see figure 4.55) is the MultiCLAD LF4000 machine located in the Rapid Manufacturing Platform of Ecole Centrale de Nantes (France). It is a prototype hybrid manufacturing machine with both subtractive and additive manufacturing capabilities as it is equipped with a machining spindle and two LMD heads.

Figure 4.55: MultiCLAD LF4000 hybrid LMD manufacturing center

The numerically-controlled manufacturing center is a Huron K2X8 (5-axis) milling machine with high axis rigidity and precision. The mounting table has 1 translation (Y-axis) and 2 rotational degrees degree of freedom. The carriage bearing the machining spindle and LMD heads has 2 translational degrees of freedom (X- and Z-axis), allowing 5-axis subtractive and additive manufacturing.

The Laser Metal Deposition head is composed of optical and focus heads from HIGHYAG with a focusing length of 460mm, at the end of which is mounted a coaxial powder projection nozzle. The laser power source IPG YLS-2000 is a 2kW Nd:YAG (1070nm) laser linked to the focus head via a fiber with a diameter of 600µm.

The powder projection nozzle is based on a patented design by IREPA LASER (EP0574580, US5418350). It is an assembly of 3 cones (outer, intermediate and inner cone) mounted coaxially to define 3 separate flow channels inside the nozzle. A central gas flow travels through the inner cone, i.e. the inner flow channel, along the laser beam, mainly to

prevent particles from travelling back up the central gas flow channel. A carrier gas flow brings the powder particles from the reservoir to the nozzle outlet by travelling in-between the outer and intermediate cones, i.e. in the outer flow channel. A shape gas flow runs between the intermediate and inner cones, i.e. in the intermediate flow channel, to shape the powder jet at the nozzle outlet so that it will take the form of a hollow cone with its tip located at or near the focus plane of the laser beam. The cones are made of copper and the nozzle is actively cooled so as to ensure proper heat dissipation and thus preserve the nozzle from getting deformed or damaged. The inert gas used in the present work is pure Argon.

The MEDICOAT powder distribution system comes with powder reservoirs and a distribution unit that provides control over the volumetric flowrate of the powder particles. The reservoir is a chamber containing a mechanical mixer to facilitate the powder flow, as well as an inverted cone at the bottom outlet which serves to limit the influence of powder quantity inside the reservoir on the gravitational flow of powder from the reservoir towards the distribution unit. The latter is located directly beneath the outlet of the reservoir and contains a rotating distribution disk that carries the powder from the reservoir outlet toward the distribution unit outlet where the powder is mixed with the carrier gas to form a gas/powder flow, and is then carried through the pneumatic transport system. A top plate is placed on the distribution disk to guide the powder particles towards the outlet of the distribution unit. The pneumatic piping system includes pipes made of an anti-static polymer to limit the buildup of electrostatic charges and thus avoid the formation of particle agglomerates due to electrostatic effects.

b. Laser Scanner

A laser profilometer Keyence LJ-V7200, shown in figure 4.56, is used as a range scanner to provide in-situ, local geometrical information on the defective part. The profilometer is rigidly mounted on the carriage bearing the LMD head, so that the position of the scanner is fixed with respect to the LMD nozzle. By a change of reference frame, geometrical information from the scanner can be directly used for generating toolpaths for the LMD nozzle. The trajectory of the scanner can thus also conveniently be defined through machine code as it is fastened to the carriage and can freely follow its movements.

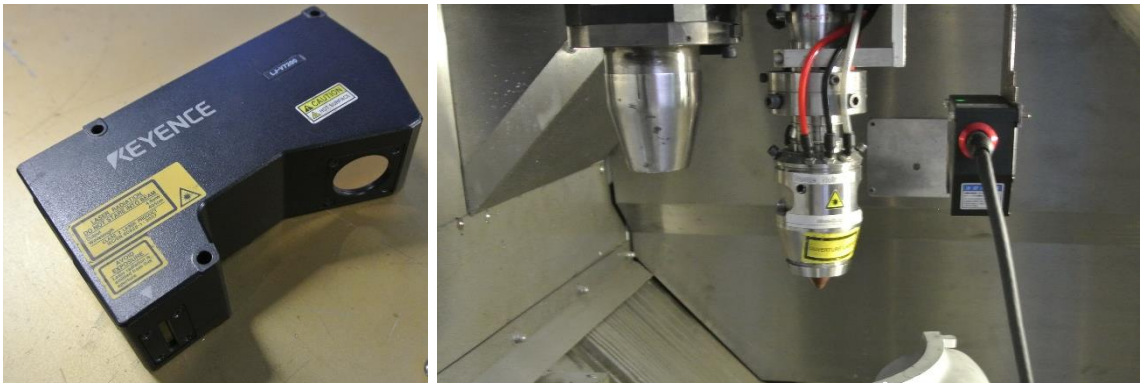

Figure 4.56: Laser profilometer (left) - LMD / Laser profilometer setup

The laser profilometer used in the present work is traditionally used for direct dimensional control of small parts such as electronic components. A scanline consisting of 800 laser dots sweeps over the geometry to yield a range measurements with a repeatability of 1µm in the vertical direction and 20µm in the horizontal direction. The acquisition is performed in loop mode where the range measurements are performed at discrete time intervals during the scanning sweep.

The range measurement is based on a triangulation principle, where the laser signal from the emitter bounces on the surface and its reflections are registered onto a Charge-Coupled Device (CCD). From the position of the major reflection on the CCD with respect to the location of the emitter can be deduced the distance covered between the emitter and the surface. Each of the 800 laser beams of the laser scanline are analyzed in this way to give a discrete range profile of the geometry across the scanline at a particular point in time. In loop mode, the timestamps of each range measurements are used conjointly with the sweep trajectory to reconstruct the geometry scanned during a sweep of the profilometer. For simplicity in defining the sweep trajectory and reconstructing the geometry, a linear sweep at constant speed is typically performed whenever possible. The sweep velocity should sufficiently low with respect to the acquisition frequency so that there is no significant aliasing in the reconstructed geometry and no crucial details are missed. The acquisition frequency being comprised between 20Hz and 40Hz based on observations, a constant sweep velocity of 200mm/min yields a measurement every 83 to 167µm, which for our purposes offers a suitable compromise between scanning speed and geometrical accuracy.

In the specific application of surface repairs on aluminium parts, where the geometry of the defective zone is to be measured by the range scanner to generate LMD toolpaths, multiple issues can arise with the laser scanning step. Because the repair typically consists in depositing material inside a machined cavity to recover the geometry and properties of the design specified part, the geometry of interest is generally concave and occlusions and shadow zones can thus be expected. The occlusion effect occurs because the laser reflection

corresponding to the true position of the surface can be blocked beneath the edge of the cavity and thereby not reach the CCD sensor. Shadow zone occur when the laser signal is blocked before it can reflect at the correct position on the surface. Indeed, most of the 800 laser signals originating at the emitter travel at an angle with respect to the vertical axis, so that the span or length of the scanline is much wider than the emitter, allowing for a more compact device. Corrections are then made internally to yield equally spaced data points. However, the non-vertical orientation of the laser signal means that they cannot always reach parts of the geometry with abrupt angle due to a shadowing effect. Moreover, when scanning aluminium surfaces, the high reflectivity of the surface means that there is a poor coupling with laser signal and multiple secondary reflections are typically generated.

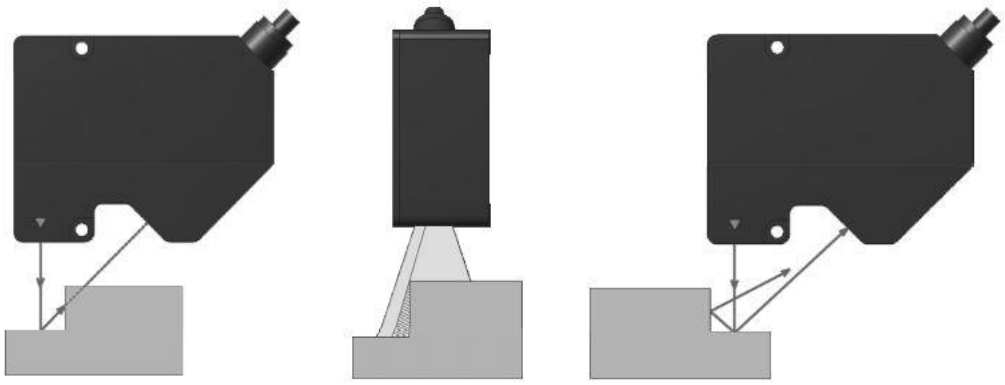

Figure 4.57: Potential issues with triangulation-based laser profilometers (left: occlusion effect – centre: shadow effect – right: secondary reflection)

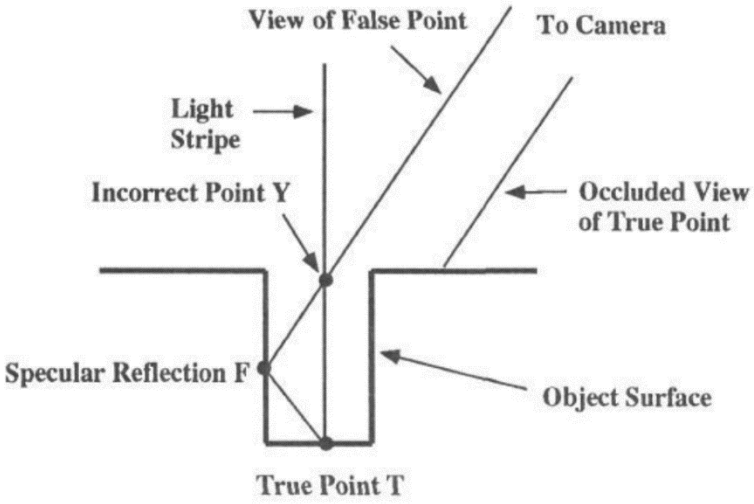

Figure 4.58: Spurious peaks generated by a combination of occlusion and secondary reflections (Trucco et al. 1994)

To enhance the accuracy and avoid measurement artefacts, the profilometer uses a visible blue semiconductor laser beam at 405nm. It also contains a double polarization function that serves to cancel spurious signals created by secondary reflections. Despite these design

adaptations, measurement errors still occur when scanning a concave geometry with a highly reflective surface. Combined with an occlusion effect, this can lead to large measurement errors due to spurious signals, which are misinterpreted by the profilometer to yield a point located much higher or lower than it really is (see figure 4.58). For spherical cavities on aluminium parts for instance, this translates into large positive and negative peaks near the edge of the cavity (see figure 4.59), as well as a deformation or artificial smoothing of the sharp edges of the cavity, particularly when the surface in inclined with respect to the scanline of the laser profilometer. As seen on figure 4.60, the edge location and sharpness are slightly altered compared to the true edge of the cavity, which is shown here as a yellow circle. The cavity no longer appears as being perfectly spherical near the edge, which can lead to significant discrepancies between the segmented repair volume and the true geometry of the cavity. These adversarial effects, further detailed in (Gao et al. 2005; Wang and Feng 2014), represent an added challenge for the segmentation of the repair volume.

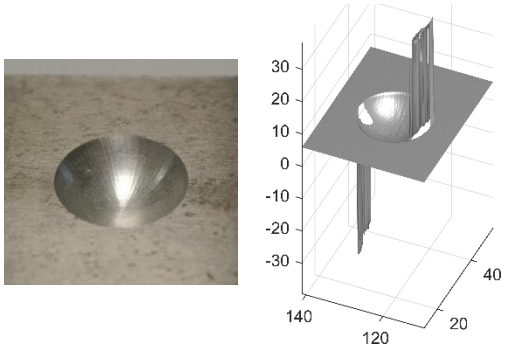

Figure 4.59: Spurious measurement peaks near cavity edges due to surface reflectivity and concavity

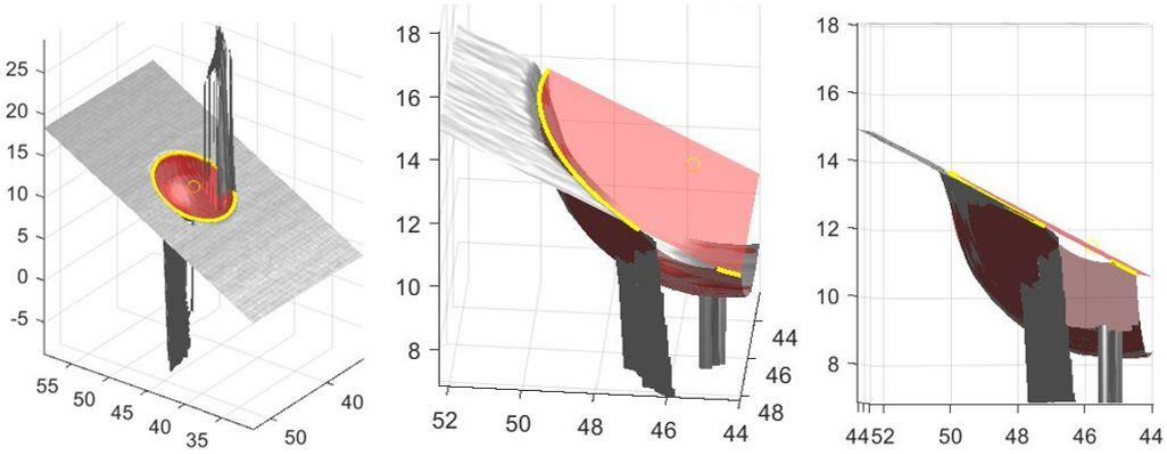

Figure 4.60: Deformed edges for inclined surfaces (yellow circle = true edge)

A median filter could be used to suppress erroneous peaks within the raw range dataset due to its edge-preserving and noise removal properties (Bešić et al. 2011), but this approach usually still requires manual intervention in order to be applied effectively and reliably. It is also not very practical when there are many large error peaks as the median filter may end up significantly modifying the local geometry.

Based on the range dataset, a first approach to segment the cavity from the range dataset could consist in using an edge detection filter as is typically done for segmentation tasks in intensity image processing. The edge detection process essentially amounts to convolving a 2D or 3D edge filter kernel (Scharr, Sobel-Feldman, Canny, Prewitt etc.) on the range data. However, the presence of spurious measurement peaks as well as smoothing effect near edges can prevent getting the true edge without significant manual doctoring of the range data and/or the segmented edges. Additional operations are often required such as edge thinning (non-maxima suppression) and edge closing for obtaining a clean and continuous edge for the cavity.

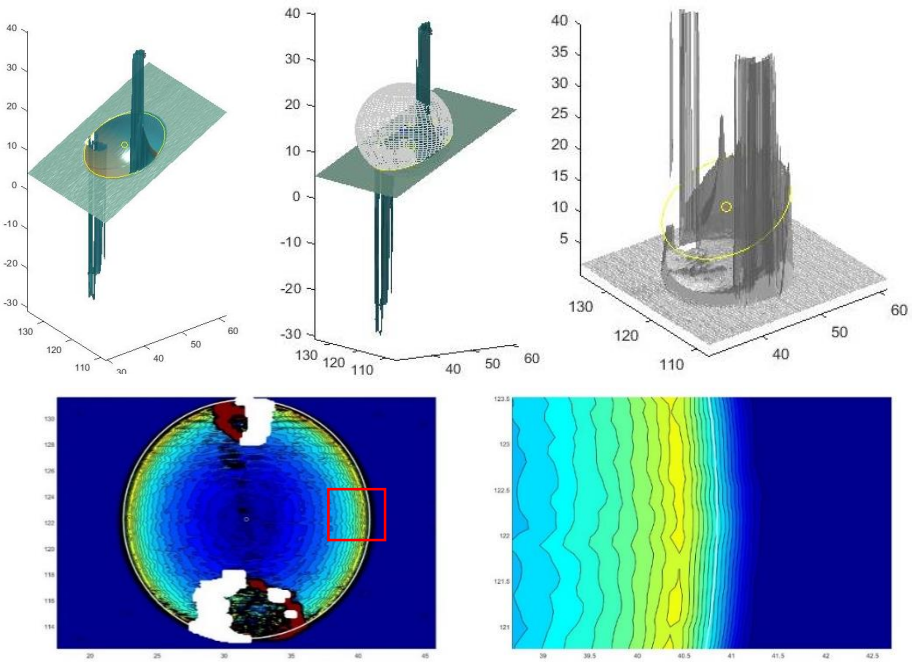

Figure 4.61: Edge location discrepancy on inclined surfaces due to scanning errors (Top Left: 3D range data of inclined cavity with yellow circle representing the true edge – Top Middle : Sphere fitted to cavity with RANSAC algorithm - Top Right: Height map of Scharr filtered range data – Bottom Left: Edge detection filter contour based on a 2D 3x3 Scharr kernel, true edge shown as white circle – Bottom

Figure 4.61 shows an example of edge detection on raw range data performed with MATLAB using a 2D 3x3 Scharr operator after a median filtering operation. A 3D circle, generated with parametric equations, is shown based on the sphere segmentation result

performed with the RANSAC algorithm (see following sections). While the fit of the sphere inside the cavity is very satisfactory despite scanning errors, the edge detection filter is highly disturbed by the measurement artefacts. It also typically displays an edge shifted by about 0.1 to 0.5 mm compared to the 3D circle projection on the 2D plane, depending on the inclination and size of the spherical cavity. Such an error is significant for the LMD process of the present work as the typical layer thickness is on the order of 0.1 mm. This difference could be caused by the filter kernel, by the artificial edge smoothing from the range scanner, or by the convolution operation that changes the dimensions of the dataset on which it is applied, in which case appropriate compensation should be used to avoid such discrepancies. In any case, even if the filtered coincided more precisely with the actual edge, it only gives 2D information about the cavity, and no particular information on its overall shape. Canonical 2D shapes could fitted to the edge data, again after appropriate edge cleaning steps such as edge thinning and closing, however information is lacking regarding the overall 3D geometry of the region, such as the depth of the cavity. Using a 3D kernel instead would not resolve this issue.

Segmenting edge features with convolution kernels is therefore not straightforward to automate, especially in the presence of measurement artefacts within the range data. Moreover, the edge filter cannot capture all the required information of the 3D geometry such as depth to allow the reconstruction of the envelope of the cavity, which is necessary for defining the LMD toolpath and perform the repair by LMD. Another approach is thus required to generate sufficiently accurate toolpaths with respect to the true geometry of the cavity, and thus ensure a suitable repair quality.

Because the range scanning process can yield rather inaccurate measurements near edges (Berra et al. 2007; Businaki et al. 1992), it is more advantageous to calculate the edge feature by leveraging the information contained in the bulk of the shapes (top and bottom surfaces) rather than relying on the edge data points alone. Indeed, the data points in the bulk as less susceptible to measurement artefacts and should remain truer to the actual geometry, in addition to the fact that there are many more points in the bulk than on the edges, which helps smoothing out the effect of punctual measurement errors. If the cavity and its neighbourhood can be represented as analytic surfaces, the edge feature and, even more importantly, the entire envelope of the cavity could be obtained by an intersection operation of those surfaces. It is however desired to perform the segmentation of the cavity's envelope in a highly automated manner, thus directly on the raw range data without manual pre-processing.

To fit analytical surface models on the raw range data of the cavity despite large measurement errors, a robust segmentation algorithm should be used. The InterSAC algorithm (Hascoët et al. 2018a; Touzé et al. 2018) presented in this chapter performs the repair volume segmentation by implementing a RANSAC-based parameter estimation algorithm (Fischler

and Bolles 1981), which permits robust fitting of predefined surface models on range datasets despite the presence of measurement errors and model outliers. By machining the bottom surface of the cavity into a known canonical shape (sphere, cylinder…) during the rough machining step, the InterSAC algorithm is able to reconstruct the geometry of the repair volume by fitting a surface model on the bottom surface of the cavity using raw range scanner data. The type of canonical shape acts as a marker of the defective region within the range dataset. Once the bottom surface of the cavity is segmented, InterSAC then proceeds to the identification of the "neighbouring" or "top" surface surrounding the bottom surface to fully define the envelope of the repair volume.

During the intersection step, a digital model of the repair volume's envelope is reconstructed based on the analytical representation of the previously segmented top and bottom surface models of the cavity. This can be done without any prior knowledge of the geometry of the part, provided the defect area has been machined into a surface cavity with a known type of canonical shape. The digital model of the repair volume can then be used to generate scan paths for a subsequent repair by LMD. The InterSAC method therefore removes the need for major pre-processing of the range data by the user, or the need for performing multiple scans and fusing the range data to filter out scanning errors (Trucco et al. 1998). Moreover, this method does not require a CAD model as it only uses local information provided by the range dataset. Advantageously, the exact orientation and location of the part with respect to the laser range scanner does not matter for the InterSAC method to work effectively as long as the cavity is not excessively occluded by the rest of the part's geometry and there is sufficient data to define the cavity's bottom and top surfaces.

III. Repair Volume Reconstruction from raw 3D data: InterSAC algorithm

a. InterSAC method

i. General principle

The InterSAC (Intersection SAmple Consensus) method (Hascoët et al. 2018a; Touzé et al. 2018) aims at reconstructing a digital model of a repair volume based on raw range data of a cavity area obtained, for example, by a laser range scanner. As described earlier, such a range scanner may be directly mounted on a LMD projection head, whether it be in a hybrid or a purely additive manufacturing context.

As detailed in (Hascoët et al. 2018a), the InterSAC method assumes that both the general shape of the cavity and the surface around it (a.k.a. "neighbouring surface" or "top surface") are both amenable to an analytic representation. This is generally at least approximately true if the local geometry is sufficiently smooth around the cavity. The cavity is then to be refilled by an additive manufacturing process such as LMD in order to locally recover the shape of the neighbouring surface.

Since the repair volume is usually fully dense (i.e. no internal holes), it is uniquely defined by its envelope. To extract this envelope from the range data, the InterSAC method successively segments the bottom and top surface of the cavity using a modified RANSAC algorithm.

The shape of the bottom surface corresponds to the toolprint resulting from the defect machining step, which depends on the shape of the milling cutter and its effective milling trajectory. For example, a ball nose mill along a linear path defines a cylindrical bottom surface. The shape of the top surface is based on the geometry surrounding the cavity. This top surface corresponds to the local geometry of the part that is to be recovered through the repair process. The top and bottom surfaces can be combined to form the envelope of the repair volume defined by the cavity. The segmentation of the bottom and top surface is performed successively on the raw laser range data using a RANSAC (RANdom SAmple Consensus) algorithm (Fischler and Bolles 1981) that has been modified in several ways to adapt it the repair volume reconstruction problem.

The InterSAC method can be summarized by the following steps:

1. Range scan of the cavity area
2. Segmentation of the cavity's bottom surface
3. Segmentation of the cavity's top surface
4. Intersection operation to construct the envelope of the repair volume based on the top and bottom surfaces

For the RANSAC-based segmentation (step 2 and 3), a shape model needs to be chosen before its parameters are subsequently estimated based on the raw range data. Such shape models will usually include canonical surfaces expressed in implicit or explicit form (sphere, cylinder, cone, quadrics, algebraic surfaces…). As with most RANSAC-based methods, the range of usable analytical models is only limited by the capacity to quickly solve for model parameters based on a minimal sample.

The shape model for the cavity's bottom surface may be input manually by the operator based on visual inspection. As mentioned earlier, it can also be defined based on the type of milling toolbit used and effective milling trajectory. In any case, choosing the right model for the bottom surface is essential for the InterSAC method to successfully identify the location and shape of the cavity.

For the segmentation of the top surface, the choice of shape model is not as stringent. Indeed, in most cases, it suffices to choose an explicit surface model ($z = f(x, y)$) with sufficiently high flexibility (e.g. polynomial surface of degree 3) since it is only necessary to approximate the local geometry around the cavity's bottom surface, the latter being already segmented at this stage (i.e. its parameters have been estimated).

Once the parameters of both the bottom and neighbouring surface have been evaluated, the envelope of their volumetric intersection, i.e. the repair volume, can then be reconstructed.

ii. RANSAC algorithm

The RANSAC-based algorithm used for the first and second segmentation step (bottom surface and top surface segmentation, respectively) is a modified version of the original RANSAC algorithm (Fischler and Bolles 1981).

1. Original RANSAC algorithm

For model parameterization, the least-squares fitting method can often be used effectively to compute model parameters by minimizing the Euclidean distance between the

surface model and all of the data points. This approach is appropriate when the dataset does not contain model outliers and the error follows a zero-mean Gaussian distribution around the surface model. The least-squares fitting method is however extremely sensitive to the presence of model outliers, such that the fit quality is largely compromised when the dataset contains measurement artefacts and model outliers (Myatt et al. 2002). And in fact, the range dataset for the repair application of the present study not only contains measurement errors (spurious peaks, smoothened edges etc.) but also cannot be represented as a unique surface model as both a top and bottom surface model are to be fitted to the dataset in order to define the geometry of the repair volume. Another approach is thus needed to perform the segmentation with good accuracy.

Other algorithms for model parameterization have been developed such as RANSAC, MINPRAN and Least Median Squares (LMS). RANSAC is however superior to LMS in the case of high noise and datasets with more than 50% of outliers, and it does not require knowledge about the outliers' distribution, unlike MINPRAN (Myatt et al. 2002). Moreover, it is conceptually simple and yet is very robust for parameter fitting, so that this particular method is chosen here for performing the segmentation of the top and bottom surfaces.

The RANSAC algorithm (Fischler and Bolles 1981) is a probabilistic voting method that can be used to robustly segment geometrical models within a dataset containing many model outliers by iteratively estimating new model parameters from minimal subset of datapoints sampled randomly within the dataset, and then retaining the model with the most support, i.e. highest consensus.

The original RANSAC algorithm for robust surface models fitting can be summarized as follows:

P : range dataset on which model(s) are being fitted
N : minimum number of points or sample size required to compute model parameters
T : distance threshold or error tolerance between surface model and datapoints
I : number of iterations

1) Randomly select in P a subset *S1* of size N
2) Compute model parameters *M1* based on subset *S1*
3) Find set of points $P1 \in P$ that lie within a distance T from surface model *M1*. *P1* is the consensus set, or set of inliers, of model *M1*
4) Iterate through step 1 to 3 for I iterations, retaining the model M with largest consensus, i.e. highest cardinality of consensus set
5) Return model M with highest consensus
6) "Gold standard" version (optional): Perform Least-Square fit over the entire consensus set (i.e. all model inliers)

The number of iterations I can be determined based on the ratio γ of model inliers to outliers and desired success probability β, which is typically set to 0.99 in this work.

$$I = \frac{\log\ 1 - \beta}{\log\ 1 - \gamma^N} \tag{4.1}$$

The original RANSAC cost function, which is equivalent to selecting the model with the largest consensus set (i.e. the consensus set with the highest cardinality), can be expressed as follows:

$$C\ p\ = \begin{cases} 0, & d < T \\ T^2, & d \geq T \end{cases} \tag{4.2}$$

$$TC = \sum_{p=1}^{n} C(p) \tag{4.3}$$

where $C\ p$ is the cost of a single data point p, T is the distance threshold separating inliers from outliers, d is a distance measure between a data point p and a surface model, n is the total number of data points and TC is the total cost based on the entire dataset. In the presence of Gaussian white noise, the threshold T may be related to the standard deviation σ of the underlying Gaussian distribution (Torr and Zisserman 2000). For example, choosing $T = 1.96\sigma$ leads to incorrectly rejecting Gaussian inliers 5% of the time.

Since the final model parameters corresponding to the best consensus set (i.e. lowest cost) have been estimated with a minimal subset, a final least-square fitting step on all the inliers is usually added, as per the so-called "gold standard" form of the RANSAC algorithm, so that the entire consensus set participates in the estimation of the final model parameters.

In its original version however, the RANSAC algorithm is not highly repeatable due to its probabilistic nature, does not always yield the optimal model parameters and does not sufficiently account for noise in the data. Hence, the RANSAC algorithm is modified based on the findings of previous works (Choi et al. 2009; Chum et al. 2003, 2004; Hast et al. 2013; Lebeda et al. 2012; Myatt et al. 2002; Torr and Zisserman 2000) in an attempt to tailor the algorithm to repair volume segmentations for use in an industrial context.

2. Sampling

The original RANSAC algorithm (Fischler and Bolles 1981) uses random sampling at each iteration for the selection of the minimal sampleset data points. In the context of InterSAC, which deals with a purely geometrical problem, the shapes to be segmented from

the range dataset have a finite localized extent. In other words, data points that correspond to a particular shape model are located contiguously and are not randomly spread out over the entire dataset.

Hence, instead of a purely random sampling, a sampling procedure like NAPSAC (Myatt et al. 2002) may be adopted for the first segmentation step. Originally dedicated to sparse N-dimensional datasets, NAPSAC sampling can also be used here to shorten the number of iterations. It consists in, firstly, randomly sampling a first data point, and secondly, sampling the rest of the data points by choosing data points located in its neighborhood. The minimal sampleset formed hereby is then more localized than with purely random sampling. If the first data point happens to be an inlier of a particular model for a given threshold, then the probability that all the data points in the sampleset belong to the model is much higher than with purely random sampling. Hence, the number of iterations theoretically required is reduced as the probability of forming a sampleset of inliers only at each iteration is increased. Indeed, if one of the data points in the minimal sample of size N belongs to the set of model inliers, there is a much higher chance that the other points of the sample also are model inliers as they are closely located to the first sample point. A rough approximation of the number of iterations I_{NAPSAC} with NAPSAC sampling could be expressed as follows, provided that the predefined distance between points of a NAPSAC minimal sample is small compared to characteristic dimensions of the geometry to be segmented:

$$I_{NAPSAC} \approx \frac{\log\ 1-\beta}{\log\ 1-\gamma} \tag{4.4}$$

Advantageously, with a gridded dataset as obtained with a laser profilometer, NAPSAC sampling can be applied directly, unlike with point clouds where point to point distances have to be computed first, which can be relatively expensive although it only needs to be done once.

While NAPSAC-like sampling may be used for the first segmentation step (i.e. the bottom surface segmentation step), it is not beneficial to use it for the second segmentation step since the goal is to approximate the surface that surrounds the bottom surface of the cavity, which is better performed by a sampling distribution that is spread out around the cavity and located in the direct vicinity of the bottom surface.

To reflect this, the sampling pool may be restricted to those data points located within a certain range distance from the bottom surface. For implicitly defined surface models ($F\ x, y, z\ = 0$), this can be done using level sets of the surface. For a spherical bottom surface of radius R and a sampling range SR of $0.5R$, the sampling pool for the neighbouring surface segmentation may be chosen as those data points located at a range distance of R to $1.5R$ from the center of the sphere, i.e. inside concentric spheres of radius R and $1.5R$.

Given a distance function $d_1(x, y, z)$ measuring the distance between a data point $p(x, y, z)$ and the bottom surface, the sample pool is chosen as the set of data points for which $d_1 \in [\varepsilon, SR]$, where ε may be set to the distance threshold T of the firstly segmented model (i.e. the bottom surface), which amounts to discarding the consensus set of the segmented bottom surface.

The size of the sampling pool is thus reduced by using SR, and the ratio γ of the number of inliers to the number of outliers most likely increases as the sampling region has become more relevant to the top surface model and should therefore mostly contain top surface model inliers, except for measurement artefacts located near the edges of the cavity. This in turn decreases the number of iterations theoretically required. Also, the models evaluated based on sample sets chosen from such a restricted sampling range are generally more representative of the neighbouring surface than models evaluated on sample sets drawn randomly over the entire range dataset.

A representative sampleset from the restricted sampling pool would contain data points dispersed throughout the sample pool. Hence, unlike the first segmentation step where a NAPSAC-like localized sampling was beneficial, it is here advisable to either keep a random sampling process or use some form of guided sampling to enforce a proper spatial distribution of the sample points around the bottom surface.

3. Parameters estimation

The RANSAC algorithm is based on model parameters evaluation from minimal subsets of point provided by the sampling procedure. The size of the minimal subset, i.e. the number of sample points at each RANSAC iteration, is equal to the number of independent model parameters that define the model surface. For instance, 3 points (non-collinear) define a unique plane and 4 points (non-coplanar) define a unique sphere.

To obtain the coefficients of an algebraic surface given a minimal subset of points belonging to the surface, an exact fit is performed on those points using the standard determinant method (Pratt 1987). This method allows the use of various polynomial basis, also called generators, representing various surfaces (plane, sphere, z-axis cylinder or cone, hyperboloid, quadric…) for which the polynomial coefficient can be directly computed by constructing and computing a determinant. This method enables the use of multivariate algebraic surfaces of arbitrary degree as shape models.

Shape	Polynomial Basis
Plane	1, x, y, z
z-axis aligned Cylinder	1, x, y, x^2+y^2
z-axis Cone	x^2+y^2, z^2
Sphere	1, x, y, z, x^2+y^2+z^2
Quadric	1, x, y, z, xy, yz, zx, x^2, y^2, z^2

Table 4.24: Generators for canonical surface models

Once a suitable basis has been established, the minimal sample size can be determined (4 non-coplanar points for a sphere, 3 non-collinear points for a plane etc.) and the constraints on the sample points be checked. In the case of a sphere, which requires 4 non-coplanar points, sample points $p_1 = (x_1, y_1, z_1)$ to $p_4 = (x_4, y_4, z_4)$ are coplanar when they define a volume that is equal to zero, that is, they satisfy the following relation:

$$\begin{vmatrix} x_1 & y_1 & z_1 & 1 \\ x_2 & y_2 & z_2 & 1 \\ x_3 & y_3 & z_3 & 1 \\ x_4 & y_4 & z_4 & 1 \end{vmatrix} = 0 \tag{4.5}$$

Provided that constraints on sample points such as equation 4.5 are respected within some tolerance, which depends on the accuracy of the measurement system, the determinant method allows to find the parameters of the surface model based on the chosen basis and the coordinates of the minimal set of sample points that belong to the surface to be fitted. The determinant is constructed as the mapping of sample point coordinates to the polynomial basis, with an added last line corresponding to the polynomial basis itself in symbolic form. Computing this determinant, shown in equation 4.6 for a sphere, leads to the implicit equation of the surface that goes through the sample points. Some normalization is usually applied on the coefficients, for example setting the coefficient of the highest order term to 1, or, in the case of the plane, normalizing the plane normal vector defined by the plane equation coefficients and setting the sign such that the normal vector points upward.

$$\begin{vmatrix} 1 & x_1 & y_1 & z_1 & x_1^2 + y_1^2 + z_1^2 \\ 1 & x_2 & y_2 & z_2 & x_2^2 + y_2^2 + z_2^2 \\ 1 & x_3 & y_3 & z_3 & x_3^2 + y_3^2 + z_3^2 \\ 1 & x_4 & y_4 & z_4 & x_4^2 + y_4^2 + z_4^2 \\ 1 & x & y & z & x^2 + y^2 + z^2 \end{vmatrix} = 0 \tag{4.6}$$

All surfaces that can be represented by these polynomial basis can thus be directly used as shape models in the InterSAC method. However, some surfaces cannot be expressed in the general case using a particular polynomial basis. For instance, there is no unique basis for a general cylinder with arbitrary orientation. To perform an exact fit of a general cylinder, several methods are available depending on the number of sample points used in the minimal subset. To obtain a unique solution, a minimal subset size of 7 or 9 may be chosen (Beder and Wolfgang 2006). With 9 points, the equation for the corresponding cylinder is obtained through the solution (nullspaces) of a singular value decomposition problem, with some additional constraints being added when using only 7 points (Beder and Wolfgang 2006). However it is not straightforward to extract the radius of the segmented cylinder from the solution. Other solution methods exist using 5, 6 or 8 points, but they lead to multiple solutions (Beder and Wolfgang 2006), which is undesirable for our application. Another approach based on (Schnabel et al. 2007) is adopted here instead. It consists in using two points p_1, p_2 and their normal vectors $\overrightarrow{n_1}$, $\overrightarrow{n_2}$ to define a cylinder, which is then validated by checking that normal vectors orientation and distance of the sample points fall within given thresholds compared to the estimated model. A given sample point on a regular 2D Cartesian grid has 8 direct neighbouring points, such that 8 triangular facets can be defined using pairs of neighbors and the sample point. A plane is fitted through each of the point triplets forming the triangular facets, and the plane normal vector is calculated based on the plane equation after normalization of its coefficients. The surface normal vector at the sample point is evaluated as the average of the surface normals of each of the 8 triangular facets, similarly to (Klasing et al. 2009). The parameters of the cylinder are then found by first computing the axis vector of the cylinder as the cross-product $n = \overrightarrow{n_1} \times \overrightarrow{n_2}$. A projection plane is defined as the plane with normal n passing through p_1, and point p_2 is projected onto the projection plane as point ${p_2}'$. Parametric lines L_1 and L_2 are defined as the lines going through points p_1 and p_2 respectively and extending along their normal vectors $\overrightarrow{n_1}$ and $\overrightarrow{n_2}$. Solving for their intersection yields a center point C of the cylinder that lies on the cylinder axis. The radius of the cylinder R is then equal to $\|p_1 - C\|$. Finally, the cylinder equation in implicit form can be determined using symbolic point $= (x, y, z)$:

$$\left(p - C \times n \right)^T \left(p - C \times n \right) - R^2 = 0 \tag{4.7}$$

To perform least-square fitting of a surface model over an entire consensus set, as in the final step of the "gold standard" version of RANSAC or during a local optimization step, a non-linear Least-Square minimizer using the Levenberg-Marquardt algorithm is used to find the best parameters, in the least-squares sense, of the surface models based on all of the model inliers. It can also be used for the overfitting mode of the present algorithm, where the top

surface can be segmented using a non-minimal sample size to provide a better fit around the cavity, at the cost of an increased runtime as the computation becomes more expansive with sample size.

4. Cost function

For the segmentation of the cavity's bottom surface, i.e. the first segmentation step, the cost function of MSAC (Torr and Zisserman 2000) is used instead of the original RANSAC cost function, as it better accounts for noise within the range dataset at no extra computational cost by giving a non-zero cost to inliers:

$$C(p) = \begin{cases} d^2, & d < T \\ T^2, & d \geq T \end{cases} \tag{4.8}$$

$$TC = \sum_{p=1}^{n} C(p) \tag{4.9}$$

For primitive shapes such as spheres and cylinders, the distance function d is the standard Euclidian geometric distance. For a sphere of radius R centered at a point (a, b, c), the distance between a point (x, y, z) and the surface of the sphere is classically expressed as $d = \sqrt{(x-a)^2 + (y-b)^2 + (z-c)^2} - R$. Point to surface distance calculations for other primitives such as cones and cylinders are given in (Barbier and Galin 2004).

For a general algebraic surface defined implicitly as $F\ x, y, z\ = 0$, there is no obvious definition of the geometric distance between a random point p and the surface. The geometric distance is here replaced by the Turner-Sampson non-algebraic distance d' (Pratt 1987), which is a normalized version of the algebraic distance $F\ p$:

$$d' = \frac{F(p)}{|\nabla F(p)|} \tag{4.10}$$

This distance metric presents several desirable properties, as it is insensitive to the scaling of F, is as invariant as the geometric distance and coincides with the geometric distance for planar surfaces. Higher order distance metrics such as the Nalwa-Pauchon distance metric can also be used in the case of very scattered data (Pratt 1987).

For the segmentation of the top surface, i.e. the second segmentation step, two modifications related to the bottom surface are included compared to the first segmentation step. Firstly, similarly to the sampling range, a cost range CR can be introduced (with $CR \geq$

SR) so that only data point within a certain range distance from the first model will be included in the cost calculation. This serves to speed up calculations and help define a more representative cost function for the top surface. The cost dataset for the second model is thus chosen as the set of data points for which $d_1 \in [\varepsilon, CR]$, where ε may be set to the distance threshold T of the firstly segmented model (i.e. the bottom surface), which again amounts to discarding the consensus set of the segmented bottom surface. Secondly, the MSAC cost function may be modified so as to vary with the distance of the data points to the firstly segmented model. More specifically, the cost contribution of data points is set to decrease as their distance from the first model increases. In this way, the cost function is biased towards selecting models that better fit the data points near the first model rather than further away. For instance, assuming that two distinct sets of model parameters yield the exact same MSAC cost, the model parameters whose corresponding inliers are closest to the first model would give the lowest weighted cost. If instead the costs were to be distributed uniformly around the first model (i.e. no distance-based weighing of the individual cost), models with the same MSAC cost but whose inliers are located further away, i.e. better fits the dataset further away from the location of the first segmented model, would be seen as equivalent. The distance-based weighing thus helps improving the quality and reliability of the segmentation of the neighbouring surface and thus of the overall repair volume. If the cost range is chosen to be relatively small (i.e. $CR \approx SR$ with a low SR), a uniform cost function may be sufficient. However, as the cost range and sampling range are increased, it may become beneficial to include a distance-based weighing of the cost function to ensure that the parameters obtained for the second model (the neighbouring surface) yield a model that closely fits the vicinity of the cavity where the first model is located.

A generalized logistic function such as Richard's curve (Richards 1959) can be used as a distance-based weighing function:

$$R\ D_{CR}\ = A + \frac{K - A}{(C + Qe^{-B\ D_{CR} - M}\ )^{1/\upsilon}} \tag{4.11}$$

with the parameters chosen to yield a function decreasing from 1 to 0 with the relative distance D_{CR}, which is defined as $D_{CR} = \frac{d_1}{CR}$. The parameters of the Richard curve may for example be set to $A = 1, K = 0.01, C = 1, Q = 15, B = 7, M = 0, \upsilon = 0.2$. The resulting curve is illustrated in figure 4.62.

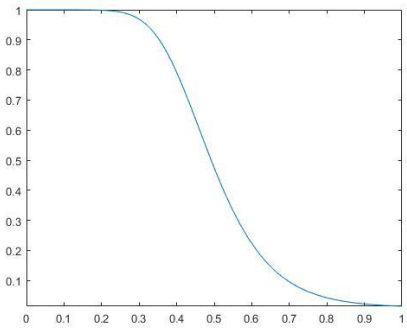

Figure 4.62: Richard's curve with A = 1, K = 0.01, C = 1, M = 0, B = 7, Q = 15, υ = 0.2

A new cost function for the top surface segmentation can then be defined as:

$$C(p) = \begin{cases} R\ D_{CR}\ \times d^2, & d < T \\ R\ D_{CR}\ \times T^2, & d \geq T \end{cases} \tag{4.12}$$

$$TC = \sum_{p=1}^{n} C(p) \tag{4.13}$$

Such distance-based weighing of the cost function for the segmentation of the top surface can be adapted to arbitrary geometries defined in implicit form using distance functions such as equation 5.10. This also includes explicit representation as these can be straightforwardly converted to an implicit representation.

5. Local Optimization

Once the RANSAC-based algorithm has selected a set of parameters and a corresponding consensus set (i.e. inliers) based on cost function minimization, a final least-square fit is usually performed on all model inliers, as done in the "gold standard" version of RANSAC, using the Levenberg-Marquardt algorithm,. The final model parameters are thus evaluated based on the entire consensus set, i.e. model inliers, rather than on a minimal subset.

In order to increase the repeatability of the InterSAC method from one run to another, a local optimization step (Hast et al. 2013) is also included. It consists in iteratively reevaluating model parameters based on the entire consensus set, then recomputing the cost and consensus set with these new model parameters. When parameters are reevaluated, new inliers may enter the consensus set and previous inliers may become outliers and thus leave the consensus set. If the new cost is lower than the best cost found so far, the new model parameters are retained and the program goes to the next local optimization iteration. The

local optimization loop exits when the newly calculated cost presents marginal or no improvement over the cost calculated in the preceding iteration. A maximum number of iterations is also set to keep the overall execution time reasonable as the non-linear least-squares fitting process over a large dataset can be computationally costly.

iii. Intersection operation

Once the bottom and top surfaces of the cavity have been segmented, i.e. an implicit or explicit analytical representation has been obtained, the InterSAC method proceeds to combining them in order to form the envelope of the repair volume.

InterSAC first generates points on both the bottom and neighbouring surfaces using their analytical expression in order to form a surface mesh of the envelope of the repair volume. Because we are using the analytical expressions of the segmented shape models to generate those points, the density of this mesh can be determined arbitrarily depending on the required accuracy, available time and computing power.

To form the bottom of the repair volume's envelope, the points on the bottom surface whose z-coordinate is inferior to the corresponding z-coordinate of the neighbouring surface are selected. In other words, all the points on the bottom surface that are located below the neighbouring surface are kept.

Similarly, to form the top of the repair volume's envelope, the points on the top surface that are above or inside the bottom surface are conserved.
With implicit or explicit surfaces, those conditions are easy to verify as the analytical expression of each surface directly yields that information by plugging in the coordinates of each data point into the equation and checking for an inequality.

Assuming a spherical bottom surface S (defined implicitly by $F_S\ x, y, z\ = 0$), a polynomial neighbouring surface P (defined explicitly by $z = F_P(x, y)$), and points $p = (x, y, z)$, the envelope E is defined as:

$$E = \{p\ \in S \mid z < F_P(x, y)\} \cup \{p\ \in P \mid F_S\ p\ < 0\} \tag{4.14}$$

A similar approach is used for cavities made of a composite shape such as a "closed" cylindrical groove (one cylinder and two end spheres).

In the case of multiple neighbouring surfaces, i.e. when the cavity is located at the crossroad of multiple surfaces (e.g. on an edge or angular region of the part), the expression above can be extended. With two contiguous top surfaces, assuming a spherical bottom surface S (defined implicitly by $F_S\ x, y, z\ = 0$), two polynomial top surfaces P_1 and P_2 (defined

explicitly by $z = F_{P1}(x, y)$ and $z = F_{P2}(x, y)$), and points $p = (x, y, z)$, the envelope E is defined as:

$$E = \{p \in S \mid z < F_{P1}\ x, y \ \& \ z < F_{P2}(x, y)\} \cup \{p \in P_1 \mid F_S\ p < 0 \ \& \ z > F_{P2}(x, y)\} \cup \{p \in P_2 \mid F_S\ p < 0 \ \& \ z > F_{P1}(x, y)\} \tag{4.15}$$

This expression could be rather straightforwardly extended to any number of top and bottom surfaces provided sufficient information on their connectivity is available.

Once the envelope of the repair volume is reconstructed, its convexity can be evaluated. If it is indeed a convex repair volume, a convex hull algorithm such as Quickhull (Barber et al. 1996) can be run to compute the volume contained within the envelope of the repair volume, which leads to a unique solution. If the volume is concave, then the actual volume may be computed using a concave hull algorithm, based for example on a k-nearest neighbor algorithm (Moreira and Santos 2007) or on alpha shapes (Edelsbrunner and Mucke 1994). Note however that in the concave case, the solution is not unique as concave hull algorithms require the setting of at least one parameters. In the present work, alpha shapes are used where a coefficient $\alpha \in [0; 1]$ needs to be predetermined, where $\alpha = 0$ corresponds to the convex hull solution.

iv. Summary of the InterSAC method

The flowchart in figure 4.63 shows a general flowchart of the InterSAC algorithm, which again contains 3 main stages, i.e. a RANSAC-based bottom surface segmentation, a RANSAC-based top surface segmentation with a cost function that accounts for the bottom surface through a distance-weighing function, and finally an intersection step that forms both a point cloud envelope and, through a Delaunay triangulation, a triangulated surface representation (e.g. as an STL file).

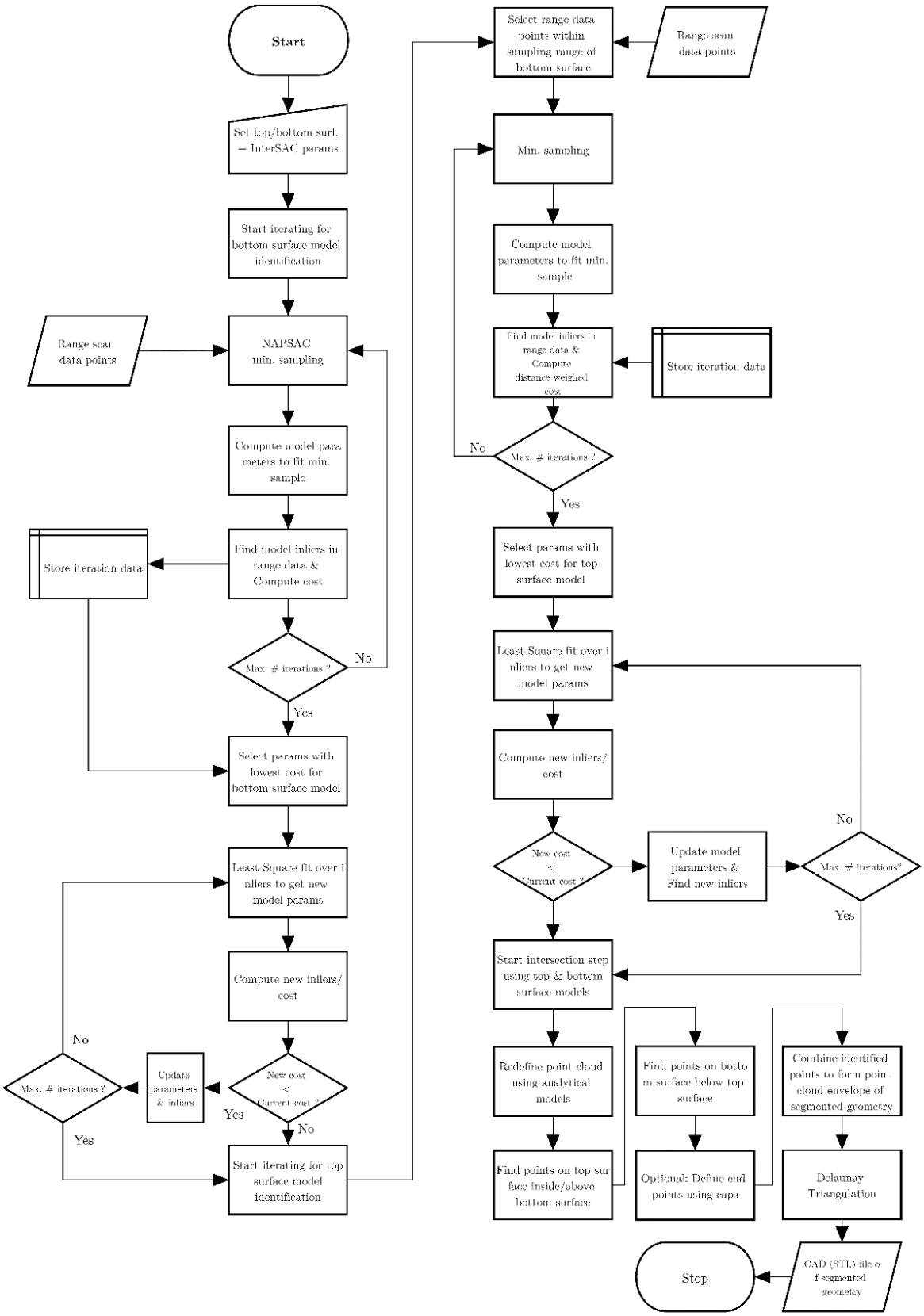

Figure 4.63: Flowchart of the InterSAC algorithm for repair volume segmentation based on raw range data

v. Embodiment of the InterSAC algorithm

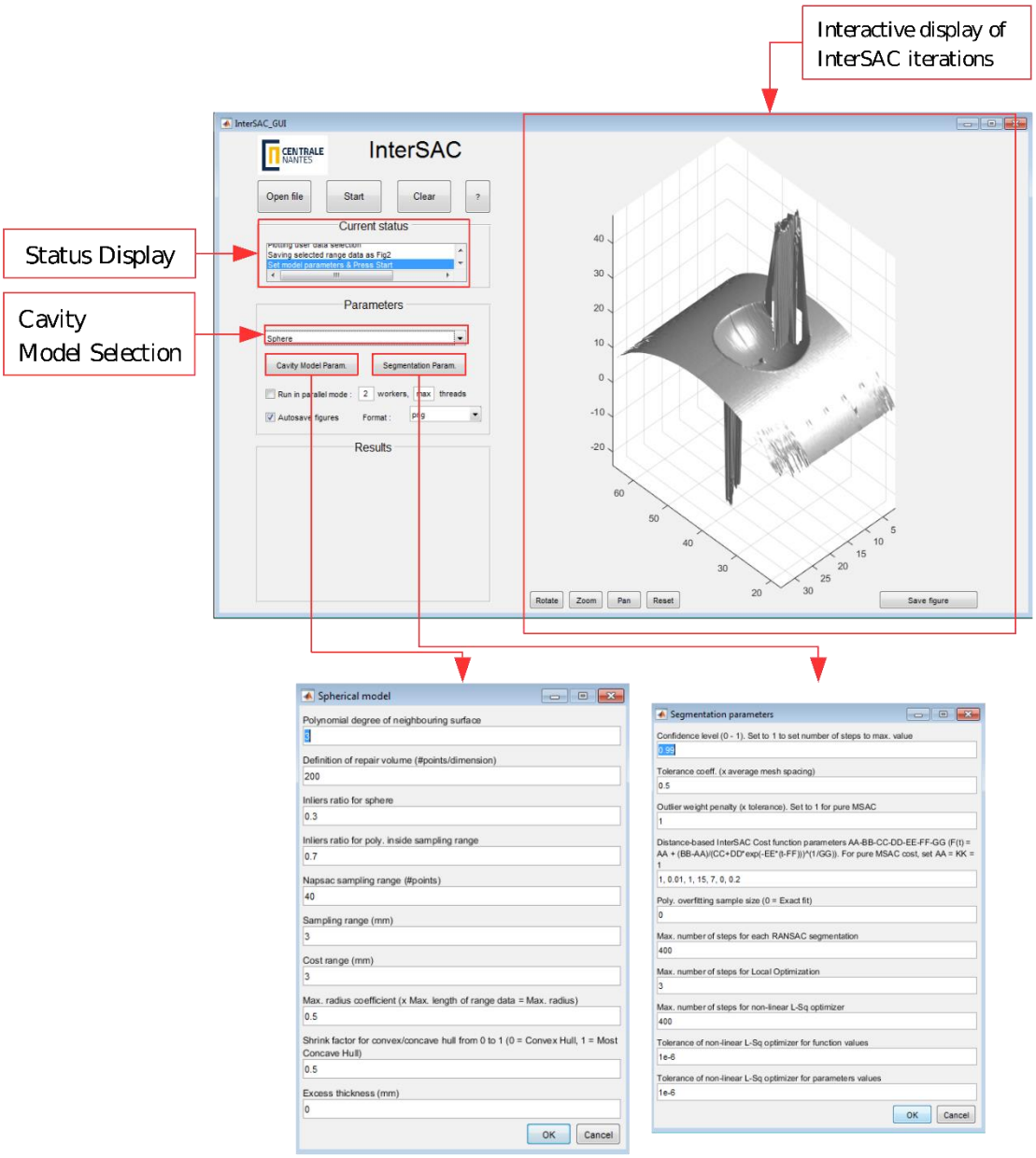

Figure 4.64: Graphical User Interface of the InterSAC algorithm developped in MATLAB

The InterSAC algorithm of the present chapter was coded in MATLAB© and includes a Graphical User Interface (GUI) for ease of use. The code base contains about 9000 lines of code written specifically by the present author to implement the InterSAC algorithm. A few auxiliary code files, found in online repositories, are used for processing the results such as saving figures into high quality images or generating the STL file based on the Delaunay triangulation. As shown on figure 4.64, there are quite a few parameters to be set by the user, however in practice most of those parameters can be left to their default values. The parameters that are most often changed are the type of bottom surface (sphere, cylinder without end caps, cylinder with planar end caps, cylinder with spherical caps) and the order

of the implicit algebraic top surface (usually between 1 and 3). A parallel mode is included, where the iterative loops are distributed over several threads, in order to decrease runtime although some overhead cost is induced at the beginning of the iterative process to setup the parallel workers and threads. In this mode, the runtime can be significantly shortened depending on the capacity of the computer, however the results of each iteration cannot be displayed as the iterations are now distributed and processed in parallel. An option to save figures in a desired format (png, jpg, tiff, pdf) is also included, so that the progress of the InterSAC segmentation and the result of each stage can be saved.

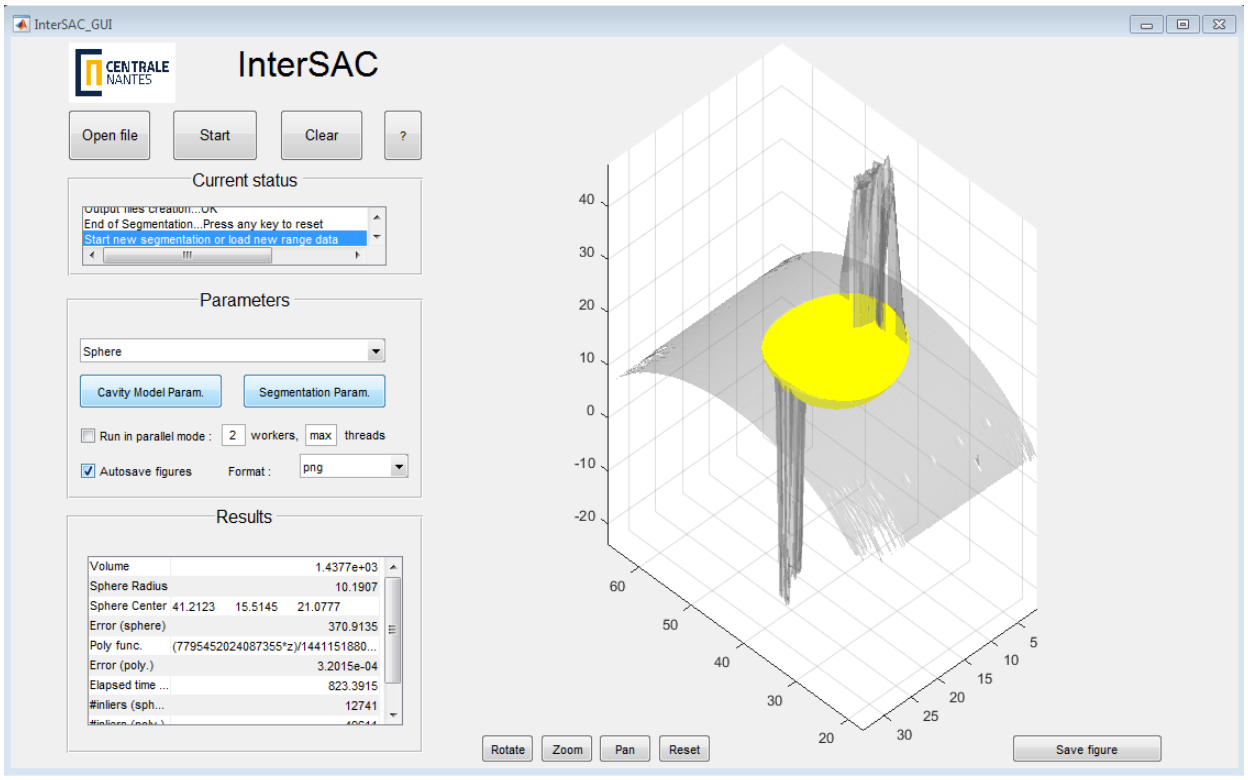

Figure 4.65: Final InterSAC segmentation of a spherical cavity on a curved surface

vi. Applications

For repair applications, it is usually desirable that the cavity to be refilled presents no sharp corners in the bottom of the cavity. Hence, a ball nose mill is usually used for the rough machining step to yield a rounded cavity, thus avoiding sharp corners which are generally detrimental to welding and AM processes as it can induce stress concentration and lack of material feed.

Among the geometries that can be created by a ball nose end or hemispherical mill, the most common ones are a spherical cavity and a cylindrical groove. Depending on the shape of the surface (planar, free-form…) the cavities are machined on, the shape of the resulting repair

volume varies. The cylindrical grooves can present various shapes at their extremities, depending on the type of top surface and machining toolpath, so that end caps may be added to correctly define the geometry of the cavity created by the ball nose end mill.

A few applications of the InterSAC method, including spherical and cylindrical cavities, are given hereafter to illustrate its efficiency on practical cases.

1. Spherical cavity on freeform surface

The simplest geometry obtainable with a ball nose end mill is a spherical cavity, machined either on a flat or curved surface depending on the location of the defect. In the example hereafter, such a spherical cavity has been machined on a freeform surface of an aluminium part using a hemispherical toolbit of diameter 10mm and was subsequently scanned by a laser profilometer.

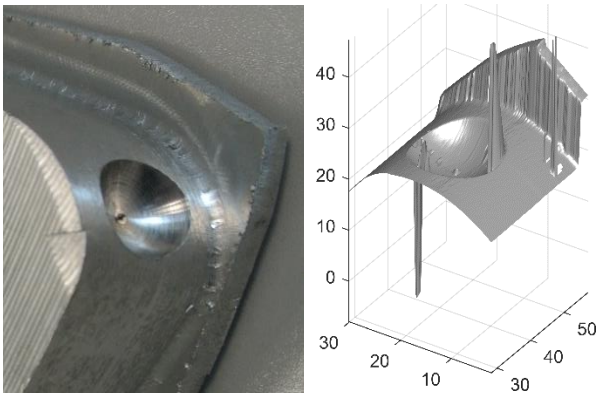

Figure 4.66: Aluminium part with surface cavity to be repaired machined with a hemispherical toolbit of 10 mm radius (left) – Corresponding range data of cavity area (right)

Due to the metal's reflectivity and the concavity of the cavity, there are spurious peaks in the range data located mostly near the edge of the cavity. The InterSAC algorithm is run directly on the raw range data, with no particular pre-processing or filtering. Instead of using a confidence level to compute the number of iterations, the latter can be set directly by the user for convenience, especially when considering the fact that with NAPSAC sampling, the required number of iterations is given approximately by equation 4.4.

After 50 RANSAC iterations using NAPSAC sampling, followed by 5 local optimization iterations, the spherical bottom surface is segmented, as illustrated in figure 4.67.

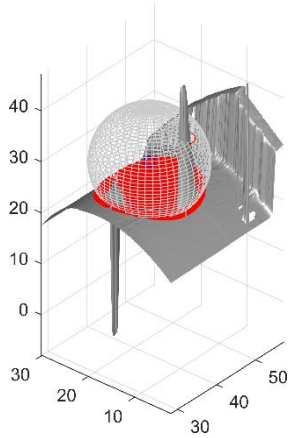

Figure 4.67: Segmented sphere (inliers in red)

The neighbouring surface around the cavity is then segmented using a polynomial surface of degree 3, 50 RANSAC iterations with $SR = CR = 5\ mm$ and 8 local optimization iterations. The segmented surface is illustrated in figure 4.68, where the weighed cost function is projected on the plane $z = 0$. The cost function is defined only over the cost range CR, hence the ring-like shape of its contour plot for a spherical bottom surface. The points within the CR located further away from the segmented spherical bottom surface have a reduced weight compared to those points located closer, as seen by the color getting darker on the outskirts of the ring-like representation of the cost function on the plane $z = 0$. Each of the points within the CR is either a model outlier or a model inlier, the latter being shown in yellow color in figure 4.68. If it is a model outlier, i.e. it is located at a distance beyond the threshold T from the surface model, its associated cost is the product of its weight and the square of threshold T, and optionally a predefined constant superior to 1. If the point lies within a distance T, it is a model inlier and its associated cost is the product of its weight and the square of the actual distance to the previously segmented spherical bottom surface (see equation 4.12). The total cost TC is the sum of all the cost contributions of each individual point within the CR, as per equation 4.13.

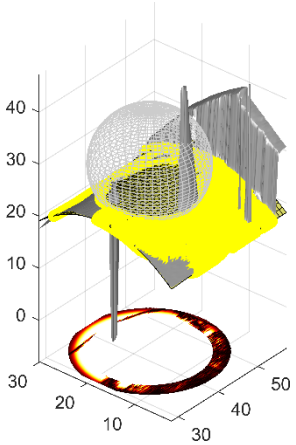

Figure 4.68: Segmented top surface with contour of cost function projected on plane z = 0

In the case of figure 4.68, it is seen that the data points with the biggest weight, i.e. closest to the sphere near the inside of the ring, are for a large part classified as inliers, i.e. low absolute cost. Conversely, many points located further away are classified as outliers, i.e. high cost, but have a comparatively very small weight. Overall, this leads to a relatively low total cost. If the same number of inliers were located more towards the outside of the cost range ring, and outliers towards the inside, the total cost would be much higher. This cost function thus does select for the model that best fits the range data around the cavity, i.e. in the direct vicinity of the bottom surface.

Finally, both the bottom and top surfaces are used to compute the repair volume's envelope according to equation 4.14, as illustrated in figure 4.69.

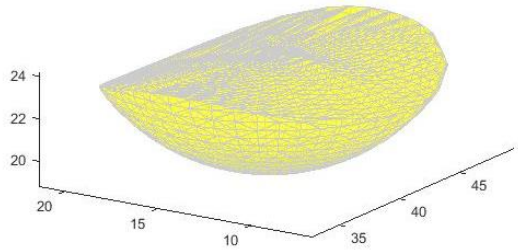

Figure 4.69: Repair volume surface based on top and bottom surfaces analytical representations

To validate the result, the repair volume is embedded into the raw scan data to check for discrepancies, as illustrated in figure 4.70.

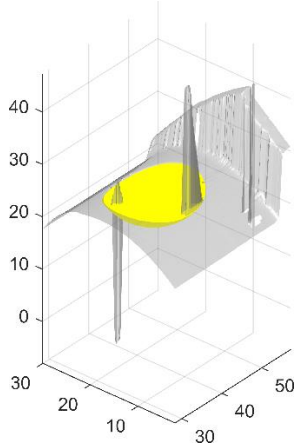

Figure 4.70: Repair volume (yellow) embedded in scan data

The results are summarized in table 4.25 and figure 4.71. The repair volume as obtained by the InterSAC algorithm generally satisfactorily fits the cavity despite the presence of large error peaks. The mean sphere radius is usually very close to the actual radius of 10mm, with the error being typically one order of magnitude below the typical layer thickness of 0.1mm with the LMD experiments of the present work. This envelope is thus sufficiently accurate to

be subsequently utilized for generating tool paths for the LMD process using appropriate CAM software.

Mean Sphere Radius (std. dev.) [mm]	**Mean Repair Volume (std. dev.) [mm³]**
9.976 (0.198)	625.50 (21.65)

Table 4.25: InterSAC Results over 10 runs for a spherical cavity on a curved surface

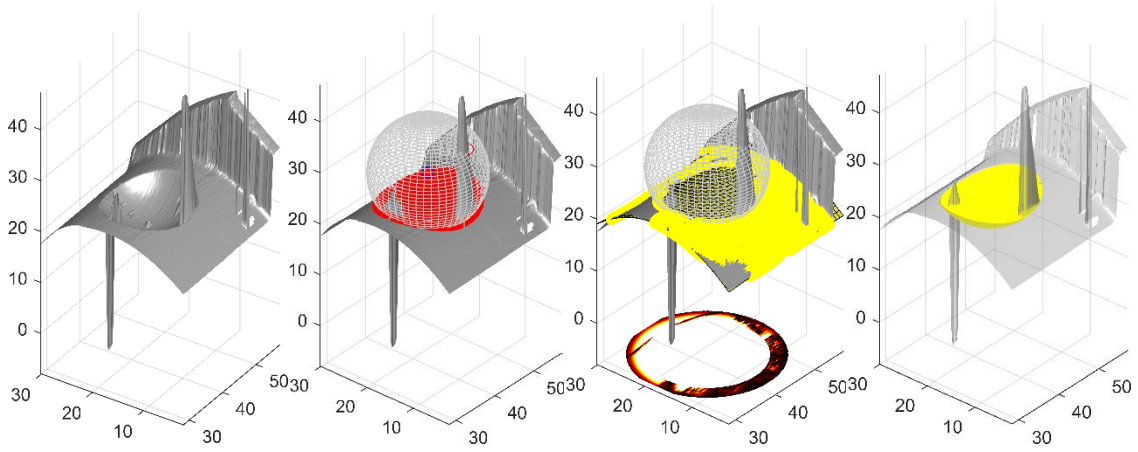

Figure 4.71: Example of segmentation result of a particular run of InterSAC for a spherical cavity on a curved surface - From left to right: raw range data, segmented sphere (inliers in red), segmented algebraic surface (inliers in yellow, cost function represented below), segmented repair volume (in yellow)

2. "Open" Cylindrical groove on freeform surface

The cylindrical groove is milled using a ball nose end mill toolbit traveling along a linear path. Unlike a sphere, a finite cylinder has a direction and two end caps. When the milling tool cuts the part through and through, the extremities of the cylindrical repair volume are capped directly by the neighbouring surface. Here, we call this configuration an "open" cylindrical groove, as opposed to a "closed" cylindrical groove described hereafter.

The distance-based weighing of the cost function with respect to the cylinder model is done by using the geometrical distance between the sample point and the cylinder axis minus the cylinder radius.

The envelope E of the repair volume is then obtained as follows, similarly to equation 4.14, where C is the cylindrical surface, F_C is the implicit cylinder function such that $F_C\ x, y, z\ = 0$, P is the top surface and F_P is its explicit representation function such that $z = F_P(x, y)$:

$$E = \{p \in C \mid z < \ F_P\} \cup \{p \ \in P \mid F_C(p) \leq 0\ \} \tag{4.16}$$

An example is given here after, where figure 4.72 illustrates the "open" cylindrical groove machined with a hemispherical mill of diameter 8mm and its range scan dataset. Figure 4.73 shows the cylinder segmentation, the top surface segmentation and finally the resulting repair volume envelope.

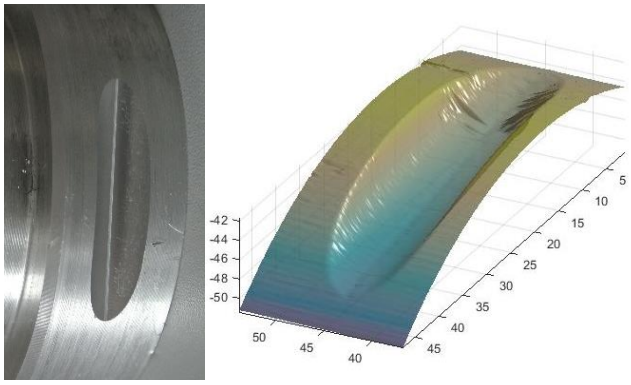

Figure 4.72: Photography of open cylindrical groove (left) –Laser scanner range data (right)

As seen on figure 4.72 (right), the range data presents measurement errors as it is not quite cylindrical near one of the extremities. However, despite those measurement artifacts that are due to concave geometry and reflectiveness of the surface, the repair volume can still be correctly segmented as illustrated in figure 4.73.

Mean Cylinder Radius (std. dev.) [mm]	**Mean Repair Volume (std. dev.) [mm^3]**
3.958 (0.121)	202.60 (7.95)

Table 4.26: InterSAC Results over 10 runs for an open cylindrical cavity on a curved surface

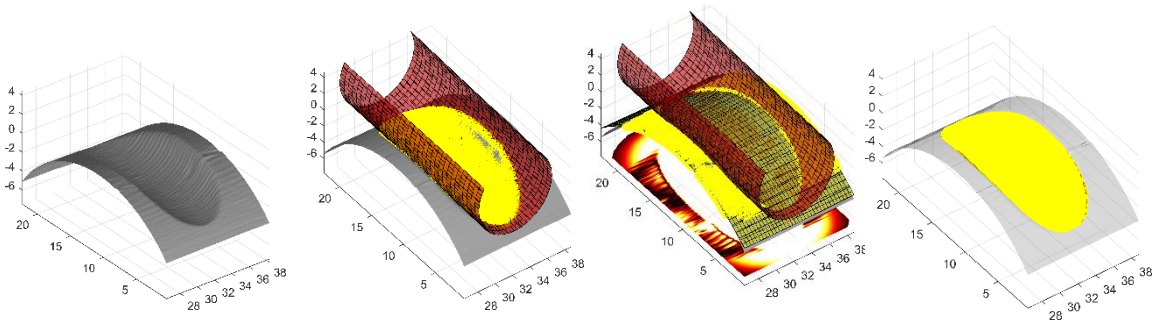

Figure 4.73: Example of segmentation result of a particular run of InterSAC for a cylindrical cavity on a curved surface - From left to right: raw range data, segmented cylinder (inliers in yellow), segmented algebraic surface (inliers in yellow, cost function represented below), segmented repair volume (in yellow)

3. "Closed" Cylindrical groove on planar surface

By a "closed" cylindrical groove, it is meant that the hemispherical milling tool does not cut the part through and through, so that the end caps of the cylindrical groove are spherically shaped, as the hemispherical milling toolbit. The InterSAC approach described so far can be adapted to this cylindrical groove segmentation problem using the sphere segmentation.

In this case, there are 4 shapes to be segmented from the range dataset: the cylindrical body, the two spherical extremities and the neighbouring surface (here a plane). There are two main approaches for this task. A first, more naïve, approach would be to first segment the cylindrical part, and then segment the two end spheres with a prescribed radius equal that of the segmented cylinder. The sampling for the two spheres may be restrained to those data points inscribed within the cylinder. Finally the neighbouring surface can be detected and the repair volume be constructed. Another, more efficient approach would be to first segment one of the end spheres, thereby determining the radius of the groove. With the radius information already available, the other end sphere is then segmented using 3 points instead of 4 as its radius is already determined by the first segmented sphere, and thus only 3 parameters are to be identified for the second sphere. The cylindrical body is then constructed directly based on the two spheres (center positions, radius), without the need to run a third segmentation step. The top surface is segmented in a final step as before. The latter approach is adopted here as it requires one less segmentation step.

The sampling is also adjusted so that data points within a certain range of previously segmented models are ignored, thus forcing the sampling of the second sphere to be carried on an unsegmented portion of the range dataset at a sufficient distance from the first sphere, i.e. the first extremity, in order to limit runtime.

The repair volume's envelope E may then be constructed as follows:

$$\begin{aligned} E = \{p \in C \mid z < F_P \,\&\, proj_A\ p \in [S_{C1}, S_{C2}]\} \cup \{p \in P \mid F_C(p) \\ \leq 0 \,\&\, proj_A\ p \in [S_{C1}, S_{C2}]\} \cup \{p \in S_1 \mid z < F_P \,\&\, proj_A\ p \\ \in [S_{C1}, S_{C1} - AR]\} \cup \{\ p \in P \mid F_{S1}(p) < 0 \,\&\, proj_A\ p \\ \in [S_{C1}, S_{C1} - AR]\} \cup \{p \in S_2 \mid z < F_P \,\&\, proj_A\ p \\ \in [S_{C2}, S_{C2} + AR]\} \cup \{\ p \in P \mid F_{S2}(p) < 0 \,\&\, proj_A\ p \\ \in [S_{C1}, S_{C1} + AR]\} \end{aligned} \tag{4.17}$$

where $p = (x, y, z)$ is the position of a data point, C is the infinite cylinder's surface, S_{C1} and S_{C2} are the positions of the sphere center of the first and second spherical cap, A is a unit vector along the cylinder axis A pointing from S_{C1} towards S_{C2}, $proj_A\ p$ is the projection of

p on the cylinder axis A, R is the radius of the cylinder and spherical caps, and F_P, F_C, F_{S1}, F_{S2} are the explicit or implicit functions representing surfaces P (top surface), C (cylinder), S_1 (first sphere) and S_2 (second sphere).

Reconstructing the repair volume envelope according to equation 4.17 involves generating points on the infinite cylinder, the two spheres and the planar neighbouring surface. The points on the spheres and cylinder that are located above the plane are discarded. The points on the plane located beyond the cylinder-spheres assembly are also discarded. The remaining points on the cylinder that are beyond the two spheres' center points are removed, and the remaining points on the spheres that are between the two spheres' center points, inside the cylindrical part, are also removed. The remaining points define the repair volume envelope, whose volume may then be computed using a convex hull or concave hull algorithm.

An example is given below in figure 4.74, which illustrates a "closed" cylindrical groove, its range data from the laser scanner, the spherical caps segmentation and resulting cylinder, the top surface segmentation and finally the resulting repair volume envelope.

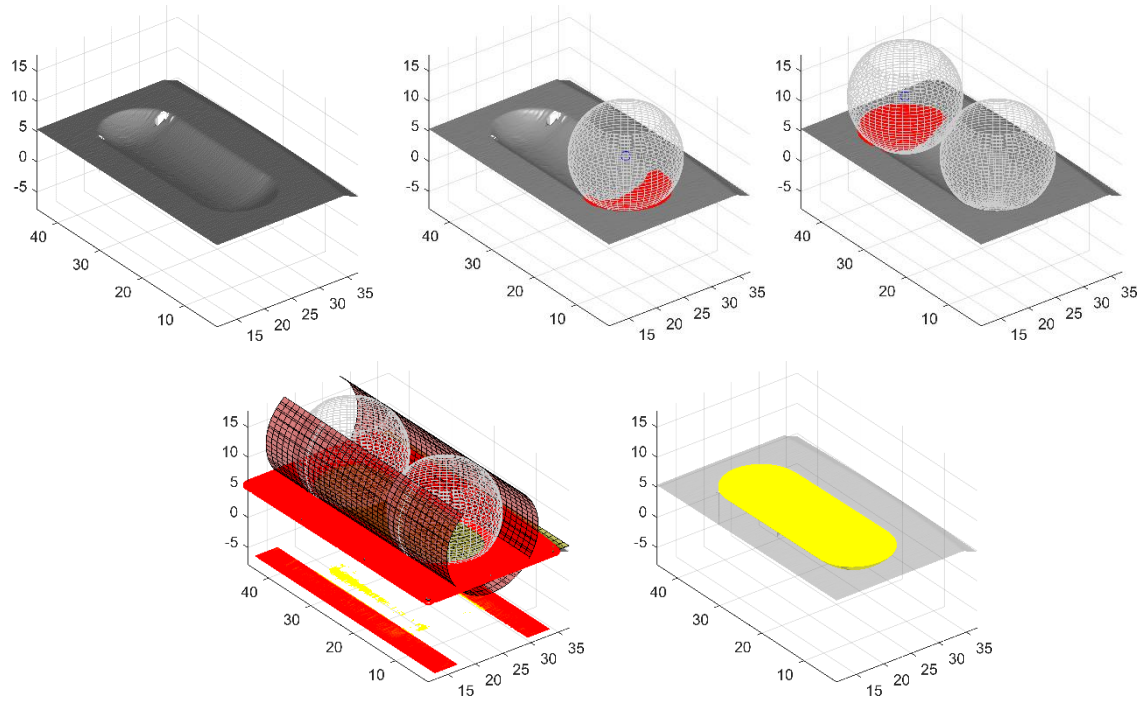

Figure 4.74: Range data of cylindrical groove with spherical end caps (top left) – First segmented sphere using 4 points (top middle) – Second segmented sphere using 3 points and fixed radius (top right) – Cylinder from 2 spherical end caps and top surface segmentation (bottom left) – Segmented repair volume (bottom right)

In this case, after 74 RANSAC iterations for each end sphere and 23 RANSAC iterations for the planar neighbouring surface, the radius of the groove is found to be 7.67 mm (theoretical value: 8 mm, i.e. around 4% error) and the volume is around 667.9 mm^3.

Instead of spherical end caps, planar end caps can be defined. In this case, the cylinder is segmented first, as in the case of the "open" cylindrical groove. The planar end caps are then fitted through the cylinders inliers lying at the extremities, as shown on figure 4.75. Despite the presence of numerous spurious peaks in the raw range data, the cylinder and the overall repair volume envelope could be found with satisfactory accuracy.

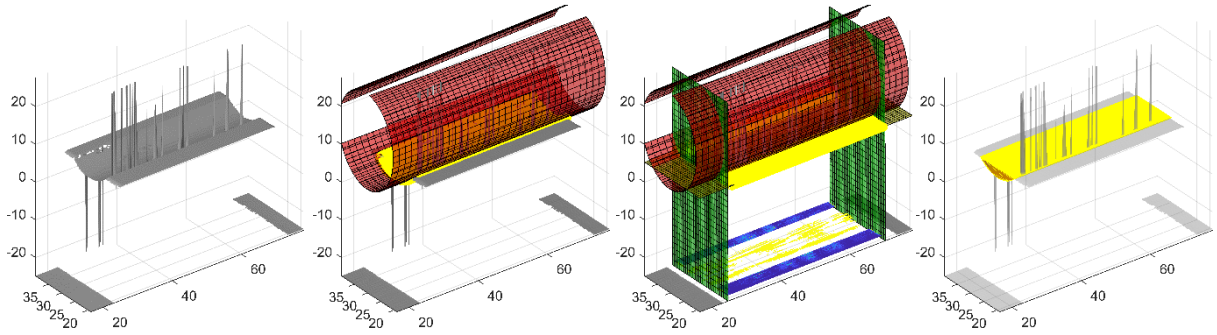

Figure 4.75: Range data for cylindrical groove with planar end caps – Cylinder segmentation – Planar end caps and top surface segmentation – Segmented repair volume (from left to right)

b. Limitations and Extensions of InterSAC

The InterSAC algorithm, published in (Hascoët et al. 2018a; Touzé et al. 2018) provides a new cost function to the RANSAC-based fitting process to improve the performance of the top surface segmentation. Together with its local optimisation step, the RANSAC-based InterSAC algorithm provides a reasonably accurate and repeatable segmentation of repair volumes for fairly general surface types.

Thus, with InterSAC, repair volume envelopes can be segmented directly from raw range data even in the presence of noise and spurious peaks, which is typically expected with parts made of reflective materials such as aluminium alloys. Moreover, the edges of the segmented repair volume should reflect the true edge of the cavity, which can differ from the raw range data where the edges can be artificially smoothened by the range scanner. The raw range data can be given in a structured manner on a grid, or in an unstructured manner as a point cloud depending on the type of range scanning device used for the measurement of the local geometry. In the case of a point cloud, a few adjustments are required such as pre-computing inter-points distances for NAPSAC sampling, but the method is equally applicable.

The top surface model fitted on the range dataset may also be used for the finishing step, as the LMD process is usually programmed to overfill the cavity, for example using level sets of the neighbouring surface function. This is done to ensure that the cavity is fully refilled.

A finish machining step is thus performed to remove the extra layers of deposited material, which can be guided by the analytical model of the top surface.

For the InterSAC algorithm to be applicable, the cavity must be a (composite) shape which is sufficiently smooth to be accurately represented by an analytic surface or a set of analytic surfaces with a known general analytical expression (in explicit or implicit form). A suitable toolbit and milling trajectory must thus be chosen by the human operator. Regarding the top surface, its shape (e.g. plane, cylinder…) could also be indicated by the human operator if it corresponds to a particular primitive, or it could be generally approximated using algebraic surfaces of sufficiently high order. In practice, an order between 1 and 3 is usually sufficient. Note also that care should be taken if the cavity and the surface on which it is machined have the same general shape (e.g. a sphere), or if there are multiple instances of cavities with the same shape model, as with most RANSAC-based methods. If there are several instances of the same shape model within the range data, whether due to multiple similar cavities or the top surface being of the same general shape as the cavities, then the sampling data set for each instance of the shape should be mutually exclusive. For instance, the consensus set of the firstly segmented instance of the shape model should be discarded of the sample pool for segmenting the next instance. Moreover, a maximum characteristic dimension (e.g. radius for a sphere) could also be set for each instance.

The InterSAC method presented so far requires selecting the general shape of the bottom surface of the cavity, but it could be extended by using a library of shape models with a multiBaySAC (Kang and Li 2015) or multiRANSAC (Zuliani et al. 2005) algorithm to tentatively segment multiple types of models and automatically select the relevant shape models.

Another possible extension could consist in more systematically allowing for composite shapes for the cavity, as in the case of cylinders with spherical caps. If the cavity is a combination of canonical shapes (spheres, cylinders, cones etc.), and some information is available regarding their connectivity, then the calculation of the repair volume envelope could in principle be performed, similarly to equations 4.14 to 4.17.

IV. Summary

In this chapter, a repair methodology and its implementation were presented, where an in-situ range scanner is used to gather geometrical information on the defective part mounted in the LMD workspace.

The InterSAC algorithm devised in this work allows for segmenting the repair volume and generating the corresponding CAD file based on raw range data from the range scanner. The robustness, accuracy and repeatability of the algorithm were shown to be satisfactory for a repair application as the error on characteristic dimensions (e.g. sphere radius) is about an order of magnitude lower than the layer thickness (about 0.1mm) generally obtained with the LMD head of the present work.

The experimental setup and the InterSAC algorithm presented in this chapter effectively provide the necessary 3D information to generate the toolpaths for the LMD nozzle and the corresponding machine code.

The repair methodology of this chapter and the powder flowability analysis presented in the previous chapters allows to contemplate repairing an actual defect with the 224.0 aluminium alloy powder. The last remaining step is the LMD process parameter setting, which is presented in the next chapter together with a metallographic analysis of the LMD deposits with aluminium powder 224.0.

Chapter V: Aluminium-Copper Casting Repairs with Laser Metal Deposition

Abstract

This chapter first provides a theoretical assessment of the solidification behavior of alloy 224.0 based on numerical models. Experiments are then conducted to identify suitable operating parameters for the LMD processing of alloy 224.0 based on thin-wall deposits. The results are further confirmed with the deposition of full blocks. Eventually, cavity repairs are on a high performance 224.0 casting based on previous findings, and a metallurgical evaluation of the deposits is performed and is ultimately compared to that of the cast part.

I. Solidification of Alloy 224.0

a. CALPHAD-based assessment

Alloy 224.0 (Al-Cu-Mn-Ti-V-Zr) is a challenging material to process by traditional manufacturing and welding processes such as lost-wax casting and GTAW, notably because of its propensity to copper segregation and hot cracking during solidification. Premium high performance 224.0 castings are thus not only difficult to manufacture but are also hard to repair with standard welding processes. For these reasons, it is not commonly employed in the aeronautics industry despite its high mechanical properties at elevated service temperature (up to about 200°C).

This 224.0 alloy is also not extensively characterized in the literature, so that many of its temperature-dependent physical properties are not typically known, or are only available at specific temperatures for a baseline chemical composition that may not reflect the exact compositions, and thus properties, of the particular 224.0 alloy used for LMD repair experiments. For instance, the weight percent range of copper in standard 224.0 specification is between 4.5 and 5.5wt%Cu, which is a fairly large range considering the sensitivity of segregation and hot cracking susceptibility (HCS) to copper concentration (see chapter 1). The actual concentration of 224.0 alloy for both the LMD powder and the defective cast part is around 4.7wt%Cu, which is in the lower region of the specified 224.0 copper concentration range. This can contribute to the relatively high HCS of this alloy composition, since higher copper content (as in alloy 2219 with 6.3wt%Cu) typically induces more liquid eutectic near the end of solidification that can backfill hot cracks and thus limit this type of defect. However, increased copper content can modify the mechanical properties and affect corrosion resistance of the manufactured part so a compromise has to be made in terms of copper content.

The temperature-dependent properties of an arbitrary alloy composition such as its enthalpy, heat capacity, density or viscosity, as well as key thermodynamics properties such as liquidus and solidus temperatures, are important parameters to relate processing conditions to the solidification behavior of the material, whether it be through analytical assessments (see section on combined heat input parameter) or numerical simulations (see section on LMD melt pool and bead deposit simulation).

The CALPHAD (CALculation of PHAse Diagrams) method has had notable success so far in calculating thermodynamic phase diagrams for multicomponent industrial alloys (Lukas et al. 2007; Perrut 2015). It essentially relies on thermodynamic databases, usually in TDB format, to provide information on chemical elements and phases such as their Gibbs free energy G, which is minimal at equilibrium in an isobaric, isothermal system with fixed composition.

Polynomial phase models are expressed based on elemental Gibbs energy functions, and the polynomial coefficients are typically fitted to experimental data to yield a realistic representation of the Gibbs free energy function of each phase at various conditions of temperature, pressure and composition. A phase diagram can then be computed over a discretized range of temperatures and elemental compositions by minimizing the total Gibbs energy of the system at every temperature-pressure-composition condition and thereby identify the stable equilibrium phases. Multicomponent phase diagrams can be deduced from unary, binary, and ternary diagrams, and thus provide a reasonable thermodynamic assessment of such complicated systems for which experimental data is not always available. In addition to phase diagrams, a number of other state variables and properties can be derived according to classical thermodynamics relations and for example give the temperature dependence of the enthalpy, entropy and heat capacity of the system based on the Gibbs energy function of the alloy system.

The CALPHAD method has been implemented in commercial software such as ThermoCalc©, PandaT©, MatCalc© or JMatPro© that are provided with encrypted thermodynamic databases, usually in TDB format, and atomic mobility databases for diffusion problems. In this work, an open-source alternative to these commercial packages called OpenCALPHAD (Sundman et al. 2015) was used to assess the Al-Cu-Mn system based on an open-source, unencrypted thermodynamic database for Al alloys from MatCalc (MatCalc 2015). Due to the absence of some elements such as vanadium V in the database, the calculations were performed for the system Al-Cu4.7-Mn0.23, ignoring minor alloying elements V and Ti as well as trace elements such as Si and Fe. This also helps in preventing unphysical results as it is unclear whether the database is entirely accurate, although it is said to have been validated in Al-rich systems ($>$ 90wt%Al) with elements Al, Cr, Cu, Fe, Mg, Mn, Ni, Si, Ti, Zn, and Zr.

The first set of calculations consisted in a mapping of the binary Al-Cu system, which can be compared to experimental results. The global phase diagram with a focus on the Al-rich side is shown in figure 5.76 and figure 5.77. The results are in close agreement with the typical Al-Cu phase diagram (see chapter 1), notably in terms maximum solubility limit of copper near 5wt%Cu and eutectic composition near 33wt%Cu. This could be expected considering that the binary Al-Cu system is well characterized and that the CALPHAD method leverages experimental data in phase models. Adding other elements however triggered convergence issues that could not be resolved, although the alloy elements besides Cu are present in small quantities ($<$ 1wt%) so that the Al-Cu phase diagram should not be significantly altered when including these other elements.

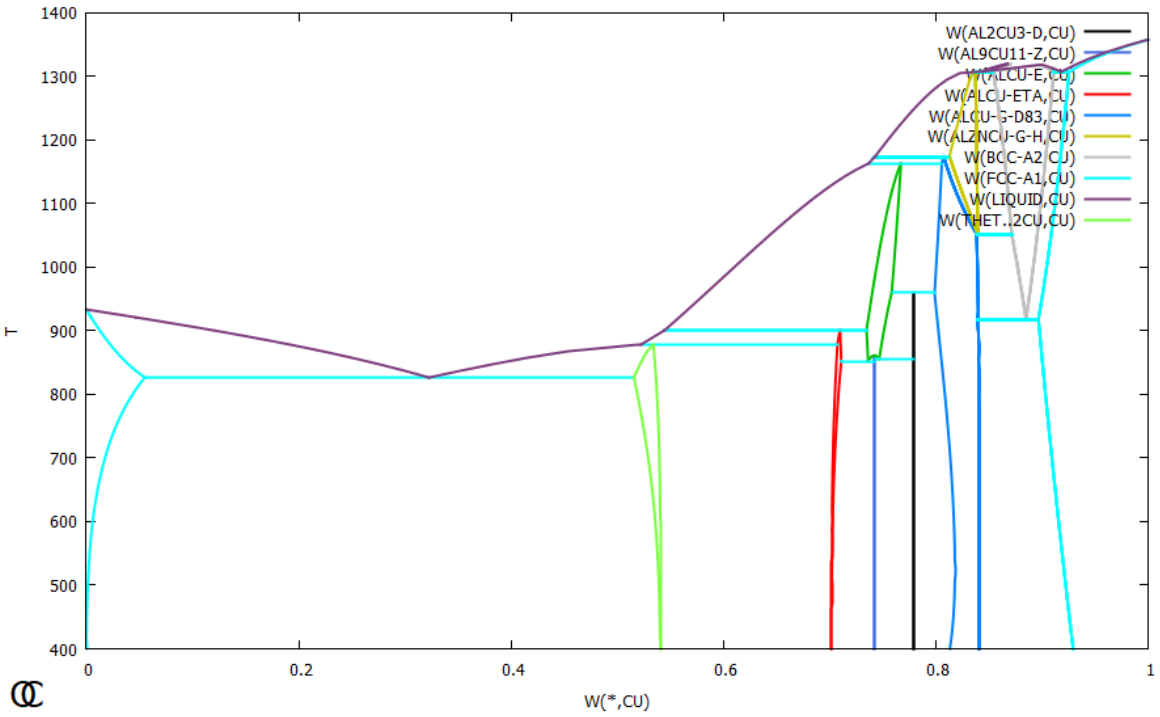

Figure 5.76: Phase diagram of the binary Al-Cu system computed with OpenCALPHAD code and MatCalc© open database

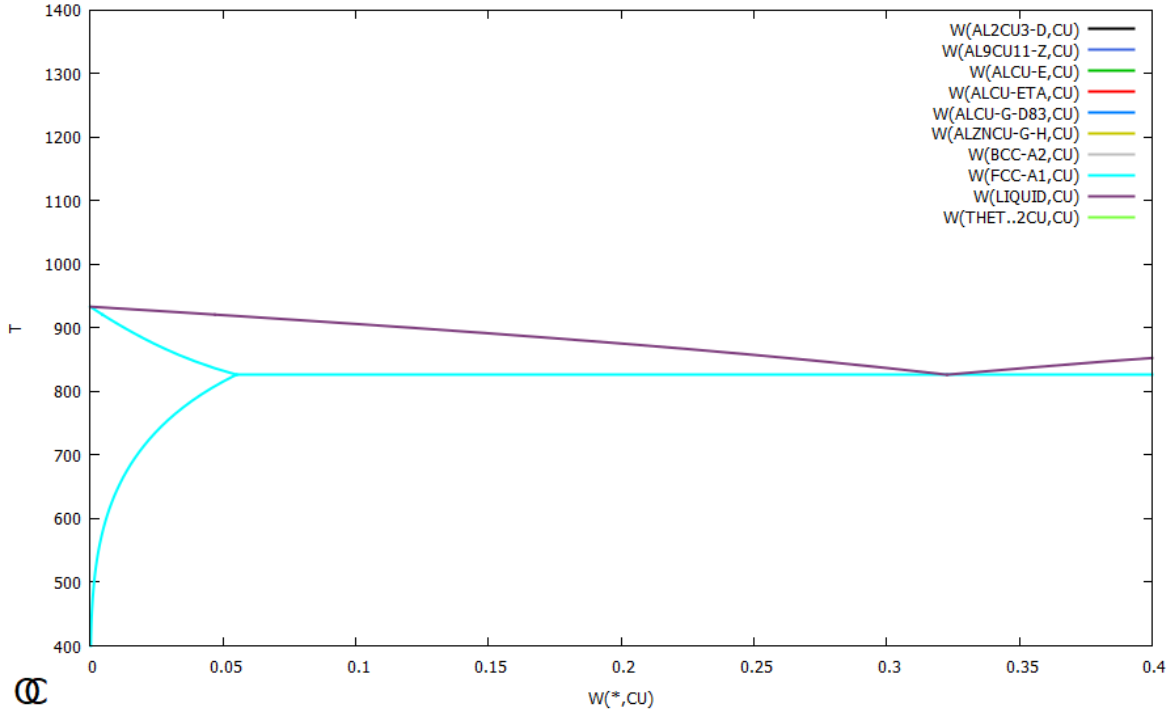

Figure 5.77: Focus on the Al-rich side of the phase diagram of the binary Al-Cu system computed with OpenCALPHAD code and MatCalc© open database

A step calculation was performed on alloy 224.0 (Al-Cu4.7-Mn0.23-0.16Ti-0.13Zr) to yield the equilibrium phases formed by cooling from the liquid to solid state, resulting in the molar composition curve of figure 5.78. It is seen that the main phases present at the end of a quasi-equilibrium solidification are FCC-Al and θ-Al_2Cu. The corresponding enthalpy curve is shown in figure 5.79 and the specific heat, i.e. the derivative of enthalpy with respect to temperature, is displayed in figure 5.80. These results could be a suitable approximation of various temperature-dependent thermodynamic and physical properties when experimental data is lacking, it assumes that solidification occurs in quasi-equilibrium according to the lever rule, so that the phase composition from figure 5.78 cannot be relied upon for rapid solidification processes.

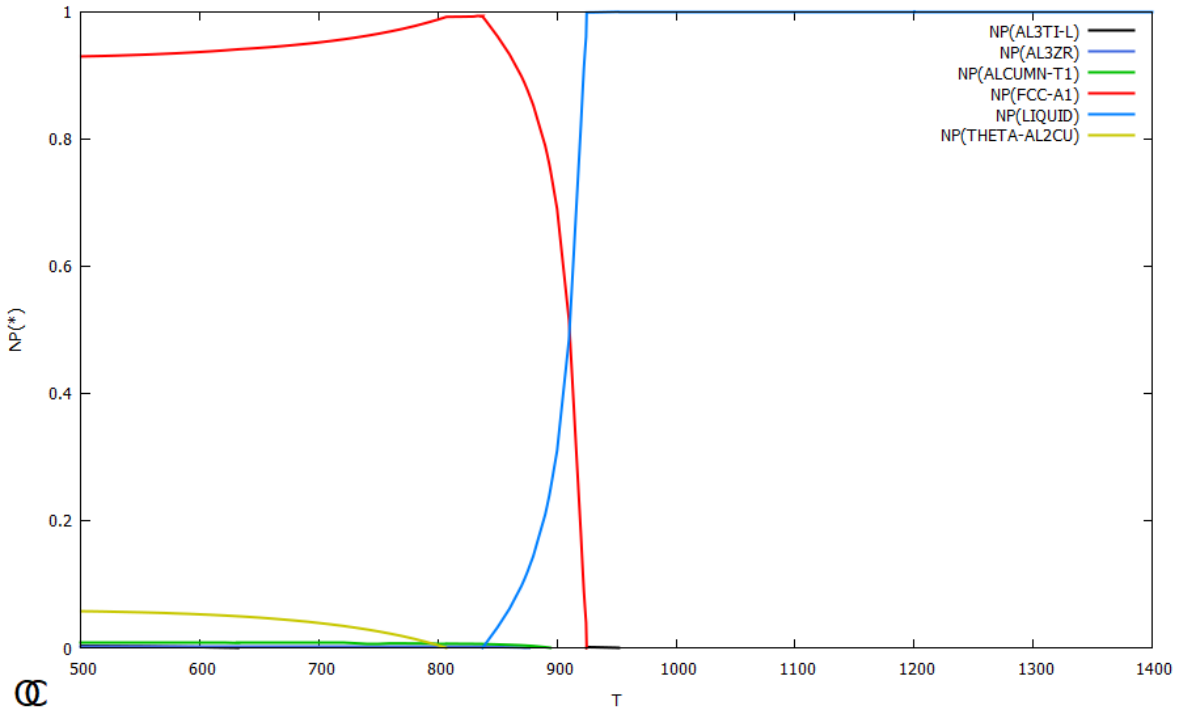

Figure 5.78: Molar composition of phases vs. Temperature (K)

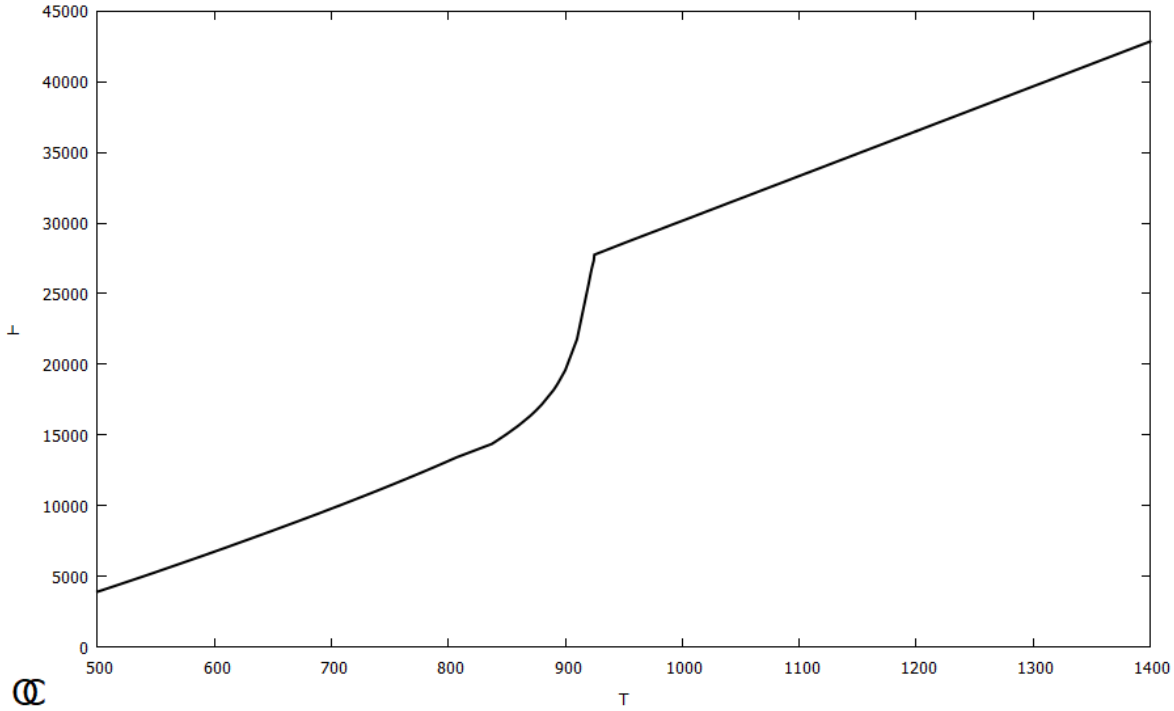

Figure 5.79: Enthalpy (J/mol) vs Temperature (K) of 224.0 alloy according to CALPHAD calculations

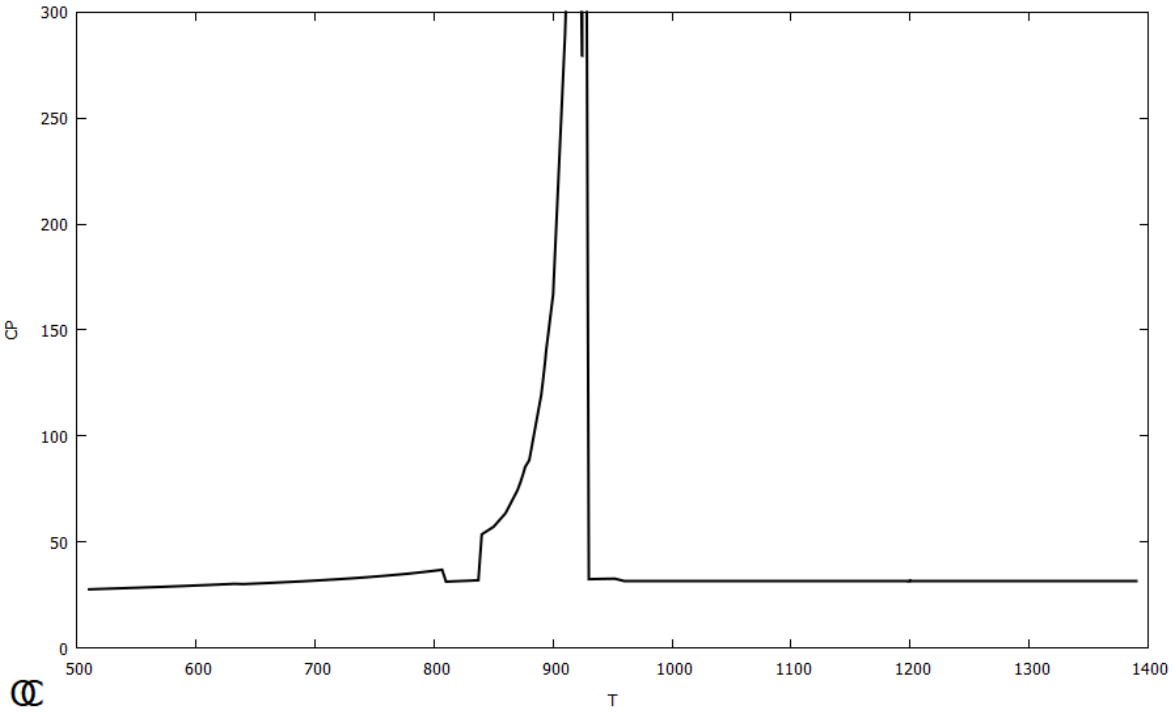

Figure 5.80: Specific heat (J/mol.K) vs. Temperature (K) according to CALPHAD calculations (erroneous peak corresponds to melting range)

b. Hot cracking susceptibility

Instead of using the lever rule, the Scheil solidification model (Kou 2003) can be used instead in conjunction with the thermodynamic database and the OpenCALPHAD code to yield a more appropriate solidification model. Although not directly applicable to rapid solidification processes where kinetic effects at the solidification interface typically influence the solidification path, segregation phenomena and phase composition, it nonetheless gives an upper bound on the extent of element segregation and yields a solidification curve (temperature T vs. solid fraction f_S) that can be used to compare the HCS of various alloys using the Kou criterion (Kou 2015a; b). This Kou criterion, recalled in equation 5.1, has a fairly simple expression and can be directly calculated from the solidification curve.

$$HCS = max \;\; dT/d(\sqrt{f_S}) \tag{5.1}$$

A Scheil calculation add-on to the OpenCALPHAD software was run on alloy 224.0 as well as alloys 2219 and 2024 for comparison. The direct coupling between the Scheil solidification model and the CALPHAD thermodynamic models has the benefit of accounting for the actual curvature of the liquidus and solidus during solidification, unlike purely analytical assessments where the Scheil calculation is usually performed on a linearized phase diagram (see chapter 1). The solidification curves according to the Scheil-CALPHAD calculations are shown in figure 5.81. The Kou criterion was calculated on this discrete curve by using a backward finite difference scheme for the derivative and finding its maximum along the solidification curve, which occurs near the end of solidification. The results are displayed in

figure 5.82, which shows that the HCS of 224.0 is slightly higher than 2024, an alloy largely reported to have a low weldability and is seldom welded with traditional welding processes such as GTAW. The calculated HCS of both 224.0 and 2024 are much higher than that of 2219, which is in contrast one of the few weldable alloys of the 2xxx series due to its high copper content (6.3wt%Cu). The HCS results are thus coherent with common experimental observations regarding the relative weldability of alloys 2024 and 2219, and also further demonstrate the low weldability of cast alloy 224.0 that prevents repairs with a GTAW process.

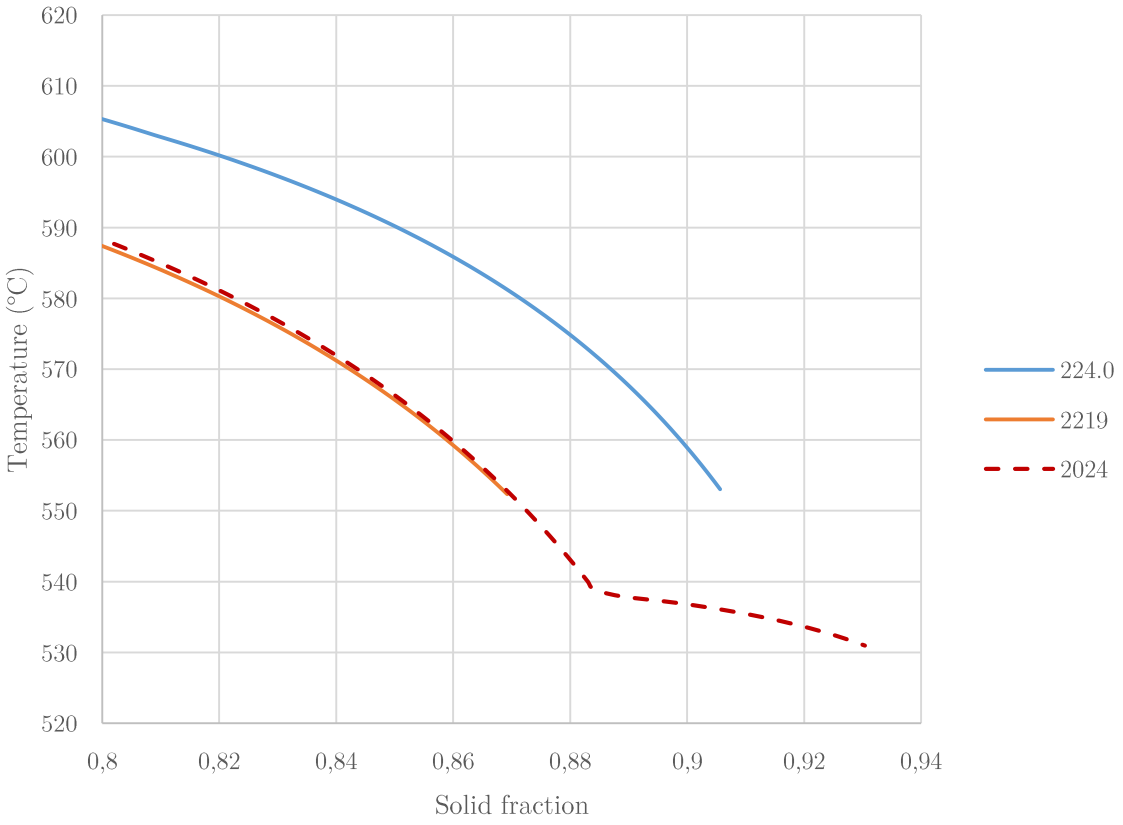

Figure 5.81: Solidification curve of alloys 224.0, 2219 and 2024 according to the Scheil model with OpenCALPHAD coupling

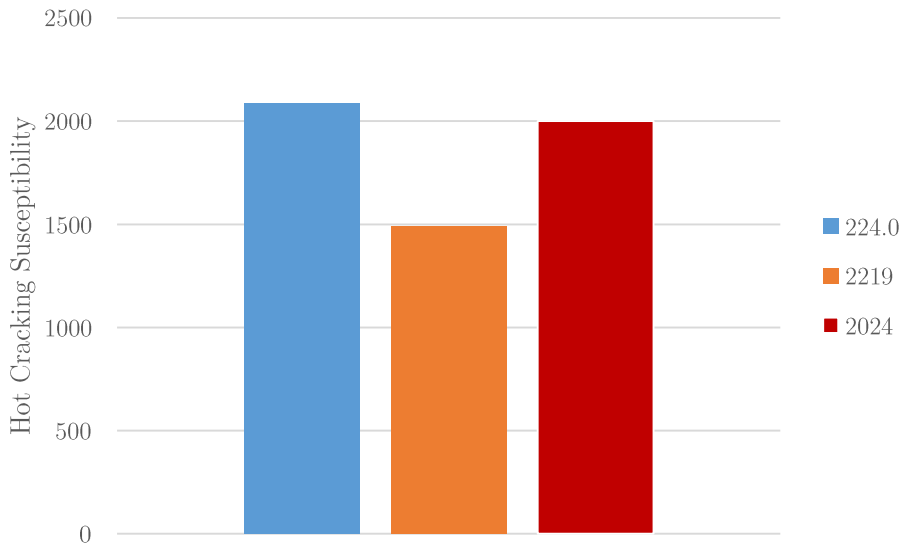

Figure 5.82: Hot Cracking Susceptibility of alloys 224.0, 2219 and 224.0 according to the Kou criterion and CALPHAD calculations

Although the solidification curve calculation does not end at the same solid fraction for the 3 alloys, these results demonstrate that the Scheil-CALPHAD coupled model can in principle reasonably predict the relative HCS between various aluminium alloys. There are however limitations with the current results as the open thermodynamic database and Scheil calculations would have to be further validated to provide quantitative results. This shows nonetheless that open-source tools could in the end be used to theoretically assess the solidification behavior of a material under quasi-equilibrium conditions according to the Scheil model, which provides an upper bound on the solute segregation phenomenon and allows to compute a HCS criterion.

The solidification sequence of alloy 224.0 (without elements Ti and V) predicted by the Scheil-CALPHAD coupling based on the open thermodynamic database from MatCalc© is given in table 5.27, which suggests that the only phases present in the fully solidified material are Al_3Zr, Al (fcc) and θ-Al_2Cu. This is unlike the equilibrium solidification sequence where the AlCuMn_T1 phase remains. It is however noted that this is valid for near equilibrium solidification conditions, which may be applied to casting processes and extended to arc-welding process but may not be valid for laser melting processes such as LMD where kinetic effects would likely change the composition and possibly the phases that are present at the end of solidification.

Temperature	**Solid fraction**	**Phases**
647.04	0	LIQUID
645.04	0.148	FCC_Al + LIQUID
626.04	0.659	ALCUMN_T1+FCC_Al+LIQUID
603.04	0.813	AL3ZR+ALCUMN_T1+FCC_Al+THETA_Al2Cu
553.04	1	AL3ZR+FCC_Al+THETA_Al2Cu

Table 5.27: Solidification sequence of alloy 224.0 according to coupled Scheil-CALPHAD calculations

c. LMD process modeling and simulation

In an effort to model the LMD process and evaluate the solidification behavior of alloy 224.0, a multiphysics modeling approach was pursued with Flow3D© based on a Volume of Fluid (VOF) method. Unlike many modeling approaches of the LMD process that adopt a finite-element method (Peyre et al. 2017; Tran et al. 2017), the VOF method allows for a computational fluid dynamics simulation of multiphase flows that resolves the interface between the solidifying material and the ambient atmosphere. Additional physical models allow to account for the laser heat source, the solidification behavior and the inflow of material

in particle form. A realistic shape for the deposit can thus be obtained with this method, which can eventually lead to more reliable models based on actual physical parameters of the alloy.

Some of the assumptions for the VOF model are as follows:

- Particles have a diameter of 100µm
- Particle temperature is 298K
- Particles do not interact with laser but are preheated by the ambient atmosphere set at 500K to emulate laser preheating
- Laser absorptivity varies from 0.1 in the solid state to 0.6 in liquid state
- Substrate is 5mm-thick and 3mm-wide, with continuative boundary conditions in the X-direction and atmospheric pressure at the top plane along the Z-axis
- The liquidus temperature, solidus temperature and solidification curve were computed with the Scheil model using OpenCALPHAD
- Other material properties were based on Al-4.5wt%Cu temperature-dependent properties (e.g. material density, thermal conductivity, viscosity) available in the software database

The simulated process parameters for 3 different conditions are shown in table 5.28 and some of the material properties used for alloy 224.0 are given in table 5.29. These conditions are relatively close to actual process parameter values used later on (600-700W, 2000 mm/min at about 2g/min).

Simulation	**Powder flowrate (g/min)**	**Laser Power (W)**	**Scan Speed (mm/min)**
A	2	600	2000
B	2	900	2000
C	1	600	2000

Table 5.28: Input process parameters for LMD process simulation with VOF method

Liquidus temperature (°C)	**Solidus temperature (°C)**	**Specific heat (J/kg.K)**	**Latent heat (J/kg)**	**Surface tension (N/m)**	**Laser absorptivity**
647	553	850-1140	3.89e5	0.91	0.1-0.6

Table 5.29: Material properties used for simulating the solidification of 224.0 alloy based on CALPHAD results and Flow3D© database for Al-4.5wt%Cu

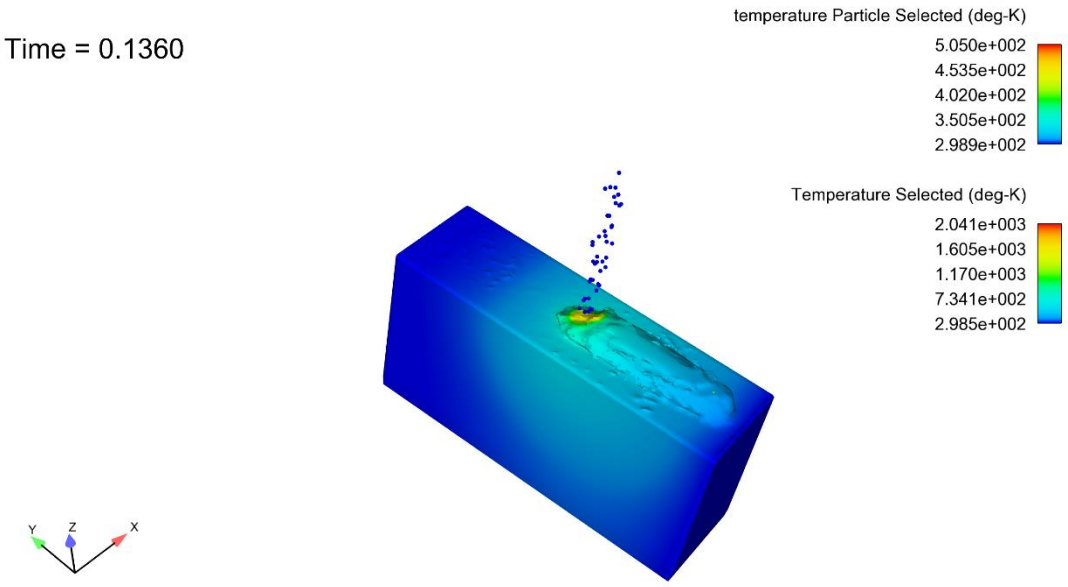

Figure 5.83: Temperature field for simulated LMD bead deposit according to simulation condition A

The particles are effectively melted at a laser input of 600W, which is fairly close to experimental observations. The resulting layer width and height are estimated at about 1.5mm and 0.49mm, respectively, for simulation condition A. When doubling the input laser power, as in simulation condition B, the layer height decreases to 0.39mm while the width increases to 2.3mm. In simulation condition C, where the powder input is halved, the layer width is barely impacted while the layer height decreases significantly to 0.3mm. These values are in reasonable agreement with experimental results shown later on where layer height is on the order of 0.1-0.2mm and width is on the order of 2mm. The layer height is however slightly higher in the simulation than in the experiments, possibly due to errors in estimating the surface tension and its variation with temperature.

This VOF simulation approach is able to provide a realistic geometry of the deposit using appropriate models for the laser and particle inflow, which is a significant improvement over the finite-element based LMD models for which an approximate geometry is assumed a priori.

While further work would be required to link these results to experimental observations, these simulation outcomes suggest that the layer width is hardly impacted when changing the powder flowrate, unlike the case of a significant laser power increase, in which case the layer width is the most affected. Indeed, the change in laser power significantly changes the temperature of the melt pool, which influences the lateral spread of the melt pool due to a decrease in viscosity and surface tension. Changing the material input flowrate however mostly affects the height of the layer as the temperature field is not as impacted, especially for a single bead where a lot of the laser energy is dissipated through the substrate.

Simulation	Powder flowrate (g/min)	Laser Power (W)	Scan Speed (mm/min)	Layer width (mm)	Layer height (mm)
A	2	600	2000	1.5	0.49
B	2	900	2000	2.3	0.39
C	1	600	2000	1.4	0.3

Table 5.30: LMD bead geometry according to VOF simulation

This model was also used to simulate multilayer deposits to form a 1cm-long thin wall using parameters form simulation A for a simulated time of about 3s, yielding the results illustrated in figure 5.84 and figure 5.85. The average temperature of the deposit and vorticity of the melt pool increase while the mean kinetic energy in the melted region remains roughly constant. The computational cost becomes quite high as the number and size of the layers increase, which currently limits the possibility of performing simulations on realistic deposits such as thin walls and cavity repairs. This cost is mostly associated with the tracking of the free surface and computing surface tension effects. At the melt pool scale, it could also be employed to assess the melt pool behavior including its temperature and velocity field, and evaluate thermal gradients and cooling rates during this rapid solidification process.

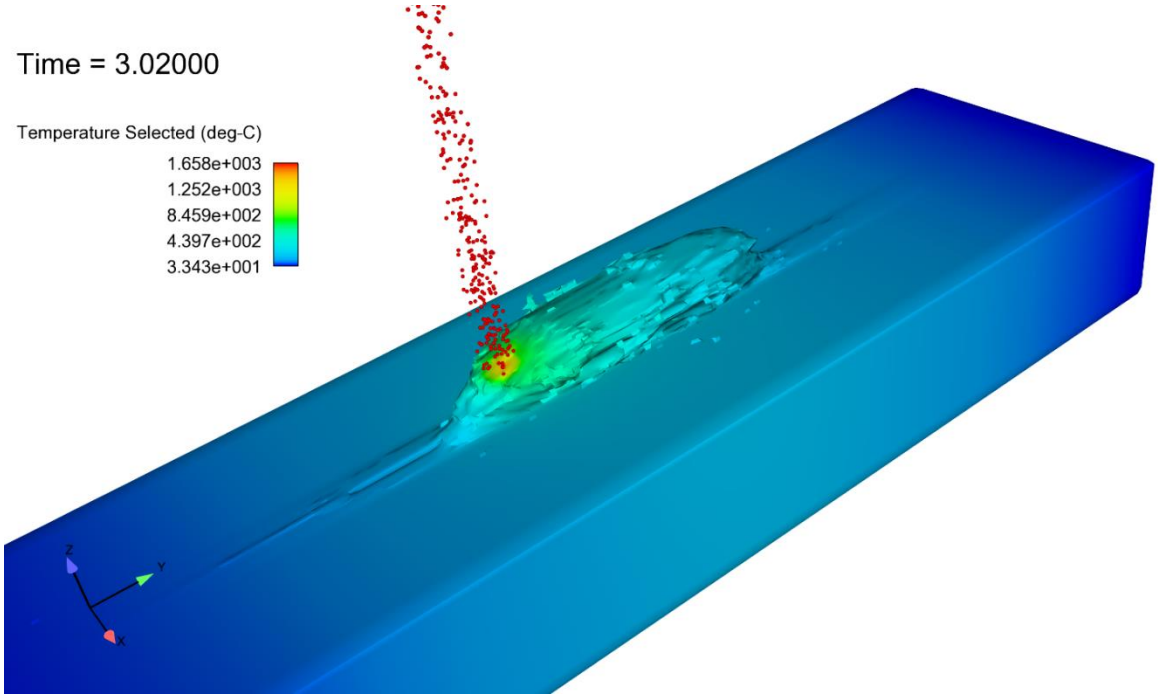

Figure 5.84: Single track wall simulation by VOF method according to parameters from simulation A

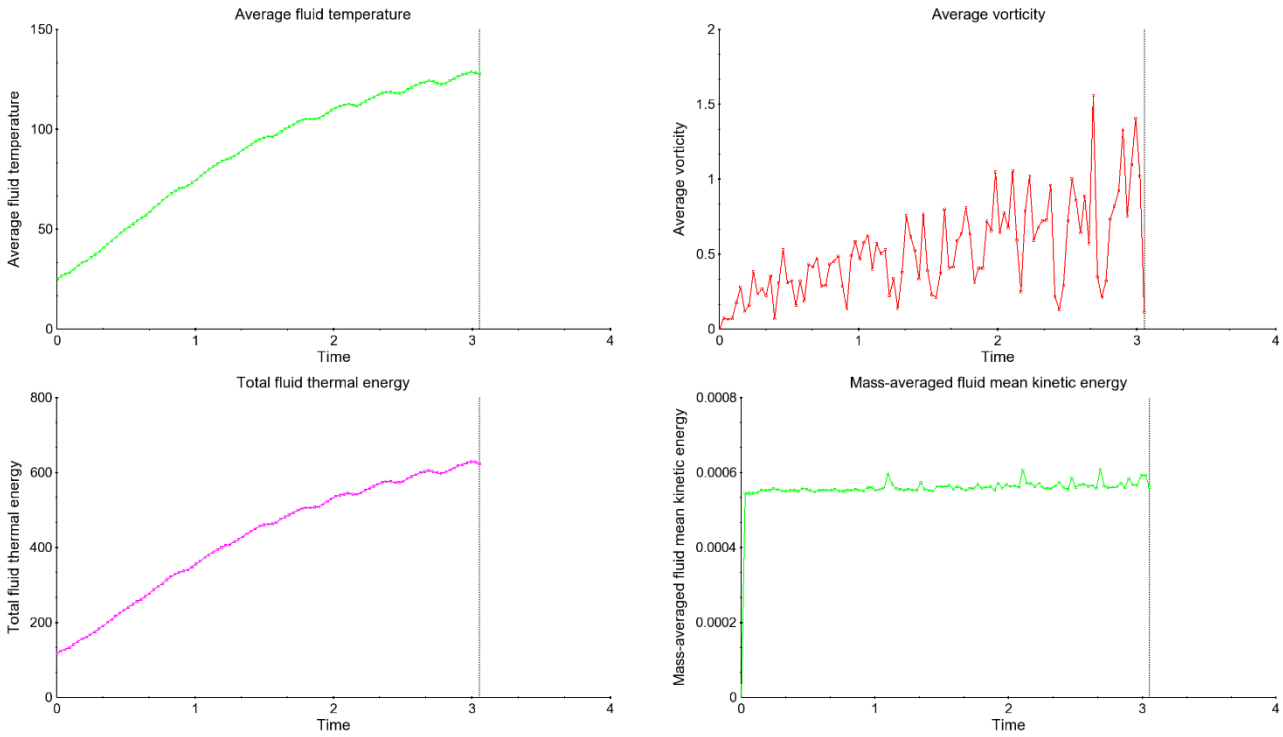

Figure 5.85: Plots of various quantities of interest (average fluid temperature, vorticity, thermal energy and kinetic energy) during the simulated deposition of a thin wall

d. Phase Field modeling

The end goal of the theoretical and numerical assessment of a challenging alloy such as 224.0, for which high copper segregation and cracking susceptibility can be expected, would be to evaluate a priori its solidification behavior depending on processing conditions such as thermal gradients and cooling rates at the solidification interface of the melt pool. Indeed, solidification during casting can generally be considered as occurring near equilibrium so that the Scheil model may be applicable, especially for Al-Cu alloys where the solid diffusivity of copper in the aluminium matrix is almost negligible compared to other solutes such as Mg. The assumption of zero solute diffusion in the solid phase and equilibrium at the interface then holds and the Scheil model can be applied. For more rapid solidification conditions with high cooling rates and thermal gradients, as encountered in laser-based processes such as LMD, kinetic effects at the interface may arise, leading for example to a solute trapping effect where solute atoms cannot migrate in time towards the liquid phase due to the rapidly advancing solidification front. Solute atoms are then partially trapped in the solid phase where their diffusivity is much lower, which leads to reduced segregation levels.

Phase field models allow to numerically simulate a number of physical phenomenon such as solidification without explicitly tracking a sharp interface, making use instead of an

order parameter, or phase field variable, which is a scalar field that varies continuously across the interfacial region. It typically results in a partial differential equation (PDE) with the phase field variable as a dependent variable. Phase field models can be applied to alloy solidification problem by coupling the phase field PDE to a diffusion PDE that models solute diffusion. Due to the non-zero thickness of the diffuse interface in phase field modeling, artificial solute trapping naturally arises from the solution, thereby requiring the phase field interface thickness to be extremely small for correspondingly extremely small time steps. An anti-trapping current was therefore added to the solute equation to compensate for this effect and, together with appropriate interpolating functions, could lead to a phase field model that converges to a thin interface solution, which enables much larger interface thickness to be used in practice while suppressing the artificial solute trapping effect (Echebarria et al. 2004; Karma 2001). Although this led to results such as the dendrite tip velocity being independent from the interface thickness, it however assumed equilibrium at the interface so that kinetic effects such as solute trapping are not included. This quantitative model has thus been constrained to low solidification conditions. Recently, this model was augmented by modifying the interpolating functions and coefficients so that a controllable chemical potential jump at the interface could be obtained, which could effectively map the partition coefficient to a particular velocity-dependent segregation model such as the well-known Continuous Growth Model (Pinomaa and Provatas 2019). This allows to control the segregation level in the phase field model and account for kinetic effects at the interface.

A Python code was developed in the present work using the FiPy library (Guyer et al. 2009) to solve for the coupled PDEs of the well-known EFKP model (Echebarria et al. 2004) in dimensional form, including the modifications given in (Pinomaa and Provatas 2019) to obtain a more accurate solute segregation behavior. The simulation was setup for a generic Al-4.7wt%Cu alloy based on a linearized phase diagram with equilibrium partition coefficient $k_e = 0.14$. A Cartesian grid of 1000x400 cells was used, corresponding to a domain size of 259x103µm. The coupled PDEs were solved by an implicit solver with a constant time step of about 3µs and an interface width 20 times larger than the capillary length. A constant temperature of 5°C below the solidus temperature was used, and the results are displayed in figure 5.86. The simulation starts with a perfectly flat interface on the left hand side, which becomes gradually perturbed due to the inclusion of noise in the PDEs to eventually yield a coarsening columnar structure with higher copper content in the intercolumnar regions where a dotted segregation pattern is generated.

While further work is required to quantitatively evaluate the convergence and accuracy of the results and their variation with processing conditions, such phase field models open the way towards the quantitative simulation of rapid solidification conditions encountered in AM processes such as LMD, although Adaptive Mesh Refinement techniques should be employed

to perform the computations more efficiently and thus enable simulations on larger scales. The simulation could ultimately be coupled to a CALPHAD solver such as OpenCALPHAD so that the model could be informed by an actual phase diagram rather than a linearized one. This would allow to compute solidification curves more accurately compared to the Scheil model, which could be used to assess hot cracking susceptibility and improve the VOF modeling of the LMD process.

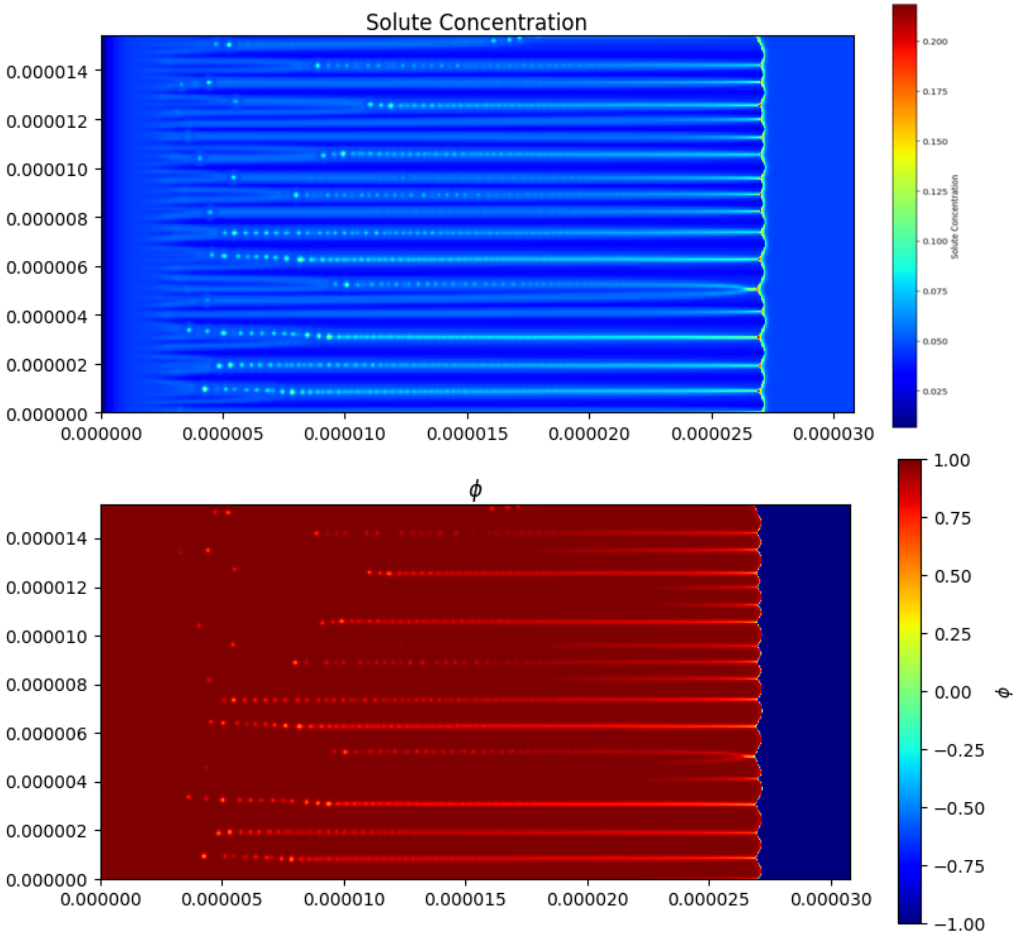

Figure 5.86: Solute concentration (top) and phase field (bottom)

II. Parameterization of the LMD process

a. Combined Heat Input parameter for LMD

The Laser Metal Deposition additive manufacturing process requires many process variables to be set, including laser power, speed, powder feedrate, as well as carrier and shape gas velocities. The level for these variables highly depends upon the material and the LMD system configuration. Some authors have presented dimensional analysis of additive manufacturing (AM) processes such as LMD and SLM (Selective Laser Melting or powder-bed fusion) in an effort to combine relevant physical parameters into characteristic dimensionless numbers, thereby reducing the number of variables to be tracked during experiments (Fabbro 2019; Mukherjee et al. 2017; Rubenchik et al. 2018). Such characteristic numbers could in principle be used to scale process parameters and compare experimental results across various LMD system configurations and materials.

However, such characteristic numbers are not systematically used in the literature when reporting experimental results. In fact, no set of characteristic numbers is widely accepted for LMD thus far. However characteristic numbers allow the experimenter to better assess the important phenomena and variables within the process, and permits the comparison of experimental results across various materials and LMD system configuration. AM process maps would also greatly benefit from using a standard set of characteristic numbers instead of using dimensional quantities. It is thus of particular interest to define useful combined parameters or characteristic dimensionless numbers for LMD that can be used to compare experimental results across different LMD systems and materials.

A simple measure of laser heat input is the laser irradiance. For a uniformly distributed laser source, it can simply expressed as P/A (W/m^2) for a top hat laser of radius w and surface area $A = \pi w^2$. Another classic combined parameter is the volumetric energy density VED (J/m^3) or some of its variants. However it has been shown that VED is generally not a satisfactory combined parameter in the context of powder-bed processes (Scipioni Bertoli et al. 2017). Indeed, it does not usually account for material properties. In the present work, the following form of VED is proposed:

$$VED = \frac{\eta P}{w \delta V} = \frac{\eta P}{\sqrt{2 \alpha V w^3}} \tag{5.2}$$

where η is the laser absorptivity, P is the laser power, V is the scan speed and δ is a measure of melt pool depth. The latter can be evaluated as the thermal diffusion length $\delta_T = \zeta \sqrt{\alpha \tau} \approx$

$\zeta\sqrt{\frac{2w\alpha}{V}}$, with laser dwell time or interaction time $\tau = \frac{2w}{V}$, thermal diffusivity α and shape factor ζ usually set to the values 1 or 2 (Bäuerle 2011). Note that the *VED* as defined here above accounts for the thermal diffusivity of the material.

To better take into account material properties, the dimensionless normalized enthalpy $\Delta H/h_s$ has been shown to be a good predictor of melt pool shape as well as of keyhole transition across a range of metallic alloys and processing parameters in laser welding and SLM (Hann et al. 2011; King et al. 2014).

$$\frac{\Delta H_{max}}{h_s} = \frac{\eta P}{h_s \rho \sqrt{\pi \alpha V w^3}} \tag{5.3}$$

where ΔH is the change in enthalpy from the input of laser energy and $h_s = \rho C_p T_m$ is the enthalpy of melting of the material. Material properties are usually evaluated near the melting point where most of the heat exchange occurs.

As shown recently by (Rubenchik et al. 2018) for powder-bed fusion using dimensional analysis on a simplified thermal model, the temperature distribution in the melt pool can also be characterized by the ratio of laser dwell time to thermal diffusion time $p = \alpha/VD$, which is effectively a Fourier number. For p < 1, usually encountered with lower conductivity metals such as stainless steel, inconel and titanium alloys, the melt pool tends to be shallow and elongated. For p > 1, as for higher conductivity metals such as aluminium or copper, the laser beam speed has a lesser effect on the melt pool shape, which tends to be more circular. Also, the peak temperature in the melt pool should become less dependent on scan speed and approach that of a stationary beam. A beam diameter of 600 µm and a scan speed of 0.033 m/s (2000 mm/min), as used in the experiments of the present study, yield a value of p on the order of 5 for aluminium alloys. Using $p = 4$ as a criterion for the transition towards the stationary beam solution for the temperature, it results that the scan speed should be on the order of at least 1 m/s with aluminium to observe significant dependence of the temperature distribution on the scan speed. Such a value is rarely encountered in practice and well above common values in LMD. For ratio p >>1, it has been shown that the dimensionless normalized enthalpy is better expressed as $\Delta H_{max}/h_s\sqrt{\pi p}$ (Rubenchik et al. 2018). Using both the normalized enthalpy and ratio p, the melt pool shape and keyhole threshold can be characterized. In this analysis however, two forms of the dimensionless normalized enthalpy are given, depending on whether the ratio p is large or small. In (Hann et al. 2011), an enthalpy balance is performed on the melt pool to yield a unique form for the dimensionless normalized enthalpy: $\Delta H_{max}/h_s(1 + S'\sqrt{Fo})$ where S' a modified shape factor with dimensions of length. This form of the dimensionless normalized enthalpy should be valid for all Fourier number, but the value of the modified shape factor is unclear.

To elucidate the proper form of a dimensionless normalized enthalpy for DED processes such as LMD or WAAM when taking into account losses by conduction, an enthalpy balance is performed on a simplified melt pool using a qualitative macroscopic model to give a new form of the dimensionless normalized enthalpy that includes both the powder mass inflow and the Fourier number. As in (Bäuerle 2011; Hann et al. 2011), it is here assumed that the melt pool depth δ can be estimated by the thermal diffusion length δ_T for process optimization purposes, and that the melt pool half-width $w_l = \zeta_l w$ is proportional to the laser spot half-width. Although it weakly depends on laser power and other process parameters, it is most strongly correlated with the laser spot size and therefore be assumed constant in a first approach. Similarly to (Hann et al. 2011) in the case of laser welding, an enthalpy balance is derived by considering a reference frame fixed with the previously deposited layers or substrate and a span of length $2w$ for the melt pool. The average enthalpy balance over the entire simplified melt pool is written as:

$$\Delta H(\rho\delta\pi w_l^2 + \int_{-\infty}^{\infty} \beta m dt) = \int_{-\infty}^{\infty} APdt - \int_{-\infty}^{\infty} S\alpha\rho\Delta H dt \tag{5.4}$$

where ΔH is the average change in enthalpy during laser interaction time. It is here assumed that the material is only heated by the direct interaction with the laser, from an initial temperature T_0 to the average temperature in the melt pool T. The total enthalpy of fusion can be defined as $\Delta H_f = C_p\ T_m - T_0\ + L_f$ where C_p is the heat capacity (assumed constant for temperatures above and below the melting temperature range), L_f is the latent heat of fusion, T_m is the melting (solidus) temperature and T_0 is the initial temperature of the previous layers or substrate before interaction with the laser beam. T_0 usually increases with heat accumulation in the deposit and thus with build time, unless the deposit is actively cooled or if there is important forced convection cooling from the shield or carrier gas. Coefficient β corresponds to powder catchment efficiency, which can be somewhat arbitrarily set to 0.5 for LMD. For WAAM process, it can be set to 1 as loss of feeding material is negligible.

The macroscopic balance presented in equation 5.4 essentially states that the enthalpy change of the melt pool and the mass inflow is equal to the laser energy effectively absorbed through the melt pool surface minus a cooling term, which is here written as a function of enthalpy change rather than temperature difference, as done in (Hann et al. 2011). Cooling also depends on the thermal diffusivity of the material α, material density ρ and a shape factor S. This cooling term results from heat losses by conduction through previously deposited layers or the substrate. Other heat losses, such as convection losses, are here ignored for simplicity. The overall laser absorption coefficient A is here assumed constant and evaluated for the liquid phase. The absorption could be further divided into powder jet absorption A_p and substrate

or deposited layer absorption A_l, such that $A = A_p + (1 - A_p)A_l$. However these components are hard to evaluate so, for the present case of thin walls built by LMD where the powder and deposited layers have the same chemical composition, a single global absorption coefficient A is considered.

In the one-dimensional approximation, where heat input from the laser essentially flows axially, the laser source may be considered as a single rectangular pulse traveling at speed V with uniform (top hat) distribution with pulse duration τ and pulse length $2w$. At times $t < 0$ and $t > \tau$, the laser and mass flow source does not directly interact with the substrate or deposited layers. It is here assumed that heating only occurs with direct interaction with the laser. Thus, the heating phase over a length $2w$ has a duration τ. At $t = 0$, the laser beam passes through the origin $x = y = 0$ with scan speed V, and travels a full beam diameter $2w$ at time $t = 2w/V$, also called interaction time or laser dwell time τ (Bäuerle 2011). With constant parameters and the above assumption on laser heating, the average enthalpy change can then be integrated as:

$$\Delta H(\rho\delta\pi w_l^2 + \beta m\tau) = AP\tau - S\alpha\rho\Delta H\tau \tag{5.5}$$

And thus, after grouping the terms and substituting the value of melt pool depth δ with thermal diffusion length $\delta_T = \zeta\sqrt{2w\alpha/V}$:

$$\Delta H = \frac{AP}{\rho\pi C\sqrt{\alpha V w^3} + \beta m - S\alpha\rho} \tag{5.6}$$

where $C = \frac{\zeta\zeta_l^2\sqrt{2}}{2}$. The shape factor S can often be defined as $S = C'\pi\delta$, where for example $C' = 2$ for an hemisphere immersed in a semi-infinite substrate. Assuming here that the melt pool is hemispherical rather than cylindrical for the purposes of heat loss estimation, and that the substrate is not semi-infinite but a thin wall, let us somewhat arbitrarily set $C' = 1$. For a bulk shape deposit, a value $C' = 2$ might be more suitable, as the deposit is more akin to a semi-infinite substrate if the deposited geometry is large with respect to the characteristic dimensions of the melt pool. With the above form of the shape factor, the following expression for the dimensionless normalized enthalpy HR is obtained:

$$HR = \frac{\Delta H}{\Delta H_f} = \frac{AP}{H_f\rho\pi\sqrt{\alpha V w^3}(C + C''Fo) + \beta m} \tag{5.7}$$

where $Fo = \frac{\alpha}{2wV}$ is the Fourier number and $C'' = \zeta C' \frac{\sqrt{2}}{2}$. For further simplification, let us set the thermal shape factor $\zeta = 1$ and melt pool width shape factor $\zeta_l = \sqrt{2}$, although more appropriate values could be used based on experimental data:

$$HR = \frac{\Delta H}{\Delta H_f} = \frac{AP}{(C_p\ T_m - T_0\ + L_f)(\rho\pi\sqrt{\alpha V w^3}(1 + \frac{\sqrt{2}}{2}Fo) + \beta m)} \tag{5.8}$$

The combined heat input parameter or dimensionless normalized enthalpy $HR = \frac{\Delta H}{\Delta H_f}$ derived here above takes a very similar form to the results found in (Hann et al. 2011; King et al. 2014; Rubenchik et al. 2018; Scipioni Bertoli et al. 2017). This dimensionless combined parameter has been shown to be a good predictor of melt pool dimensions and of the transition from conduction to keyhole regime in laser welding and powder-bed fusion (Hann et al. 2011; Scipioni Bertoli et al. 2017). The expression derived here above for LMD and WAAM explicitly includes the Fourier number and present the advantage of obtaining simple explicit expressions of coefficients C and C' thanks to a few simplifications. Note that the enthalpy of fusion, rather than enthalpy of melting as in (Hann et al. 2011; King et al. 2014), was used for normalizing the enthalpy change. Also, ΔH is here evaluated as an average value rather than a maximum as in (Hann et al. 2011).

This combined parameter HR is based on rather crude approximations and a simplified energy balance, akin to what was done in previous works. Notably, it assumes no convection in the melt pool, isothermal heat exchange regarding heat conduction losses, constant track width and a melt pool depth that follows the thermal diffusion length. It also does not account for powder granulometry. This should however still allow to capture important physics, and thus characteristics, of the melt pool, as shown by (Hann et al. 2011) with laser welding. For instance, note that the enthalpy ratio approximately varies as $P/\sqrt{V}$, just like the VED defined previously, so that doubling the speed is not equivalent to halving the power. Moreover, the dimensionless normalized enthalpy ratio allows to define a dimensionless combined heat parameter that can be applied across various LMD systems and feedstock materials. Moreover, various deposit configurations (thin wall, bulk shape) could be accounted for by modifying the shape factor appropriately. In any case, using a dimensionless normalized enthalpy is a significant improvement over using simpler heat input parameters such as laser fluence or volumetric energy density, or even more simply laser power and scan velocity. Indeed, it wraps most of the important process and material parameters into a single expression. Using reasonable estimates of those parameters, which are here set as constants, should allow the comparison of the results of LMD experiments between various system configurations and materials as long as coherent values are used for the parameters.

Note that the effect of convection due to the carrier and shape gas flows over the wall could be included in the above relation so as to factor in the speed of the gas. However, gas speed is not usually a parameter that is varied during experiments, so that the inclusion of convection cooling is ignored here for simplicity. Let it simply be noted that the convection heat exchange coefficient typically grows as the square of the gas velocity (Bäuerle 2011).

The above dimensionless normalized enthalpy can also be used to help determine the appropriate time evolution of process parameters. With the assumption that the same value of normalized enthalpy should yield similar results, the evolution of some parameters such as wall temperature T_0 can be accounted for and the laser power (or speed) be adjusted accordingly by requiring the dimensionless normalized enthalpy to remain constant throughout the build, at a prefixed values that is known experimentally to give satisfactory results. Such a change in temperature can be caused by pre-heating the substrate, or by overall accumulation of heat inside the wall during build time, which is usually the case unless the substrate or deposit is actively cooled.

An important phenomenon that was so far left out of the analysis, and yet could have a significant impact on melt pool behavior, is the effect of convection within the melt pool. In metal AM, convection currents within the melt pool are mostly created by surface tension gradients that are caused by temperature gradients. If the velocity of such currents exceeds some critical value, instabilities can arise. The prevalence of such thermocapillary convection currents can be estimated by the Marangoni number:

$$Ma = \left|\frac{d\sigma}{dT}\right| \frac{2w\Delta T}{\mu\alpha} \tag{5.9}$$

where $\frac{d\sigma}{dT}$ is the surface tension gradient, μ is the dynamic viscosity and ΔT is the temperature difference within the melt pool that we here define as the difference between the average temperature in the melt pool T and the liquidus temperature T_l. Some authors consider the solidus temperature instead, however it is not clear whether significant convection currents can be expected in a partially melted state. The characteristic length of the melt pool is here taken as the laser beam spot diameter $2w$. With these definitions, the temperature difference can be expressed using enthalpy and specific heat of the liquid alloy C_p^l:

$$\Delta T = \frac{\Delta H - \Delta H_f}{C_p^l} = \frac{\Delta H_f}{C_p^l}(HR - 1) \tag{5.10}$$

which yields the following expression for the Marangoni number:

$$Ma = \left|\frac{d\sigma}{dT}\right| \frac{2w\Delta H_f}{\mu\alpha C_p^l}(HR-1) \tag{5.11}$$

Convection currents become more significant as the Marangoni number increases. As the Marangoni number grows linearly with the dimensionless normalized enthalpy HR, it is expected that an increase in HR will lead to a less stable melt pool and lead to a potential balling phenomenon. The analysis could be completed by evaluating the Peclet number to assess the main mechanism of heat transfer within the melt pool (conduction or convection) as in (Mukherjee et al. 2017).

Also, following the energy balance for simple macroscopic model described here above, a simple mass balance yields the following approximation of layer height h_l:

$$h_l = \frac{\beta m}{\rho V w_l} \tag{5.12}$$

Experimental measurements could provide more realistic estimates of powder catchment efficiency β and of ζ_l. Of course, in reality, ζ_l is not a constant and depends on process parameters such as laser power, but it is most highly correlated with spot diameter if laser power variation remains limited, so this assumption should suffice in a first approach.

b. Design of Experiments

Among the many additive manufacturing (AM) processes developed so far, Laser Metal Deposition (LMD) process appears to be ideally suited for parts repair and remanufacturing and could thus play a big role in the Maintenance, Repair and Overhaul industry. Indeed, LMD allows to make deposits on pre-existing parts with minimal heat input while providing good bonding and good mechanical properties. So far, LMD has been used with many different material such as titanium alloys, steels and Inconel. However, aluminium alloys, which are of great interest to the aeronautical industry, are notoriously hard to process by LMD. Not only are they highly reflective, but they also present relatively high thermal conductivity and specific heat, which hinders the laser melting process. Once melted, aluminium alloys typically have a relatively low viscosity which can lead to an unstable melt pool. In addition, some aluminium alloys such as Al-Cu alloys (2000 series) are notoriously difficult to process due to the many potential defects that can be created during solidification such as chemical segregation, hot cracking and porosities. Finally, aluminium alloy powders usually have a

relatively low flowability, which may prevent proper transport from the powder reservoir to the LMD nozzle.

There have thus been relatively few published studies on aluminium alloys processing by LMD with a coaxial nozzle, especially for aluminium-copper alloy. Dinda et al (2012) used an Al-11.28wt.%Si alloy to deposit thin walls for various processing parameters and deposition strategies. The porosity, surface roughness and microstructure of thin walls made of Al-11.7wt.%Si has been studied in (Rumman et al. 2019). The geometry and microstructure of single tracks of aluminium alloy 2024 powders for a range of processing parameters has been analyzed in (Caiazzo et al. 2017; Caiazzo and Caggiano 2018).

To study the feasibility of homogeneous repairs of castings by Laser Metal Deposition (LMD) for low weldability aluminium alloys, alloy powder 224.0-A (63-80, 80-100 and 100-125 µm) was processed by LMD to form single-track walls of size 30x10 mm as well as blocks of 10x10x10 mm on a 2024-T4, 4 mm thick rolled plate. The Laser Metal Deposition system used for these experiments is a system with a coaxial nozzle and a fiber-delivered diode Ytterbium laser beam emitting at a wavelength of 1070 nm in a top hat distribution with a spot diameter of 0.6 mm at the focus plane. The fabrication of the thin walls with the 80-100 µm Al-Cu powder followed a full-factorial, two-factor, three levels experimental plan yielding a set of 9 processing conditions where laser powder and scan speed have been varied between 640 and 700 W and between 1500 and 2000 mm/min (table 5.31), respectively. The powder feedrate was kept constant at around 2 g/min. Argon is used for carrying the powder and shaping the powder cone at the nozzle exit, using flowrates of 3 and 5 L/min respectively. The processing levels have been set according to preliminary experiments with single track deposits. Prior to deposition, the aluminium substrate was sandblasted to clean its surface and remove the oxide layer. The aluminium powders Al-Cu 80-100 µm were dried at 180°C for 10 hours to evacuate residual humidity and thus ensure proper flowability between the powder reservoir and the nozzle. Preliminary thin wall deposits established that a vertical increment of 0.12 mm kept the working distance approximately constant during thin wall deposition for various parameters. The deposition strategy for the single-track walls followed a “zig-zag” pattern, where the start of the next layer starts on top of the end of the last layer. This is preferred to a “zig-zig”/“one-way” strategy (next layer starts on top of where the previous layer started) since the feedrate is kept constant, thus minimizing contamination of previously deposited layers by unmelted powders. Once deposited, the sample thin walls were cut into 3 cross-sections along the length of each wall. Each cross-section was cold mounted in resin and mirror polished using 9 µm, 6 µm, 1µm diamond solutions followed by polishing with a silica solution. A chemical etching using Kroll’s reagent (92 mL H_2O, 6 mL HNO_3, 2 mL HF) was also performed by sample immersion for a duration of 45 seconds to reveal the grains as well as the fusion lines.

Trial	Scan speed (mm/min)	Laser Power (W)
1	1500	640
2	1500	670
3	1500	700
4	1750	640
5	1750	670
6	1750	700
7	2000	640
8	2000	670
9	2000	700

Table 5.31: Parameters of experimental plan for deposition of thin walls by LMD

Trial	Speed (mm/min)	Power (W)	*VED* (x10^{10} W/m^3)	*Fo*	*HR*	*Ma*
1	1500	640	4,04	1,98	2,50	2775
2	1500	670	4,23	1,98	2,61	2992
3	1500	700	4,42	1,98	2,73	3209
4	1750	640	3,74	1,70	2,52	2814
5	1750	670	3,91	1,70	2,63	3033
6	1750	700	4,09	1,70	2,75	3252
7	2000	640	3,50	1,49	2,52	2829
8	2000	670	3,66	1,49	2,64	3049
9	2000	700	3,83	1,49	2,76	3269
Caiazzo 2017	300	2000	2,52	2	2,27	11337
Caiazzo 2017	500	2000	1,96	1,2	2,30	11573
Caiazzo 2017	400	2500	2,73	1,5	2,88	16768
Caiazzo 2017	300	3000	3,79	2	3,41	21459
Caiazzo 2017	500	3000	2,93	1,2	3,45	21813

Table 5.32: Fourier number, Enthalpy Ratio HR and Marangoni number for trial 1 to 9 with 224.0 alloy, with estimates for the experiments of (Caiazzo et al. 2017) with 2024-T4 alloy

In this work, a combined heat input parameter *HR* was derived specifically for LMD (or WAAM) so as to provide a reference criteria against which other experimental results from the literature can be compared, even if the LMD system configuration or material differ. This can hopefully improve the repeatability of experiments between various research groups by following the principle of similitude and scaling laws. In other words, the characteristic numbers presented hereafter should yield the same behavior for the melt pool when they have similar values. Note that an energy balance approach was followed rather than a pure dimensional analysis as usually done when trying to derive scaling laws. Indeed, as shown by

(Hann et al. 2011), this also allows to extract the dimensionless normalized enthalpy all the same while also clarifying the value of some of the constants.

In table 5.32, values for the volumetric energy density *VED*, the Fourier number *Fo*, the dimensionless normalized enthalpy *HR*, and the Marangoni number *Ma* are calculated for the input parameters of trials 1 to 9 as well as for the single tracks experiments by (Caiazzo et al. 2017) with alloy 2024 using our best possible estimates, assuming a powder catchment efficiency $\beta = 0.5$ and laser absorptivity of 0.4 for the liquid phase in both cases. Thermophysical properties for the alloy of the present study are approximated by those of Al-4.5wt.%Cu found in (Valencia 2008). Properties for alloy 2024-T4 are also taken from this reference. In case of missing data, the rule of mixtures is used where the properties of the base elements are combined to form an estimate for the property of the alloy, such as material density.

Values of VED in the experiments are roughly comprised between 3.5 and 4.4, which is slightly higher than in the experiments by (Caiazzo et al. 2017) where *VED* is between 2 and 3.8. Values of *HR* and *Fo* are on the same order of magnitude for both sets of experiments, where a narrow range of values is obtained in the present experiments as the levels of process parameters were narrowed down beforehand through preliminary experiments. This was necessary as the geometry of thin wall deposits is more complex than the single tracks from (Caiazzo et al. 2017). The Marangoni numbers *Ma* are significantly greater in the single-track experiments by (Caiazzo et al. 2017), which essentially comes from the comparatively larger laser spot size (3 mm) and thus larger melt pool.

c. Analysis

The experimental plan used to build single-track walls involved 9 different trials, varying the laser power between 640 and 700 W and the scan speed between 1500 and 2000 mm/min. Examples of deposited thin walls are pictured in figure 5.87.

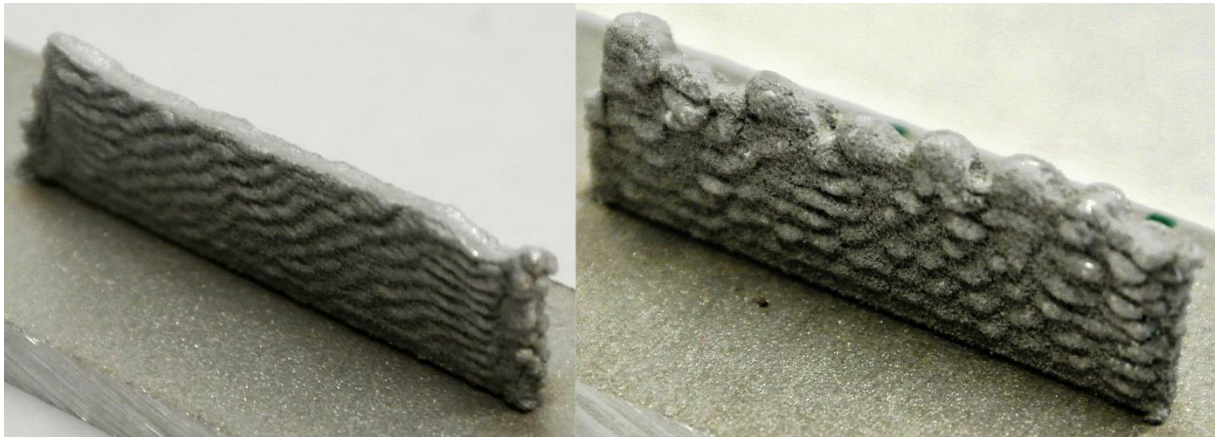

Figure 5.87: Single-track wall deposit by LMD of allow powder 224.0-A 80-100µm using parameters from trial 8 (left) and trial 5 (right)

Four criteria of interest were used to assess the quality of the deposited samples. The wall width was measured at the base of the wall with a digital caliper. It gives a sense of both the width of the deposit and the geometrical regularity of the side walls where protuberances lead to increased width measured by the caliper. The wall height deviation was calculated as the relative error between the target height of 10 mm and the measured height, taken as the average between the minimal and maximal wall height measured with a caliper along the length of the wall, with an accuracy estimated at 0.1 mm. A "stability" response was evaluated between 0 (worst) and 1 (best) based on qualitative visual inspection to represent the extent of the balling phenomena sometimes observed in the last deposited layers of the thin walls. This balling effect hints at melt pool instability due to heat accumulation or at suboptimal vertical increment, which is here set at a constant value of 0.12mm in the machine code based on preliminary experiments to limit the experimental space. A good performance for those geometrical criteria are expected to lead to good performance when depositing filled shapes such as blocks. Indeed, defects such as lack of fusion between layers are expected to be better avoided with stable, regular deposit tracks. For instance, in figure 5.87, the sample from trial 8 displays fairly regular side and top surfaces, in contrast to the sample built using parameters from trial 5 where a balling phenomenon is apparent on the last deposited layers with side walls displaying greater irregularity.

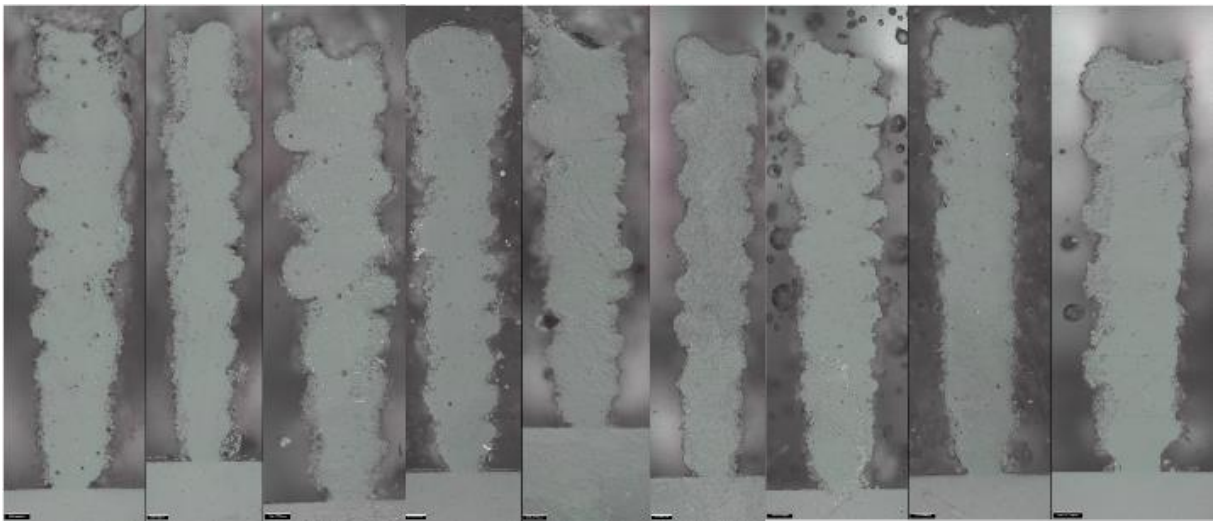

Figure 5.88: Macrographs of one of the three cross-sections of single-tracks walls deposited with 224.0-A 80-100 µm powder for each trial 1 to 9 (from left to right), after polishing and before etching (images not on the same scale)

In addition to the geometrical criteria, the porosity content was also evaluated based on 3 cross-section macrographs of each of the 9 sample walls, where a single cross-section for each condition is shown in figure 5.88. As a first approach for porosity content estimation, an image analysis was performed on 2D images extracted from the ALICONA Infinite Focus 3D optical microscope. This was performed before etching to facilitate the image segmentation process as porosities and inclusions are the main internal features revealed at this stage. On each cross-section, the largest possible rectangular area contained within each wall was used for defect segmentation, dismissing the edges. Pores were segmented using a thresholding method after pre-processing the image for better contrasts (see figure 5.89). The area of the defects divided by the total area yields an estimate of the defect content. However, porosities and other defects (inclusions, unmelted powders etc.) can be hard to differentiate using 2D information only, thus diminishing the reliability of the porosity content estimates.

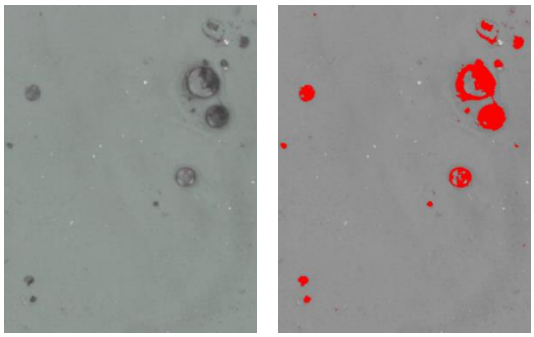

Figure 5.89: Example of 2D defect segmentation (left: original image – right: segmented defects)

As another approach to porosity content estimation, topographic measurements with the 3D optical microscope were performed on 3 cross-sections from each of the 9 samples walls, as illustrated in figure 5.90. The depth information allows to segment pores by thresholding the data points according to their depth with respect to the surface of the sample, thus clearly differentiating between pores and most other defects or measurements artefacts. The horizontal spacing of the data points is on the order of 5µm, depending on the particular sample, so that smaller features are not detected. To identify the surface plane of the sample, which is often not perfectly horizontal, a variant of the RANSAC (RANdom SAmple Consensus) algorithm (Fischler and Bolles, 1981) was implemented and applied to the height map of each cross-section. RANSAC is a robust probabilistic method for identifying model parameters from data with many outliers. Indeed, data points associated to pores or measurement artefacts triggered by the high reflectivity of aluminium must be ignored when computing the parameters of the plane, which prevents the use of simpler method such as least-square fitting.

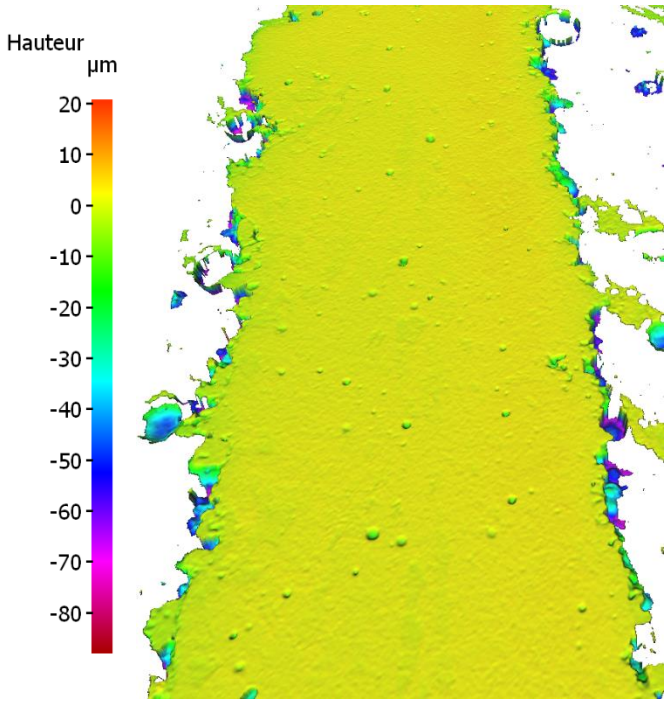

Figure 5.90: 3D topographical measurement of polished wall surface with visible pores

As illustrated in figure 5.91, the RANSAC-based approach to porosity estimation consists of the following steps. First, parameters of the best fitting plane for the topographical data are estimated with the RANSAC method, using 40 iterations per sample cross-section with a distance threshold of 1 µm. A local optimization is performed at the end of the plane segmentation process using least-square fitting on the inliers identified by RANSAC. After a first least-square fit, the set of inliers (red data points in figure 5.91) is recalculated. If the error decreases and the number of inliers increases, the parameters from this least-square fit is

selected as a new set of model parameters. This local optimization process is repeated up to 5 times, so long as some improvement is observed. A distance threshold of 5 µm with respect to the plane is then applied to the topographical dataset. All data points that fall below this threshold are identified as being part of a pore (yellow data points in figure 5.91). The overall porosity content is then estimated as the ratio of the number of data points lying inside a pore to the total number of data points. Such a porosity estimation method ought to provide a relatively good measure of porosity content between samples, and improves upon more common methods based on 2D image analysis of pixel intensity as it better discriminates between pores and inclusions or other features.

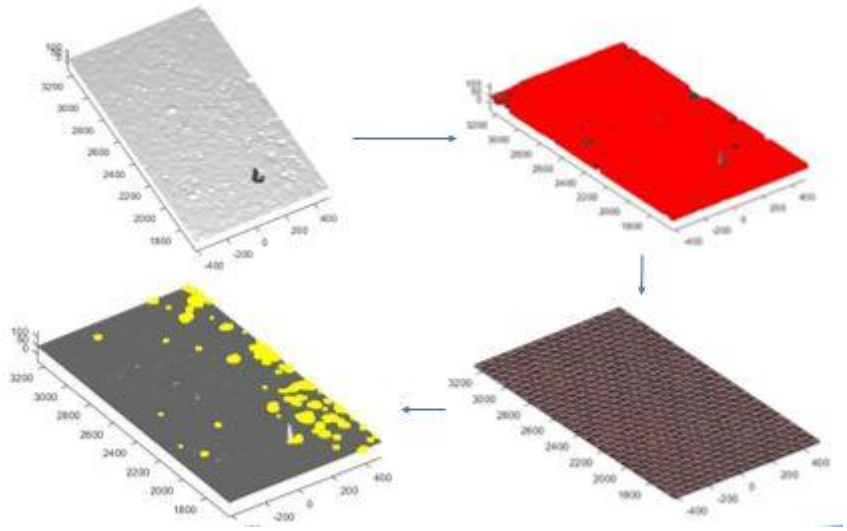

Figure 5.91: RANSAC-based porosity content estimation based on topographic measurements (height map inverted for better visibility of the pores)

This RANSAC-based method for porosity estimate was run 3 times on each of the 3 cross-sections of each sample. The porosity estimate, as shown in table 5.33 along with the other factors, was taken as the average of the porosity content over the 3 cross-sections of each sample wall.

Overall, all 9 sample walls were fabricated in a somewhat satisfactorily manner. Indeed, despite the flowability and expected fusion and solidification issues encountered with Al-Cu powders, the thin wall deposits did not present major defects such as external cracks or lack of fusion upon visual inspection of the SEM images of the cross-sections. However, geometrical irregularities and instabilities as well as some deviation from target height were observed.

Trial	Speed (mm/min)	Power (W)	Average Porosity (%)	Height Deviation (%)	Width (mm)	Stability
1	1500	640	0.602	2	2.23	0
2	1500	670	1.014	6.5	2.05	0
3	1500	700	0.469	6.5	2.15	0
4	1750	640	0.572	3	2.25	0
5	1750	670	0.325	8	2.45	0
6	1750	700	0.032	5	2.55	0.5
7	2000	640	0.181	16.5	2.05	0.8
8	2000	670	0.424	7.5	1.9	1
9	2000	700	0.347	23	2.05	1

Table 5.33: Results of single-track walls experiments with 224.0-A 80-100 µm powder

The average porosity content estimate is between about 0.03 and 1 %, which is quite satisfactory for a resolidified aluminium alloy. The standard deviation of the average porosity content over 3 cross-sections of a thin wall is between 0.019 (trial 6) and 0.49 (trial 2), excluding trial 7 for which only 1 out of the 3 cross-sections survived the polishing process.

The height deviation is reasonably close to 1 except for trial 9, thus demonstrating that in this parameter range, a constant vertical increment of 0.12 mm allows the walls to grow at a sufficient rate to keep the working distance roughly constant. However, looking at the measures of width and stability, there is a definite variation in terms of deposit geometry and quality.

To further assess the influence of input parameters (laser power and scan speed) on each response, a regression model was applied to each of the outputs and was analyzed by ANOVA, as presented in table 5.34. Note that the porosity estimates, which were transformed with a logarithm function for a better fit, are the only factor with repeated measurements and thus pure error estimate available, which amounts to about 15.6% based on sum of squares. All regression models presents an R^2_{pred} value close to the R^2_{adj} value, which shows that the model is not overfitting and can be used for predictions. These models should be validated with additional experiments in future work, but they nonetheless suggest that laser power and scan speed are significant factors in explaining the measured responses.

Response	R^2_{pred}	Model p-value	Model F-value	Intercept	Power (W)	Speed (m/s)	Power²	Speed²	Power x Speed	Power x Speed²
Log_{10}(Porosity)	0.81	< 1e-4	56.98	-831.02	1.489	806.94	-3.26e-4	-233.22	-1.239	0.357
Width (mm)	0.94	< 1e-4	228.53	188.58	-0.360	-170.1	8.5e-5	47.80	0.283	-0.080
Stability	0.97	< 1e-4	425.43	297.12	0.468	-312.19	6.5e-5	88.97	0.442	-0.125
Height deviation (%)	0.87	< 1e-4	79.75	-25366.3	72.24	16551.8	-0.051	-876.53	-45.32	1.413

Table 5.34: Results of ANOVA and regression for thin wall experiments

To establish the best set of parameters based on those multiple responses, a desirability approach was adopted. Because the overall porosity content obtained in all those trial experiments was quite low, especially for an aluminium alloy, a smaller weight was attributed to the porosity content compared to the other 3 factors as the latter have more impact on manufacturability. The calculated desirability map is shown in figure 5.92, where the maximum is located near the processing conditions of 670 W and 2000 mm/min (trial 8), which corresponds to $Fo = 1.49$, $HR = 2.64$ and $Ma = 3049.5$. It can be shown that Fourier number Fo is the dimensionless equivalent of scan speed and heat input ratio HR takes the role of laser power. Performing the ANOVA with these two characteristic numbers instead yields very similar statistical results, as expected, but provided the added advantage of being dimensionless and thus being more translatable to other LMD systems and materials. The Marangoni number, in the form expressed previously, is proportional to HR. These two factors are thus not independent, hence Ma is not considered in the statistical analysis.

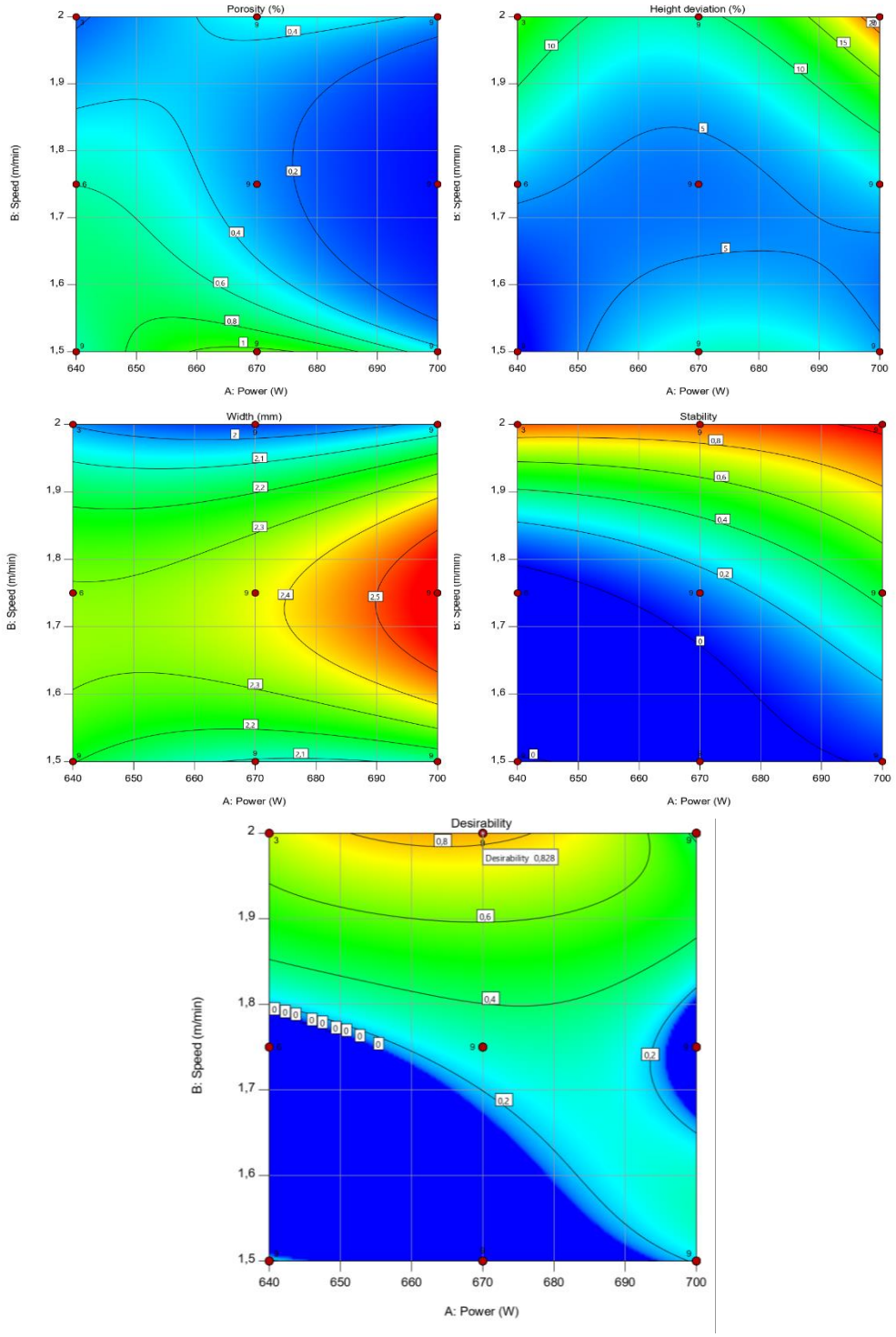

Figure 5.92: Desirability and surface response maps of thin wall experiments

From the desirability calculations, it follows that parameters from trial 8 (670 W at 2000 mm/min) lead to the best outcome. Further experiments around this operating point, at speeds of 1900 and 2100 mm/min, further suggested that those parameters were appropriate. Further testing of these process parameters was done by fabricating a 20mm-high thin wall with parameters from trial 8, thus doubling the target height from the previous experiments (figure 5.93). While no balling phenomenon is observed, the top surface does become slightly

wavier with the increased wall height. Note that the waviness of the side walls could be cause by a slight excess of powder flowrate, which also leads to unmelted powders stuck to the sides. In a bulk deposit with proper overlapping between contiguous layers, it can be expected that these imperfections will be melted away, as will be shown hereafter with block deposits.

Figure 5.93: Thin wall built with 224.0-A 80-100 µm powder, target height 20 mm

To further evaluate the quality of thin wall sample 8, a chemical etching with Kroll's reagent performed by swabbing the specimens for 45 seconds. As shown on figure 5.94, a clear pattern appears alternating between lighter and darker regions due to the remelting of previously deposited layers. Beyond the porosities previously observed, some fine cracks are revealed, especially at the base of the wall. These are most likely hot cracks which can typically arise during solidification of low weldability alloys such as the Al-Cu alloy of the present study. Let it be also noted that beyond the first layers, no macrocracks were observed. The occurrence of cracks within the first deposited layers could likely be mitigated by a slight increase in the laser power for the first layers to ensure proper remelting and bonding to the substrate, although this is beyond the scope of the present work. Moreover, keeping the parameters constant allows for better comparison between trials.

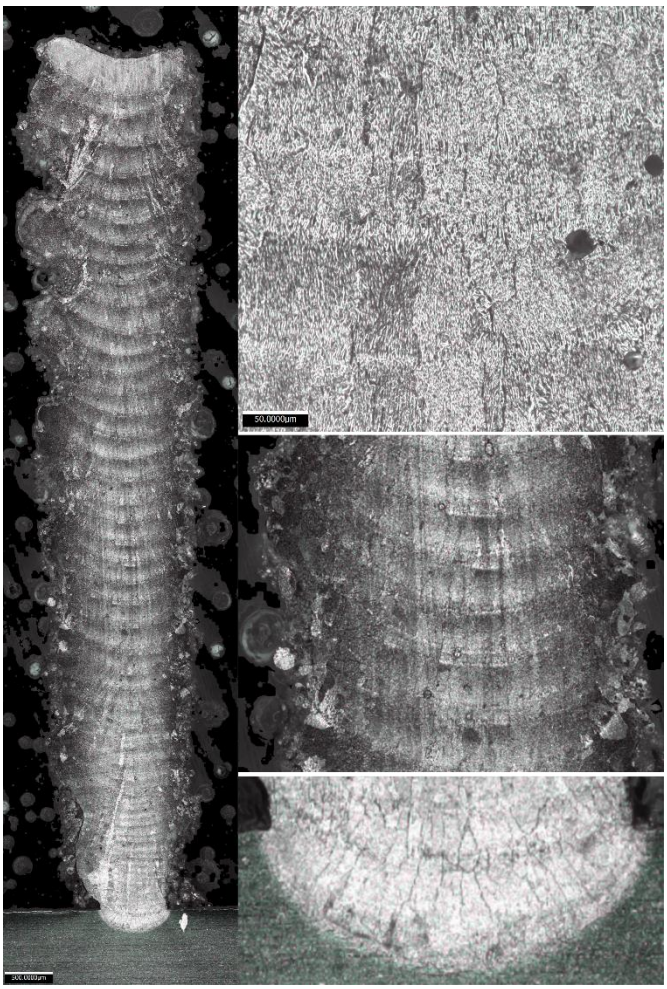

Figure 5.94: Microstructure of 224.0-A thin wall (trial 8) after chemical etching

III. LMD repairs with alloy 224.0

a. Full Blocks

To validate the feasibility of depositing the Al-Cu 80-100 µm powder with a LMD process using the set of parameters identified in the single-track walls experiment, solid blocks of 10x10x10 mm were fabricated using a hatching space of 0.4 mm. The vertical increment was increased to 0.30 mm, which is significantly greater than the vertical increment used for thin walls. While a slight increase in the vertical increment is expected between thin walls and blocks, the change is here relatively large. This may be caused by the accumulation of unmelted powder on the previously deposited layer, by a suboptimal overlapping distance of beads in each layer, or by an insufficient vertical increment in the thin wall experiments in the first place. It is also possible that the powder feedrate is not sufficiently steady with 224.0-A powders due to their low flowability, which would imply that the vertical increment and thus

layer height is not constant, as hypothesized here as in most published works on LMD. The vertical increment for the blocks is thus set to a fairly large value compared to the thin walls, which is preferable to an excessively small value as it could lead to a contact between the deposit and the LMD head and cause significant damage, especially considering the rather small working distance (5mm). Future work should revisit the settings of the vertical increments of thin walls and blocks with the 224.0-A powders.

The deposition strategy for the blocks used a contour followed by a zig-zag deposition path for filling the layer inside the contour, with a 90° change in orientation angle between subsequent layers. As before, the samples were cut, mirror polished and etched with Kroll's reagent.

Figure 5.95 shows a solid block made with the 224.0-A 80-100 µm powder following parameters from trial 8. The overall quality of the block is satisfactory in terms of fusion defects as few porosities and lack of fusion are apparent, as revealed by a height map of the sample taken with the ALICONA Infinite Focus 3D optical microscope. Interlayer and intralayer bonding seems satisfactory. As expected, the unmelted particles observed on the sides of the thin walls are properly melted in this case. The deposit strategy used is also clearly revealed. The contour tracks are reasonably well bonded to the internal filling tracks, whose zigzag trajectory, alternating 90° between layers, appears clearly figure 5.95 as an alternating pattern between layers. The height of the block reaches about 9.2 mm for a target of 10 mm, which is reasonable but could be improved by using more optimized values for the vertical and horizontal increments in the machine code.

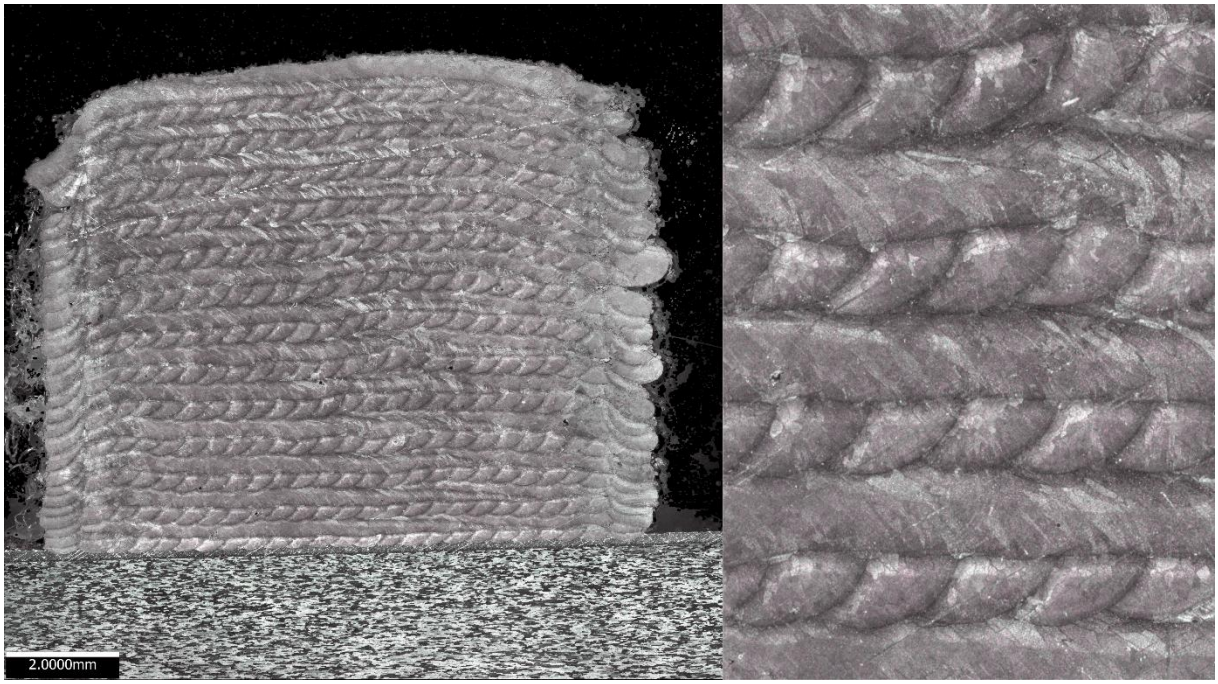

Figure 5.95: Solid block in 224.0-A alloy using parameters from trial 8

To assess the influence of the granulometry of the powder, blocks of 10x10x10 mm are built with 63-80 µm and 100-125 µm powders of the same chemical composition as the 80-100 µm, using the same parameters and deposit strategy as for the block made with the 80-100 µm powder (figure 5.96). The height of the blocks is around 7.5 mm and 7.2 mm for the blocks built with the 63-80 µm and 100-125 µm, respectively. The blocks with the 80-100 µm grows more satisfactorily than with the other two granulometries. Since the only variation in controllable parameters between those deposits is the granulometry of the powders, i.e. their median diameter and standard deviation, it appears that the distribution of powder particle sizes has a clear impact on the deposits.

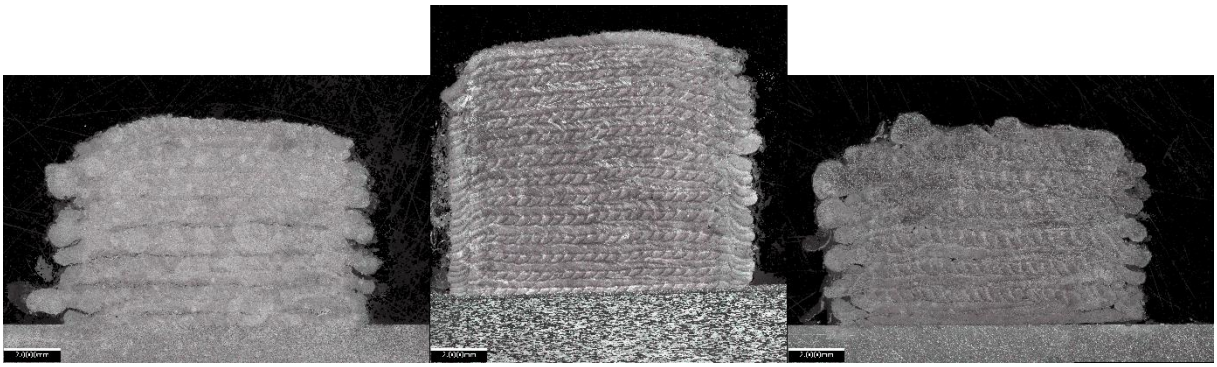

Figure 5.96: Solid blocks in 224.0-A alloy built with (from left to right): 125-100 µm, 80-100 µm, 63-80 µm

Blocks built with 63-80 µm and 100-125 µm powder both show noticeable defects, as illustrated in figure 5.97. On the left are shown lack of fusion and interlayer bonding defects generated with the 100-125 µm powder in the form of melted or unmelted lumps at the interface between layers. By inspection of figure 5.97, it appears that those defects range between 70 and 170 µm in size, which matches the range of powder particle diameter for this granulometry. Those defects are likely due to powder particles or aggregates that were improperly melted during deposition. This can be expected for powder particles of larger size as their decreased surface to volume ratio renders them harder to melt by a laser source. The unmelted particles that remain stuck to the deposited layer hinder bonding with the next layer as it introduces irregularities on the surface, which must be remelted during the next pass.

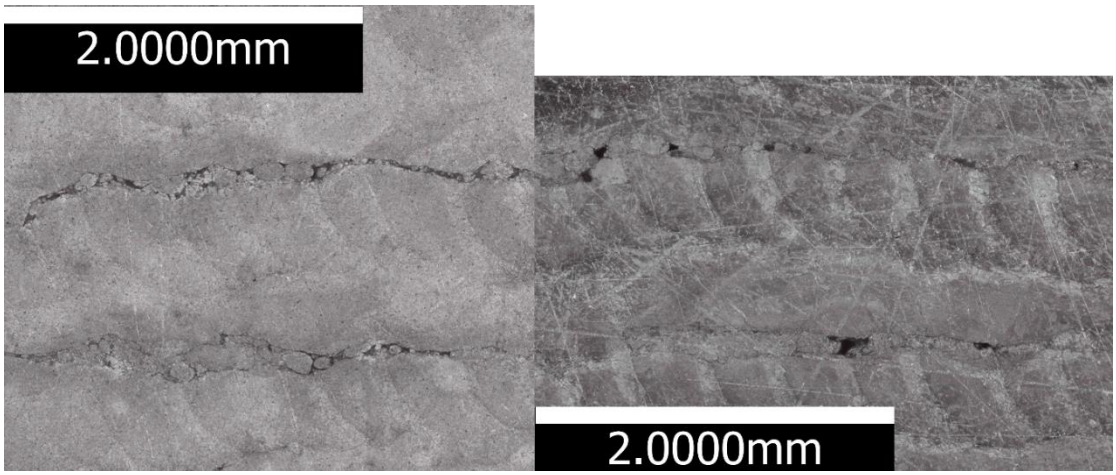

Figure 5.97: Fusion defects between layers in solid blocks made with 224.0-A powder 100-125 µm (left) and 63-80 µm (right)

Lack of fusion defects are also observed for the 63-80 µm powder, as shown on the right of figure 5.97, which are likely due to unsufficient melting and feeding of material at those locations. This can be caused by a greater instability of the powder jet at the nozzle exit due to the relatively lower weight of individual particles for this granulometry. Indeed, the particle Stokes number varies with the square of particle size, which indicates that smaller particles tend to follow fluid streamlines more closely due to their decreased response time. Instabilities and turbulence in the carrier gas flow can more easily disturb the powder jet flow with particles of smaller size, thus modifying the particle distribution on the powder focus plane and potentially impacting the powder catchment efficiency. The resulting inhomogeneity in the flux of powder particles can lead to lack of fusion defects due to unsufficient feeding of powder particles at those locations.

For the set of parameters considered, the 80-100 µm powder offers the best compromise in terms of deposit quality, both in terms of geometry and metallographic aspects. Together with similar tests for thin wall geometry, it appears quite clearly that powder granulometry has a non-negligible impact on the build quality. Thus, process parameters should account for such changes to ensure the best possible outcomes for each granulometry. Also note that a change in granulometry can lead to a change in powder flowability and powder mass flowrate. The observed variation caused by the change in granulometry could thus be caused not only the change in particle size but also by the overall change in mass flowrate. Further work should be pursued to address this question.

For the 80-100 µm, process parameters of 670 W and scan speed of 2000 mm/min gave the best results on aluminium casting alloy Al-4.7wt.%Cu-0.23wt.%Mn. This translates into the following combined parameters : $VED = 3.66$, $Fo = 1.49$, $HR = 2.64$ and $Ma = 3049.5$.

Since granulometry impacts the deposit quality, it could be included in the expression of the dimensionless normalized enthalpy, for example by introducing the median diameter d_{50}

in the formulation of the mass flowrate or in the expression of a particle absorptivity A_p coefficient, which, together with a solid layer absorptivity A_l, can be combined into a global absorptivity A.

Further work could also include the validation of the dimensionless normalized enthalpy for controlling process parameters during the deposition. Indeed, because of heat accumulation, the average wall temperature T_0 increases with build time. The maintain the same average or maximum change in enthalpy or temperature within the melt pool, the energy input should be adjusted accordingly.

The overall content in macroporosities and other defects such as inclusions remains limited. The feasibility of fabricating full solid blocks was also established using these process parameters. The impact of granulometry was assessed by varying the particle diameter range (63-80 µm, 80-100 µm, 100-125 µm). It results that granulometry can impact the quality of the deposit as it can promote certain types of defects. Smaller particles can lead to a less stable powder jet, thus increasing the propensity for lack of fusion defects. In contrast, larger particles suffer from lower meltability due to their increased surface to volume ratio combined to the high reflectivity of aluminium alloys, which can create lack of fusion and diminished bonding between layers. Moreover, granulometry impacts powder flowability and powder mass flowrate through the powder distribution system, as well as powder catchment efficiency. For the process parameter used, the 80-100µm sieve granulometry offers a good compromise. Larger particles (e.g. 100-125µm) could be beneficial in terms of flowability but an increase in laser power is likely required to ensure the proper melting of particles.

Further work should therefore be conducted to quantify the impacts of powder granulometry on build quality and how process parameters should be scaled between various granulometries. Granulometry parameters such as median diameter d_{50} could also possibly be included in the formulation of the dimensionless normalized enthalpy, for example through powder catchment efficiency β or laser absorptivity A (or A_p), to help define the scaling relations. Also, further experiments could help determine whether the dimensionless normalized enthalpy derived in this paper can effectively assist in controlling process parameters as experimental conditions, such as average wall temperature, evolve during build time. Additional studies should help verify that the dimensionless normalized enthalpy can help the reproducibility of experiments across various LMD systems by scaling process parameters accordingly. Finally, a set of dimensionless parameters should be defined within the community to assist in defining useful process maps that can be applied across diverse system configurations and materials.

b. Cavity repairs

Once suitable toolpaths and process parameters have been determined, and the corresponding machine code has been generated by a post-processor, the repair operation by the Laser Metal Deposition process can follow. Before the LMD repair can safely proceed, the calculated toolpaths must be checked to ensure that the LMD head behaves as expected and can access the region of interest throughout the entire toolpath without risks of interference with the part itself or the mounting fixtures. Informed by the geometrical information from the range scanner, basic checks can be performed to anticipate such issues and help in determining the actual feasibility of the repair for a given part geometry and LMD head bulkiness.

In a purely additive manufacturing repair scenario, the defective part is placed inside the working space of the LMD system with its local surface defect(s) already machined out. The part must be mounted such that the orientation of the region of interest is compatible with the orientation of the range scanner and LMD head, the latter being generally confined to near vertical orientations. Once the part is securely mounted, an operator inputs the type of cavity (spherical, cylindrical etc.) to be detected and defines the trajectory of the range scanner so that it will sweep over the cavity at an appropriate scanning distance and velocity. The InterSAC algorithm can then run to robustly segment the geometry of the cavity within the range data points. The process parameters, deposition strategy and corresponding toolpaths are then defined based on the defect geometry, the type of material and LMD system characteristics.

The LMD nozzle of the present work uses a rather small laser beam diameter (0.6mm) and powder jet size to enable the deposition of fine layers (0.1-0.2mm). The working distance of the nozzle is fairly small, on the order of 5mm, so that particular care must be taken in terms of accessibility as the LMD head must come close to the surface of the part. After accessibility requirements have been met, the LMD repair can proceed based on the process parameters and toolpaths previously determined to give repaired cavities as illustrated in figure 5.98. Two particular examples of cavity repairs, samples A and B, are studied here, which were machined in a 224.0 cast part (table 5.35). Sample A was done with powder 224.0-A 80-100µm using LMD parameters akin to those used previously for depositing thin walls. Sample B was deposited with powder 224.0-B 90-125µm with a smaller powder flowrate in an attempt to get finer deposited beads and avoid lack of fusion defects.

Cavity	Powder	Laser Power (W)	Scan Speed (mm/min)	Powder Flowrate (g/min)	Vertical Increment (mm)	Horizontal increment (mm)
A	224.0-A 80-100µm	670	2000	2.4	0.24	0.4
B	224.0-B 90-125µm	490-450	2000	0.7	0.08	0.35

Table 5.35: Process parameters for two examples of cavity repair samples performed with powder 224.0-A 80-100µm (cavity A) and powder 224.0-B 90-125µm with reduced powder flowrate (cavity B) on a cast part

Figure 5.98: Examples of repaired cavity samples on a premium high-strength Al-Cu

A metallographic analysis of repaired cavities is carried out in order to assess the type of microstructure and general quality of the deposit. The typical grain size and level of copper segregation are of particular interest as they are a direct indicator of the macroscopic properties of the repaired zone. Presence of cracks, gas porosities, lack of fusion defects and lack of bonding with the substrate should also be evaluated.

The metallurgical analysis is performed by first sawing a sample cavity repair so as to reveal a particular cross-section, typically near the midsection. The sample is cold-mounted using a conductive acrylic resin to form a suitable sample for polishing and for analysis by Scanning Electron Microscopy (SEM).

The polishing process is performed in six successive steps. The sample is first levelled with silicon carbide (SiC) paper using grit P320 and continuous water lubrication under a force of 4daN for about 180sec, and is further grinded using grit P600 for 60sec and P1200 for 60sec. The following 3 polishing steps make use of a diamond suspension of 9, 3 and 1µm for 240, 180 and 60 sec at 2.5daN, respectively. The final polishing step involves a silica suspension of 0.03µm with counter-rotation of the head and table during 60sec and a 2daN force, followed by a final rinse with water for 60sec. To reveal the microstructural features of the samples, Kroll's reactant (HNO_3 6 mL, HF 2 mL, water 92 mL) is used for chemical etching by immersion for about 45sec. This reactant is most commonly used for titanium alloys but it is also appropriate for Al-Cu alloys.

Prior to SEM analysis, the topography of the sample is measured using an Alicona InfiniteFocus 3D optical microscope to check for gas porosities and lack of fusion defects, as

shown in Figure 5.99. As long as the powder jet remains stable and the toolpaths and process parameters are appropriately chosen, lack of fusion defects are limited. The zig-zag strategy is clearly appears as the overlapping beads are only visible in every other layer.

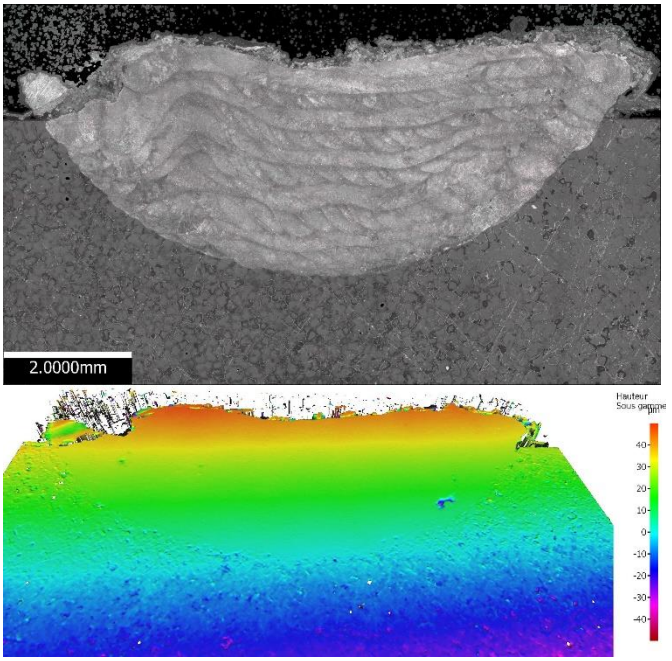

Figure 5.99: Optical view of cavity repair A (top) – Height map of cavity repair A

The SEM analysis was performed using a JCM-6000Plus in both secondary (SED, as in Secondary Electron Diffusion) and backscattered electron (BED, as in backscattered electron diffusion) imaging modes, with the BED-Composition (BED-C) mode being particularly useful for showing contrasts in chemical composition and thus highlighting the copper microsegregation phenomenon. Other modes such BED-Shadow (BED-S) are used to show both topological variations and chemical heterogeneities.

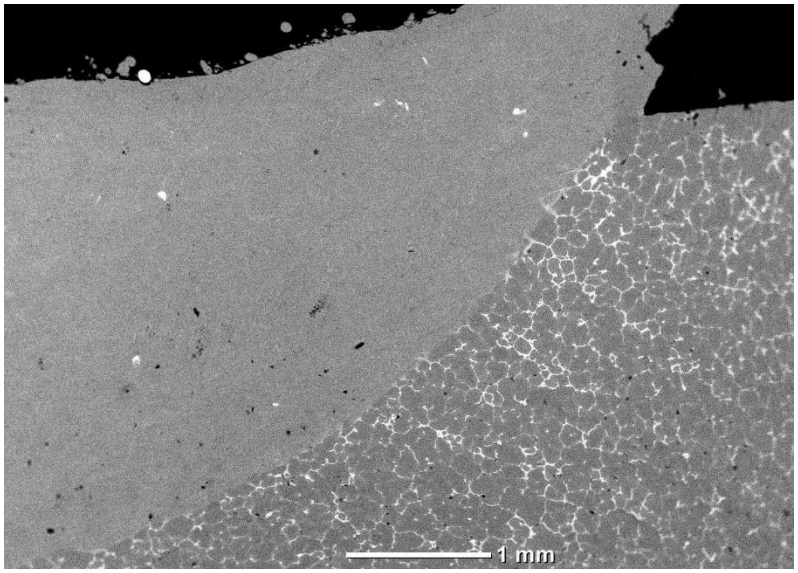

Figure 5.100: SEM imaging of 224.0 cavity repair B in BED-C mode at 15 kV

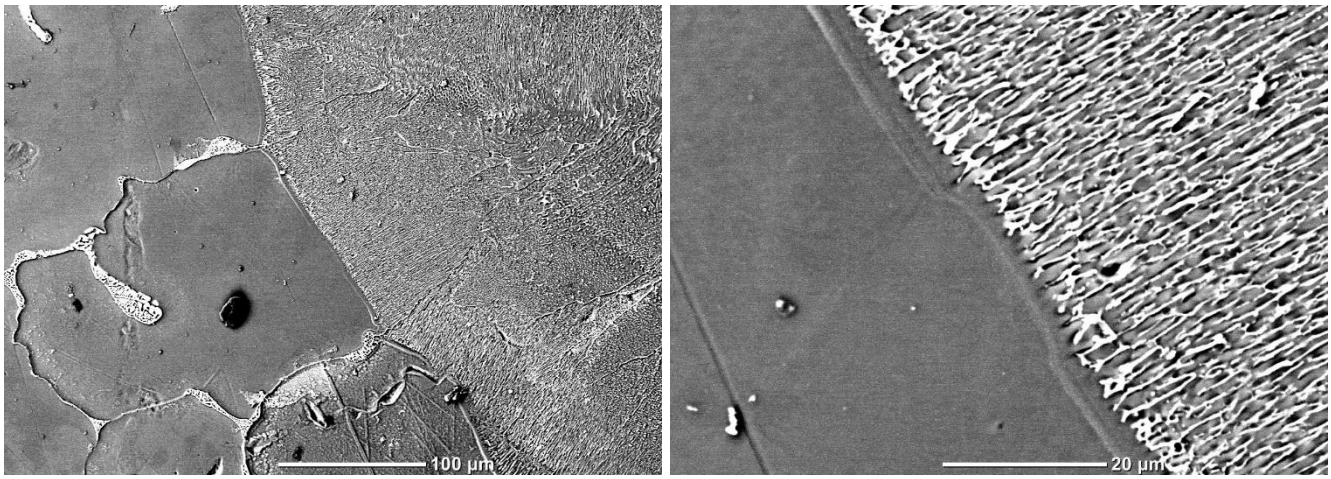

Figure 5.101: SEM imaging of 224.0 cavity repair A in BED-S mode at 15 kV with a focus on the bonding interface between LMD deposit and cast substrate

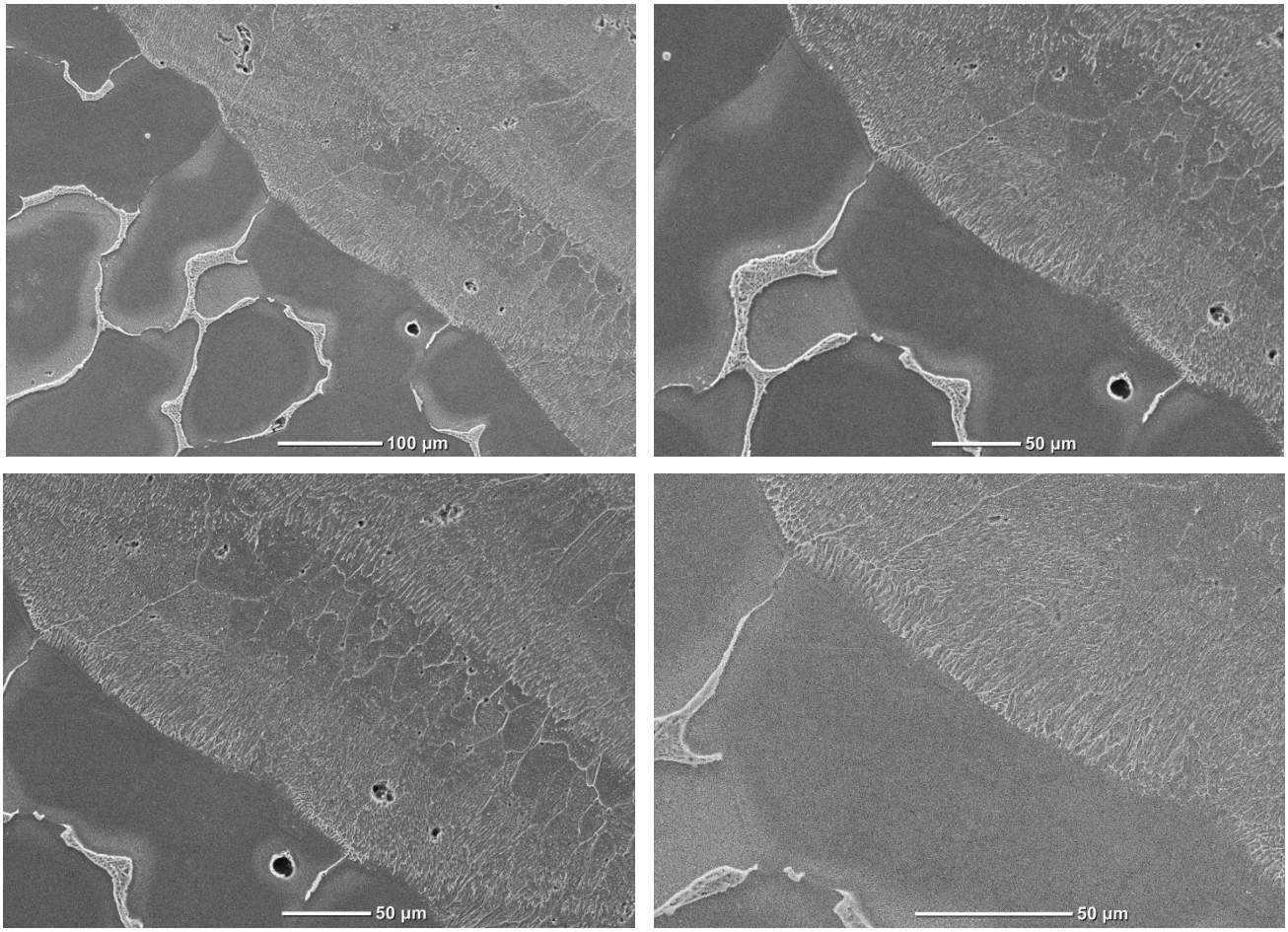

Figure 5.102: SEM imaging of 224.0 cavity repair B in SED mode at 15 kV with focus on bonding interface at various scales

There is no obvious discontinuity at the bonding interface between the LMD deposit and 224.0 cast substrate, as shown in figure 5.100 to figure 5.101. The deposit penetration inside the substrate is satisfactorily accomplished, which is paramount for the good integrity of the repaired region. A large difference in grain size is also observed between the cast and LMD material, as the average size of the 224.0 cast part is on the order of several 100µm while it is on the order of several 10µm for the 224.0 LMD deposit. The microstructural features are also much finer in the LMD deposit, with columnar cells near the substrate and refusion lines (figure 5.102 and figure 5.103) being a few micrometers wide and about 10 to 20µm long. Gas microporosities, most likely created by hydrogen gas entrapment during the rapid cooling phase, are present throughout the microstructure although their size is mostly limited to a diameter on the order of 5µm or less.

As in most metal AM microstructure, the microstructural growth mode alternates between columnar morphologies near refusion lines and more equiaxial structures in between the refusion lines (figure 5.104 to figure 5.106). In the equiaxial region, the grains are more defined as the grain boundaries are thicker due to high copper concentrations (white regions in the SEM images).

Figure 5.106 shows a region located near a refusion line where a few types of defects are concentrated. While not a common occurrence within the microstructure, there is here a relatively long hot crack with its top extremity being partially-backfilled by eutectic liquid. There is also a fine distribution of gas microporosities as well as lack of fusion or void zones, either formed due to improper material feeding, porosities or hot cracking.

In figure 5.107, relatively large grains from an equiaxial region are displayed in two different modes: SED (secondary electrons) and BED-S (backscatter electrons). The BED-S mode enhances both composition and topological differences, clearly revealing both microporosities and copper segregation. The SED mode better reveal the microsegregation than the microporosities in this instance, displaying clearly the copper segregates at the grain boundaries but also within the grain as diffuse or spot segregates. Coming back to figure 5.101 where the focus is made on substrate/deposit bonding interface, there is long lighter liner near the penetration region that follows the shape of the cavity. This line is also clearly caused by the microsegregation of copper during the refusion of the substrate upon deposition of the first layers. It is reminiscent of the banded or plate-like microsegregation so commonly reported in aluminium-copper alloys, including cast alloy 224.0 (Dumant 1996; Planchamp et al. 1993). Figure 5.108 offers an additional view of the microstructure and the type of microsegregation that is typically observed in cavity repair samples, although only a few cavity samples observations can be reproduced here. Again there are fine microsegregates distributed along boundaries of columnar cells and grains, with some diffuse or spot microsegregation within equiaxial grains, as highlighted in figure 5.110. In columnar regions however, there are less

spot microsegregates as they appear to be mostly distributed as thin layers at cell boundaries, as can be seen in figure 5.109.

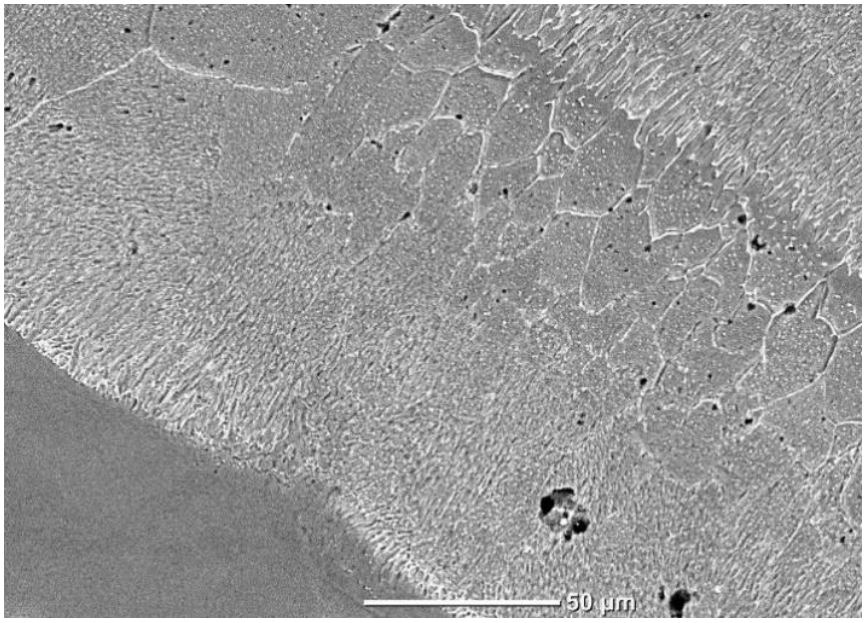

Figure 5.103: SEM imaging of 224.0 cavity repair B in BED-C mode showing a columnar microstructure near substrate bonding interface and refusion zones, and a more equiaxial structure inbetween. Porosities are also observed.

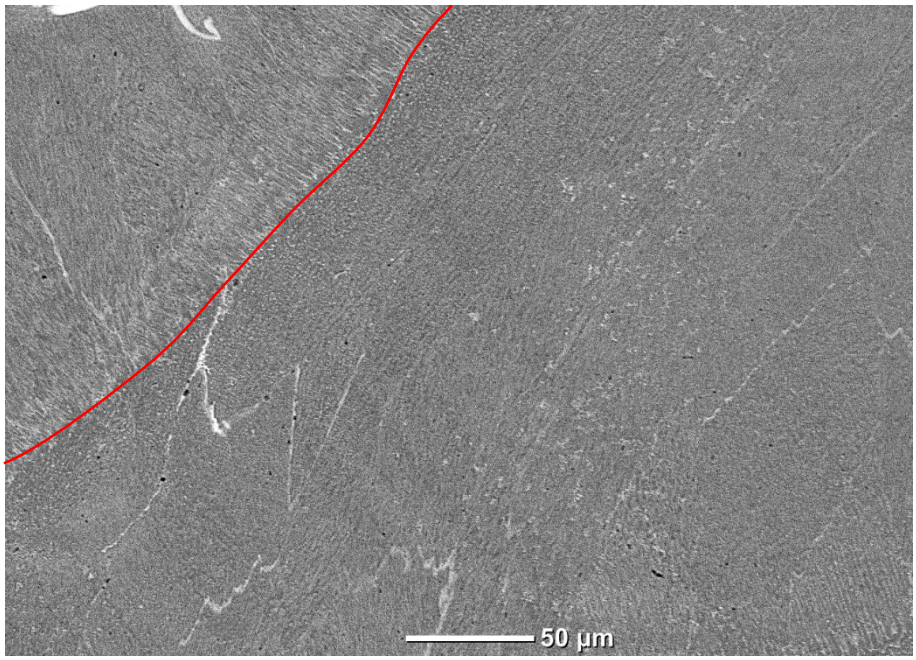

Figure 5.104: Refusion line (shown in red) in SEM BED-C imaging of 224.0 cavity repair B

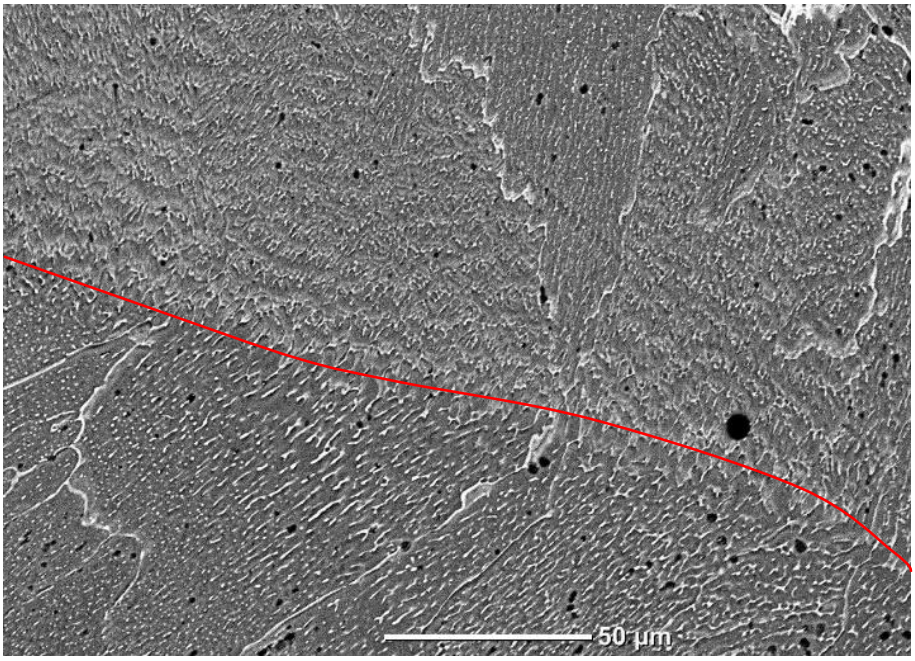

Figure 5.105: Refusion line (shown in red) in SEM BED-C imaging of 224.0 cavity repair B

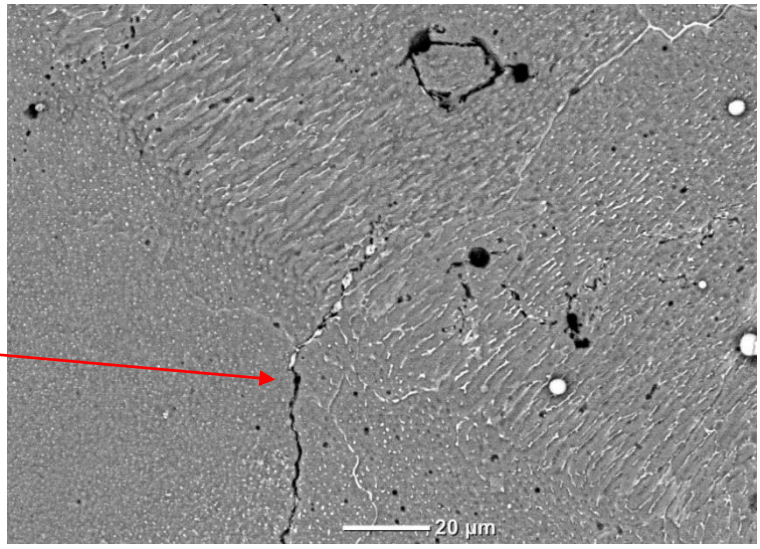

Figure 5.106: Refusion zone with defects in SEM BED-S imaging of 224.0 cavity repair A

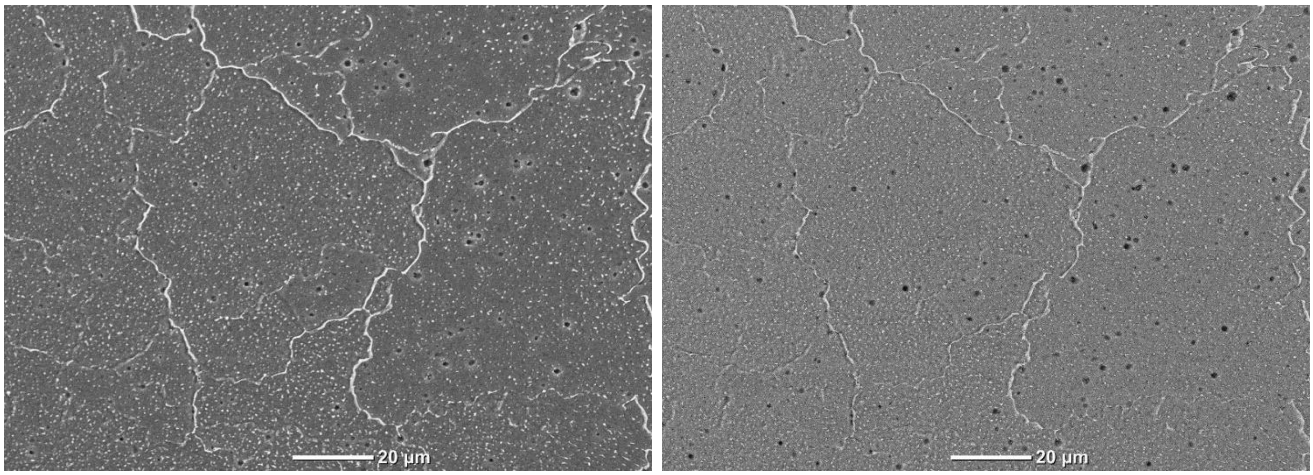

Figure 5.107: Equiaxial region with clear grain boundaries and diffuse (spot) copper microsegregation in SEM imaging of 224.0 cavity repair B – SED mode (left) – BED-S mode (right)

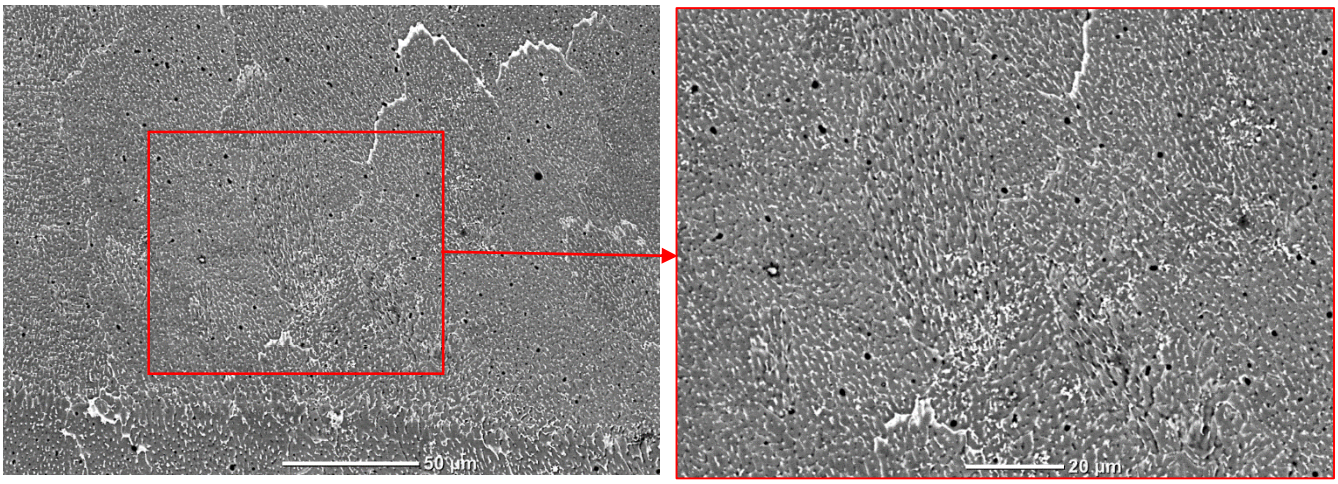

Figure 5.108: Microstructure above refusion line showing a fine copper distribution with thin regions of higher copper concentration in SEM BED-C imaging of 224.0 cavity repair B

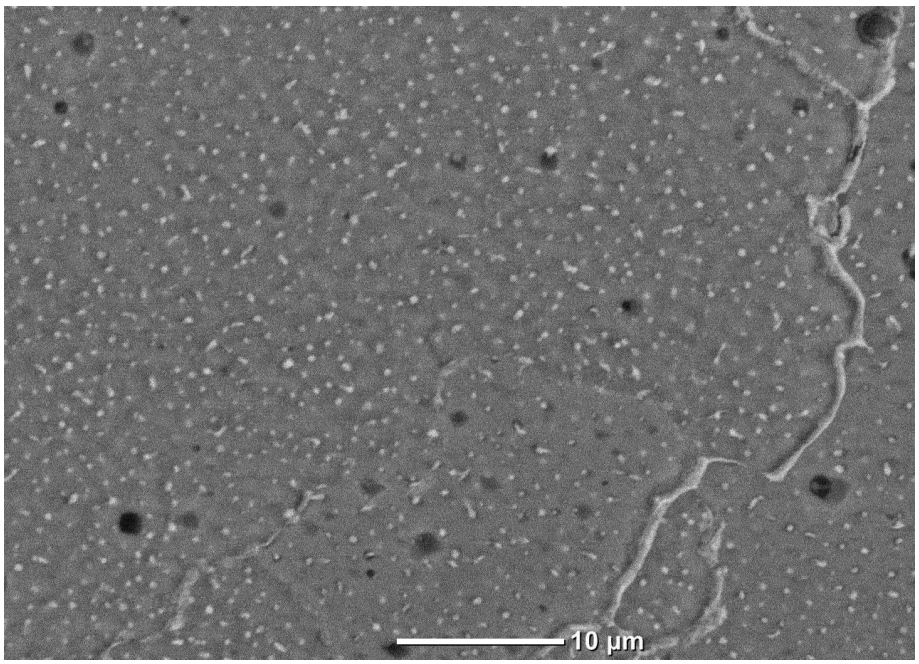

Figure 5.110: Copper segregates in equiaxial region appearing as diffuse (spots) within the grains and as thin layers at grain boundaries in SEM BED-C imaging of 224.0 cavity repair B

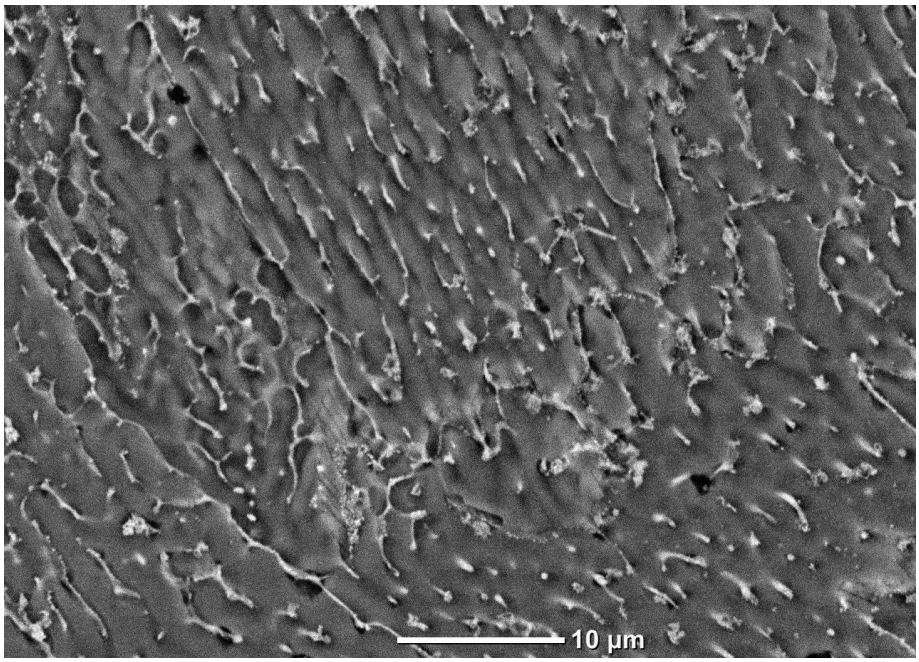

Figure 5.109: Copper segregates in columnar region appearing mostly as thin layers at cell boundaries and grain boundaries in SEM BED-C imaging of 224.0 cavity repair B

To confirm the heterogeneities in chemical composition observed on the SEM images, an elemental mapping is carried out using Energy-Dispersive Spectroscopy (EDS). The results, reproduced in figure 5.111 as an overlay of the Al map and the Cu map, demonstrate that the lighter areas in SEM imaging, whether in SED, BED-C or BED-S mode, do correspond to copper-rich regions, composed of phases θ or $\theta + \alpha$, and the darker areas are aluminium-rich regions, as expected.

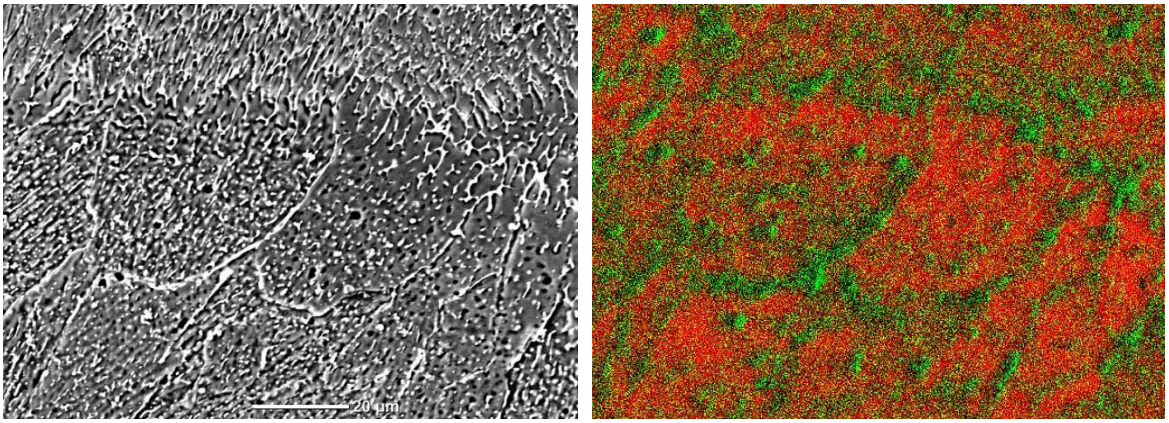

Figure 5.111: Copper microsegregation in SEM imaging and EDS mapping – BED-S mode (left) : copper in white, aluminium matrix in grey – EDS elemental mapping (right) : copper in green, aluminium matrix in red

The level of microsegregation of the copper atoms within the 224.0 material is of particular interest as the microsegregation phenomenon generates chemical heterogeneities that can be detrimental to the mechanical and corrosion resistance properties of the material. Copper-rich regions where eutectic liquid concentrates at the end of solidification are typically located at the grain boundaries. In LMD deposits, segregates can also be found within the grains throughout the aluminium matrix as diffuse or spot segregates, unlike the cast material where copper segregates are mostly concentrated at the grain boundaries. The hard but brittle phase θ-Al_2Cu is concentrated in these regions with high copper content, where incipient cracks can more easily propagate. Higher concentration of phase θ-Al_2Cu in the segregated regions means that the aluminium matrix is all the more depleted in copper atoms, so that mechanical properties are more heterogeneous within the material. When the characteristic microstructural size decreases, for instance through an increase in solidification rate that shortens the crystal growth phase, the intergranular/intercellular/interdendritic regions represent a higher volume portion of the microstructure compared to microstructures with larger features as found in the cast material. Given an equal overall copper content and microsegregation level, the smaller microstructure results in copper segregates being more finely distributed and less concentrated, so that the material integrity is less impacted by the microsegregation phenomenon. In addition, higher solidification rates can limit the level of microsegregation as the solidification becomes more diffusion-limited, thus further mitigating the impact of solute microsegregation on the overall mechanical and properties.

To assess the difference in copper atoms segregation between LMD and the lost-wax casting process, an EDS sequential analysis can be performed at the grain boundaries and within the grains of the LMD deposit and cast substrate of cavity repair sample A. Beforehand, a chemical composition analysis of the 224.0 substrate and LMD deposit at a

mesoscopic scale is conducted to confirm the similarity in chemical composition, as seen on figure 5.112 and figure 5.113 as well as in table 5.36 and table 5.37. Although some discrepancies are observed in terms of atom concentration, the elements identified in both materials are essentially the same, except for Vanadium, Silicium and Manganese which are not detected in all cases although this could be caused by limitations on the sensitivity of the EDS analysis itself, as the 224.0 powder material used for the LMD deposit should approximately present the same composition as the cast material. In the LMD region selected for EDS analysis, the overall copper content appears to be higher than in the cast material. There is however some amount of uncertainty associated with EDS measurements, as represented by the sigma values in table 5.36 and table 5.37. For comparison, an independent chemical analysis of the 224.0-A 80-100µm powder by Inductively Coupled Plasma – Atomic Emission Spectroscopy (ICP-AES) provided by UTBM/Bureau Veritas is shown in table 5.38. The chemical composition of the 80-100µm powder remains very close to the chemical composition of the ingot (not shown) used for atomizing this powder according to the ICP-AES analysis, although the powder is slightly more oxidized. The copper content measured by ICP-AES is much closer to the expected value of about 4.7wt%Cu and the EDS measurement in the 224.0 cast substrate (4.55wt%Cu). Let us therefore assume that the chemical composition, and specifically the copper content, of the 224.0-A 80-100µm powder used for the LMD deposit is roughly equivalent to that of the 224.0 cast substrate.

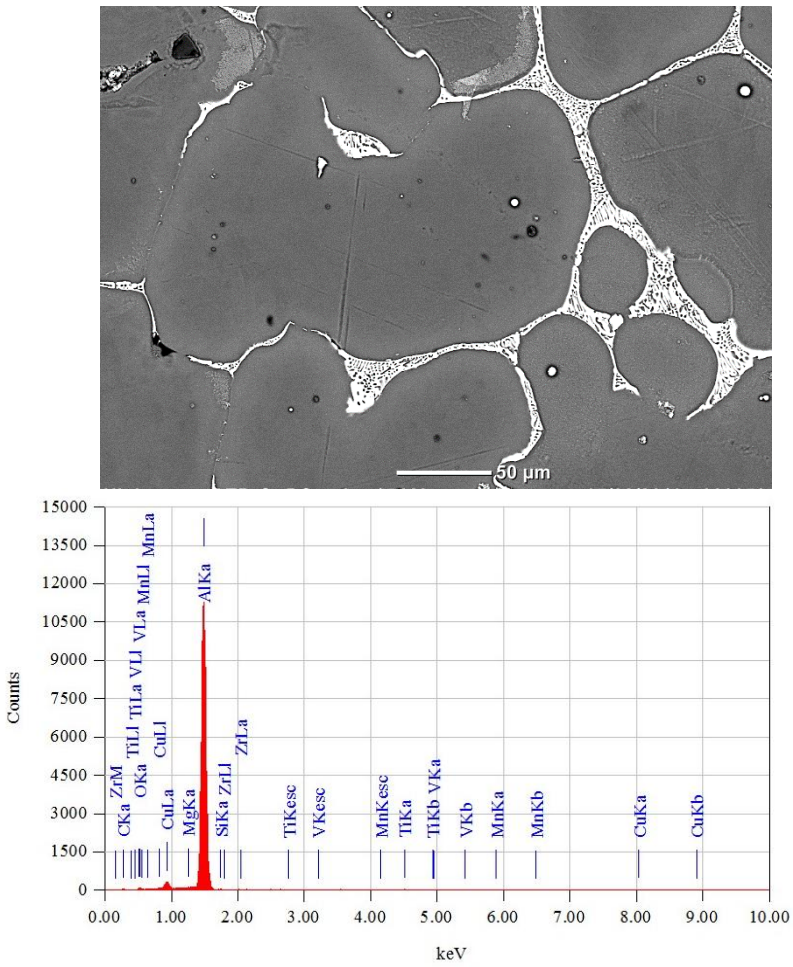

Figure 5.112: SEM BED-C image used for EDS analysis of 224.0 casting (top) – corresponding EDS spectrum (bottom)

Element	Al	Cu	Mn	V	Zr	Ti	Si	Mg	C	O
wt%	83.40	4.55	0.25	ND	0.33	0.20	0.09	0.05	8.09	3.03
sigma	0.33	0.30	0.07	-	0.10	0.05	0.05	0.03	0.24	0.12

Table 5.36: Chemical composition (wt%) of 224.0 casting according to EDS analysis (ND= Not Detected)

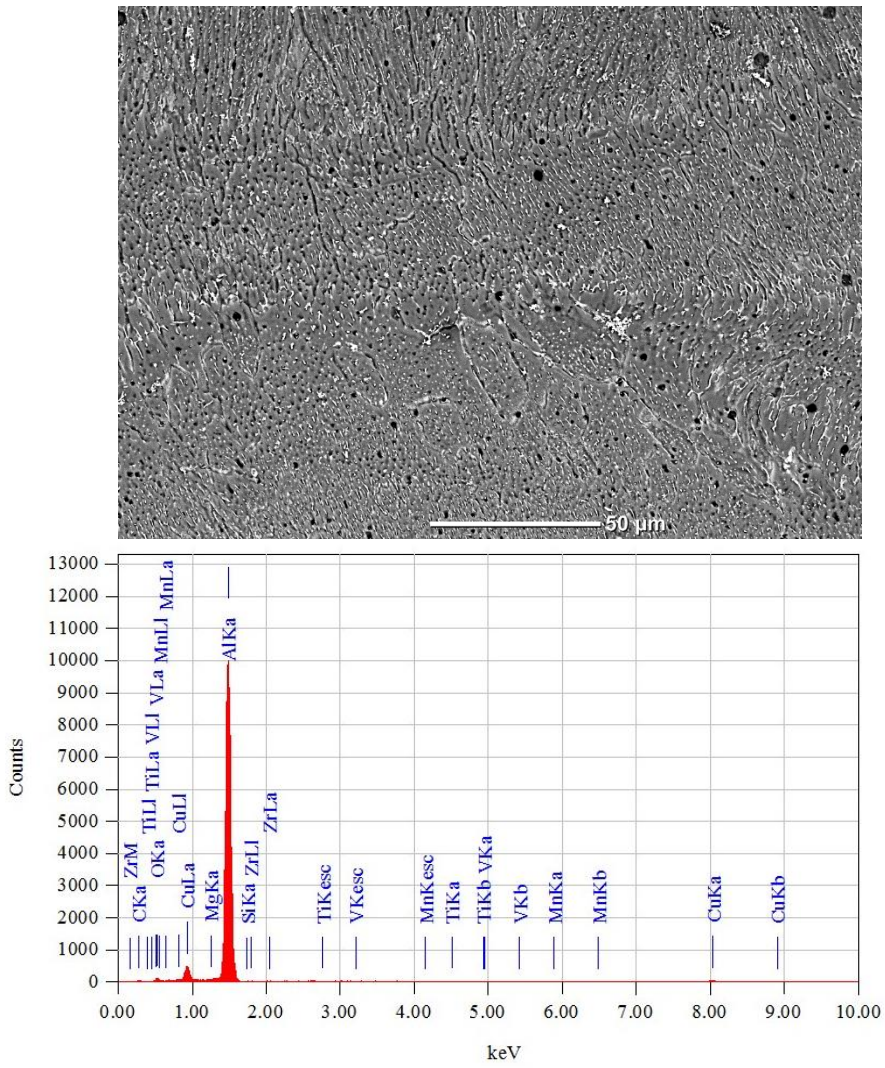

Figure 5.113: SEM BED-C image used for EDS analysis of LMD deposit with 224.0-A 80-100 µm powder (top) – corresponding EDS spectrum (bottom)

Element	Al	Cu	Mn	V	Zr	Ti	Si	Mg	C	O
wt%	80.07	7.05	ND	0.09	0.23	0.38	ND	0.05	8.85	3.28
sigma	0.34	0.36	-	0.05	0.10	0.05	-	0.03	0.25	0.13

Table 5.37: Chemical composition (wt%) of LMD deposit with 224.0-A 80-100µm powder according to EDS analysis (ND= Not Detected)

Element	Al	Cu	Mn	V	Zr	Ti	Si	Mg	C	O
wt%	Matrix	5.2	0.22	0.098	0.12	0.16	< 0.1	< 0.1	< 0.011	0.045
Uncertainty (+/- wt%)	-	0.16	0.0044	0.0078	0.0024	0.0032	-	0.03	-	0.0031

Table 5.38: Chemical composition (wt%) of 224.0-A 80-100µm powder according to ICP-AES analysis (other element such as Cobalt, Antimony, Nickel, Iron, Zinc are also present in trace quantities)

Considering the LMD repair to be approximately chemically homogeneous, the copper distribution in the 224.0 cast material and in the 224.0 80-100µm LMD deposit can be compared.

Focusing first on the 224.0 cast material, figure 5.114 shows the copper distribution along a line (left) and on a 2D elemental mapping (right). Along the line are shown the qualitative content in aluminium (sky blue curve) and copper (purple curve), where the troughs of the aluminium curve match the peaks of the copper curve, thus demonstrating the heterogeneities in aluminium and copper concentrations. This is further shown by the elemental mapping where there is again a clear correspondence between the light regions in SEM imaging and high copper concentration regions as shown by EDS analysis. For a more quantitative evaluation, figure 5.115 shows rectangular region in which the aluminum and copper contents are evaluated and the results displayed in table 5.39. Although other elements are discarded from this analysis in a first approach, there is a clear difference in copper content between regions 1 and 2 (grain boundaries) and regions 3 and 4 (aluminium matrix). A more refined analysis that includes most elements found in the material is shown in figure 5.116 and table 5.40. Points 14 to 20 and point 25, located in copper-rich regions (light regions in SEM images), have a copper concentration that varies between approximately 34wt%Cu and 57wt%Cu (46.9wt%Cu on average), and aluminium concentrations comprised between 14.5wt%Al and 36wt%Al (26.6wt%Al on average). In contrast, points 21 to 26 except point 25, located in the aluminium matrix, have a copper concentration that varies between approximately 1.5wt%Cu and 4wt%Cu (2.49wt%Cu on average), and aluminium concentrations comprised between 68wt%Al and 74wt%Al (70.9wt%Al on average). Using an average copper concentration reference of 4.7wt%Cu for alloy 224.0, the copper atoms in the grain boundaries are on average 9.4 times (and up to 12 times) more concentrated at the grain boundaries than in the base material.

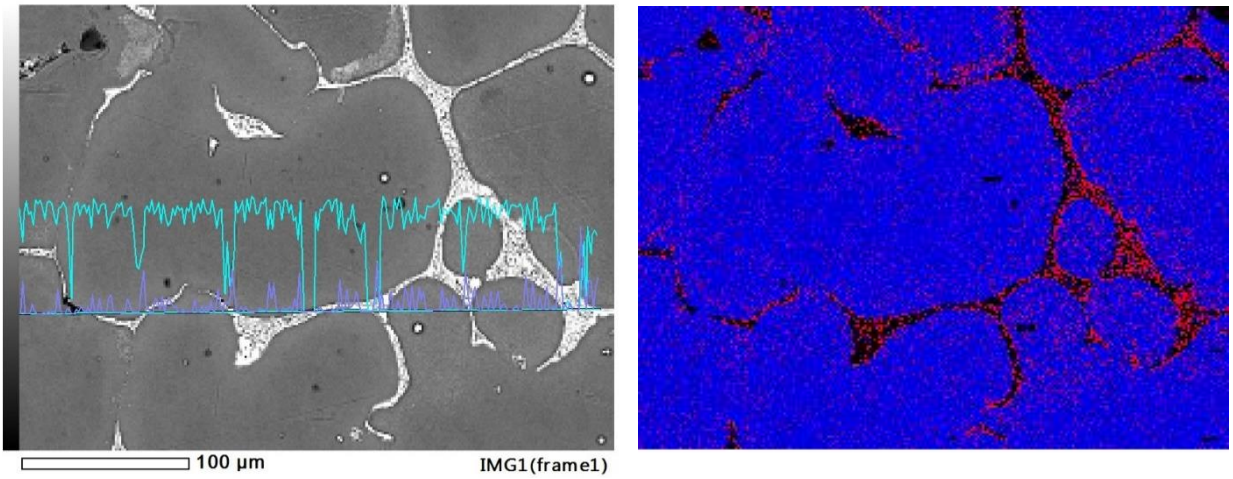

Figure 5.114: Elemental content of 224.0 cast material along line on SEM BED-C image, with aluminium in sky blue color and copper in purple (left) – Elemental mapping of 224.0 cast material with aluminium in blue and copper in red (right)

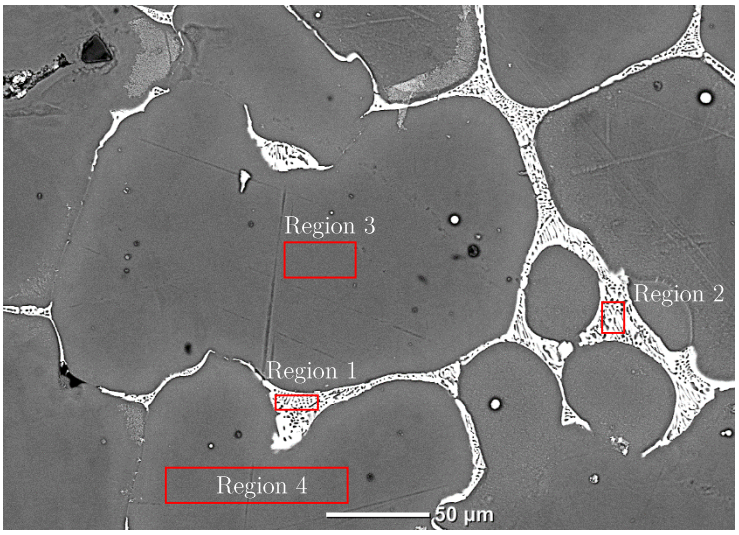

Figure 5.115: Rectangular regions 1 to 4 for EDS analysis of 224.0 cast material

Region	Al	Cu	O
1	39.41	46.10	14.49
2	51.82	38.69	9.49
3	95.51	1.70	2.79
4	95.98	1.62	2.40

Table 5.39: Average elemental concentrations (wt%) of Al, Cu and O (neglecting other elements) within regions 1 to 4 of 224.0 cast material

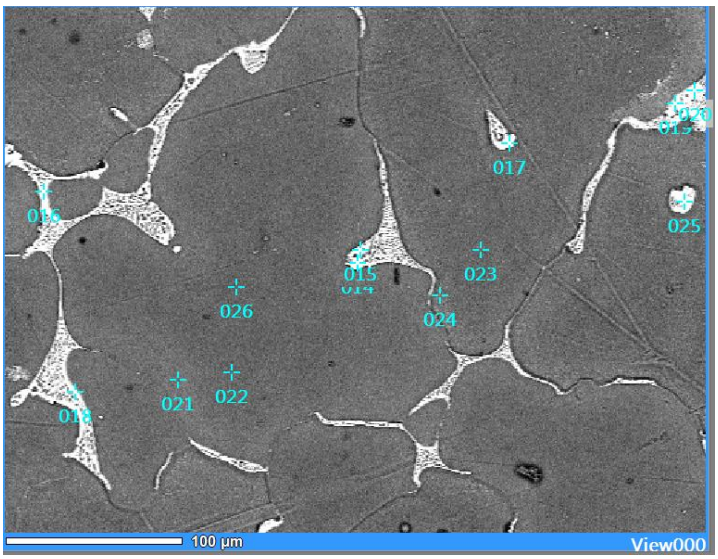

Figure 5.116: Point locations 14-26 for EDS sequential analysis of 224.0 cast material – points 14 to 20 and 25 are located in copper-rich regions, points 21 to 26 except 26 are located in aluminium matrix

Point	Al	Cu	Mn	V	Zr	Ti	Si	Mg	C	O
14	14.48	52.62	ND	ND	ND	0.06	0.25	0.18	17.97	14.44
15	24.21	46.53	0.08	ND	0.10	0.01	0.13	0.10	15.11	13.72
16	25.90	42.18	0.23	0.03	0.08	0.13	0.23	0.15	16.78	14.29
17	14.56	56.59	0.13	0.24	ND	ND	0.07	0.04	18.43	9.94
18	41.27	33.74	0.43	ND	0.22	0.08	ND	0.05	15.89	8.32
19	35.96	44.07	0.10	ND	0.33	ND	ND	ND	15.89	3.64
20	27.67	50.65	ND	0.24	0.61	ND	0.31	0.08	14.72	5.71
25	28.81	48.85	ND	ND	ND	0.19	0.29	0.05	12.04	9.78
21	71.01	3.55	0.12	ND	ND	ND	0.04	ND	23.49	1.79
22	71.30	1.67	0.34	ND	0.07	0.57	0.12	0.02	23.26	2.64
23	73.63	1.52	0.38	0.19	0.20	0.80	ND	ND	22.08	1.19
24	68.15	4.17	ND	0.12	ND	0.03	ND	0.02	23.45	4.06
26	70.56	1.53	0.19	ND	0.08	0.55	ND	0.07	24.05	2.96

Table 5.40: Elemental concentrations (wt%) at points 14 to 20 and 25 (located in copper-rich regions at grain boundaries) and at points 21 to 26 except 25 (located in aluminium matrix) of 224.0 cast material

Regarding the LMD deposit, figure 5.117 shows the elemental concentration along a line and on a 2D elemental map. Again, the line concentrations shows that the chemical composition varies between regions of high Cu concentration and regions of lower Cu concentration, which respectively correspond to regions of lower Al concentration and regions of higher Al concentrations. The copper segregation levels in the cast material can be compared to the values found in the LMD deposit, shown in table 5.41 based on figure 5.118. Points 1 to 8, located in copper-rich regions (light regions in SEM images), have a copper concentration

that varies between approximately 13wt%Cu and 31wt%Cu (20.4wt%Cu on average), and aluminium concentrations are comprised between 32wt%Al and 62wt%Al (51.2wt%Al on average). In contrast, points 9 to 13, located in the aluminium matrix of the LMD deposit, have a copper concentration that varies between approximately 0.8wt%Cu and 4.4wt%Cu (2wt%Cu on average), and aluminium concentrations are comprised between 64.5wt%Al and 68.5wt%Al (66.9wt%Al on average). Using an average copper concentration reference of 4.7wt%Cu for alloy 224.0, the copper atoms in the grain boundaries are on average 4.3 times (and up to 6.6 times) more concentrated at the grain boundaries than in the base material.

The average copper segregation level can be estimated as the ratio of average copper content in the intergranular region to the average copper content found in the aluminium matrix, yielding an average segregation ratio of 18.85 in the cast material and 10.24 in the LMD deposit. The average copper segregation in the LMD deposit is thus almost half of the segregation level observed in the cast material. The chemical heterogeneities are thus less pronounced in the LMD deposit, so that the mechanical properties are expected to be more homogeneous than in the cast material. The lower segregation level of copper atoms is most likely due to the higher solidification rate in LMD compared to the lost wax casting process with rapid cooling, as shown by the smaller size of the microstructure. The grain growth phase is thus much shorter, and the velocity of the solid/liquid interface is much higher than in a casting process, so that the interface cannot maintain local thermodynamic equilibrium due to kinetic effects being non-negligible. The copper atoms, which are more soluble in liquid than solid aluminium, cannot diffuse all the way towards the liquid phase during the rapid cooling phase. The solute trapping that results from this diffusion-limited reaction translates into a lower level of copper segregation throughout the microstructure.

Moreover, the smaller size of the microstructural features obtained by LMD should generally induce higher mechanical properties as can be shown by the empirical Hall-Petch relation, which states that the critical yield stress varies as the inverse square root of grain size.

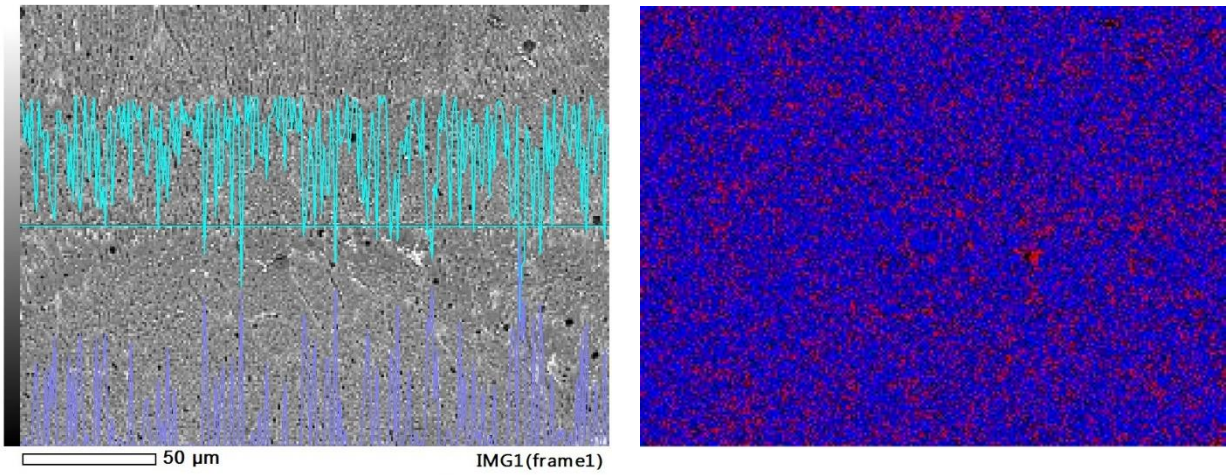

Figure 5.117: Elemental content of 224.0-A 80-100µm LMD deposit along line, with aluminium in sky blue color and copper in purple (left) – Elemental mapping of 224.0 cast material with aluminium in blue and copper in red (right)

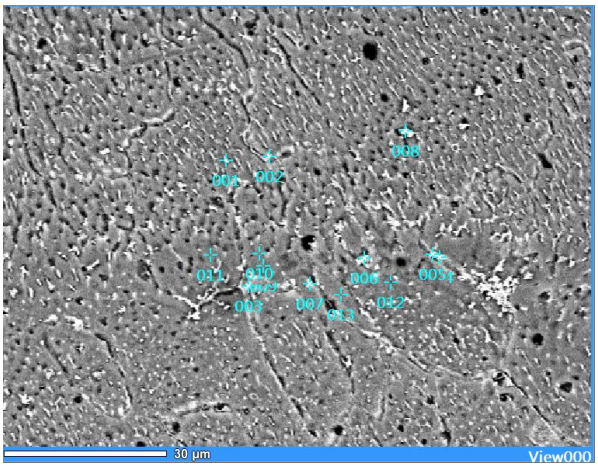

Figure 5.118: Point locations 1-13 for EDS sequential analysis of 224.0-A 80-100µm LMD deposit - points 1 to 8 are located in copper-rich regions, points 9 to 13 are located in aluminium matrix

Point	Al	Cu	Mn	V	Zr	Ti	Si	Mg	C	O
1	49.05	20.80	0.17	0.09	0.01	0.15	ND	0.13	12.59	17.03
2	59.44	15.42	0.01	0.31	0.31	0.14	0.05	0.12	18.00	6.20
3	51.30	12.64	0.19	0.11	0.16	0.02	ND	0.10	26.10	9.37
4	55.75	16.08	0.22	ND	0.11	ND	ND	0.08	19.06	8.71
5	59.64	22.01	0.27	0.36	ND	0.10	0.12	0.11	12.96	4.43
6	31.79	32.18	0.06	ND	0.15	ND	0.19	0.12	20.01	15.50
7	61.82	13.71	0.26	ND	ND	ND	0.05	0.06	22.20	1.89
8	40.95	30.68	ND	ND	ND	0.32	0.32	0.14	15.38	12.20
9	66.63	1.49	0.07	0.30	ND	0.18	ND	ND	29.94	1.39
10	67.42	0.81	0.28	ND	0.47	0.17	0.14	ND	29.43	1.28
11	67.27	1.98	0.04	0.12	0.31	0.32	ND	ND	28.65	1.30
12	64.58	4.43	0.19	ND	0.14	0.19	ND	0.12	28.51	1.84
13	68.49	1.27	ND	0.47	0.39	0.17	ND	0.01	27.85	1.36

Table 5.41: Elemental concentrations (wt%) at points 1 to 8 (located in copper-rich regions at grain boundaries and at points 9 to 13) (located in aluminium matrix) of 224.0 LMD deposit

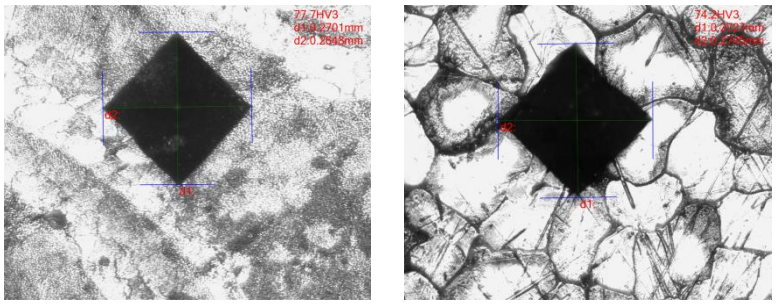

Figure 5.119: Vickers hardness testing in LMD deposit (left) and cast substrate (right) of cavity repair B

Finally, Vickers hardness testing was conducted on cavity repair B at random locations in the cast substrate and in the LMD cavity deposit using a load of 3kgf (HV3) and a dwell time of 10s. Examples of indent geometries in both cases are displayed in figure 5.119. The average and standard deviation of the hardness testing results over 7 sample locations in the cast substrate that are remote from the deposit (i.e. out of the HAZ) and 12 sample locations in the LMD deposit are reproduced in table 5.42. Interestingly, the hardness in the LMD deposited region is slightly above that found in the cast substrate before heat treatment. This implies that the fineness of the LMD microstructure obtained when depositing alloy 224.0 with the prescribed LMD process parameters induces mechanical properties that are slightly higher than the raw cast material. Although this should be further confirmed through proper mechanical testing, which are beyond the scope of the present work, those results indicate that the mechanical properties of the repaired part should be recovered after heat treatment of the repaired part.

Region	Average Hardness HV3	Standard deviation of hardness HV3
Substrate	69.0	2.91
LMD cavity repair	74.1	2.38

Table 5.42: Hardness testing results (average and standard deviation) in cavity repair B

IV. Summary

In this chapter, a numerical assessment of alloy 224.0 behavior was first performed using CALPHAD calculations coupled to a Scheil model. It not only provided a possible solidification path for a quasi-equilibrium solidification with no solute diffusion in the solid phase and infinite diffusion in the liquid phase. While this model is somewhat remote from rapid solidification conditions, it nonetheless provide a more suitable evaluation of solidification conditions compared to pure equilibrium solidification using the lever rule. This open-source solution could thus eventually yield an efficient evaluation of various alloys, such as their hot cracking susceptibility, before embarking on costly and time-consuming experimental trials. Indeed, the thermodynamic information obtained from the CALPHAD method and the solidification curve obtained by coupling with a Scheil model can be fed directly into a CFD software such as Flow3D© as well as phase field models. Unlike most LMD numerical simulations found in the literature, the VOF approach coupled to a solidification model, a laser heat source model and a particle flow model allows to explicitly compute the geometry of an LMD bead under various processing conditions.

While further work is required to calibrate the model to experimental results, these types of numerical simulations could be further developed to emulate the deposition of more complex geometries such as thin walls and eventually cavity repairs, thereby yielding an a priori assessment of solidification conditions under various LMD process parameters. It is eventually hoped that a simulation-based approach with VOF, possibly coupled to phase field models, could lead to a numerical optimization of the process, whether to guide the initial selection of constant process parameter ranges, or even proceed to the optimization of non-constant process parameters during deposition. For example, it could help in evaluating an adequate time-dependent laser power profile required during the deposition of material to account for heat build-up (i.e. temperature increase) inside the region of interest, which are bound to impact the ideal process operating point for LMD deposition. This could thus pave

the way towards time-dependent LMD process parameterization, which are typically taken as constant for simplicity throughout the literature and the presented experiments.

A series of LMD experiments were performed to first identify a suitable operating point for the LMD deposition based on thin walls. Cavity repairs could then be carried out based on this operating point, with toolpaths generated based on the cavity geometry segmentation obtained with the InterSAC method of the previous chapter.

An evaluation of the metallurgical aspects of the repaired cavities (microstructure, solute segregation, hardness) showed that the deposits were well-bonded with the cast substrate, offered a very refined microstructure with finely distributed segregates where a lower copper concentration than in the cast substrate was observed. The rapid solidification conditions thus effectively diminished the extent of copper segregation, most likely due to the solute trapping effect during rapid solidification. This diminution in copper segregation is highly desirable as it limits the chemical heterogeneity of the material and reduces the extent of brittle phases θ-Al_2Cu, which are generally harmful in terms of mechanical properties.

Finally, a slightly higher Vickers hardness was obtained in the as-deposited region inside the cavity compared to the heat treated cast part. Although the actual mechanical properties should be further evaluated through mechanical testing, this strongly suggest that the properties of the LMD deposit are at least comparable to that of the cast part, with the added benefit of not having gone through a heat treatment. This is highly desirable for repair application as it would remove the requirement of heat treatment after repairs and thus provide a shorter repair cycle time.

Chapter VI: Conclusions and Perspectives

I. Summary

a. Chapter 1

The first chapter focused on alloy 224.0, otherwise called alloy AU5MVZr, which is a not a commonly used alloy in industry to its relatively low castability and low weldability, i.e. low reparability with current processes such as GTAW. A review of the literature on Al-Cu alloys revealed that they are indeed prone to issues during solidification such as copper segregation, leading to chemical heterogeneities in the cast material and welding repairs, as well as a high propensity to hot cracking. The use of such alloys for AM processing, and particularly DED processes such as LMD, is also scarcely reported, possibly due to solidification issues as well as flowability issues when provided in powder form.

It is however desirable to be able to efficiently repair Al-Cu alloys such as 224.0 as they provide high mechanical properties even at elevated service temperatures, making it a very suitable alloy for parts such as compressor volutes of jet engines. The LMD process was thus selected as a potential replacement for GTAW in the hope of obtaining higher quality of repaired zones and thus diminish the recycling of 224.0 high performance castings. The repair application for LMD, if successful, could pave the way for Al-Cu part remanufacturing and fabrication using the LMD process, and thus potentially allow for a more widespread use of such alloys for manufacturing parts with high mechanical performance at elevated service temperatures.

b. Chapter 2

Powder flowability issues with LMD are scarcely reported in the literature, compared to SLM, although the range of powder flow conditions are more diverse with LMD, making this process more stringent of powder flowability. The optimization of the powder in LMD would also follow different constraints as the flowability aspects are paramount compared to powder packing issues found in SLM.

In chapter 2, a population-dependent granular Bond number Bo_g^*, recently correlated with flowability function coefficients of pharmaceutical powders, was applied to a variety of LMD powder samples using state-of-the art models of van der Waals and capillary forces for rough particles.

The Bo_g^* calculations for the various samples were correlated with funnel-based flowability measurements based on a new flowability measurement method for cohesive, non-flowing powders. This method employs high frequency vibrational excitations applied to the funnel to provide a local displacement of particles, thereby initiating and sustaining the flow of particles through the funnel, even for the more cohesive powders. This allows for a funnel-based assessment of flowability, which is a flowability testing method that closely resembles the conditions encountered in powder reservoirs. It was shown that with vibrations being applied, the Bo_g^* and the span of the particle size distribution of each sample could help predict the funnel-based flowability measures when vibrations are applied.

A particular heat treatment was also found to significantly improve the in-process flowability of cohesive aluminium powders. Together with an adjustment of the LMD powder distribution system, this unlocked the possibility of using such cohesive aluminium powders with the LMD process.

c. Chapter 3

In chapter 3, flowability issues with the cohesive 224.0 powder in the fluidized regime are assessed. To elucidate the behavior inside the nozzle, where observations cannot be directly made, 2.5D CFD-DEM simulations of the gas-particle flow inside the LMD nozzle were performed on a supercomputer to assess the recirculation behavior of particles inside the homogenization chamber of the nozzle. This led to a new design of the LMD cones, which were numerically shown to suppress the recirculation behavior by providing a more favorable rebound of the particles as they enter the nozzle and by suppressing the gas vortex inside the chamber.

A segmentation method based on image processing operations and a Hough transform was also shown to provide a suitable assessment of powder jet stability based on low-speed, i.e. low cost, imaging. Low resolution high-speed imaging was also carried out, and estimates of the particle velocities at the nozzle outlet under various conditions were obtained despite the fairly low resolution of the captured images. Both of these methods could thus be used to better evaluate the geometry and stability of the powder jet as well as the particle velocity at the nozzle outlet under various LMD processing conditions.

d. Chapter 4

In the perspective of using LMD for repair applications, chapter 4 sought to develop a repair methodology and a robust cavity segmentation algorithm based on raw 3D scan data, which was applied to spherical and various cylindrical geometries. This so-called InterSAC method allows to fairly accurately obtain the geometry of the cavity to be repaired in the reference frame of the LMD system using a priori information on the cavity geometry. This permits a higher automation level of the repair process as the LMD scan path for performing the cavity repair can be directly generated based on the segmentation results.

e. Chapter 5

Considering the relative lack of experimental data for numerous alloys such as 224.0, numerical methods were employed to assess the solidification behavior of alloy 224.0. A first step consisted in performing CALPHAD and Scheil solidification calculations based on open-source tools, the results of which being fed as input parameters for a CFD (VOF) simulation of LMD deposits. This VOF modeling approach improves upon most of the numerical models of the LMD process found in the literature as it does not assume the geometry of the deposit to be known a priori and offers a more realistic shape of the bead compared to methods based on finite-elements. It also yields the temperature and velocity field of the fluid and could thus eventually provide a fairly accurate estimate of melt pool behavior and bead geometry. Although the VOF model should be calibrated to experimental observations to obtain more qualitatively accurate results, it already gives interesting information in relative terms. For instance, it appears that the powder flowrate does not significantly impact the width of the bead, unlike laser power. A phase field code was also briefly presented considering recent advances found in the literature that could finally enable the quantitative simulation of rapid solidification with binary alloys.

A dimensionless heat input parameter combining process and material parameters was developed for DED processes such as LMD and WAAM process to provide an appropriate basis for comparing experimental conditions between various systems and materials. Using such characteristic numbers instead of the more usual dimensional process parameters (e.g. laser power, scan speed) is already an improvement as it is poised to constitute a more comparable indicator of processing conditions across research groups. The characteristic heat input number is based on significant simplifications of the melt pool behavior, akin to what

was used elsewhere for laser welding and SLM for instance, and could possibly be further improved while retaining its purely analytical form.

Furthermore, an experimental plan established a suitable set of operating parameters for LMD processing of alloy 224.0 using geometrical criteria and a method for porosity content estimation. This ultimately allowed to perform cavity repair on an actual high performance casting. The metallurgical analysis demonstrated that a fine microstructure with limited copper segregation could be obtained, with good bonding between the deposit and the substrate. Hardness tests further revealed that the mechanical properties of the repaired region could at least match that of the original part without the need for heat treatment. Although this would require confirmation through proper mechanical testing, the presented results strongly suggest that LMD is indeed very suitable for homogeneously repairing low weldability Al-Cu alloys such as 224.0, provided that potential powder flowability issues could be resolved, which was successfully demonstrated in previous chapters.

f. Conclusion

This manuscript was focused on enabling the use of the LMD process with an aluminium-copper casting alloy, which revealed to be particularly challenging due to its low weldability, according to the literature review carried out in chapter 1. Chapters 2 and 3 highlighted and resolved another challenging aspect of this Al-Cu powder, i.e. its low flowability. Once the powder could processed by LMD, a method had to be devised in order to be able to perform repairs in an automated manner, which was done in chapter 4. Finally, in chapter 5, LMD processing conditions for this alloy were optimized and a metallurgical analysis of the deposits was performed. The primary application of this work was the repair of high performance aeronautical parts, suggesting that such repairs could be done despite the challenges faced with this particular alloy. The results and methods developed in this work could be extended to the remanufacturing of existing parts as well as the fabrication of new parts with other low weldability, low flowability alloy powders.

II. Perspectives

a. Numerical modeling

Numerical modeling and simulation could provide interesting information on the conditions encountered during LMD processing where direct observations are not always possible.

The gas-flow behavior of cohesive powders inside the LMD system should be further explored using CFD-DEM simulations and employing more accurate models for cohesion forces such as van der Waals forces. Capillary forces could also be included, together with triboelectric charging phenomenon and thus electrostatic interactions. Moreover, the perspective of performing fully 3D simulations should be pursued to provide an even more realistic behavior for the gas-particle flow inside the nozzle as well as at the nozzle outlet. This would require an improved setup of the CFD-DEM software on the supercomputer so that it could mobilize more computing power and thus yield more acceptable runtimes.

Additionally, the evaluation of the solidification behavior of a particular multicomponent commercial alloy such as 224.0 during LMD processing should be further pursued by improving upon the parameterization and calibration of the VOF model. This modeling approach, only known to have been used recently for the SLM process, is very promising in that it mostly employs physical models and almost no a priori information regarding the geometry of the deposit, unlike finite-element-based methods. Despite being fairly costly computationally, it could serve as the basis a simulation-based optimization of the LMD process, provided the results can be calibrated with experimental results. Despite the limitations of the current model, it already shows qualitatively appropriate behavior of the melt pool and bead deposit using realistic material properties and process parameters (e.g. scan speed, laser power) and should be used to model more complex deposit geometries such as thin walls and eventually cavity repairs. Incorporating the scan path of the LMD head could thus yield a model that can assess a given set of operating conditions before going into the experimental phase. It could also enable the optimization of time-dependent laser power of scan velocity profiles to maintain suitable conditions along the duration of the LMD deposition process, during which heat accumulates and thus could lead to a variation of the ideal operating point.

Before looking at the melt pool, an improvement on the solidification modeling and the coupling with thermodynamic packages should also be pursued to provide more realistic solidification curves for rapid solidification conditions. A prime candidate method are phase

field models, for which recent findings finally allow to quantitatively model rapid solidification conditions and provide a more realistic solute segregation behavior.

Finally, the pertinence of using characteristic numbers for reporting and evaluating LMD processing conditions should be further evaluated by devising a set of LMD or WAAM experiments across various system configurations and using different materials. Establishing a robust set of characteristic, non-dimensional numbers combining material and process parameters could nonetheless enable better comparisons between experiments as well as numerical simulations between research groups.

b. Repair method

The repair method of the present work is a RANSAC-based segmentation method called InterSAC. The range of geometrical shapes for the cavities to be segmented could be further extended, although it already includes spherical and various cylindrical shapes that are typically obtained with hemispherical toolbits. It could also be improved to properly segment arbitrary combinations of analytical shapes.

In this work, the repair method was dedicated to the case of purely AM repairs (LMD, WAAM), i.e. where the machining of the defect is performed in a separate machine tool. An integrated method could be devised to enable hybrid repairs, although a different approach would be required to automatically identify the defect to be machined out before the performing the LMD repair. The integration post-deposition machining or laser polishing could also be explored to provide a fully automated repair method using a hybrid LMD-machining process. Higher automation would further justify the use of the LMD process for repair application as it would drastically reduce the level of human intervention, improve on the repeatability and efficiency of the repair process. Although focused on aluminium-copper alloys, the method could be applied to other types of metallic alloys with other AM processes, particularly of the DED family.

c. Analysis of LMD deposits

The metallurgical analysis of the repaired cavities using LMD show promising results in terms microstructure and substrate bonding, which have been demonstrated to be satisfactory with the identified process parameters despite the difficulty of processing Al-Cu alloys. Indeed, the copper segregation is very limited compared to the cast part, and the occurrence of hot cracks is very limited. Hardness testing also showed promising results in that the LMD deposit without heat treatment may perform as well as the heat treated cast part.

However, this would require further confirmation through proper mechanical testing. The impact of LMD process parameters on the microstructure should also be evaluated in more depth to evaluate the sensitivity of deposit quality with LMD processing parameters.

Bibliography

Abbaschian, L., and Lima, M. (2003). "Cracking susceptibility of aluminum alloys during laser welding." *Materials Research*, 6(2), 273–278.

Agrawal, V., Shinde, Y., Shah, M. T., Utikar, R. P., Pareek, V. K., and Joshi, J. B. (2018). "Effect of drag models on CFD–DEM predictions of bubbling fluidized beds with Geldart D particles." *Advanced Powder Technology*, Society of Powder Technology Japan, 29(11), 2658–2669.

Ahuja, B., Karg, M., Nagulin, K. Y., and Schmidt, M. (2014). "Fabrication and characterization of high strength Al-Cu alloys processed using Laser Beam Melting in metal powder bed." *Physics Procedia*, Elsevier B.V., 56(C), 135–146.

Alfieri, V., Caiazzo, F., and Sergi, V. (2015). "Autogenous laser welding of AA 2024 aluminium alloy: Process issues and bead features." *Procedia CIRP*, 33, 406–411.

Allimant, A., Planche, M. P., Bailly, Y., Dembinski, L., and Coddet, C. (2009). "Progress in gas atomization of liquid metals by means of a De Laval nozzle." *Powder Technology*, Elsevier B.V., 190(1–2), 79–83.

Arrizubieta, J. L., Tabernero, I., Exequiel Ruiz, J., Lamikiz, A., Martinez, S., and Ukar, E. (2014). "Continuous coaxial nozzle design for LMD based on numerical simulation." *Physics Procedia*, 56(C), 429–438.

Arunkumar, S., Rangarajan, P., Devakumaran, K., and Sathiya, P. (2015). "Comparative study on transverse shrinkage, mechanical and metallurgical properties of AA2219 aluminium weld joints prepared by gas tungsten arc and gas metal arc welding processes." *Defence Technology*, Elsevier Ltd, 11(3), 262–268.

ASM International. (2009). *Casting Design and Performance. ASM International Technical Book Committee (2008–2009), Lichun L. Chen, Chair.*

Bai, J. Y., Yang, C. L., Lin, S. B., Dong, B. L., and Fan, C. L. (2016). "Mechanical properties of 2219-Al components produced by additive manufacturing with TIG." *International Journal of Advanced Manufacturing Technology*, 86(1–4), 479–485.

Barber, C. B., Dobkin, D. P., and Huhdanpaa, H. (1996). "The quickhull algorithm for convex hulls." *ACM Transactions on Mathematical Software*, 22(4), 469–483.

Barbier, A., and Galin, E. (2004). "Fast Distance Computation Between a Point and Cylinders, Cones, Line-Swept Spheres and Cone-Spheres." *Journal of Graphics Tool*, 9(2), 11–19.

Bäuerle, D. (2011). *Laser Processing and Chemistry*. Springer Berlin Heidelberg, Berlin, Heidelberg.

Beder, C., and Wolfgang, F. (2006). "Direct Solutions for Computing Cylinders from Minimal Sets of 3D Points." *European Conference on Computer Vision*, 135–146.

Bergström, L. (1997). "Hamaker constants of inorganic materials." *Advances in Colloid and Interface Science*, 70, 125–169.

Berra, S., Etcheverry, J., and Bonadeo, N. (2007). "Laser displacement sensor characterization for use in optical gauging of threaded pipes."

Bešić, I., Van Gestel, N., Kruth, J. P., Bleys, P., and Hodolič, J. (2011). "Accuracy improvement of laser line scanning for feature measurements on CMM." *Optics and Lasers in Engineering*, 49(11), 1274–1280.

Bi, G., and Gasser, A. (2011). "Restoration of nickel-base turbine blade knife-edges with controlled laser aided additive manufacturing." *Physics Procedia*, 12(PART 1), 402–409.

Boettinger, W. J., and Coriell, S. R. (1984). "Mechanisms of Microsegregation-free Solidification." *Materials Science and Engineering*, 65, 27–36.

Brake, M. R. W., Reu, P. L., and Aragon, D. S. (2017). "A Comprehensive Set of Impact Data for Common Aerospace Metals." *Journal of Computational and Nonlinear Dynamics*, 12(6), 061011.

Bremer, C. (2005). "Automated repair and overhaul of aero-engine and industrial gas turbine components." *Proceedings of the ASME Turbo Expo 2005, Vol 2*, 841–846.

Brown, T. J., Idoine, N. E., Raycraft, E. R., Shaw, R. A., Hobbs, S. F., Everett, P., Deady, E. A., and Bide, T. (2018). *World mineral production 2012-2016. British Geological Survey, Keyworth, Nottingham.*

Nottingham.

Businaki, M., Levine, A., and Stevenson, W. H. (1992). "Performance Characteristics of Range Sensors utilizing Optical Triangulation." *Aerospace and Electronics Conference, 1992. NAECON 1992., Proceedings of the IEEE 1992 National*, 3, 1230–1236.

Caiazzo, F., Alfieri, V., Argenio, P., and Sergi, V. (2017). "Additive manufacturing by means of laser-aided directed metal deposition of 2024 aluminium powder: Investigation and optimization." *Advances in Mechanical Engineering*, 9(8), 1–12.

Caiazzo, F., Alfieri, V., Cardaropoli, F., and Sergi, V. (2013). "Butt autogenous laser welding of AA 2024 aluminium alloy thin sheets with a Yb:YAG disk laser." *International Journal of Advanced Manufacturing Technology*, 67(9–12), 2157–2169.

Caiazzo, F., and Caggiano, A. (2018). "Laser direct metal deposition of 2024 al alloy: Trace geometry prediction via machine learning." *Materials*, 11(3), 444.

Cao, G., and Kou, S. (2006). "Predicting and reducing liquation-cracking susceptibility based on temperature vs. fraction solid." *Welding Journal (Miami, Fla)*, 85, 9s–18s.

Capece, M., Ho, R., Strong, J., and Gao, P. (2015). "Prediction of powder flow performance using a multi-component granular Bond number." *Powder Technology*, Elsevier B.V., 286, 561–571.

Capece, M., Huang, Z., To, D., Aloia, M., Muchira, C., Davé, R. N., and Yu, A. B. (2014). "Prediction of porosity from particle scale interactions: Surface modification of fine cohesive powders." *Powder Technology*, 254, 103–113.

Capece, M., Silva, K. R., Sunkara, D., Strong, J., and Gao, P. (2016). "On the relationship of inter-particle cohesiveness and bulk powder behavior: Flowability of pharmaceutical powders." *International Journal of Pharmaceutics*, Elsevier B.V., 511(1), 178–189.

Carson, J. W., and Pittenger, B. H. (1998). "Bulk Properties of Powders." *Powder Metal Technologies and Applications*, ASM Handbook, 287–301.

Castellanos, A. (2005). "The relationship between attractive interparticle forces and bulk behaviour in dry and uncharged fine powders." *Advances in Physics*, 54(4), 263–376.

El Cheikh, H., Courant, B., Branchu, S., Hascoët, J. Y., and Guillén, R. (2012a). "Analysis and prediction of single laser tracks geometrical characteristics in coaxial laser cladding process." *Optics and Lasers in Engineering*, 50(3), 413–422.

El Cheikh, H., Courant, B., Branchu, S., Huang, X., Hascoët, J. Y., and Guillén, R. (2012b). "Direct Laser Fabrication process with coaxial powder projection of 316L steel. Geometrical characteristics and microstructure characterization of wall structures." *Optics and Lasers in Engineering*, 50(12), 1779–1784.

El Cheikh, H., Courant, B., Hascoët, J. Y., and Guillén, R. (2012c). "Prediction and analytical description of the single laser track geometry in direct laser fabrication from process parameters and energy balance reasoning." *Journal of Materials Processing Technology*, Elsevier B.V., 212(9), 1832–1839.

Chen, X. Q., Wang, D., and Li, H. Z. (2009). "A hybrid method of reconstructing 3D airfoil profile from incomplete and corrupted optical scans." *International Journal of Mechatronics and Manufacturing Systems*, 2(1–2), 39–57.

Chen, Y., Yang, J., Dave, R. N., and Pfeffer, R. (2008). "Fluidization of coated group C powders." *AIChE Journal*, 54(1), 104–121.

Choi, S., Kim, T., and Yu, W. (2009). "Performance Evaluation of RANSAC Family." *Procedings of the British Machine Vision Conference 2009*, 81.1-81.12.

Chum, O., Matas, J., and Kittler, J. (2003). "Locally Optimized RANSAC." *Proceedings of the DAGM*, 2781, 236–243.

Chum, O., Matas, J., and Obdrzalek, S. (2004). "Enhancing RANSAC by generalized model optimization." *Asian Conference on Computer Vision*, 2, 812–817.

CIRAL et al. (1996). "Advanced Aluminium Precision Casting for Integrally Stiffened Net-Shape Components (ADVACAST)." *European Community Project - BRITE/EURAM Programme*, CIRAL - Thyssen FeinguB - Mirtec S.A. - University of Lisboa - Technische Universität München - University of Patras.

Cong, B., Ding, J., and Williams, S. (2015). "Effect of arc mode in cold metal transfer process on porosity of additively manufactured Al-6.3%Cu alloy." *International Journal of Advanced Manufacturing Technology*,

76(9–12), 1593–1606.
Coniglio, N., and Cross, C. E. (2013). "Initiation and growth mechanisms for weld solidification cracking." *International Materials Reviews*, 58(7), 375–397.
Cottam, R., Liu, Q., Wong, Y. C., Wang, J., and Brandt, M. (2011). "Laser cladding of high strength aluminium alloy 7075 powder on a 7075 substrate for repair of damged components." *Materials Forum*, 35, 89–94.
D. G. Eskin (Ed.). (2008). *Physical Metallurgy of Direct Chill Casting of Aluminium Alloys*. CRC Press.
Dinda, G. P., Dasgupta, A. K., and Mazumder, J. (2012). "Evolution of microstructure in laser deposited Al-11.28%Si alloy." *Surface and Coatings Technology*, Elsevier B.V., 206(8–9), 2152–2160.
Dumant, X. (1996). "Choix d'alliages de fonderie pour applications moteurs aéronautiques." *Internal Report*, Howmet CIRAL (ALCOA).
Dunst, P., Bornmann, P., Hemsel, T., and Sextro, W. (2018). "Vibration-Assisted Handling of Dry Fine Powders." *Actuators*, 7(2), 18.
Echebarria, B., Folch, R., Karma, A., and Plapp, M. (2004). "Quantitative phase-field model of alloy solidification." *Physical Review E - Statistical Physics, Plasmas, Fluids, and Related Interdisciplinary Topics*, 70(6), 22.
Edelsbrunner, H., and Mucke, E. P. (1994). "Three-dimensional Alpha Shapes." *ACM Transactions on Graphics*, 13(1), 43–72.
Fabbro, R. (2019). "Scaling laws for the laser welding process in keyhole mode." *Journal of Materials Processing Technology*, 264(September 2018), 346–351.
Fayed, M. E., and Otten, L. (1997). *Handbook of Powder Science and Technology. Powder Technology*, Springer US, Boston, MA.
Feng, J. Q., and Hays, D. A. (2003). "Relative importance of electrostatic forces on powder particles." *Powder Technology*, 135–136, 65–75.
Fischler, M. a, and Bolles, R. C. (1981). "Random Sample Consensus: A Paradigm for Model Fitting with Applications to Image Analysis and Automated Cartography." *Communications of the ACM*, 24(6), 381–395.
Freneaux, O., Poulet, J.-B., Lepre, O., and Montavon, G. (1993). "Buse coaxiale de traitement superficiel sous irradiation laser, avec apport de matériaux sous forme de poudre." Patent EP057458B1, IREPA Laser, Electricité de Strasbourg S.A.
Fronius International GmbH. (2013). "CMT : Cold Metal Transfer." <http://www.digitalweldingsolutions.com/CMT.pdf> (Mar. 10, 2019).
Galenko, P. (2007). "Solute trapping and diffusionless solidification in a binary system." *Physical Review E*, 76(3), 031606.
Galenko, P. K., Abramova, E. V., and Herlach, D. M. (2011). "Phase-Field Study of SOlute Trapping Effect in Rapid Solidification." *Discrete and Continuous Dynamical Systems*, (Suplement), 457–466.
Gao, J., Chen, X., Yilmaz, O., and Gindy, N. (2008). "An integrated adaptive repair solution for complex aerospace components through geometry reconstruction." *International Journal of Advanced Manufacturing Technology*, 36(11–12), 1170–1179.
Gao, J., Chen, X., Zheng, D., Yilmaz, O., and Gindy, N. (2006). "Adaptive restoration of complex geometry parts through reverse engineering application." *Advances in Engineering Software*, 37(9), 592–600.
Gao, J., Folkes, J., Yilmaz, O., and Gindy, N. (2005). "Investigation of a 3D non-contact measurement based blade repair integration system." *Aircraft Engineering and Aerospace Technology*, 77(1), 34–41(8).
Garg, R., Galvin, J., Li, T., and Pannala, S. (2012a). "Open-source MFIX-DEM software for gas-solids flows: Part I-Verification studies." *Powder Technology*, 220, 122–137.
Garg, R., Galvin, J., Li, T., and Pannala, S. (2012b). "Documentation of open-source MFIX-DEM software for gas-solids flows." <https://mfix.netl.doe.gov/documentation/dem_doc_2012-1.pdf>.
Ghaini, F. M., Sheikhi, M., Torkamany, M. J., and Sabbaghzadeh, J. (2009). "The relation between liquation and solidification cracks in pulsed laser welding of 2024 aluminium alloy." *Materials Science and Engineering A*, 519(1–2), 167–171.
Gibson, I., Rosen, D., and Stucker, B. (2015). *Additive Manufacturing Technologies. Springer New York*

Heidelberg Dordrecht London.

Gill, S. C., and Kurz, W. (1993). "Rapidly solidified AlCu alloys-I. experimental determination of the microstructure selection map." *Acta Metallurgica Et Materialia*, 41(12), 3563–3573.

Gill, S. C., and Kurz, W. (1995). "Rapidly solidified AlCu alloys-II. Calculation of the microstructure selection map." *Acta Metallurgica Et Materialia*, 43(1), 139–151.

Götzinger, M., and Peukert, W. (2003). "Dispersive forces of particle-surface interactions: Direct AFM measurements and modelling." *Powder Technology*, 130(1–3), 102–109.

Graf, B., Gumenyuk, A., and Rethmeier, M. (2012). "Laser Metal Deposition as Repair Technology for Stainless Steel and Titanium Alloys." *Physics Procedia*, 39, 376–381.

Gu, J., Bai, J., Ding, J., Williams, S., Wang, L., and Liu, K. (2018). "Design and cracking susceptibility of additively manufactured Al-Cu-Mg alloys with tandem wires and pulsed arc." *Journal of Materials Processing Technology*, Elsevier B.V., 262, 210–220.

Guyer, J. E., Wheeler, D., and Warren, J. A. (2009). "FiPy: Partial Differential Equations with Python." *Computing in Science & Engineering*, 11(3), 6–15.

Hamaker, H. C. (1937). "The London—van der Waals attraction between spherical particles." *Physica*, 4(10), 1058–1072.

Hann, D. B., Iammi, J., and Folkes, J. (2011). "A simple methodology for predicting laser-weld properties from material and laser parameters." *Journal of Physics D: Applied Physics*, 44(44).

Hascoët, J.-Y., Querard, V., and Rauch, M. (2017). "Interests of 5 Axis Toolpaths Generation for Wire Arc Additive Manufacturing of Aluminium Alloys." *Journal of Machine Engineering*, 13(3), 51–65.

Hascoët, J.-Y., Touzé, S., and Rauch, M. (2018a). "Automated identification of defect geometry for metallic part repair by an additive manufacturing process." *Welding in the World*, Metz, France, 62(2), 229–241.

Hascoët, J., Quérard, V., and Rauch, M. (2018b). "Wire Arc Additive Manufacturing of aluminium alloy structure on curved metal sheet using 5 axis tool paths and CMT welding process." *Soudage et Techniques Connexes*, (Mars-Avril), 37–40.

Hast, A., Nysjö, J., and Marchetti, A. (2013). "Optimal RANSAC - Towards a repeatable algorithm for finding the optimal set." *Journal of WSCG*, 21(1), 21–30.

Hatch, J. E. (1984). *Aluminum Properties and Physical Metallurgy*. ASM International.

Hitchcox, T., and Zhao, Y. F. (2018). "Random walks for unorganized point cloud segmentation with application to aerospace repair." *Procedia Manufacturing*, Elsevier B.V., 26, 1483–1491.

Hu, B., and Richardson, I. M. (2006). "Mechanism and possible solution for transverse solidification cracking in laser welding of high strength aluminium alloys." *Materials Science and Engineering A*, 429(1–2), 287–294.

Huang, C., Cao, G., and Kou, S. (2004). "Liquation cracking in partial penetration aluminium welds: assessing tendencies to liquate, crack and backfill." *Science and Technology of Welding and Joining*, 9(2), 149–157.

Huang, C., and Kou, S. (2000). "Partially Melted Zone in Aluminum Welds — Liquation Mechanism and Directional Solidification." *Welding Research*, (May), 113–120.

Huang, C., and Kou, S. (2003). "Liquation cracking in partial-penetration aluminum welds: Effect of penetration oscillation and backfilling." *Welding Journal*, 7(82), 184S–194S.

Huang, C., and Kou, S. (2004). "Liquation Cracking in Full-penetration Al-Cu Welds." *Welding Journal*, 83(4), 50S–58S.

Huang, Z., Scicolone, J. V., Gurumuthy, L., and Davé, R. N. (2015). "Flow and bulk density enhancements of pharmaceutical powders using a conical screen mill: A continuous dry coating device." *Chemical Engineering Science*, Elsevier, 125, 209–224.

Ibarra-Medina, J., and Pinkerton, A. J. (2010). "A CFD model of the laser, coaxial powder stream and substrate interaction in laser cladding." *Physics Procedia*, Elsevier, 5(PART 2), 337–346.

Ireland, P. M. (2010). "Triboelectrification of particulate flows on surfaces: Part II - Mechanisms and models." *Powder Technology*, 198(2), 199–210.

Isanaka, S. P., Karnati, S., and Liou, F. (2016). "Blown powder deposition of 4047 aluminum on 2024 aluminum substrates." *Manufacturing Letters*, Society of Manufacturing Engineers (SME), 7, 11–14.

Israelachvili, J. N. (2011). *Intermolecular and Surface Forces*. Elsevier Inc.

Jackson, R. L., Green, I., and Marghitu, D. B. (2010). "Predicting the coefficient of restitution of impacting elastic-perfectly plastic spheres." *Nonlinear Dynamics*, 60(3), 217–229.

Jiang, K., and Pinchuk, P. (2016). "Temperature and size-dependent Hamaker constants for metal nanoparticles." *Nanotechnology*, IOP Publishing, 27(34), 1–9.

Jones, J. B., McNutt, P., Tosi, R., Perry, C., and Wimpenny, D. I. (2012). "Remanufacture of turbine blades by laser cladding, machining and in-process scanning in a single machine." *23rd Annual International Solid Freeform Fabrication Symposium, Austin, Texas, USA*, 821–827.

Kang, Z., and Li, Z. (2015). "Primitive Fitting Based on the Efficient multiBaySAC Algorithm." (29), 1–21.

Karma, A. (2001). "Phase-field formulation for quantitative modeling of alloy solidification." *Physical Review Letters*, 87(11), 115701-1-115701–4.

Kathuria, Y. P. (2000). "Some aspects of laser surface cladding in the turbine industry." *Surface and Coatings Technology*, 132(2–3), 262–269.

Kaufman, J. G. (2000). *Introduction to Aluminum Alloys and Tempers*. *ASM International*.

Kaufman, J. G., and Rooy, E. L. (2004). *Aluminium Alloy Castings: Properties, Processes, and Applications*. ASM International.

Kerbrat, O., Mognol, P., and Hascoët, J. Y. (2011). "A new DFM approach to combine machining and additive manufacturing." *Computers in Industry*, 62(7), 684–692.

Kerninon, J., Mognol, P., Hascoet, J.-Y., and Legonidec, C. (2008). "Effect of path strategies on metallic parts manufactured by additive process." *Solid Freeform Fabrication Symposium*, 352–361.

King, W. E., Barth, H. D., Castillo, V. M., Gallegos, G. F., Gibbs, J. W., Hahn, D. E., Kamath, C., and Rubenchik, A. M. (2014). "Observation of keyhole-mode laser melting in laser powder-bed fusion additive manufacturing." *Journal of Materials Processing Technology*, 214(12), 2915–2925.

Klasing, K., Althoff, D., Wollherr, D., and Buss, M. (2009). "Comparison of surface normal estimation methods for range sensing applications." *IEEE International Conference on Robotics and Automation*, 3206–3211.

Koehler, H., Partes, K., Seefeld, T., and Vollertsen, F. (2010). "Laser reconditioning of crankshafts: From lab to application." *Physics Procedia*, Elsevier, 5(PART 1), 387–397.

Kou, S. (2001). "Partially Melted Zone in Aluminum Welds : Solute Segregation and Mechanical Behavior." *Welding Journal*, Welding Re, 9s–17s.

Kou, S. (2003). *Welding Metallurgy Second Edition*. John Wiley & Sons, Inc.

Kou, S. (2015a). "A criterion for cracking during solidification." *Acta Materialia*, Acta Materialia Inc., 88, 366–374.

Kou, S. (2015b). "A Simple Index for Predicting the Susceptibility to Solidification Cracking." *Welding Journal*, 94(12), 374s–388s.

Kovalev, O. B., Bedenko, D. V., and Zaitsev, A. V. (2018). "Development and application of laser cladding modeling technique: From coaxial powder feeding to surface deposition and bead formation." *Applied Mathematical Modelling*, Elsevier Inc., 57, 339–359.

Kowalczuk, P. B., and Drzymala, J. (2016). "Physical meaning of the Sauter mean diameter of spherical particulate matter." *Particulate Science and Technology*, Taylor & Francis, 34(6), 645–647.

Kurz, W., and Trivedi, R. (1994). "Rapid solidification processing and microstructure formation." *Materials Science and Engineering A*, 179–80(pt 1), 46–51.

Laitinen, O., Bauer, K., Niinimäki, J., and Peuker, U. A. (2013). "Validity of the Rumpf and the Rabinovich adhesion force models for alumina substrates with nanoscale roughness." *Powder Technology*, Elsevier B.V., 246, 545–552.

LaMarche, C. Q., Leadley, S., Liu, P., Kellogg, K. M., and Hrenya, C. M. (2017). "Method of quantifying surface roughness for accurate adhesive force predictions." *Chemical Engineering Science*, Elsevier, 158(July 2016), 140–153.

LaMarche, C. Q., Miller, A. W., Liu, P., and Hrenya, C. M. (2016). "Linking micro-scale predictions of capillary forces to macro-scale fluidization experiments in humid environments." *AIChE Journal*, 62(10), 3585–3597.

Lavernia, E. J., and Chang, C. I. (1997). "Theoretical Analysis of Powder Size Distribution." *Air Force Office of Scientific Research*, (Grant no. F49620-97-1-0301).

Lebeda, K., Matas, J. J., and Chum, O. (2012). "Fixing the Locally Optimized RANSAC." *Procedings of the British Machine Vision Conference 2012*, 95.1-95.11.

Lefèvre, G., and Jolivet, a. (2009). "Calculation of Hamaker constants applied to the deposition of metallic oxide particles at high temperature." *Proceedings of International Conference on Heat Exchanger Fouling an Cleaning VIII*, 2009, 120–124.

Lei, X., Deng, Y., Yin, Z., and Xu, G. (2014). "Tungsten inert gas and friction stir welding characteristics of 4-mm-thick 2219-T87 plates at room temperature and -196 °C." *Journal of Materials Engineering and Performance*, 23(6), 2149–2158.

Leite, F. L., Bueno, C. C., Da Róz, A. L., Ziemath, E. C., and Oliveira, O. N. (2012). "Theoretical models for surface forces and adhesion and their measurement using atomic force microscopy." *International Journal of Molecular Sciences*, 13(10), 12773–12856.

Leturia, M., Benali, M., Lagarde, S., Ronga, I., and Saleh, K. (2014). "Characterization of flow properties of cohesive powders: A comparative study of traditional and new testing methods." *Powder Technology*, Elsevier B.V., 253, 406–423.

Li, T., Garg, R., Galvin, J., and Pannala, S. (2012). "Open-source MFIX-DEM software for gas-solids flows: Part II — Validation studies." *Powder Technology*, Elsevier B.V., 220, 138–150.

Li, W., Zhang, X., and Liou, F. (2018). "Modeling analysis of argon gas flow rate's effect on pre-mixed powder separation in laser metal deposition process and experimental validation." *International Journal of Advanced Manufacturing Technology*, The International Journal of Advanced Manufacturing Technology, 96(9–12), 4321–4331.

Lippold, J. C. (2015). *Welding Metallurgy and Weldability*. John Wiley & Sons.

Liu, P., LaMarche, C. Q., Kellogg, K. M., and Hrenya, C. M. (2016a). "Fine-particle defluidization: Interaction between cohesion, Young's modulus and static bed height." *Chemical Engineering Science*, Elsevier, 145, 266–278.

Liu, P., LaMarche, C. Q., Kellogg, K. M., and Hrenya, C. M. (2016b). "Fine-particle defluidization: Interaction between cohesion, Young's modulus and static bed height." *Chemical Engineering Science*, Elsevier, 145, 266–278.

Liu, Z., Jiang, Q., Li, T., Dong, S., Yan, S., Zhang, H., and Xu, B. (2016c). "Environmental benefits of remanufacturing: A case study of cylinder heads remanufactured through laser cladding." *Journal of Cleaner Production*, Elsevier Ltd, 133, 1027–1033.

Louvis, E., Fox, P., and Sutcliffe, C. J. (2011). "Selective laser melting of aluminium components." *Journal of Materials Processing Technology*, Elsevier B.V., 211(2), 275–284.

Lukas, H. L., Fries, S. G., and Sundman, B. (2007). *Computational Thermodynamics: The CALPHAD Method*. Cambridge University Press.

Lumley, R. N. (Ed.). (2018). *Fundamentals of Aluminium Metallurgy: Recent Advances*. Woodhead Publishing.

Malone, K. F., and Xu, B. H. (2008). "Determination of contact parameters for discrete element method simulations of granular systems." *Particuology*, 6(6), 521–528.

Marazani, T., Madyira, D. M., and Akinlabi, E. T. (2017). "Repair of Cracks in Metals: A Review." *Procedia Manufacturing*, The Author(s), 8(October 2016), 673–679.

Marinack, M. C., Musgrave, R. E., and Higgs, C. F. (2013). "Experimental investigations on the coefficient of restitution of single particles." *Tribology Transactions*, 56(4), 572–580.

Marshall, J. S., and Li, S. (2014). *Adhesive Particle Flow: A Discrete-Element Approach*. Cambridge University Press.

MatCalc. (2015). "Open databases." <https://www.matcalc.at/index.php/databases/open-databases>.

Mathers, G. (2002). *The welding of aluminium and its alloys*. Woodhead Publishing.

Matsusaka, S., Maruyama, H., Matsuyama, T., and Ghadiri, M. (2010). "Triboelectric charging of powders: A review." *Chemical Engineering Science*, Elsevier, 65(22), 5781–5807.

Matsusaka, S., and Masuda, H. (2003). "Electrostatics of particles." *Advanced Powder Technology*, Society of Powder Technology Japan, 14(2), 143–166.

Matsusaka, S., Urakawa, M., and Masuda, H. (1995). "Micro-feeding of fine powders using a capillary tube with ultrasonic vibration." *Advanced Powder Technology*, Society of Powder Technology Japan, 6(4), 283–293.

Michaud, E. J., Kerr, H. W., and Weckman, D. C. (1995). "Temporal pulse shaping and solidification cracking in laser welded Al-Cu alloys." *Trends in Welding Research, Proceedings of the 4th International Conference*, 153–158.

Mondolfo, L. F. (1976). *Aluminium Alloys: Structure and Properties*. Butterworth.

Moreira, A., and Santos, M. Y. (2007). "Concave Hull : A k-Nearest Neighbours approach for the computation of the region occupied by a set of points." *GRAPP*, 61–68.

Mukherjee, T., Manvatkar, V., De, A., and DebRoy, T. (2017). "Dimensionless numbers in additive manufacturing." *Journal of Applied Physics*, 121(6).

Muller, P. (2013). "Fabrication additive de pièces multimatériaux." PhD thesis, Ecole Centrale de Nantes.

Muller, P., Mognol, P., and Hascoet, J. Y. (2013). "Modeling and control of a direct laser powder deposition process for Functionally Graded Materials (FGM) parts manufacturing." *Journal of Materials Processing Technology*, Elsevier B.V., 213(5), 685–692.

Muster, T. H., Hughes, A. E., and Thompson, G. E. (2009). *Copper Distributions in Aluminium Alloys*. Nova Science Publishers.

Myatt, D., Torr, P., Bishop, J., and Craddock, R. (2002). "Napsac: High Noise, High Dimensional Model Parameterisation-It's in the Bag." *Proceedings of the 13th British Machine Vision Conference*, Cardiff, 458–467.

Navarro, H. A., and de Souza Braun, M. P. (2013). "Determination of the normal spring stiffness coefficient in the linear spring-dashpot contact model of discrete element method." *Powder Technology*, Elsevier B.V., 246, 707–722.

Norman, A. F., Drazhner, V., and Prangnell, P. B. (1999). "Effect of welding parameters on the solidification microstructure of autogenous TIG welds in an Al–Cu–Mg–Mn alloy." *Materials Science and Engineering: A*, 259(1), 53–64.

Nowotny, S., Scharek, S., Beyer, E., and Richter, K. H. (2007). "Laser beam build-up welding: Precision in repair, surface cladding, and direct 3D metal deposition." *Journal of Thermal Spray Technology*, 16(3), 344–348.

Oguchi, T., and Tamatani, M. (1993). "Contact electrification phenomena and powder surface treatments." *Wear*, 168(1–2), 91–98.

Okayasu, M., Ohkura, Y., Takeuchi, S., Takasu, S., Ohfuji, H., and Shiraishi, T. (2012). "A study of the mechanical properties of an Al-Si-Cu alloy (ADC12) produced by various casting processes." *Materials Science and Engineering A*, Elsevier B.V., 543(July 2013), 185–192.

Olakanmi, E. O. (2013). "Selective laser sintering/melting (SLS/SLM) of pure Al, Al-Mg, and Al-Si powders: Effect of processing conditions and powder properties." *Journal of Materials Processing Technology*, Elsevier B.V., 213(8), 1387–1405.

Olakanmi, E. O., Cochrane, R. F., and Dalgarno, K. W. (2015). "A review on selective laser sintering/melting (SLS/SLM) of aluminium alloy powders: Processing, microstructure, and properties." *Progress in Materials Science*, Elsevier Ltd, 74, 401–477.

Osborne-Lee, I. W. (1988). "Calculation of Hamaker Coefficients for Metallic Aerosols from Extensive Optical Data." *Particles on Surfaces 1*, Springer US, Boston, MA, 77–90.

Özbilen, S. (2014). "Satellite formation mechanism in gas atomised powders." *Powder Metallurgy*, 42(1), 70–78.

Pan, S., and Zhang, Z. (2019). "Fundamental theories and basic principles of triboelectric effect: A review." *Friction*, 7(1), 2–17.

Peart, J. (2001). "Powder electrostatics: Theory, techniques and applications." *KONA Powder and Particle Journal*, 19(May), 34–45.

Péchet, G., Hascoët, J.-Y., Rauch, M., Ruckert, G., and Thorr, A.-S. (2019). "Manufacturing of a hollow propeller blade with WAAM process - From the material characterisation to the achievement." *Sustainable Smart Manufacturing*, Manchester, UK.

Perrut, M. (2015). "Thermodynamic modeling by the calphad method and its applications to innovative materials." *AerospaceLab*, (9), 1–11.

Petrat, T., Graf, B., Gumenyuk, A., and Rethmeier, M. (2016). "Laser metal deposition as repair technology for a gas turbine burner made of inconel 718." *Physics Procedia*, 83, 761–768.

Peyre, P., Dal, M., Pouzet, S., and Castelnau, O. (2017). "Simplified numerical model for the laser metal deposition additive manufacturing process." *Journal of Laser Applications*, 29(2), 022304.

Pfeiler, W. (2007). *Alloy Physics*. Wiley-VCH Verlag GmbH & Co. KGaA.

Pinkerton, A. J. (2010). "Laser direct metal deposition: theory and applications in manufacturing and maintenance." *Advances in Laser Materials Processing: Technology, Research and Application*, 16, 461–491.

Pinkerton, A. J. (2015). "Advances in the modeling of laser direct metal deposition." *Journal of Laser Applications*, 27(October), S15001.

Pinkerton, A. J., and Li, L. (2004). "Modelling Powder Concentration Distribution From a Coaxial Deposition Nozzle for Laser-Based Rapid Tooling." *Journal of Manufacturing Science and Engineering*, 126(1), 33.

Pinkerton, A. J., Wang, W., and Li, L. (2008). "Component repair using laser direct metal deposition." *Proceedings of the Institution of Mechanical Engineers Part B Journal of Engineering Manufacture*, 827–836.

Pinomaa, T., and Provatas, N. (2019). "Quantitative phase field modeling of solute trapping and continuous growth kinetics in quasi-rapid solidification." *Acta Materialia*, Elsevier Ltd, 168, 167–177.

Piya, C., Wilson, J. M., Murugappan, S., Shin, Y., and Ramani, K. (2011). "Virtual Repair : Geometric Reconstruction for Remanufacturing Gas." *Proceedings of the ASME 2011 International Design Engineering Technical Conferences & Design for Manufacturing and the Life Cycle Conference, IDETC/CIE 2011*, ASME, ed., Washington DC, USA, 1–10.

Planchamp, C., Carlier, P., and Dumant, X. (1993). "Etude de l'amélioration de la technique de coulée cire perdue procédé SOPHIA de pièces à parois minces en AU5MVZr." *Programme de développement STPA-CIRAL*, Howmet CIRAL - Pechiney, Marché STPA n°8996025004717586.

Polizzi, M. A., Franchville, J., and Hilden, J. L. (2016). "Assessment and predictive modeling of pharmaceutical powder flow behavior in small-scale hoppers." *Powder Technology*, Elsevier B.V., 294, 30–42.

Ponche, R. (2013). "Méthodologie de conception pour la fabrication additive, application à la projection de poudres." PhD Thesis, Ecole Centrale de Nantes.

Ponche, R., Hascoet, J.-Y., Kerbrat, O., and Mognol, P. (2012). "A new global approach to design for additive manufacturing." *Virtual and Physical Prototyping*, 7(2), 93–105.

Ponche, R., Kerbrat, O., Mognol, P., and Hascoet, J. Y. (2014). "A novel methodology of design for Additive Manufacturing applied to Additive Laser Manufacturing process." *Robotics and Computer-Integrated Manufacturing*, Elsevier, 30(4), 389–398.

Pratt, V. (1987). "Direct Least-Squares Fitting of Algebraic Surfaces." *Computer Graphics*, 21(4), 145–152.

Quérard, V., Hascoët, J.-Y., and Rauch, M. (2018). "Toolpath generation for Wire Arc Additive Manufacturing of aluminum alloy: Non parallel slicing for WAAM parts." *Conférence MUGV2018 & Manufacturing'21*, ENSAM ParisTech, Campus Bordeaux-Talence.

Quinsat, Y., Dubreuil, L., and lartigue, C. (2017). "A novel approach for in-situ detection of machining defects." *International Journal of Advanced Manufacturing Technology*, 90(5–8), 1625–1638.

Quintino, L., Miranda, R., Dilthey, U., Iordachescu, D., Banasik, M., and Stano, S. (2010). "Laser Welding of Structural Aluminium." *Structural Connections for Lightweight Metallic Structures. Advanced Structured Materials, vol 8*, Springer Berlin Heidelberg, 33–57.

Rabinovich, Y. I., Adler, J. J., Ata, A., Singh, R. K., and Moudgil, B. M. (2000a). "Adhesion between nanoscale rough surfaces. I. Role of asperity geometry." *Journal of Colloid and Interface Science*, 232(1), 10–16.

Rabinovich, Y. I., Adler, J. J., Ata, A., Singh, R. K., and Moudgil, B. M. (2000b). "Adhesion between nanoscale rough surfaces: II. Measurement and comparison with theory." *Journal of Colloid and Interface Science*, 232(1), 17–24.

Rao, K. S., Reddy, G. M., and Rao, K. P. (2005). "Studies on partially melted zone in aluminium-copper alloy welds - Effect of techniques and prior thermal temper." *Materials Science and Engineering A*, 403(1–2), 69–76.

Rappaz, M., Drezet, J.-M., and Gremaud, M. (1999). "A new hot-tearing criterion." *Metallurgical and*

Materials Transactions A, 30(2), 449–455.

Richards, F. J. (1959). "A Flexible Growth Function for Empirical Use." 10(39), 290–300.

Rubenchik, A. M., King, W. E., and Wu, S. S. (2018). "Scaling laws for the additive manufacturing." *Journal of Materials Processing Technology*, 257, 234–243.

Rumman, R., Mallaiah, M., Touzé, S., Sims, R. A., Quinton, J. S., and Hascoët, J. Y. (2019). "Laser Metal Deposition of Al-12Si alloy: characterization of thin wall deposits." *to be published*.

Rumpf, H. (1990). *Particle Technology*. Chapman and Hall, London.

Sasabe, S. (2012). "Welding of 2000 series aluminium alloy materials." *Welding International*, 26(5), 339–350.

Schnabel, R., Wahl, R., and Klein, R. (2007). "Efficient RANSAC for point-cloud shape detection." *Computer Graphics Forum*, 26(2), 214–226.

Scipioni Bertoli, U., Wolfer, A. J., Matthews, M. J., Delplanque, J.-P. R., and Schoenung, J. M. (2017). "On the limitations of Volumetric Energy Density as a design parameter for Selective Laser Melting." *Materials & Design*, 113, 331–340.

Selvi, S., Vishvaksenan, A., and Rajasekar, E. (2018). "Cold metal transfer (CMT) technology - An overview." *Defence Technology*, Elsevier Ltd, 14(1), 28–44.

Shah, U. V., Karde, V., Ghoroi, C., and Heng, J. Y. Y. (2017). "Influence of particle properties on powder bulk behaviour and processability." *International Journal of Pharmaceutics*, Elsevier B.V., 518(1–2), 138–154.

Sheikhi, M., Ghaini, F. M., Torkamany, M. J., and Sabbaghzadeh, J. (2009). "Characterisation of solidification cracking in pulsed Nd:YAG laser welding of aluminium alloy." *Science and Technology of Welding and Joining*, 14(12), 161–165.

Sheikhi, M., Malek Ghaini, F., and Assadi, H. (2015). "Prediction of solidification cracking in pulsed laser welding of 2024 aluminum alloy." *Acta Materialia*, Acta Materialia Inc., 82, 491–502.

Siliveru, K., Jange, C. G., Kwek, J. W., and Ambrose, R. P. K. (2017). "Granular bond number model to predict the flow of fine flour powders using particle properties." *Journal of Food Engineering*, Elsevier Ltd, 208, 11–18.

Spierings, A. B., Voegtlin, M., Bauer, T., and Wegener, K. (2015). "Powder flowability characterisation methodology for powder-bed-based metal additive manufacturing." *Progress in Additive Manufacturing*, Springer International Publishing, 1(1–2), 9–20.

Srdja Zekovic, Rajeev Dwivedi, R. K. (2006). "An Investigation of Gas-Powder Flow in Laser-Based Direct Metal Deposition." *International Journal of Machine Tools and Manufacture*, 558–572.

Staffa, K. H., Jahn, J., and Claussen, N. (1977). "Flowability of powders under the influence of vibrations." *Powder Metallurgy*, 9, 20–23.

Stichel, T., Laumer, T., Baumüller, T., Amend, P., and Roth, S. (2014). "Powder layer preparation using vibration-controlled capillary steel nozzles for additive manufacturing." *Physics Procedia*, Elsevier B.V., 56(C), 157–166.

Stichel, T., Laumer, T., Linnenweber, T., Amend, P., and Roth, S. (2016). "Mass flow characterization of selective deposition of polymer powders with vibrating nozzles for laser beam melting of multi-material components." *Physics Procedia*, 83, 947–953.

Sundman, B., Kattner, U. R., Palumbo, M., and Fries, S. G. (2015). "OpenCalphad - a free thermodynamic software." *Integrating Materials and Manufacturing Innovation*, 4(1), 1–15.

Sverdlin, A. (2003). "Introduction to Aluminum." *Handbook of Aluminum - Volume 1: Physical Metallurgy and Processes.*, G. E. Totten and D. S. MacKenzie, eds., Dekker, 1–32.

Sweny, R. A., Tressler, J. F., and Martukanitz, R. P. (2018). "Development and Evaluation of an Advanced Aluminum Alloy for Additive Manufacturing." *Journal of Material Science & Engineering*, 7(6), 1–10.

Syamlal, M., Rogers, W., and O`Brien, T. J. (1993). "MFIX documentation theory guide."

Tabernero, I., Lamikiz, A., Ukar, E., López de Lacalle, L. N., Angulo, C., and Urbikain, G. (2010). "Numerical simulation and experimental validation of powder flux distribution in coaxial laser cladding." *Journal of Materials Processing Technology*, Elsevier B.V., 210(15), 2125–2134.

Tan, H., Shang, W., Zhang, F., Clare, A. T., Lin, X., Chen, J., and Huang, W. (2018). "Process mechanisms based on powder flow spatial distribution in direct metal deposition." *Journal of Materials Processing Technology*, Elsevier, 254(November 2017), 361–372.

Tan, J. H., Wong, W. L. E., and Dalgarno, K. W. (2017). "An overview of powder granulometry on feedstock and part performance in the selective laser melting process." *Additive Manufacturing*, Elsevier B.V., 18, 228–255.

Tao, W., Huapeng, D., Hao, W., and Jie, T. (2015). "Virtual remanufacturing: Cross-section curve reconstruction for repairing a tip-defective blade." *Proceedings of the Institution of Mechanical Engineers, Part C: Journal of Mechanical Engineering Science*, 0(0), 1–12.

Torr, P. H. S., and Zisserman, A. (2000). "MLESAC: A New Robust Estimator with Application to Estimating Image Geometry." *Computer Vision and Image Understanding*, 78(1), 138–156.

Touzé, S., Rauch, M., and Hascoët, J.-Y. (2018). "Segmentation method for automated repair with an additive manufacturing process." *Conférence MUGV2018 & Manufacturing'21*, ENSAM ParisTech, Campus Bordeaux-Talence.

Tran, H. S., Tchuindjang, J. T., Paydas, H., Mertens, A., Jardin, R. T., Duchêne, L., Carrus, R., Lecomte-Beckers, J., and Habraken, A. M. (2017). "3D thermal finite element analysis of laser cladding processed Ti-6Al-4V part with microstructural correlations." *Materials and Design*, Elsevier, 128(January), 130–142.

Trivedi, R. (1994). "Microstructure characteristics of rapidly solidified alloys." *Materials Science and Engineering: A*, 178(1–2), 129–135.

Trucco, E., Fisher, R. B., and Fitzgibbon, A. W. (1994). "Direct Calibration and Data Consistency in 3-D Laser Scanning." *Proceedings of the British Machine Vision Conference*, 2(November 2016), 489–498.

Trucco, E., Fisher, R. B., Fitzgibbon, A. W., and Naidu, D. K. (1998). "Calibration, data consistency and model acquisition with laser stripers." *International Journal of Computer Integrated Manufacturing*, 11(4), 293–310.

Um, J., Rauch, M., Hascoët, J. Y., and Stroud, I. (2017). "STEP-NC compliant process planning of additive manufacturing: remanufacturing." *International Journal of Advanced Manufacturing Technology*, The International Journal of Advanced Manufacturing Technology, 88(5–8), 1215–1230.

Uzi, A., and Levy, A. (2018). "Energy absorption by the particle and the surface during impact." *Wear*, Elsevier B.V., 404–405(December 2017), 92–110.

Valencia, J. J. (2008). "Thermophysical Properties Sources and Availability of Reliable Data." *ASM Handbook, Volume 15: Casting*, 15(Ref 24), 468–481.

Verhaeghe, G., and Hilton, P. (2004). "Laser welding of low-porosity aerospace aluminium alloy." *Proceedings of the 34th International Matador Conference*, 241–246.

Vock, S., Klöden, B., Kirchner, A., Weißgärber, T., and Kieback, B. (2019). "Powders for powder bed fusion: a review." *Progress in Additive Manufacturing*, Springer International Publishing.

Wang, Y., and Feng, H. Y. (2014). "Modeling outlier formation in scanning reflective surfaces using a laser stripe scanner." *Measurement: Journal of the International Measurement Confederation*, Elsevier Ltd, 57, 108–121.

Wen, S. Y., Shin, Y. C., Murthy, J. Y., and Sojka, P. E. (2009). "Modeling of coaxial powder flow for the laser direct deposition process." *International Journal of Heat and Mass Transfer*, Elsevier Ltd, 52(25–26), 5867–5877.

Wilson, J. M., Piya, C., Shin, Y. C., Zhao, F., and Ramani, K. (2014). "Remanufacturing of turbine blades by laser direct deposition with its energy and environmental impact analysis." *Journal of Cleaner Production*, Elsevier Ltd, 80, 170–178.

Wilson, R., Dini, D., and Van Wachem, B. (2017). "The influence of surface roughness and adhesion on particle rolling." *Powder Technology*, The Authors, 312, 321–333.

Wu, H., Gao, J., Li, S., Zhang, Y., and Zheng, D. (2013). "A review of geometric reconstruction algorithm and repairing methodologies for gas turbine components." *Telkomnika*, 11(3), 1609–1618.

Yang, S. C. (2006). "Segregation of cohesive powders in a vibrated granular bed." *Chemical Engineering Science*, 61(18), 6180–6188.

Yang, S., and Evans, J. R. G. (2005). "Acoustic initiation of powder flow in capillaries." *Chemical Engineering Science*, 60(2), 413–421.

Yang, S., and Evans, J. R. G. (2007). "Metering and dispensing of powder; the quest for new solid freeforming techniques." *Powder Technology*, 178(1), 56–72.

Yilmaz, O., Gindy, N., and Gao, J. (2010). "A repair and overhaul methodology for aeroengine components." *Robotics and Computer-Integrated Manufacturing*, Elsevier, 26(2), 190–201.

Zhang, H., Zhu, H., Qi, T., Hu, Z., and Zeng, X. (2016). "Selective laser melting of High Strength Al-Cu-Mg alloys: Processing, microstructure and mechanical properties." *Materials Science and Engineering: A*, Elsevier, 656, 47–54.

Zhang, K., Li, D., Gui, H., and Li, Z. (2018a). "An adaptive slicing algorithm for laser cladding remanufacturing of complex components." *The International Journal of Advanced Manufacturing Technology*, Springer London, 1–15.

Zhang, X., Li, W., Adkison, K. M., and Liou, F. (2018b). "Damage reconstruction from tri-dexel data for laser-aided repairing of metallic components." *International Journal of Advanced Manufacturing Technology*, The International Journal of Advanced Manufacturing Technology, 96(9–12), 3377–3390.

Zhang, X., Li, W., Chen, X., Cui, W., and Liou, F. (2018c). "Evaluation of component repair using direct metal deposition from scanned data." *International Journal of Advanced Manufacturing Technology*, The International Journal of Advanced Manufacturing Technology, 95(9–12), 3335–3348.

Zhang, Y., Yang, Z., He, G., Qin, Y., and Zhang, H. C. (2015). "Remanufacturing-oriented geometric modelling for the damaged region of components." *Procedia CIRP*, Elsevier B.V., 29, 798–803.

Zhao, L. Z., Zhao, M. J., Song, L. J., and Mazumder, J. (2014). "Ultra-fine Al-Si hypereutectic alloy fabricated by direct metal deposition." *Materials and Design*, Elsevier Ltd, 56, 542–548.

Zhao, Y., Sun, J., Jia, Z., Cheng, W., and Wang, J. (2018). "Research on Laser Additive and Milling Subtractive Composite Remanufacturing Process of Compressor Blade." *Journal of Manufacturing and Materials Processing*, 2(4), 73.

Zhu, H. P., Zhou, Z. Y., Yang, R. Y., and Yu, A. B. (2007). "Discrete particle simulation of particulate systems: Theoretical developments." *Chemical Engineering Science*, 62(13), 3378–3396.

Zimmermann, M., Carrard, M., Gremaud, M., and Kurz, W. (1991). "Characterization of the banded structure in rapidly solidified AlCu alloys." *Materials Science and Engineering A*, 134(C), 1278–1282.

Zolotorevsky, V. S., Belov, N. A., and Glazoff, M. V. (2007). *Casting Aluminium Alloys*. Elsevier.

Zuliani, M., Kenney, C. S., and Manjunath, B. S. (2005). "The multiransac algorithm and its application to detect planar homographies." *Proceedings - International Conference on Image Processing, ICIP*, 3, 153–156.

UNIVERSITE BRETAGNE SCIENCES LOIRE POUR L'INGENIEUR

CENTRALE NANTES

Titre : Laser Metal Deposition d'alliages Aluminium-Cuivre pour la Réparation.....
....

Mots clés : Fabrication Additive, Laser Metal Deposition, Réparation, Aluminium

Résumé : Ce travail de thèse vise à démontrer la faisabilité de la réparation de pièces de fonderie à haute performance et haute valeur ajoutée faites d'un alliage aluminium-cuivre en utilisant un procédé de fabrication additive métallique par projection de poudre avec fusion laser dénommé Laser Metal Deposition. Ces alliages présentent notamment une faible soudabilité et ne peuvent donc être réparés de façon fiable par des procédés traditionnels de soudage à l'arc. Afin de permettre l'utilisation de ce procédé innovant pour la réparation de pièces en alliage Al-Cu, des difficultés majeures ont dû être levées en ce qui concerne notamment la coulabilité des poudres Al-Cu et leur comportement en fusion et en solidification, ainsi que la méthodologie de réparation pour effectuer l'opération de façon fiable et efficace. Des travaux expérimentaux, théoriques et numériques ont permis d'élucider ces aspects et in fine de permettre l'utilisation de ce matériau avec ce procédé de fabrication additive. Une méthode de réparation comprenant un algorithme de segmentation robuste a également été développée et mise en œuvre afin d'automatiser le processus de réparation en permettant la génération de trajectoire sur la base de mesures 3D in-situ. Des réparations de pièces de fonderie en aluminium-cuivre ont ainsi pu être effectuées avec le procédé Laser Metal Deposition, et les analyses métallographiques montrent que les rechargements effectués avec ce procédé offrent une microstructure très fine avec un taux de ségrégation chimique limité et peu de fissuration à chaud.

Title : Laser Metal Deposition of Aluminium-Copper alloys for Repair applications.....
....

Keywords : Additive Manufacturing, Laser Metal Deposition, Repair, Aluminium alloys

Abstract : The present thesis aims at demonstrating the feasibility of repairing high performance castings made of an aluminium-copper alloy using the Laser Metal Deposition metal additive manufacturing process. These alloys present a low weldability and thus cannot be reliably repaired with manual arc-welding processes. To instead use this innovative additive manufacturing process for repair applications and thereby improve upon current methods, major challenges had to be overcome regarding the flowability and solidification behavior of this aluminium alloy powder as well as the overall methodology to reliably and efficiently perform the repair operation. Experimental, theoretical and numerical studies allowed to elucidate some of these aspects and eventually enabled the use of a 224.0 casting aluminium alloy with the Laser Metal Deposition metal additive manufacturing process. A repair methodology including a robust segmentation algorithm was also developped to automate the repair process and permit the generation of toolpaths based on raw in-situ 3D scanning measurements.
Repairs of high performance aluminium-copper castings were carried out successfully as no major lack of fusion, bonding or cracking defects were observed. A metallographic analysis showed that the aluminium deposits obtained by Laser Metal Deposition generally offer a refined microstructure with limited solute segregation and hot cracking.